The Origin of Metalliferous Argillites in the Shoal Arm Formation of North-Central Newfoundland

Abstract of

a thesis presented to the Faculty

of the State University of New York

at Albany

in partial fulfillment of the requirements

for the degree of

Master of Sciences

College of Science and Mathematics

Department of Geological Sciences

Volker Brüchert
1992

ABSTRACT

The Middle Ordovician Shoal Arm Formation, which is located in the central volcanic belt of north-central Newfoundland, is a tripartite assemblage of hematitic argillites, grey cherts, and black shales directly underlying a flysch sequence. The hematitic argillites are enriched in Fe, Mn, Ni, Pb, and Co. Factor analysis and principal component analysis indicate the presence of a hydrothermal component, presumably derived from hydrothermal activity in the coeval Lawrence Head volcanics. Unusual, (?) calcareous Mn-Fe-oxide nodules are present in the top parts of turbidites in the hematitic argillites. Electron microprobe analysis of a color transition from a red to a green argillite indicates fractionation of Mn from Fe by diagenetic mobilization of Mn and subsequent precipitation as Mn-carbonate in adjacent green, calcareous argillites. The detrital component of the Shoal Arm Formation is influenced by several, geochemically different, clastic sources. The top part of the Shoal Arm Formation is characterized by a Zr-, Nb-, and Y-rich clastic component that may reflect either erosion or volcanic activity of lateral equivalents of the Lawrence Head volcanics. The hydrothermal component disappeared with erosion of these volcanics. The overlying grey, mottled and laminated cherts reflect a biogenic bloom, which preceded euxinification of the depositional basin. Synchronous and diachronous depositional models are proposed to explain the tectonic history of the Shoal Arm Formation. The synchronous model emphasizes the high biological productivity and limited circulation in a restricted basin as the cause for the observed euxinification. The diachronous model explains the black shale facies with a prograding, deep-water anoxic layer that developed during rapid basin subsidence as the result of thrust-loading. In this model, the black shales were deposited in front of flysch sediments derived from a southeastward prograding thrust stack.

The Middle Ordovician Taconic sequence of New York (i.e., the upper part of the Poultney Formation, the Indian River, and the Mt. Merino Formations) exhibits hematitic

argillites in a similar lithostratigraphic position relative to black shale and flysch as the Shoal Arm Formation. Comparison of the Shoal Arm Formation with this part of the Taconic sequence indicates that the two tectonic models are also applicable to this sequence. Both the Indian River Formation and the Mt. Merino Formation are slightly enriched in Fe, Mn, and the trace elements Pb and Ni. This modest metal enrichment is explained either by recycling of Fe and Mn into the seawater in expanded oxygen minimum zones and subsequent precipitation at oxic/anoxic interfaces, or by a distal hydrothermal component. A continental source of Fe is excluded. Minor enrichment of biogenically derived material in the Mt. Merino Formation suggests that biological productivity may not have been the determining factor for euxinification.

The comparison with Precambrian sequences that contain Superior-type banded iron-formations and black shales in comparable stratigraphic positions indicates little geochemical similarity with the two Ordovician sequences. Enrichments of Fe, Mn, Pb, Ni, Co, and Cr in both iron-formations and black shales are generally stronger than in the Ordovician cases. Interpretations of biological productivity are hampered by the insufficient knowledge of inorganic element associations with biological matter in Precambrian oceans. As a consequence, it is difficult to test the proposed tectonic models with the available geochemical data. Comparisons to that point have to rely upon field observations alone.

The Origin of Metalliferous Argillites

in the Shoal Arm Formation of North-Central Newfoundland

A thesis presented to the Faculty

of the State University of New York

at Albany

in partial fulfillment of the requirements

for the degree of

Master of Sciences

College of Science and Mathematics

Department of Geological Sciences

Volker Brüchert
1992

ACKNOWLEDGEMENTS

I am indebted to the members of my defense committee, John Delano, Bill Kidd, and Nick Donnelly, for their helpful comments on this manuscript. In particular, I gratefully acknowledge John Delano for his permanent advice, enthusiasm and encouragement and also for his editorial efforts throughout the preparation of this thesis. Not only did he assist me in successfully completing this study, but also taught me the more general lesson of how to approach and perform a scientific project. I would like to thank Bill Kidd for suggesting this project, for his help and his financial support during the field work. He provided invaluable information on the regional geology of Newfoundland and the Taconic Allochthon. I would like to thank my parents, who encouraged me to study abroad, and without whose financial assistance it would have never been possible for me to come to this school. Ben Hanson's help to perform the microprobe analyses is highly appreciated. Thanks also goes to the graduate students at the Department of Geology, to my friends in Germany, and in particular to my friend Sue. Financial support for this study was provided by grants from the SUNY Benevolent Fund, Sigma Xi, as well as from grants awarded to John Delano.

TABLE OF CONTENTS

LIST OF TABLES

Table

LIST OF FIGURES

Figure

1. GENERAL INTRODUCTION

1.1 The sedimentary sequence in pre-collisional continental margin sediments of the northern Appalachians

Certain Paleozoic marine sediments of the northern Appalachians show a characteristic sedimentary sequence. These sediments accumulated prior to and during the collision of a microcontinent and/or an island arc with the North American continent in the medial Ordovician. Overlying a Cambro-Ordovician clastic substrate, the following sequence can be observed: From base to top: (1) red, hematitic argillites; (2) black shales; (3) flysch sediments. The Ordovician, Taconic Allochthon in New York State contains an example of this sequence (Rowley and Kidd, 1981). Figure 1.1 schematically illustrates the tectonic environment for the deposition of the observed strata. The underlying substrate here is thought to represent the slope and rise sediments of the North American continental margin (Bird and Dewey, 1970). Accumulation of the red, metalliferous argillites took place when the substrate moved into the position of an outer trench slope relative to an advancing accretionary prism (Rowley and Kidd, 1981). Figure 1.1 displays a time period where the accretionary stack has not yet reached the shelf platform. The approach of the accretionary prism is constrained by the deposition of the overlying black shales and different petrographic characteristics of the flysch sediments. The flysch sediments are interpreted as the trench filling sequence and derive their material from the accretionary stack (Rowley and Kidd, 1981). The black shales occur both on top of shallow water (shelf carbonates) and in deep water (continental rise argillites) substrates under the flysch sediments. Black shale deposition was time transgressive to the west, and was controlled by the migration and loading of the accretionary stack (Bradley, 1989; Rowley and Kidd, 1981; Bradley and Kusky,

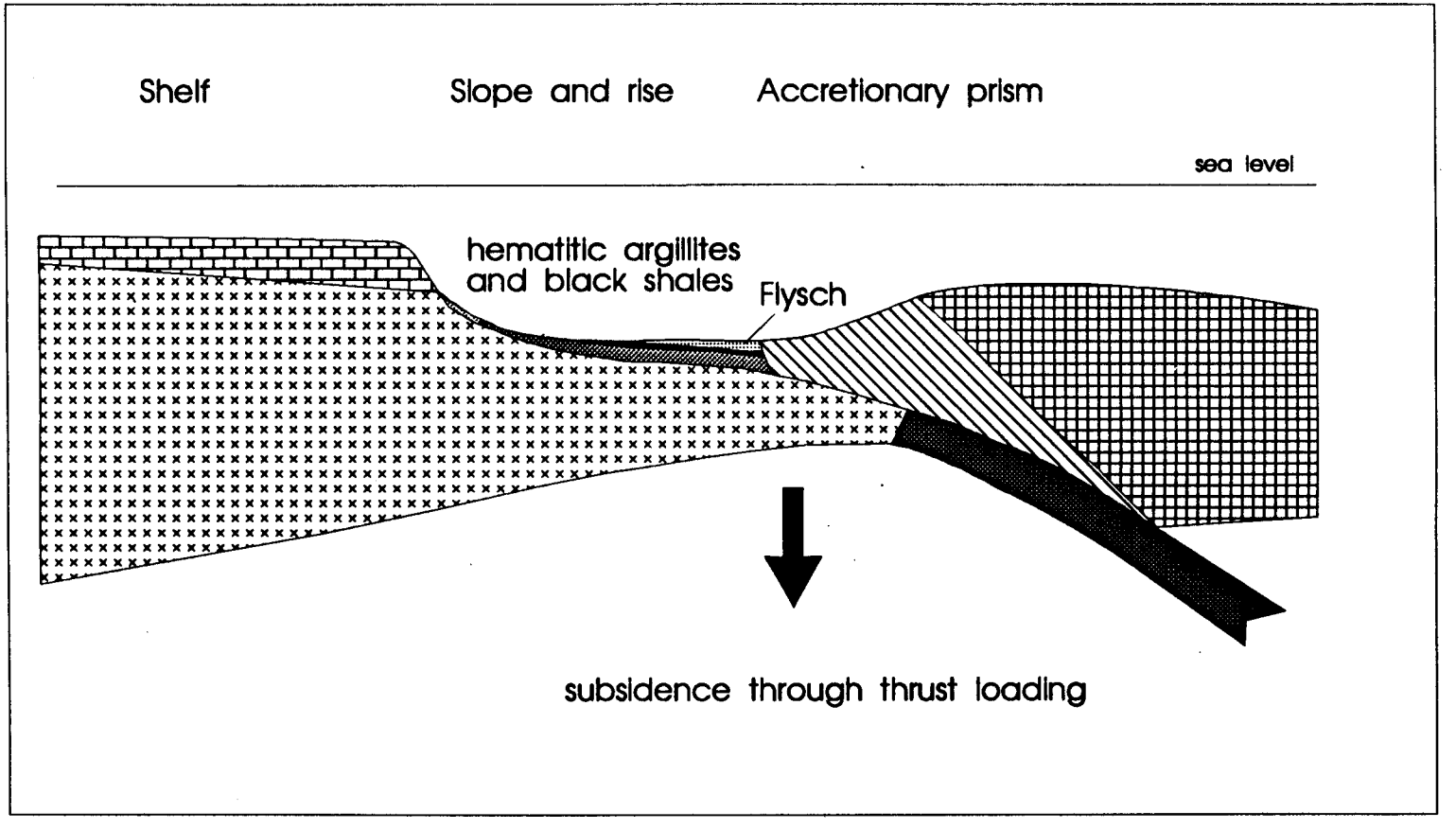

Figure 1.1: Schematic model illustrating thrust loading induced subsidence of a continental margin. Deposition of red, hematitic argillites takes place prior to the approach of the flysch and the accretionary prism (modified from Rowley and Kidd, 1981).

1986). The stratigraphic relationship on the shelf platform indicates that the deposition of the black shales marks a period of rapid subsidence caused by thrust loading of the continental margin with the advancing accretionary prism. The accretionary prism downloaded the shelf platform and ended the widespread shelf carbonate deposition (Bradley, 1989). The occurrence of the black shales on the shelf part, as well as on the rise part, of the continental margin suggests a similar environment. The rise part of the continental margin may also have subsided when it migrated towards the trench, although to a lesser degree, allowing for the original greater water depth of the continental rise. The shelf sediments that entered the outer trench slope environment after the continental slope and rise sediments are directly overlain by the black shales and the flysch sequence and do not show the red, hematitic argillites. This observation suggests that either the deposition of the red, hematitic argillites was a depth dependent phenomenon which could not be active at the shallower water depth of the shelf, or that at the time of the shelf subsidence the metal source for the hematite was not available anymore. In summary, an additional source contributed metals to the rise substrate at a time when oceanic circulation patterns and water depths were subject to a significant change, perhaps initiated by the change from a passive to an active margin environment.

1.2 The chemical sources of a pelagic/hemipelagic sediment

The chemical composition of a hemipelagic/pelagic sediment is a complex mixture of several sources (Leinen, 1987, Dymond, 1981, Heath and Dymond, 1977). In distal accumulating pelagic clays, four components have been distinguished (Dymond, 1981): (1) Detrital component. This includes elements that are derived from material weathered subaerially and are transported as particles either through wind or water currents into the basin. (2) Biogenic component. This includes organic, siliceous, and

calcareous material from the remains of organisms settling through the water column. (3) Hydrogenous component. This component is characterized by elements that may be scavenged from seawater by direct precipitation or by adsorption on clay particles or biogenic material. (4) Hydrothermal component. Hydrothermal vents at mid ocean ridges and seamounts emanate leached metals into the seawater. Hydrothermal plumes rising from the hydrothermal vents can be carried by mid- to deep water currents to deposit the metals, mainly iron and manganese, up to 2000 km away from the mid ocean ridges (Lupton and Craig, 1981). The degree to which one of these four components predominates in the environment biases the composition of the bulk sediment to that particular component.

Hydrothermal metal enrichment in modern, marine sediments (Dymond, 1981; Lyle et al., 1986) is the only presently known mechanism that allows for widespread, homogeneous metal enrichment in pelagic sediments. It is important to bear in mind that the metalliferous sediments in the described Ordovician cases overlie a thick, clastic substrate. Pelagic, hydrothermal, metalliferous sediments are in general found directly or almost directly above oceanic crust (Leggett, 1982). In sediments that accumulated more proximal to continental land masses or to subaerially exposed volcanic complexes, other metal sources than hydrothermal activity can be important. Here, there are three other main processes that can be responsible for metal enrichments: (1) Manganese may have been diagenetically mobilized into pore waters and recycled to the seawater at continental margins (Martin and Knauer, 1984). Continental margin currents may have transported the metals away from this site and provided them to the sediment at other places. (2) Iron may be of detrital origin being eroded from a lateritic source. From a paleogeographic view point this is a conceivable source regarding the near equatorial position of the North American eastern continental margin in the lower Ordovician which was about 10^{o} -15^{o} S (Van der Voo et al., 1991). (3) Iron may have been supplied by the weathering of mafic volcanic detritus from an adjacent volcanic arc.

In hemipelagic sediments the detrital component will be in general stronger (i.e., the sedimentation rate will be higher) as a result of the closer source area. In contrast to pelagic sediments, current activity and deposition in the form of turbidites and contourites increase in importance (Stow, 1986). Hemipelagic sediments show a larger grain-size variation and their mineralogical composition will be more variable when compared to pelagic sediments (Pettijohn et al., 1984). These differences result in a more heterogeneous chemical composition of the deposited sediments when compared with pelagic sediments. With increasing proximity to the land mass the detrital chemical composition is therefore less mixed than in pelagic sediments to a degree that different detrital source areas may still be distinguishable. Additionally, resedimented biogenic material as turbidites adds to the complexity of hemipelagic deposits (Stow, 1986). The variable sedimentation rates induced by the different modes of sedimentation affect the diagenetic history of the hemipelagic sediment and contrast to the diagenesis observed in pelagic sediments. Quasi-equilibrium processes during diagenesis (Froelich et al., 1979) can be observed in pelagic sediments accumulating at an almost constant rate. The abrupt influx of turbidites will disturb this equilibrium and result in different diagenetic processes (Colley et al., 1984; Thomson et al., 1986). To assess the metal origin in the metalliferous, Ordovician argillites it is necessary to discriminate the different compositional end-members of the sediment and interpret their origin. This has to be done with an account of the diagenetic changes that took place during the lithification process.

1.3 The similarity of the Ordovician sequences to Precambrian, Banded Iron Formation containing sequences

The Ordovician formations containing the red argillites also deserve interest because their stratigraphic sequence resembles that containing several of the largest Superior-type banded iron-formations of late Archean and early Proterozoic age (Hoffman, 1987). The origin of banded iron-formations is still not understood, and widely differing mechanisms were proposed to explain their origin (e.g., LaBerge, 1987; Klein and Beukes, 1989; Garrels, 1987; Holland, 1984). Recently, hydrothermal activity has more frequently been suggested as a suitable mechanism for the observed Fe-enrichment in banded iron-formations (e.g., Derry and Jacobson, 1990; Dymek and Klein, 1988; Barrett, 1988). So far, however, no mechanism proposed has been proved to be sufficiently adequate to explain all the features observed in these formations. Little attention has been paid to the stratigraphic relationship with the black shales and the flysch sediments above the iron deposits and the consequent tectonic implications. The comparable stratigraphic sequence is, however, very important because it is one of the few similarities Precambrian banded iron-formations share with generally better understood Phanerozoic sequences. Therefore, because the stratigraphic sequence implies a similar tectonic environment in the Ordovician and the Precambrian examples, the cause(s) for the observed metal enrichment may also be similar.

1.4 Location of the investigated sequences

The focus of this study is on two sequences of early to middle Ordovician age containing the described red, hematitic argillites: (1) The Wild Bight Group, the Shoal Arm Formation and the Gull Island Formation: This sequence is located in the Exploits zone in the central volcanic belt of north-central Newfoundland (Figures 2.1, 2.2, 2.3). Here the substrate (Wild Bight Group) consists of volcaniclastics and minor volcanics (Nelson, 1979). The Shoal Arm Formation contains the red, hematitic argillites. (2) The Poultney, Indian River, Mount Merino and Pawlet Formations described by Rowley and Kidd (1981), and Rowley et al. (1979) in the Taconic Allochthon of eastern New York and western Vermont. In this case the substrate (Poultney Formation) consists of shale dominated clastics and shows no association with volcanism. The red argillites are represented in this sequence by the Indian River Formation.

1.5 Purpose of study

The objective of this research is to establish a detailed chemical stratigraphy of the Shoal Arm Formation that can be used to develop an evolutionary, geochemical model. The model may place constraints on the origin of the Fe-enrichment in the red argillites and the depositional environment. It may also demonstrate why the metal enrichment appears to be restricted to a short time interval preceding a collisional process. Through comparison with the similar Indian River formation in the Taconic Allochthon of New York State, we hope to gain a generally applicable understanding of these oxic, metalliferous sediments. The combined results from the Shoal Arm Formation and the Indian River Formation potentially serve as an extended working

basis for the understanding of the origin of Fe-oxides that occur in Precambrian banded iron-formations in a similar, stratigraphic position.

The study is expected to provide additional information for geochemical provenance studies of fine-grained sediments. Most provenance studies have been performed on bulk sandstones or their constituents (e.g., Bhatia, 1983, Morton et al., 1991). Less attention, however, has been paid to fine-grained sediments. Successfully establishing different detrital source areas in silty argillites would therefore considerably extend the usefulness of geochemical provenance analyses. Furthermore, if the detrital sources can be recognized to vary in stratigraphic order, this may improve our understanding of the tectonic evolution in the vicinity of the Ordovician island arc(s). An investigation of diagenetic mobility in the Shoal Formation is thought to extend the present understanding of diagenetic processes in fine-grained, lithified sediments. At present the understanding of diagenetic reactions derives largely from investigations done on young, unconsolidated sediments in present day oceans (e.g., Colley et al., 1984). Few studies in comparable detail have been performed on paleosediments (e.g., Crerar et al., 1982; Coombs et al., 1985; Sugisaki et al., 1991; Jenkyns et al., 1991). It was therefore thought that a geochemical examination of red/green layer transitions, nodules and millimeter-laminations in the Shoal Arm Formation argillites would address some of the diagenetic changes of this sediment and improve the current understanding of diagenetically caused textures preserved in a lithified sediment.

1.6 Method of approach

For a geochemical study of the form proposed certain requirements for the formations to be studied have to be met:

(1) The stratigraphy has to be complete

(2) The degree of metamorphism must have been low

The Shoal Arm Formation in the Badger Bay area of central Newfoundland (Figures 2.1, 2.2) offers these two characteristics. The excellent exposure and well-documented stratigraphy, the low degree of metamorphism and the good understanding of the tectonic history make the Shoal Arm Formation an attractive example for this investigation. Therefore the prime focus in this study is on this unit. The work of Nelson (1979) revealed that the best exposed strata are located in the area of Gull Island and the adjacent mainland (Figure 2.3). It was therefore thought that by detailed stratigraphic measuring of the strata exposed around Gull Island a very complete and reliable sequence could be established. The continuous outcrop along the shoreline would also allow for an evenly distributed sampling over the whole stratigraphic section. Petrographic examination and whole-rock XRF analysis form the basis for this research. To address the different geochemical problems of this study, it is necessary to observe the formation on different scales:

(1) The complete sequence from volcaniclastics to flysch greywackes must be examined. This may give information on source area variation through time and can be related to a change in the depositional environment.

(2) A centimeter to millimeter scale investigation is necessary to establish diagenetically induced variations and to clarify the geochemical importance of burrowing organisms in the sediment.

The problem of discriminating different source areas is approached by application of a multivariate statistical technique. Such techniques have shown varying

success in the discrimination of different detrital source areas and different tectonic settings (Morton et al, 1991; Bhatia, 1983). Q-mode factor analysis in particular is very helpful to partition the whole-rock composition of a clay into the different end-members (Leinen, 1987). A comparative geochemical study with the Indian River Formation and the overlying Mount Merino black slates and cherts should be the next step in order to evaluate a generally valid model for the origin of the metalliferous sediments. Geochemical analyses from the Taconic Allochthon had already been obtained by J.W. Delano. Finally, I make a comparison with geochemical data from the literature of selected Precambrian, Superior-type, banded iron-formations and discuss if the results from the Shoal Arm Formation and the Indian River Formation permit comparison with banded iron-formations.

2. GENERAL GEOLOGY

2.1 Regional geological description

The Wild Bight Group, the Shoal Arm Formation and the Gull Island Formation are located in the central volcanic belt of northern Newfoundland in the Exploits zone (Dewey et al., 1983) (Figure 2.1). Figure 2.2 shows a regional map of the Notre Dame Bay area. A general description of the stratigraphy and structure of the Exploits zone is given in Dewey et. al. (1983). The terrane is bounded by two major faults: The northern and northwestern borders are marked by the Sops Head - Lukes Arm fault and the southeastern boundary is formed by the Reach fault and the Northern Arm fault (Figure 2.2). The lower part of the Exploits zone is characterized by late Cambrian (?) to early Ordovician volcanics and volcaniclastics, shales and cherts. These are followed by middle Ordovician (Caradocian) black slates, and late Ordovician to early Silurian greywacke sandstones and shales. The greywackes are overlain by early Silurian, coarse-grained paraconglomerates, olistostromes and younger shallow-marine clastics. The top part of the stratigraphic sequence is represented by Silurian volcanics and red beds. Locally, middle to late Devonian granitoids intrude the Cambro-Ordovician lithologies. In the northeast of the Exploits zone, on New World Island, a shallow-water limestone of Llandeilian age (Cobbs Arm limestone) overlies early Ordovician mafic volcanics and directly underlies the black Caradocian shale. No hematitic argillites appear here (Bergström, 1974). The eastern part of the zone consists of the Dunnage Mélange (Williams, 1979) - a mudstone with boulders and blocks of greywackes, limestones, and pillow lavas in a green and black shaley matrix. The age of parts of the mélange ranges from medial Cambrian to early Ordovician (Arnott et al., 1985). The Dunnage Mélange is also overlain by the Caradocian black shale and the greywacke sandstones. The base

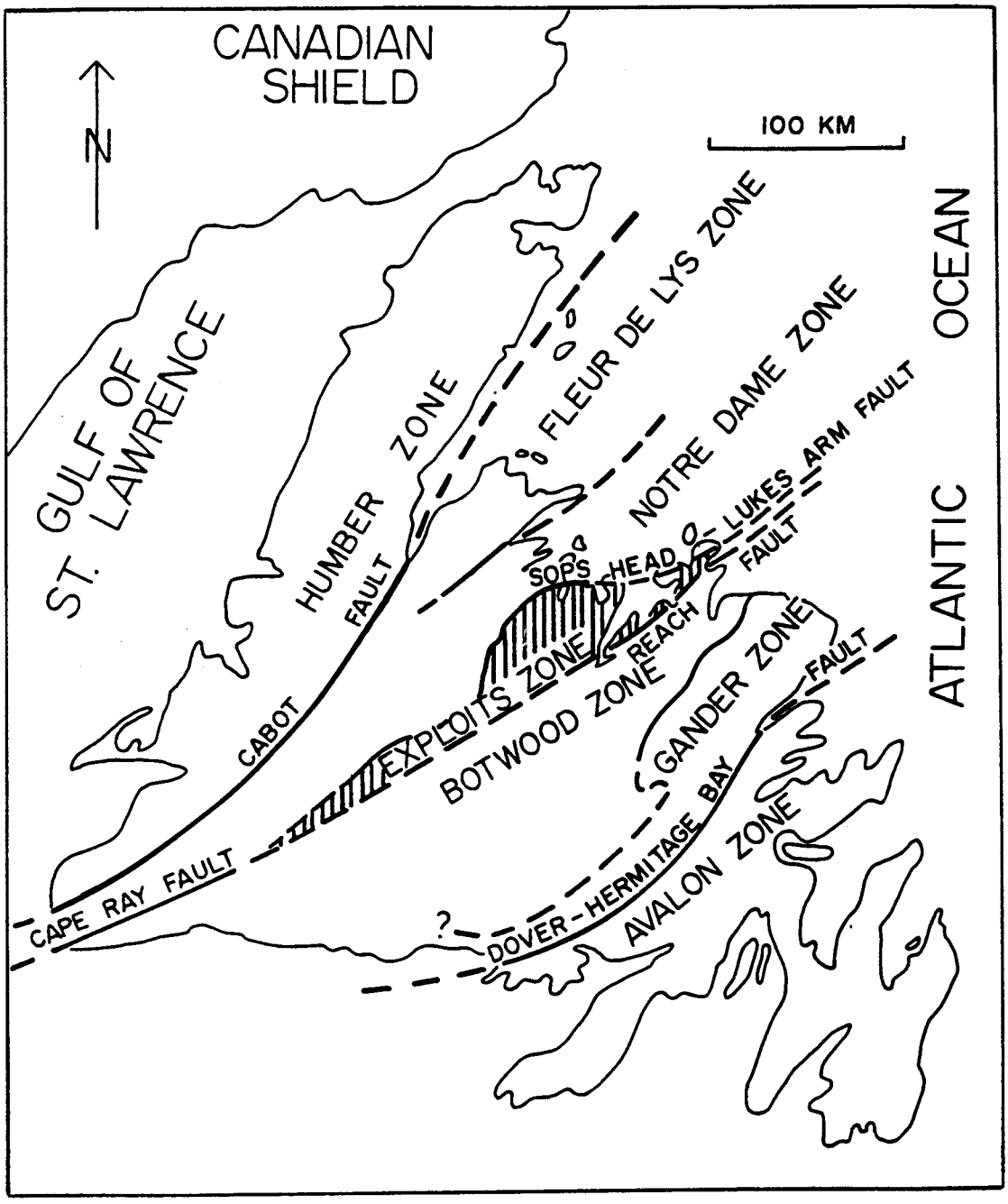

Figure 2.1: Tectonostratigraphic zones of Newfoundland (from Dewey et al., 1983)

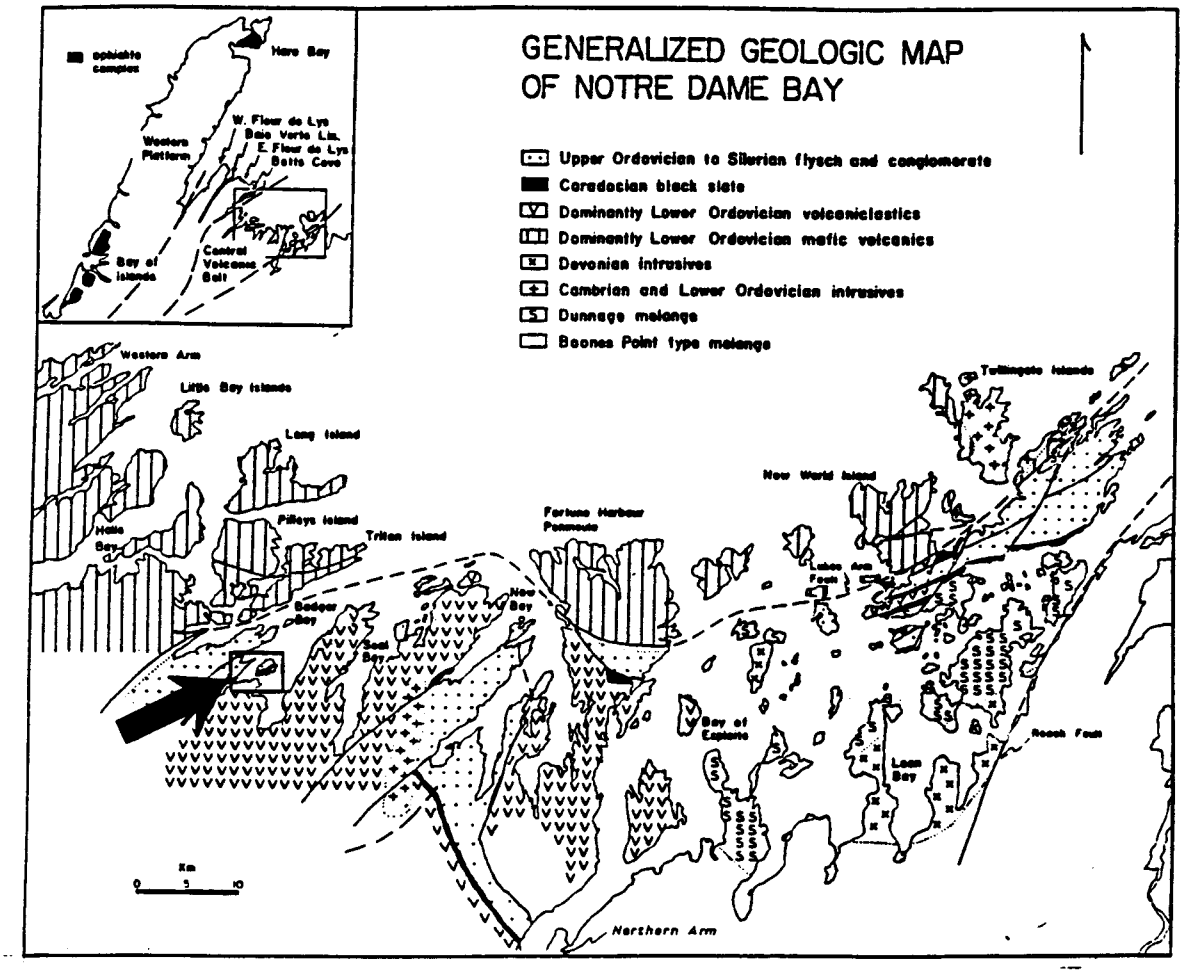

Figure 2.2: Generalized geologic map of the Notre Dame Bay (from Nelson, 1979). Arrow points to field area.

of the Exploits zone is likely to be oceanic and island arc-type crust (e.g., Dewey et al., 1983).

The area of interest lies in the western part of the Exploits zone (Figures 2.2, 2.3). The general stratigraphy is shown in Figure 2.4. The oldest exposed lithologies consist of possibly late Cambrian to early Ordovician volcaniclastics and minor volcanics of the Wild Bight Group, which are more than 8 km thick (Nelson, 1979). The Wild Bight Group passes conformably into the Shoal Arm Formation, which is characterized by generally finer-grained sediments. Nelson (1979) reported a thickness of about 500 m. From bottom to top this formation consists of 3 major lithologies: (1) Dark-brownish red, bright-red and purple, hematitic and manganiferous, siliceous argillites alternating with interbeds of green siliceous, somewhat coarser-grained volcaniclastics with the two lithologies displaying an irregularly spaced layering throughout the Shoal Arm Formation; (2) Grey, bioturbated and laminated cherts; (3) Black pyritiferous slates. The youngest rocks in this area are late Ordovician to early Silurian quartzofeldspathic sandstones and slates of about 1.3 km thickness; the Gull Island Formation. Similar stratigraphic sequences can be seen to the east in the Point Leamington area (Kusky, 1985), on the Fortune Harbour Peninsula (Helwig, 1967) and on New World Island (Helwig, 1967).

2.2 Tectonic and sedimentary environment of Wild Bight Group, Shoal Arm Formation and Gull Island Formation

The tectonic and sedimentary environment of the three formations in the Badger Bay area is interpreted in the context of deposition of sediments predating and coeval with the collision of an island arc with the North American continent in medial Ordovician. Nelson (1979) provided the most detailed work on the general geology in

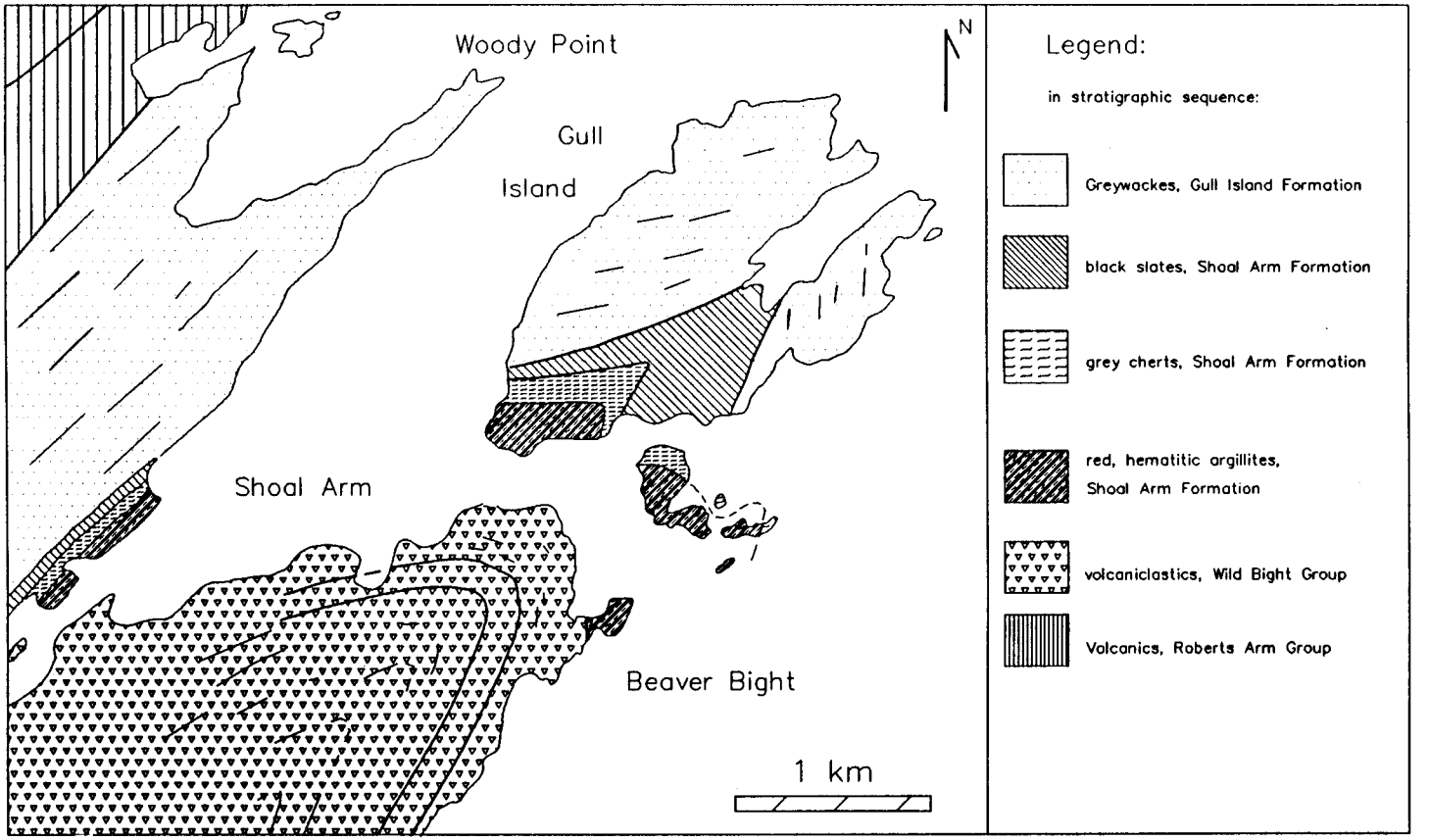

Figure 2.3: Geologic map of Gull Island and the adjacent mainland (modified from Nelson, 1979).

the Badger Bay - Seal Bay area. His Ph.D. thesis forms the basis for the understanding of the regional geology and the stratigraphic framework in the Badger Bay area. The conclusion from his work was that the sequence records three depositional periods. The base of the sequence was formed by Cambro-Ordovician island arc volcaniclastic and minor volcanic deposition (Wild Bight Group). The volcanic arc was presumably located in the northwest and served as the source area for the volcaniclastic sediments. On a regional scale it was found that the volcanics are rarer in the east than in the west, which is consistent with an arc source area to the northwest of the basin (Arnott et al. 1985). Geochemical analyses of the volcanics in the Exploits zone indicate that they consist of both arc related volcanics (e.g. Swinden et al., 1990; Bostock, 1988) and volcanics that carry a MORB-type signature (Swinden et al., 1990; Bostock, 1988; Jenner and Fryer, 1980; Jacobi and Wasowski, 1985). The non-arc volcanics may have formed in a back-arc basin setting (Swinden et al.; 1990, Bostock 1988) or in an open ocean setting as mid ocean ridge basalts (Jenner and Fryer, 1980; Kidd, pers. comm.) or as within plate basalts in the former Iapetus ocean where they formed oceanic islands (Jacobi and Wasowski, 1985). The volcaniclastics fine upwards into the Shoal Arm Formation. Perhaps the basin was gradually deepening, and the volcanic arc complex as the source area became increasingly distant or the complex became less volcanically active, with the consequence that erosion decreased the relief and finer-grained sediments reached the basin. The water depth at the time of deposition of the argillites is uncertain, but must have been below wave base. More detailed sedimentological observations (see chapter 4.2) confirm this assumption.

The second depositional period was marked by deposition of black shales throughout the Exploits zone. All the Ordovician volcanics and volcaniclastics in the Exploits zone are older than the black shales and no Ordovician igneous activity is recognized after the early Caradocian (Nelson, 1979; Arnott et al., 1985). Assuming no major strike slip faulting, this excludes subduction and related magmatic activity for this

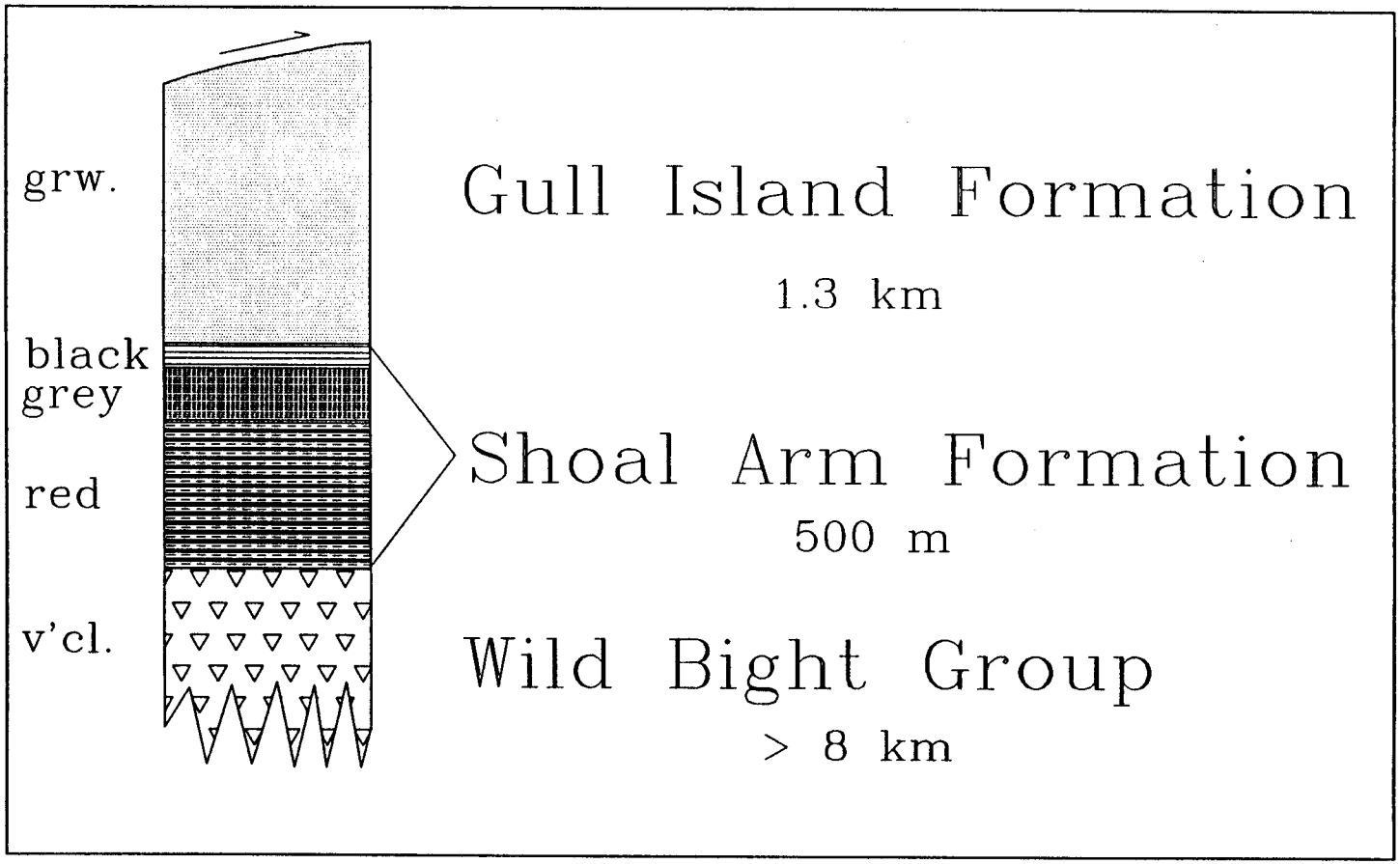

Figure 2.4: General Ordovician and lower Silurian stratigraphy in the Badger Bay

part of the orogen after the Caradocian and also excludes ridge activity or active seamounts in the remnant oceanic basin. Cessation of volcanism was found to be synchronous with ophiolite obduction on the Western Platform, deformation on the Burlington Peninsula to the west and Fleur de Lys metamorphism (Nelson, 1979). Rapid subsidence of the basin in the Caradocian is indicated by the deposition of the black shales on top of the shallow-water Cobbs Arm limestone on New World Island (Bergström et al., 1974). In contrast to the stratigraphic sequences in the Badger Bay and on the Fortune Harbor Peninsula no red, hematitic argillites are reported to underlie the black shales at this location. With respect to the depositional depth of the hematitic argillites this indicates that above a shallow-water substrate no hematitic, oxic sediment could accumulate. Due to the scarcity of fossils in the volcaniclastics the black shale serves as a regional marker horizon. The age is confirmed by graptolites of the Nemagraptus gracilis zone (lowermost Caradocian) in the Badger Bay and diverse Conodonts on New World Island and the Fortune Harbour Peninsula which are of Caradocian age (Bergström et al., 1974; Arnott et al., 1985; Neuman, 1984). Arnott et al. (1985) indicated that the age and thickness of the black shales varies across the Notre Dame Bay. These authors proposed the existence of different fault bounded intra arc/rear arc basins in the Exploits terrane in which deposition took place diachronously. Arnott et al., 1985) concluded that the Pre-Caradocian deposits in the Exploits zone cannot be directly correlated. This view has been discarded by Van der Pluijm and van Staal (1988) who indicated that the faults that were supposed to separate these basins are of early Silurian age.

The third depositional period was marked by the uplift and erosion of a terrane to the north and northwest in the late Ordovician that renewed coarser-grained clastic deposition now seen in the late Ordovician and early Silurian greywackes. The different mineralogical composition between the Wild Bight Group/Shoal Arm Formation on one side and the Gull Island Formation on the other side indicates different source areas.

Also, clasts in the volcaniclastics of the Wild Bight Group are almost exclusively volcanics whereas the clasts in the Gull Island Formation are dominantly intermediate and silicic plutonic clasts (Nelson, 1979). Detrital chromite and ophiolitic fragments in the greywackes of the Gull Island Formation demonstrate the emplacement and uplift of the ophiolite in the west (Nelson, 1979). Arnott et al. (1985) come to a similar conclusion by suggesting that the deposition of the Caradocian black shale and the influx of the overlaying coarse-grained turbidites took place diachronously, whereby the eastern part of the basin received greywackes later than the western part.

The top part of the sequence in the Exploits zone is terminated by a late Ordovician or early Silurian mélange followed by a thrust fault (Lukes Arm - Sops Head fault) (see Figures 2.2, 2.3). To the north and northwest of the Lukes Arm - Sops Head fault, dominantly volcanics of early Ordovician age (Roberts Arm Group) are exposed (Bostock, 1988). The volcanics were thrusted on top of the early Silurian greywackes (Nelson, 1979; Bostock, 1988). A similar early Silurian thrust can be found to the southeast in the Frozen Ocean fault (Kusky, 1985) (see Figure 2.2). Kusky (1985) interprets these thrusts as backthrusts related to the collision of the volcanic arc with the North American continent. It is suggested that these thrusts and associated strike-slip faults accommodated continued post-Taconic convergence between Laurentia (North America) and the oceanic plate to the east. Van der Pluijm and van Staal (1988) suggested that the stacking sequence represents an accretionary wedge that had been developed over a west-dipping subduction zone. Continued subduction after the Caradocian, however, is difficult to reconcile with the apparent cessation of volcanic activity at this time period. The sedimentary sequence and the thrust stacking are analogous to what is observed in other parts of the northern Appalachians, where closure of an oceanic basin and collision have been demonstrated (e.g., Bird and Dewey, 1970; Bradley, 1989).

3. STRATIGRAPHY AND SEDIMENTOLOGY OF THE SHOAL ARM FORMATION

3.1 Introduction

The work of Nelson (1979) focussed on the general geology of the whole Badger Bay and Seal Bay area in order to improve the knowledge of the tectonic evolution of this part of the Appalachian Orogen. Consequently, he did not pay attention to the Shoal Arm Formation in the detail that is required for this study. Also, his study did not serve a geochemical purpose with the consequence that the Shoal Arm Formation was insufficiently sampled or the location of the few samples already provided was inadequately precise. Additional field work was necessary to establish a detailed stratigraphy of the Shoal Arm Formation including the upper part of the Wild Bight Group and the lower part of the Gull Island Formation. Sufficient samples had to be taken from the field to construct a representative chemical stratigraphy. It was also necessary to examine the small-scale sedimentary structures to establish the mode of deposition of the strata and the significance of potential diagenetic alterations.

Three stratigraphic sections of the Shoal Arm Formation in the Badger Bay were examined and measured during one week in August 1990 (Figure 2.3). The three stratigraphic sections are informally named after their locations. The largest exposure appears along the south shore of Gull Island (Gull Island Section). Another section is exposed on a promontory to the south of Gull Island at Beaver Bight (Beaver Bight Section). The third locality occurs along the mainland shoreline to the west of Gull Island at Shoal Arm (Shoal Arm Section). The sections contain minor gaps where small cobble beaches interrupt the nearly continuous outcrop along the shore line. Only at Shoal Arm there is a single section running from the underlying volcaniclastic sandstones of the Wild Bight Group into the greywackes of the Gull Island Formation. The other

two sections are incomplete. The Gull Island Section does not expose Wild Bight Group strata, but provides a thicker, red Shoal Arm Formation. Also, on Gull Island the contact between the red argillites and the grey cherts is faulted. The strata exposed at Beaver Bight are composed of upper Wild Bight Group volcaniclastics and red and purple argillites of the Shoal Arm Formation, and are complementary to the lower part of the Shoal Arm Section. The thicknesses of the three sections are different, and are related to tectonic thinning during folding and/or thrust duplication. Due to the deformation, it is impossible to deduce with any precision the original thickness of the Shoal Arm Formation. We cannot provide any detailed information on the time span that was involved in the deposition, because only the paleontological age of the overlying black shales is known. Similarly, estimates of the sedimentation rates are only qualitative and inferred from the sedimentary structures.

Correlative sequences to the Shoal Arm Formation exist in the Bay of Exploits area (e.g., Wasowski, 1987; Kusky, 1985; Helwig, 1967). A road cut 5 kilometers north of Northern Arm (Figure 2.2) exposes strata that are equivalent to the upper red, grey and black Shoal Arm Formation, and to the lower part of the Gull Island greywackes, here called the Point Leamington Formation. This section was also measured and sampled; it is called the Northern Arm Section. At this locality the red/grey boundary of the Shoal Arm Formation is not faulted and the grey cherts are exposed continuously up to the black slates. The Northern Arm Section was therefore taken as the type section of the grey part. The rocks in this outcrop have a flinty appearance and do not show a strong cleavage. Primary sedimentary structures are very well preserved. A nearby Ordovician gabbrodiorite (see Figure 2.2) probably heated the argillites. There is a potential that circulating hot fluids from the gabbrodiorite contaminated the rocks. Therefore, the section was not extensively sampled for geochemical analysis, and the focus was only on measuring the thickness of the section.

3.2 Subdivisions and stratigraphic thicknesses of the Shoal Arm Formation

A subdivision of the red Shoal Arm Formation is made on the basis of the hematite-bearing argillites. The argillites change their color up-section from a purple-maroon into a bright-red and then back into a pale-purple color. The maroon/red color change is fairly sharp and very characteristic (Figure 3.1). It appears in all three stratigraphic sections of the Badger Bay. This is the first marker horizon of the stratigraphic column and taken as the top of the first subunit of the red Shoal Arm Formation (Figure 3.3). There is no sharp contact at the base of this unit. The grain-size gradually decreases from sandy and silty volcaniclastics of the Wild Bight Group to silty argillites of the Shoal Arm Formation. Based on this observation, the first 45 meters measured in the Beaver Bight Section were assigned to the upper Wild Bight Group. Similarly, at least the first 10 meters of the Shoal Arm Section belong to the upper Wild Bight Group. The remaining thickness of the maroon and purple part of the red Shoal Arm Formation is 52 meters.

The bright-red argillites form the middle part of the red Shoal Arm Formation, and extend from the maroon/red color transition at the base to a distinctive, buckled, 3 centimeter thick rhodochrosite band at the top (Figure 3.2). This rhodochrosite band is the second marker horizon of the stratigraphic column, since it was found in the Gull Island Section and in the Shoal Arm Section (Figure 3.3). In contrast to the maroon and purple argillites below, these hematitic argillites have a very characteristic bright-red color. On Gull Island, the bright-red argillites are over 74 meters thick, if one assumes that the section is not repeated by thrusts (see below). At Shoal Arm, this unit seems to be thinner, but it may occupy parts of a 19 meter wide gap (Figure 3.3).

In the upper red Shoal Arm Formation the color of the hematitic sediments changes back to a pale-purple. Depending on which section is taken for reference, the thickness of this subunit varies between 40 meter (Shoal Arm) and 50 meter (Gull

Figure 3.1: Color transition from purple/maroon argillites into bright red argillites. This transition forms the first marker horizon of the stratigraphic sequence in the Badger Bay area. Gull Island Section (level: 8 meter; Figure 3.3); south shore Gull Island. (Photograph by W. Kidd; Volker Bruchert is the geologist)

Figure 3.2: Buckled, pyrolusite stained rhodochrosite band. The band appears in the same configuration as all other rhodochrosite bands. It represents the second marker horizon of the stratigraphic column. Gull Island Section (level: 82 meter; Figure 3.3); south shore Gull Island. (Photograph by W. Kidd)

Island). The base of the upper subunit is the buckled rhodochrosite band and the top was assigned to the base of the mottled, grey cherts in the Shoal Arm Section. The top contact can also be seen in the Northern Arm Section.

The grey unit is best exposed in the Northern Arm Section. This locality is therefore taken as the type section of this lithology. The stratigraphic relationship to the sections measured in the Badger Bay area is shown in Figure 3.4. Here, the grey cherts measure 84 meters. A similar thickness (80 meters) was derived from Gull Island where the structural situation within this section is more complex and the true stratigraphic thickness measured more uncertain. The first 6 meters of the grey unit in the Northern Arm Section expose dominantly dark- and light-grey, laminated cherts. The following 72 meters exhibit intervals of alternating, mottled and laminated cherts. In the top 6 meters, black slates begin to be frequently intercalated.

Due to the strong deformation of the black slates, their thickness can only be estimated. The thickness of the strata is approximately 20 meters (estimated on Gull Island), but at other localities the black slates may be up to 30 meters thick. In the Northern Arm Section, not more than 7 meters of black slates were exposed below the first greywackes.

3.3 Structure and deformation

The map pattern of Figure 2.3 reflects a northeast plunging anticline on Gull Island whose surface trace continues to the mainland in the southwest. The upper Wild Bight Group and the Shoal Arm Formation are exposed in the core of this anticline. In outcrop, the argillites form tight folds with wavelengths of several meters to tens of meters. The thick-bedded greywackes of the Gull Island Formation show no folding at this wavelength. Beds in all formations dip in general steeply, often vertically. A

northeast trending, slaty cleavage is developed in all rock types. This cleavage appears on a regional scale, and is by some authors interpreted to be of Acadian (middle Devonian) age (Dewey et al., 1983; Nelson, 1979). The cleavage parallels the trend of the axial surfaces of the regional folds and the mesoscopic folds. This indicates a roughly similar age of folding and cleavage formation. The cleavage development is associated with a significant flattening of the beds, and is one reason why the original thickness of the Shoal Arm Formation cannot be determined. The black slates form the least competent strata of the section and display the strongest cleavage with the effect that the original bedding is almost unrecognizable. The sections are interrupted by abundant, minor detachment faults and show intense quartz veining in these zones. Most of the detachments are layer-parallel thrusts, and may be interpreted as flexural-slip faults that accommodated the folding. It is unlikely that these faults caused significant repetitions in the sections examined.

The similar-style folding of the anticline thinned the strata on the limb of the anticline and thickened the strata in the core. The Shoal Arm Section lies on the limb of the anticline whereas the Gull Island Section is exposed along the core of the anticline (Figure 2.3). Consequently, the Shoal Arm Section is much thinner than the Gull Island Section. This complicated the stratigraphic correlation between the two sections. For example, the thickness of the interval of the Shoal Arm Formation enclosed by the maroon/red color transition and the rhodochrosite band in the Gull Island Section is different from the Shoal Arm Section. At Shoal Arm, the interval between the marker horizons measures 53 meters, whereas on Gull Island the same interval measures 74 meters. Considering that the Shoal Arm Section contains a gap of 19 meters, in which a fault could be hidden, the difference may even be larger. Figure 3.3 illustrates this interval on Gull Island in 4 different blocks. Each block was found to be bounded by faults. We suspect that these faults are thrusts and have duplicated the strata. This becomes more apparent when the interval in the Gull Island Section is inspected in more

Figure 3.3: Simplified, stratigraphic column of the Shoal Arm Formation. Only this part of the complete stratigraphic sequence can be correlated in detail. The different labels in the columns mark the sample positions. The scale on the right side applies only to the Gull Island Section, because of the different thickness of the section enclosed by the two marker horizons.

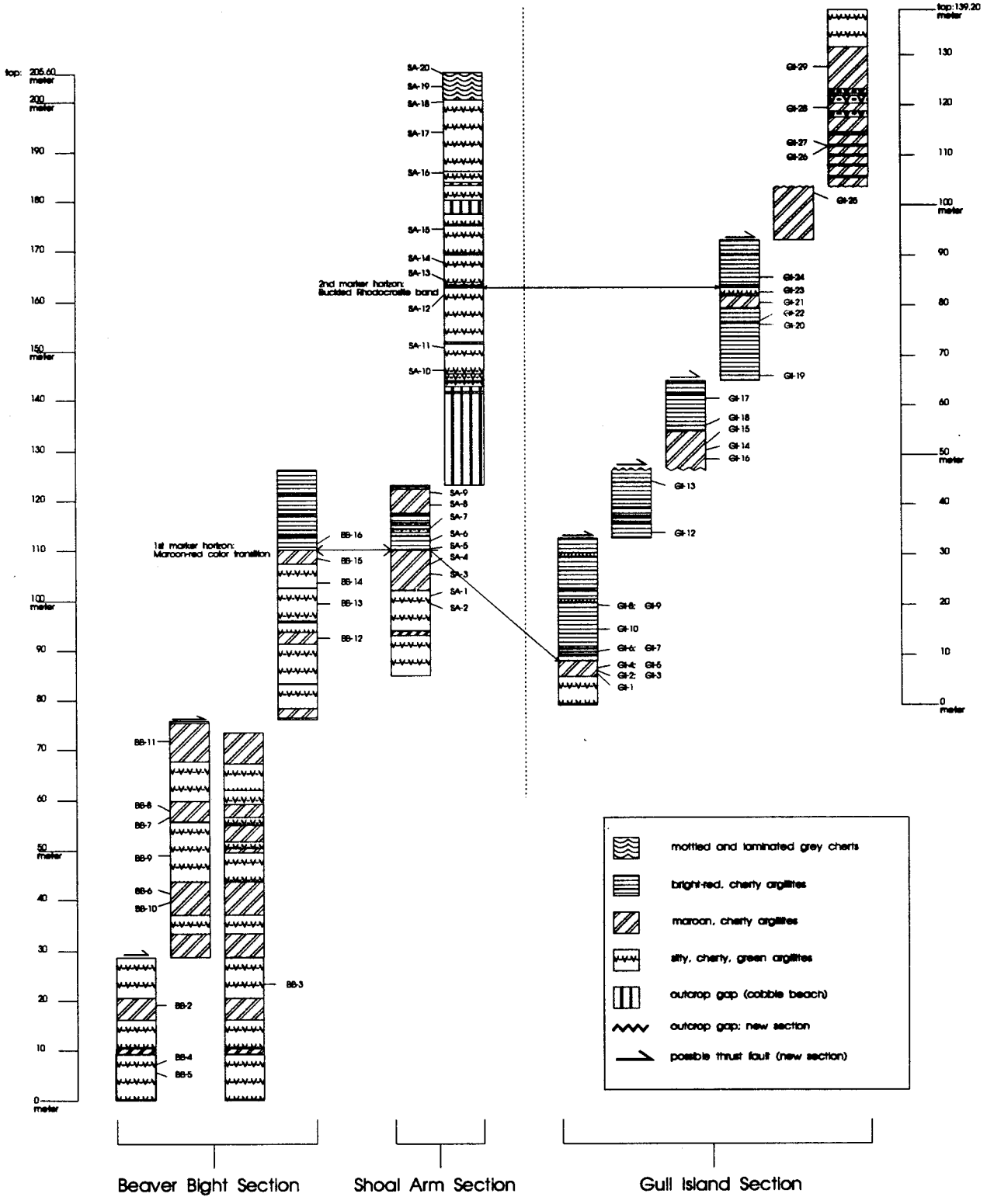
top: 205.60 meter
200 meter
190
180
170
160
150 meter
140
130
120
110
100 meter
90
80
70
60
50 meter
40
30
20
10
0 meter
top: 139.20 meter
130
120
110
100 meter
90
80
70
60
50 meter
40
30
20
10
0 meter
1st marker horizon: Maroon-red color transition
2nd marker horizon: Bucklad Rhodocrosite band
BB-16
BB-15
BB-14
BB-13
BB-12
BB-11
BB-8
BB-7
BB-9
BB-6
BB-10
BB-2
BB-4
BB-5
BB-3
SA-20
SA-19
SA-18
SA-17
SA-16
SA-15
SA-14
SA-13
SA-12
SA-11
SA-10
SA-9
SA-8
SA-7
SA-6
SA-5
SA-4
SA-3
SA-1
SA-2
GI-29
GI-28
GI-27
GI-26
GI-25
GI-24
GI-23
GI-21
GI-22
GI-20
GI-19
GI-17
GI-18
GI-15
GI-14
GI-16
GI-13
GI-12
GI-8: GI-9
GI-10
GI-6: GI-7
GI-4: GI-5
GI-2: GI-3
GI-1
mottled and laminated grey cherts
bright-red, cherty argillites
maroon, cherty argillites
silty, cherty, green argillites
outcrop gap (cobble beach)
outcrop gap; new section
possible thrust fault (new section)
Beaver Bight Section
Shoal Arm Section
Gull Island Section

detail (see Figure 3.3): At 20 meters, two prominent, green volcaniclastic layers, 1.60 meter to 1.80 meter apart, appear. A comparable couple appears again at the 36 meter and at the 61 meter mark. Aligning of these horizons shortens the interval between the maroon/red color transition and the rhodochrosite band to 36 meter. The interval is then 17 meter shorter than the one in the Shoal Arm Section. However, if one assumes that the gap in the Shoal Arm Section hides a thrust and one removes the gap, the thicknesses of the intervals would be about equal. It is difficult to prove that the gap in the Shoal Arm Section contains a fault. Furthermore, the two detachments that bound the blocks on Gull Island appear to be only minor and unlikely to have caused repetitions on a scale of 15 meters. Instead, the reappearance might have been caused by cyclic deposition. Another observation constrains the interpretation that no structural repetition is present. Using the buckled rhodochrosite band to align the Gull Island and the Shoal Arm Section, it appears that the Gull Island Section shows red argillites at a stratigraphic level, where the Shoal Arm Section already shows grey, mottled cherts of the overlying grey unit (Figure 3.3). Over 40 meters of purple argillites above the rhodochrosite band in the Gull Island Section equal only 12 meter of green argillites in the Shoal Arm Section. In general, the sedimentary environment makes it unlikely that the original thickness varied that much from one section to the other. Instead, it suggests considerable tectonic thinning of the Shoal Arm Section. During folding, the strata on the limb of the anticline were probably thinned out. It is not unlikely that the originally measured differences in the two sections were mainly caused by thinning of the Shoal Arm Section. Present evidence does not justify significant thrust repetitions in the Gull Island Section and the stratigraphic order is taken as it was measured in the field.

The faulting hypothesis was tested by comparing the chemical composition of samples GI-8 and GI-17 - both samples that are located below the prominent first green, volcaniclastic layer of the above mentioned pair. These samples are derived from

the bright-red, argillaceous tops of two turbidites in the Gull Island Section. Table 3.1 shows the composition of the two samples. They varied considerably in the elements Na, Zr, Mn, Mg, Cr, and V. On the other side, Al, Si, Fe, K and Ni appear to be of similar abundances. A conclusion from only these two analyses seems not justified. The problem could only be solved by much closer sampling of the blocks and by analyzing the pairs of green volcaniclastic layers.

In conclusion, there is a possibility that the red Shoal Arm Formation on Gull Island is thinner than shown on the profiles. However, the possible duplications are restricted to the bright-red interval, and do not repeat lithologies of the other subunits of the red Shoal Arm Formation. The true thickness of the strata is therefore uncertain, but this does not affect the interpretation of the evolution of the sedimentary environment.

Table 3.1: Comparison of the abundances of selected elements in samples GI-8 and GI-17. Major elements are expressed in weight percent; minor and trace elements in parts per million (ppm)

Element	GI-8	GI-17
SiO_2	75.00	72.29
TiO_2	0.58	0.47
Al_2O_3	9.81	8.48
Fe_2O_3*	6.17	7.41
MnO	1.39	5.96
MgO	1.00	0.60
CaO	0.31	0.56
Na_2O	3.37	2.19
K_2O	1.07	1.02
Cr_2O_3	56 ppm	81 ppm
V	43 ppm	94 ppm
Ni	57 ppm	49 ppm
Zr	107 ppm	78 ppm
Th	6 ppm	8 ppm
Pb	17 ppm	22 ppm

* Total Fe expressed as Fe_2O_3

3.4 Construction of the stratigraphic column

From the foregoing discussion it becomes apparent that the construction of the complete stratigraphic column requires several assumptions. The field data are presented under the following assumptions:

(1) None of the stratigraphic sections show significant thrust repetitions.

(2) The thickness of the Gull Island Section is taken as the reference standard for the other sections.

(3) The Shoal Arm Section is tectonically thinned.

(4) The interval above the 184 meter mark in the Shoal Arm Section is younger than the top of the Gull Island Section. This position was established by multiplying the thickness measured for the Shoal Arm Section with a stretching factor. The factor was calculated from the ratio of the thickness of the interval between the two marker horizons on Gull Island and at Shoal Arm, which is

74 meter/ 53 meter = 1.4

This method seems justified, because after recalculation of the original thickness of the Shoal Arm Section, the top of the Gull Island Section is located below the first abundant occurrence of burrowed argillites in the Shoal Arm Section. Burrowed argillites were not found in the top parts of the measured red Gull Island Section.

Based on these assumptions, the three sections measured in the Badger Bay were compiled into a single composite section. The resulting stratigraphic column ranges from the volcaniclastics of the upper Wild Bight Group to the black slates of the Shoal Arm Formation. Figure 3.3 shows the stratigraphic columns for strata ranging from the upper Wild Bight Group up to the lower grey unit. Only this part of the stratigraphic section could be measured continuously. Added to the top of this section are the strata measured in the Northern Arm Section. The first appearance of the mottled, grey cherts is used to correlate the Shoal Arm and the Northern Arm Sections (Figure 3.4).

Figure 3.4: Correlation of the Northern Arm Section with the composite Badger Bay sequence. The first appearance of grey, burrowed cherts in both sequences was used for correlation.

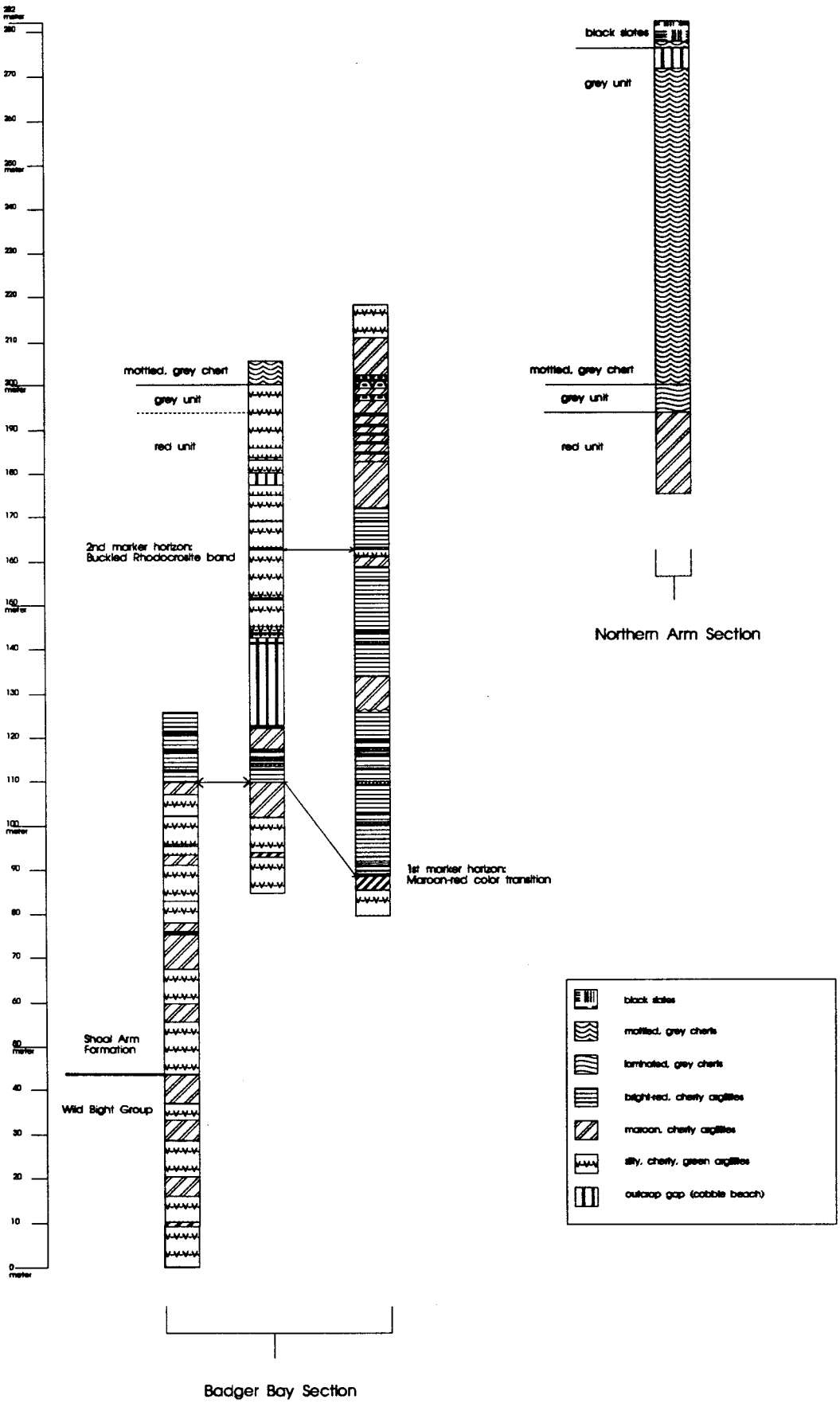
black slates
grey unit
mottled, grey chert
grey unit
red unit
Northern Arm Section
mottled, grey chert
grey unit
red unit
2nd marker horizon:
Buckled Rhodocrosite band
1st marker horizon:
Maroon-red color transition
Shoal Arm
Formation
Wild Bight Group
Badger Bay Section
black slates
mottled, grey cherts
laminated, grey cherts
bright-red, cherty argillites
maroon, cherty argillites
silty, cherty, green argillites
outcrop gap (cobble beach)

The nominal thickness of the total section measured is 355 meters and includes the thickness of the grey unit, the black slates and 45 meters of volcaniclastics of the Wild Bight Group. The total length does not appear on Figure 3.4, because it is derived from the multiplication of parts of the section by the stretching factor 1.4. The resulting, total Shoal Arm Formation measures about 310 meters. The red unit has a maximum thickness of 190 meters which refers to the thickness of the 3 units measured on Gull Island.

3.5 Sampling and stratigraphic order of samples

From Shoal Arm, Beaver Bight, and Gull Island, samples were taken in intervals ranging from 10 centimeters to 7 meters. From lithologically variable intervals, representative samples of the contrasting lithologies were collected. However, the Shoal Arm Formation contains many alternating green-red intervals, which could not all be sampled. We restricted the collection to the most strikingly different lithologies and then focussed on the best possible coverage of the exposed strata. 109 samples were taken from the Badger Bay area, which include samples from the upper Wild Bight Group, the red, grey and black Shoal Arm Formation as well as selected samples from the Gull Island Formation. The sample collection is somewhat biased to samples taken on Gull Island, where 42 of the 67 samples of the total Shoal Arm Formation were collected. Most samples were taken from the red Shoal Arm Formation. 29 samples of this unit come from the Gull Island Section, 17 samples from the Shoal Arm Section, and 8 samples from the Beaver Bight Section. Samples from the upper Wild Bight Group include the 8 remaining samples from Beaver Bight Section and further 9 volcaniclastic samples from the Seal Bay area at Seal Bay Head and at Side Harbour. These latter samples were taken to establish a local reference composition for a comparative study of

the Wild Bight Group volcaniclastics with the Shoal Arm Formation lithology. The outcrop at Side Harbour also contains red argillites; these were sampled to test the hypothesis whether similar conditions to the ones seen in the Shoal Arm Formation existed at an earlier time interval. All 6 grey cherts except for one, and all 6 black slates were sampled on Gull Island. The greywackes were only sampled in the Shoal Arm Section. Greywacke samples were taken in 8 groups of coarse- or medium- and fine-grained pairs at stratigraphic intervals of 50 - 150 meter in order to cover the whole, exposed Gull Island Formation. These samples complement the samples collected by Nelson (1979).

Figure 3.3 shows the positions of samples taken from the three sections that were measured in detail. These positions are well-constrained. Exact stratigraphic positions of samples from the grey and black unit on Gull Island cannot be given, because of faulting of this part of the section, unexposed intervals, and the oblique intersection of the exposure with large-scale folds. However, the sample sequence relative to the stratigraphy is known. The stratigraphic order of the grey chert samples and the black slates is shown in Table 3.2:

Table 3.2: Stratigraphic sequence of samples from the grey unit and the black slates

GI-42	
GI-39	
GI-40	Black slates
GI-33	
GI-41	
GI-38	
GI-35	
GI-36	Grey unit (all mottled)
GI-34	
GI-37	

As the final step, all the samples of the Shoal Arm Formation had to be compiled in stratigraphic order, and a definite position on the stratigraphic column needed to be assigned to each of the samples. In order to do this, the assumptions used in chapter 3.3 had to be applied again. The Gull Island Section is taken as the reference section, and the sample positions of the other sections are inserted into it or added to this section at the ends. Samples taken close to the marker horizons are best-constrained. However, the positions of samples in the Shoal Arm Section above the maroon/red color transition needed to be changed. The new position of a particular sample from the Shoal Arm Section was calculated by multiplying the distance of the original sample position from the maroon/red color transition by the factor 1.4. The calculated value was added to the value of the meter mark the maroon/red color transition has in the Gull Island Section. This new value defined the position of the sample relative to the Gull Island section. The scale of the Beaver Bight Section remained unchanged. Based on the common maroon/red color transition, the samples could be added to the lower part of the Gull Island Section. All grey chert samples from Gull Island were assumed to lie above the cherts exposed in the top parts of the Shoal Arm Section. The stratigraphic position of these samples on Gull Island is qualitatively constrained by their distance from the core of a small anticline on one side and the distance between their position and the first appearance of the black slates to the east on the other side (Figure 2.3). It was concluded that they belong to the middle and upper part of the grey unit in contrast to the grey cherts at Shoal Arm which are from the lower part. As a consequence, the vertical distance between the samples SA-20 (a mottled, grey, cherty argillite - the uppermost sample from the Shoal Arm Section) and GI-37 (a mottled chert - the lowermost sample of the grey unit on Gull Island) was chosen to be large (25 meter). The black slates on Gull Island were sampled as close as possible to the boundary of the grey unit. Still, a 10 meter wide outcrop gap separates the uppermost grey chert sample

from the lowest black slate sample. Table 3.3 shows the final stratigraphic order of the samples.

Table 3.3: Stratigraphic order of Badger Bay samples

Sample	Stratigraphic level	
GI-32	355 m	
GI-40	348 m	
GI-33	347 m	black slates
GI-39	345 m	
GI-41	337 m	
GI-42	335 m	
GI-38	325 m	
GI-35	320 m	
GI-36	310 m	grey, mottled cherts
GI-34	300 m	
GI-37	280 m	
SA-20	255 m	
SA-18	251 m	
SA-17	245 m	
SA-16	226 m	
GI-28	221 m	
GI-26	211 m	
SA-15	201 m	red and green argillites
SA-14	195 m	
SA-13	191 m	
SA-12	182.5 m	
GI-23	182 m	
GI-22	180 m	
SA-11 TOP	168.2 m	
SA-11 BOTTOM	168 m	
GI-21	167 m	
SA-10	154 m	
GI-19	152 m	
GI-17	145 m	
GI-14	138 m	
GI-16	135 m	
GI-13	133 m	
SA-9	132 m	
SA-8	130 m	
SA-7	125 m	
SA-6	123 m	
BB-16	122.5 m	
GI-8	120 m	
GI-10	117 m	

continued next page

Table 3.3 continued

SA-5	116 m	
GI-5	114 m	
GI-4	112 m	
GI-2	111 m	
GI-1	110 m	
BB-15	109 m	
SA-4	106 m	
SA-3	105 m	
BB-14	104.5 m	red and green argillites
SA-1	102 m	
SA-2	101.5 m	
BB-13	101 m	
BB-12	93 m	
BB-11	73 m	
BB-8	61 m	
BB-7	58 m	
BB-9	50 m	
BB-10	40 m	
BB-3	24 m	
BB-2	18 m	Wild Bight Group volcaniclastics
BB-1	0 m	

Samples from formations of similar age and lithology to the three formations in the Badger Bay area were collected at other locations in the Notre Dame Bay area. The intention was to have a set of samples whose chemical composition could be compared on a regional scale with the chemical composition of the samples from the Badger Bay. 30 samples were taken from the following localities (see Figure 2.2):

(1) Cull Island and mainland: The mainland side at the village of Leading Tickles exposes red argillites which are demonstrably equivalents of the red Shoal Arm Formation. On the opposite side, on Cull Island, the southeastern shoreline consists of Caradocian black slates and overlying greywackes.

(2) 4 kilometer north of Northern Arm on the road leading to Leading Tickles (the 'Northern Arm Section'), the uppermost red unit is exposed and transits into grey cherts, black slates and greywackes. As mentioned before, this section appeared to be baked, and may have been contaminated by fluids from an adjacent Ordovician gabbrodiorite.

(3) A fresh road cut along the Trans Canada Highway 10 kilometer west of Grand Falls at Red Cliff exposes Caradocian black slates and greywackes.

(4) Along Road No. 350 on the Fortune Harbour Peninsula samples probably equivalent to the lower Wild Bight Group were sampled from the New Bay Formation. A better correlation to the Wild Bight Group samples is not possible. Black, Llandeilian to Caradocian, graptolitic slates (Lawrence Head shale) and a malachite-colored chert probably correlative to the grey cherts were collected northwards from here along Road No. 350 just above the type section of the Lawrence Head volcanics.

In the course of the thesis, it became clear that these samples were of limited use. Geochemical correlation between the three Badger Bay sections was already appearing difficult. It will be shown that the geochemical composition within the stratigraphic sequence is varying considerably over short intervals on the scale of 10 meters. In order to apply the geochemical trends observed in the stratigraphic sequence in the Badger Bay area on a more regional scale, the stratigraphic position of the distant samples would have been required to be known on a scale that was of the same order as the geochemical composition was seen to vary in the Badger Bay sections. A correlation of this detail was not possible. As a consequence, only few geochemical analyses of these samples were obtained. The age relationship and the common characteristic sequence ranging from volcaniclastics to overlying hematitic argillites, grey cherts, and black slates to greywackes are therefore taken as the best constraint that the interpretations made from the geochemical trends observed in the Badger Bay sequence are applicable on a regional scale. The geochemical composition of few selected, poorly correlated samples would probably not have improved these interpretations.

3.6 Sedimentary structures in the Shoal Arm Formation and the interpretation of the depositional environment

3.6.1 Red Shoal Arm Formation

All argillites appear to be siliceous, are very hard and often exhibit a steely blue manganese oxide stain. The three differently colored subunits are described in their stratigraphic order.

Lower maroon and purple part:

Single hematitic beds have thicknesses of 1- 20 centimeter. They are intercalated with greenish layers of similar thickness. The proportion of red to green strata in this first unit is about seventy to thirty. Contacts are both sharp and transitional. Sharp contacts exist where the grain-size increases from a purple/maroon argillite to a sandy/silty green layer. Transitional contacts show no macroscopic change in grain-size. Frequently, the lower contact of a green layer is sharper than the upper. Fresh surfaces of the maroon argillites display a 3 - 5 millimeter thick, diffuse color banding of alternating dark maroon and purple. Weathered surfaces of the maroon parts often have a metalliferous stain suggesting a higher metal content than the purple parts. Dark brown, 0.5 centimeter to 1 centimeter thick bands with a metallic luster and sharp, upper and lower boundaries are abundant within the layers of maroon and purple argillites (Figure 3.5). They are different from the pyrolusite (MnO_2)-stained rhodochrosite bands that appear at the lower boundaries of green sandy/silty layers (Figure 3.6). Here, in general, a purple argillite forms a sharp contact to the overlying green bed. 3 millimeters to 1 centimeter above the contact within the green horizon the rhodochrosite band appears. Its thickness ranges from 0.5 to 3 centimeter. The rhodochrosite bands always show this setting suggesting that they are secondary

Figure 3.5: Orange weathering, possibly sideritic layer in the lower part of the picture. The fine grained overlying red argillite contains distinct, 0.5 centimeter thick, dark brown bands that are likely to be metal-rich. Gull Island Section, lower maroon and purple part in red unit (level: 9 meter; Figure 3.3); south shore Gull Island. (Photograph by W. Kidd)

structures and of diagenetic origin. They are more abundant and thicker in the first subunit of the red Shoal Arm Formation.

From their sedimentary features, the mode of deposition of the green layers is unclear. Although there are examples that are coarser grained than the corresponding hematitic argillites, and may therefore have been deposited in a short event, this is not the general case. We found no positive graded bedding or scour marks or another characteristic that would point to an origin as a turbidity current. The sandy/silty, green layers may be derived from particulate matter transported by canyon currents (Stow, 1986). When these currents entered the basin plain, the suspended material was deposited. Fine-grained, green layers may also have formed from the suspended fraction of a distal turbidite. One 60 centimeter thick, green unit appears to be a composite of 5 layers separated by 4 distinct dark laminations (Figure 3.6). The green layer may be a composite of several current deposits. On the other hand, the internal inhomogeneity of the unit may also be secondary. A thin rhodochrosite band was found at the base of this layer in the previously described relationship. Also, multiple color changes to purple and then back to green are visible. All these textures suggest secondary variations. Some of the intercalated non-hematitic layers appear to be sideritic as indicated by their orange-yellow weathering color (Figure 3.5). It is likely that the siderite is a diagenetic product, but the carbonate in the layer is probably primary. In many cases, the presence of carbonate in the green argillites may be the only difference from the purple and maroon argillites. It is suggested that some of the green layers represent deposits that supplied carbonate, probably in the form of biogenic calcite. The mode of sedimentation, however, can only be guessed. Episodic biogenic blooms may have resulted in an increased admixture of calcareous material to the sediment. It is alternatively possible that the green layers represent intermittent current deposits with calcareous material derived from the shelf or upper slope of the island arc.

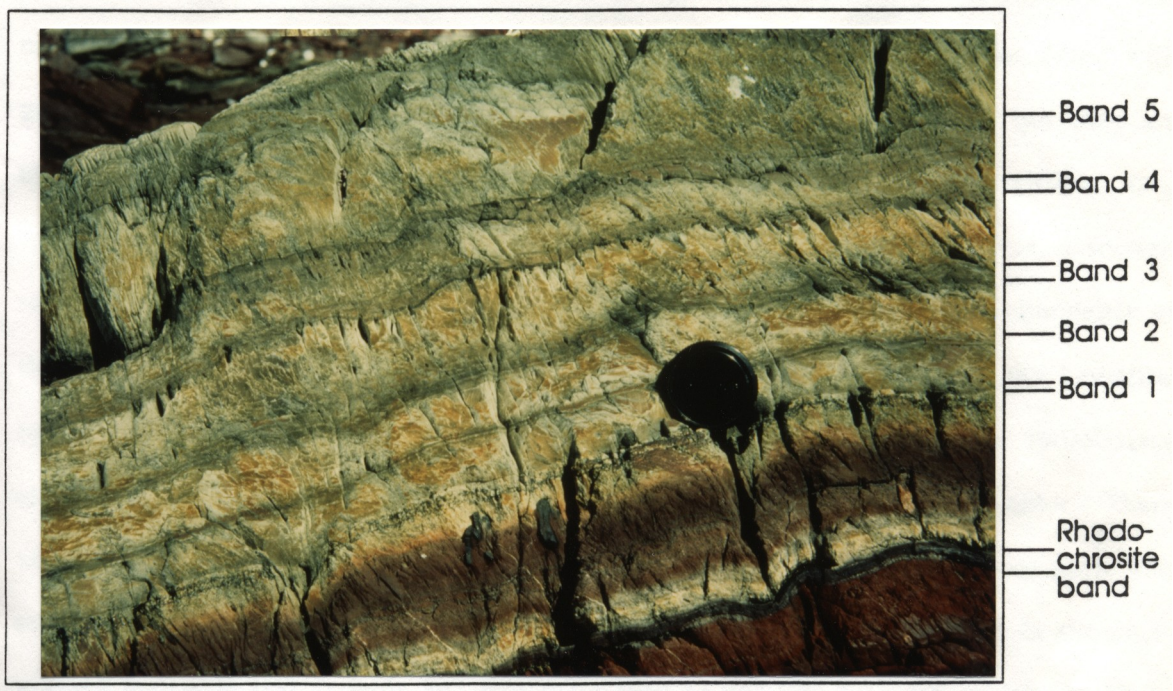

Figure 3.6: Composite silty, green argillite. The unit contains 5 grey-green, internal bands that separate the single layers. A 1 centimeter thick, pyrolusite stained rhodochrosite band is located 2-3 millimeters above the base of the unit. Secondary changes within the green layer are demonstrated by the purple coloration in the lower part of the unit. Bright-red part of the red unit, Gull Island Section (level: 20 meter; Figure 3.3); south shore Gull Island. (Photograph by W. Kidd)

Middle bright-red part:

The green layers are rarer than in the maroon and purple argillites below, and are in many cases distinctly coarser grained than the bright-red argillites. 3 intervals of 8 meter thickness do not contain any intermitting green layers. The bright-red strata contain abundant, 0.2 - 0.5 millimeter large, spherical or ellipsoidal bodies filled with quartz. These features also appear in the maroon and purple argillites, but they are more frequent in the bright-red argillites than in the maroon and purple argillites. It is very likely that these structures are derived from now recrystallized and deformed radiolarians. Their primary structure is not visible anymore. The varying abundance of the radiolarians suggests that one reason for the different coloration of the hematitic sediment is the abundance of radiolarians relative to hematite, the radiolarians apparently diluting the hematite-bearing matrix and thus lightening up the color. There are, however, thin horizons of 0.5 - 1 centimeter thickness in radiolarian-poor parts that are even more intensely colored. This implies that the amount of hematite in the fine-grained matrix is also variable and that there may be additional oxides, which are likely to be manganese oxides. Radiolarian-rich bottom beds mark intervals of 10 centimeter to 40 centimeter thickness (Figure 3.7). In some of these sequences, their abundance and size decreases upwards continuously. In other units, the radiolarian-rich bands are 2 - 3 centimeter thick, and form sharp contacts with the overlying and underlying horizons. In the red argillaceous horizon overlying the radiolarian-rich beds, 0.5 - 1 centimeters long, ellipsoidal pockets filled with quartz are oriented subparallel to bedding. They are supposedly derived from the radiolarian bed, were apparently ripped up and transported with the fine-grained matrix. Other structures are low-amplitude ripples, and distinct, 1 - 2 millimeter thick, white laminae of quartz-rich material. Some of the laminae were apparently sheared. These structures appear in the middle parts of the intervals. The top parts consist of massive, 5 - 15 centimeter thick, mud horizons which are often burrowed. The burrow fillings have varied orientations, a

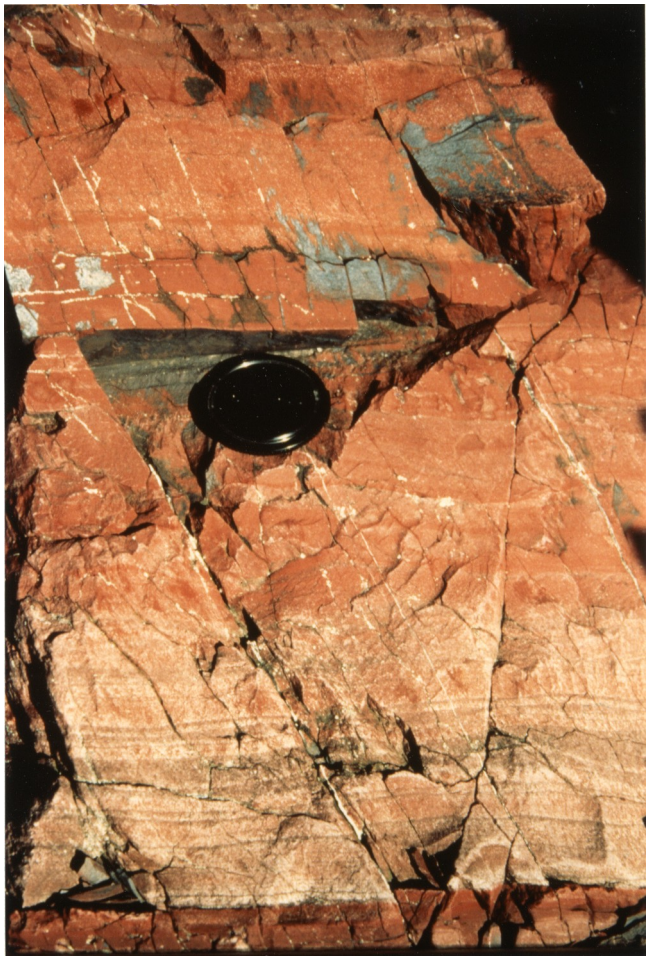

Figure 3.7: Bottom bed of a radiolarian turbidite in the bright-red unit. Note the sharp bottom of the radiolarian-rich unit, and the gradational decrease of the abundance of radiolarians upsection. Bright-red part of the red unit, Gull Island Section (level: 18 meter; Figure 3.3); south shore Gull Island. (Photograph by W. Kidd)

diameter of 5 millimeter to 2 centimeter, and appear mostly black. They may be up to 3 centimeter long. Additionally, there are spherical, black bodies with a diameter up to 8 millimeter. The nodules are oriented subparallel to bedding, and do exclusively occur in the mud horizons (Figure 3.8). They resemble manganese micronodules (Sugisaki, 1991). In some cases, the sequences exhibit a positive graded bedding, accentuated by the decrease in size of the former radiolarians upwards. Together these structures demonstrate resedimentation as fine-grained, mixed biogenic/clastic turbidites whereby the slowly accumulated, overlying muds indicate the background clay sedimentation. Other indicators of resedimentation are slump folds in purple and bright-red horizons as well as a slump horizon. Angular blocks of bright-red argillite up to 30 centimeter long sit in a matrix of the same material. One such horizon is 40 centimeter thick. The over- and underlying horizons are undisturbed. In contrast to the purple argillites the green argillites do not show any indicators of slumping. A very characteristic rhodochrosite band was found in the bright red unit. In this case, a 3 centimeter thick layer was folded into buckle-type folds with amplitudes of about 10 centimeter (Figure 3.2). The band also shows thrust-shortening. The overlying, green argillite thickens in the fold synclines whereas its upper boundary is planar. Similarly, the underlying, purple argillite thickens in the corresponding anticlines, but the layer has a flat bottom. Together, this suggests syndepositional shortening of the rhodochrosite band. Manganese oxide concretions were also found at the lower contact of a green volcaniclastic layer. They sit in pockets at the hinges of folds affecting the lower part of the layer.

Interfaces between purple and green beds indicate diagenetic mobility. One of them is the already described rhodochrosite band. Another example is shown in Figure 3.9. The photograph shows a green bed that has cut a channel into the underlying purple horizon. This underlying, purple horizon contains manganese concretions in the upper 3 centimeter and fades downwards into a pale purple to greenish color. A 5 millimeter thick, metallic, maroon band at the contact to the green bed exactly traces the

Figure 3.8: Black weathering, manganese (?) micronodules oriented subparallel to bedding in pale, purple cherts. Uppermost maroon and purple unit, Northern Arm Section (approximate level: 188 meter; Figure 3.4); 5 kilometer north of the junction in Northern Arm on Road 352. (Photograph by W. Kidd)

outline of the channel structure. This suggests that the thin, metalliferous band is not primary. Colley et al. (1984) reported the formation of similar metalliferous layers by diagenetic reduction and upward diffusion in North Atlantic turbidite-clay sequences. They presented a model where the deposition of organic-rich turbidites generated a downward-migrating organic oxidation front along which metals were reduced and diffused upwards. The mobilized metals were fixed in an oxygenated zone. Similarly, the metals in the purple layer may have been mobilized after diagenetic reduction and diffused upwards from below the nodular horizon where the purple color fades. The mobilization could have been induced by the deposition of the green bed which has the characteristics of a fine-grained turbidite.

Upper maroon/green part:

At Shoal Arm, the whole upper part of this unit is green in contrast to the Gull Island Section. In the Northern Arm Section only the uppermost part of this unit is exposed and is also purple. Evidently, secondary color changes have occurred since deposition. They may be associated with deformation and cleavage development and the position of the sections in the folds. In the lower part of this subunit, green beds become again more frequent and appear in intervals of 70 - 80 centimeters. No clear-cut grain-size difference is recognizable when the green beds are compared with the hematitic beds. In the Northern Arm Section, graded beds in purple argillites are visible, reflected by radiolarian-rich bottom beds. Laminations and/or ripples appear in the middle sections of the graded beds. The mud tops of the sequences show black and white weathering nodules with a diameter of about 5 millimeter (Figure 3.8). These features indicate the continuation of the turbiditic environment to the upper parts of the red Shoal Arm Formation. One rhodochrosite horizon was found at the top of a purple bed in the same configuration as described before. At Shoal Arm, mottled, grey horizons appear in the upper part of the section 10 meter above the buckled

Figure 3.9: Green, silty bed cutting a channel in the underlying purple bed. A band of 5 millimeter thickness traces the green bed suggesting a secondary origin. Deeper beds are horizontal. The metallic luster in the nodules indicates increased metal content. Middle part of the red unit (approximate level: 115 meter; Figure 3.3); Shoal Arm Section. (Photograph by W. Kidd)

rhodochrosite band. Mottled, purple cherts were also found in the Northern Arm Section. The mottling is a characteristic property of the overlying grey unit.

3.6.2 Grey unit

The original material of the grey cherts probably consisted of the siliceous remains of plankton providing the silica for later chert formation, but it cannot be excluded that fine-grained, siliceous, volcanogenic particles were deposited as well. The laminae observed in the lower 6 meter of the Northern Arm Section are in general 5 millimeter to 1 centimeter thick. Occasionally, the matrix contains clasts compressing the underlying laminae (Figure 3.10). The lamination in the cherts allows for different depositional interpretations. One potential explanation may be gravitational settling of mud size particles from the water column with varying accumulation rates of detrital and biogenic material. A stronger detrital accumulation rate may have produced the darker laminae. This would indicate a low-energy depositional environment. The biogenic accumulation rate may have been high assuming a biogenic bloom in the water column and increased supply of dead, biogenic matter to the sea floor. On the other hand, there are some indicators of resedimentation like ripples, graded beds in the lower part of the grey unit, and occasional silt-size, banded grey-green layers - very similar to the ones in the red Shoal Arm unit underneath. Also, the tops of the thicker, dark laminae are in general sharp whereas the contacts to the underlying light grey part are gradational. Together, these characteristics may suggest deposition of siliceous, biogenic turbidites. The dark shading at the tops may mark the mud-size top where clay sedimentation gradually revived. A turbiditic origin of chert sequences of the kind described has been proposed by several authors (e.g. Stow, 1986; Nisbet and Price, 1974).

Figure 3.10: Laminated cherts of the grey unit. Northern Arm Section (approximate level: 195 meter; Figure 3.4); 5 kilometer north of the junction in Northern Arm on Road 352. (Photograph by W. Kidd)

In the remaining parts of the grey unit the primary depositional structures are not well-preserved, because the sediment was thoroughly reworked. The mottling indicates an intense burrowing of the sediment by benthic organisms. The burrows have a diameter of 2 - 5 centimeter and are filled with dark-grey material (Figure 3.11). The fillings may consist of more clay-rich material than the surrounding matrix, which is light-grey, or greenish- to blueish-grey. The thorough reworking of large parts of the grey unit by organisms indicates a well-oxygenated seafloor at the time of deposition. In the lower part of this unit, however, the environment was apparently less favorable for the organisms as indicated by the virtual absence of any burrowing. It can only be hypothesized what the reason for this change was. Possibly, the oxygen content of the bottom seawater varied during deposition of the cherts. In the uppermost parts, black slates begin to alternate with the grey cherts.

The change from the red to the grey Shoal Arm Formation is marked by several characteristics. The hematite-bearing argillites disappear abruptly. Although it is not obvious whether the mode of sedimentation can be described as gravitational settling of particles from the water column or as turbiditic deposition, the red Shoal Arm Formation appears to be more variable and deposited in a higher energy environment than the grey unit. This change may reflect an increase in water depth and a more remote, clastic source area along with a biogenic bloom of planktonic organisms. Together, the characteristics indicate that the sedimentary environment changed from a "continental" margin setting controlled by siliciclastic and biogenic deposition to a distal pelagic, dominantly biogenic, deep sea environment.

Figure 3.11: Mottled grey cherts. The original lamination is still visible. Northern Arm Section (exact level not known; Figure 3.4); 5 kilometer north of the junction in Northern Arm on Road 352. (Photograph by W. Kidd)

3.6.3 Black slates

In contrast to the underlying lithologies, the preservation of sedimentary structures in the black slates is poor. This is due to the fact that the black slates represent the most strongly deformed unit of the Shoal Arm Formation. The black slates are in places cherty, and vary in their color. Slaty beds are black, anthracite-colored and siliceous; silty beds tend to be grey and silvery black. Some horizons are clearly carbon-rich. Weathered surfaces exhibit a yellow or orange stain, which is derived from the weathering of iron sulfides in the black slates. A few centimeter thick, silt-sized greywacke bands are interspersed in the lower part of the black Shoal Arm Formation. They form graded beds indicating turbiditic deposition. The bands are discontinuous and can only be traced for 5 or 6 meters. They become more abundant in the upper parts of the black slates. There, an amalgamated greywacke bed of 1 meter thickness was found heralding the deposition of the overlying, thick greywacke sequence. The field observations do not allow any detailed interpretation of the sedimentary environment. The slaty appearance contrasts to the cherts underneath and can be explained by an increased accumulation of detrital, clayey material relative to the dominantly biogenic, siliceous deposition below. A continuum to the greywackes above can be suggested. The sharp change to black, oxygen-deficient strata is striking. This change must have occurred fairly rapidly, because the cherts in the upper part of the grey unit appear to be burrowed indicating an oxygenated sea floor. They suggest a major change in the seawater oxygen content at the end of the deposition of the grey Shoal Arm Formation.

3.6.4 Greywackes

The overlying greywackes of the Gull Island Formation show a wide range of grain-sizes ranging from silts to coarse sands. Nelson (1979) assigned a thickness of 1.3 kilometer to the Gull Island Formation in the western Badger Bay area. The whole formation is a composite of turbiditic beds. The thickness of the turbidites varies from 50 centimeter to amalgamated beds of 10 meter thickness which appear in higher levels of the Gull Island Formation. The grain-size in the turbiditic units increases up-section. Paleocurrent indicators include flute casts, cross laminations, and flame structures and demonstrate a general transport direction to the southeast (Nelson, 1979). Rip-up clasts and slump structures are also frequent. It is concluded that the greywacke sequence marks the rapid uplift and erosion of a new, proximal source area to the northwest. The greywackes show a general color change from dark grey in the lower Gull Island Formation to greenish in higher levels. This could be interpreted as being sympathetic with a reoxygenation of the basin during greywacke deposition.

4. MICROSCOPE-SCALE SEDIMENTARY STRUCTURES AND PETROGRAPHY

4.1 Introduction

The previous section demonstrated that the different units of the Shoal Arm Formation display a variety of different lithologies. In outcrop, however, it was not possible to determine the mineral composition of the different rock types, or the detailed structure and composition of small features like the black micronodules. Also, bed contacts appeared to have been locations of secondary variations as, for example, evidenced by the occurrence of the rhodochrosite bands at the bottom of greenish beds. The observations made to that point were insufficient to explain the origin of these features. In order to extend the information provided by the field data and further constrain assumptions made from these observations, petrographic work and examination of the sedimentary structures at the microscope scale were necessary. The small grain-size of the sediments required microscopic work using magnifications at a minimum of 40 x. At these magnifications, the thin sections of purple, maroon and bright-red colored argillites appeared very dark under transmitted light. Most of the light was reflected by the hematitic pigment, with the consequence that minerals and textures were difficult to determine. Unfortunately, under reflected light, the clastic matrix and the radiolarians were difficult to separate. Also, single, hematite crystals were still not recognizable because of their small grain-size.

The use of the microprobe at the Rensselaer Polytechnic Institute, which is equipped with a backscattered electron microscope, gave a better opportunity than the standard optical microscope to investigate the petrographical composition and the sedimentary structures of these fine-grained lithologies. In contrast to transmitted light microscopy, the backscattered electron microscope produces images that depict the

varying degree of reflection of different minerals. Minerals that consist of elements with high atomic numbers (having a high, negative charge), reflect the incoming electron beam better than minerals that contain elements with low atomic number. As a result, more reflective minerals appear to be brighter on backscattered electron images than the less reflective minerals. The different shadings of the minerals often permitted a straightforward identification of different phases.

Additional information on the composition of a particular mineral was obtained by energy dispersive analysis. A selected point on a mineral emits a spectrum of characteristic X-ray radiation after being hit by the electron beam. The characteristic wavelengths emitted have different intensities which depend on the relative abundances of the elements present. The measured intensity of the radiation per time unit for a particular wavelength is displayed on a binary graph where the wavelength is plotted against the intensity of the emitted radiation. Every peak appears at the characteristic wavelength of the element that emitted this radiation. The peak positions therefore indicate the elements present in the analyzed point, and, because the amount of emitted radiation is proportional to the abundance of an element, the height of the peaks indicate the relative proportions of elemental abundances in the analyzed point. This qualitative, chemical composition of a particular point permitted an identification of the analyzed phase. The method is not able to unequivocally distinguish minerals whose chemical constituents are similar (e.g., Muscovite and K-feldspar). Therefore, for a correct identification of an unknown phase on backscattered electron images, the combined information from the mineral shape, the degree of reflection and the energy dispersive spectrum were necessary. With the described methods, it was possible to estimate the mineral composition of the dark, hematitic matrix. The energy dispersive spectra also provided the opportunity to attain information on the main carrier phases of particular major elements of interest.

The following assemblage is common to all thin sections:

Quartz + Albite + Muscovite + Chlorite + Accessories.

This assemblage is not diagnostic, because it occurs at P/T conditions ranging from prehnite-pumpellyite facies to greenschist facies (Frey, 1987).

Hematite-free thin sections permitted a better optical identification. The assemblage regularly occurring in these thin sections is:

Quartz + Muscovite + Albite + Chlorite + Prehnite + Epidote + Accessories.

Although pumpellyite was not found in the thin sections, the small grain-size of the minerals may have caused it to be overlooked. In the case of its presence, the mineral assemblage would have been diagnostic for the prehnite-pumpellyite facies. Nelson (1979) described pumpellyite in the underlying volcaniclastic sandstones of the Wild Bight Group and the greywackes of the Gull Island Formation. The metamorphic assemblages in the two formations are diagnostic of the Prehnite-Pumpellyite - Lower Greenschist facies (Nelson, 1979). It seems reasonable that metamorphic conditions in the Shoal Arm Formation were not different from the two other formations, and also range between lower Greenschist and Prehnite-Pumpellyite facies.

In the following subchapters, the thin sections are divided into groups of hematite-bearing and hematite-free argillites. The descriptions are based on observations with a standard optical microscope under transmitted, reflected, transflected light and on backscattered electron images. The latter method was done at magnifications ranging from 40 x to 3600 x.

4.2 Hematitic argillites

4.2.1 Petrography

The constituents of this group are quartz, muscovite, albite, prehnite, minor potassium feldspar, apatite, chlorite, carbonate, hematite, ilmenite, magnetite, and Mn-oxide.

Quartz is the major constituent of all thin sections. The mineral appears both as round to slightly elliptical bodies and finely dispersed in the matrix (e.g. GI-19, Figure 4.1). The assumption that the spherical bodies represent recrystallized radiolarians is constrained by the multi-crystalline appearance of the fillings. Detrital quartz would be expected to form a more heterogeneous mixture with mica and albite. The quartz here is clearly present as a separate component. In a few cases, muscovite is included in the spheres and ellipsoids which is interpreted to indicate detrital impurities. The fine-grained quartz in the matrix is presumably also biogenic, and may be a product of recrystallization during diagenesis and low-grade metamorphism. It cannot be excluded, however, that some of the fine-grained quartz is actually derived from a silicic volcanic source.

In backscattered electron images, the muscovite can be recognized as the elongated crystals and by its medium-grey color (Figure 4.2). The muscovite minerals are subparallel to each other and lie in the direction of cleavage. Energy dispersive spectra of these minerals did not show Mg or Fe, indicating that they are true muscovites rather than phengitic muscovites.

Albite has a varying grain-size in the thin sections. It appears as a fine-grained constituent in the matrix, but is also displayed as angular, fragmented, large minerals and occasionally as large, euhedral minerals of clearly secondary origin. The large, angular grains are interpreted as detrital albite of volcaniclastic origin which may have been derived from a silicic or altered mafic volcanic source. On backscattered electron

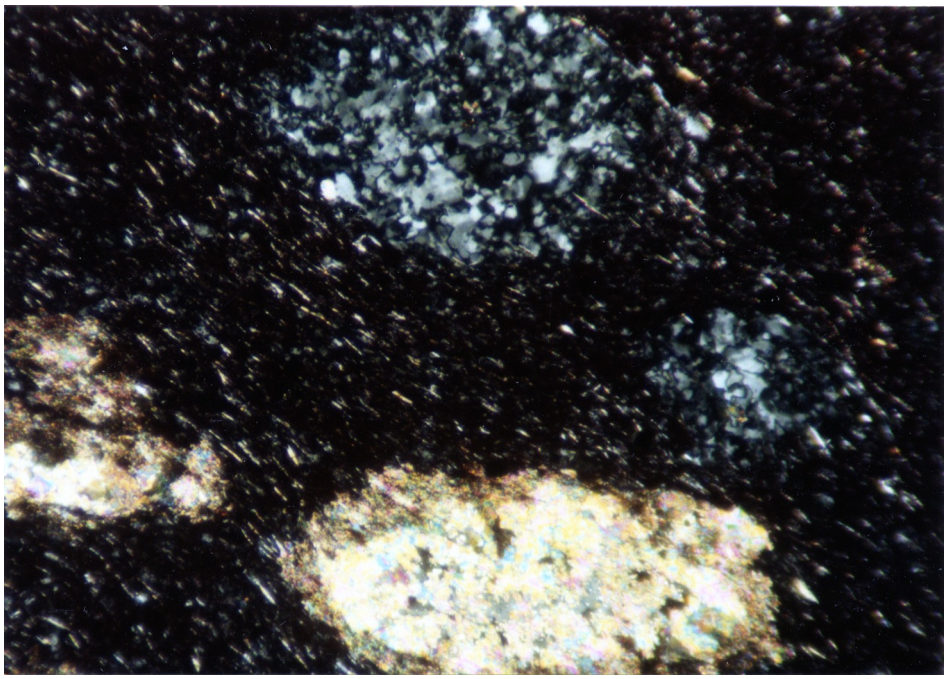

Figure 4.1: Thin section photograph of hematitic argillite (GI-19) with recrystallized radiolarians. Radiolarians are either filled with quartz, or show secondary replacement by carbonate. Matrix consists of fine-grained quartz, muscovite, +/- accessories. Crossed polarizers, 10x magnification. Broad side of print is about 0.86 millimeters long.

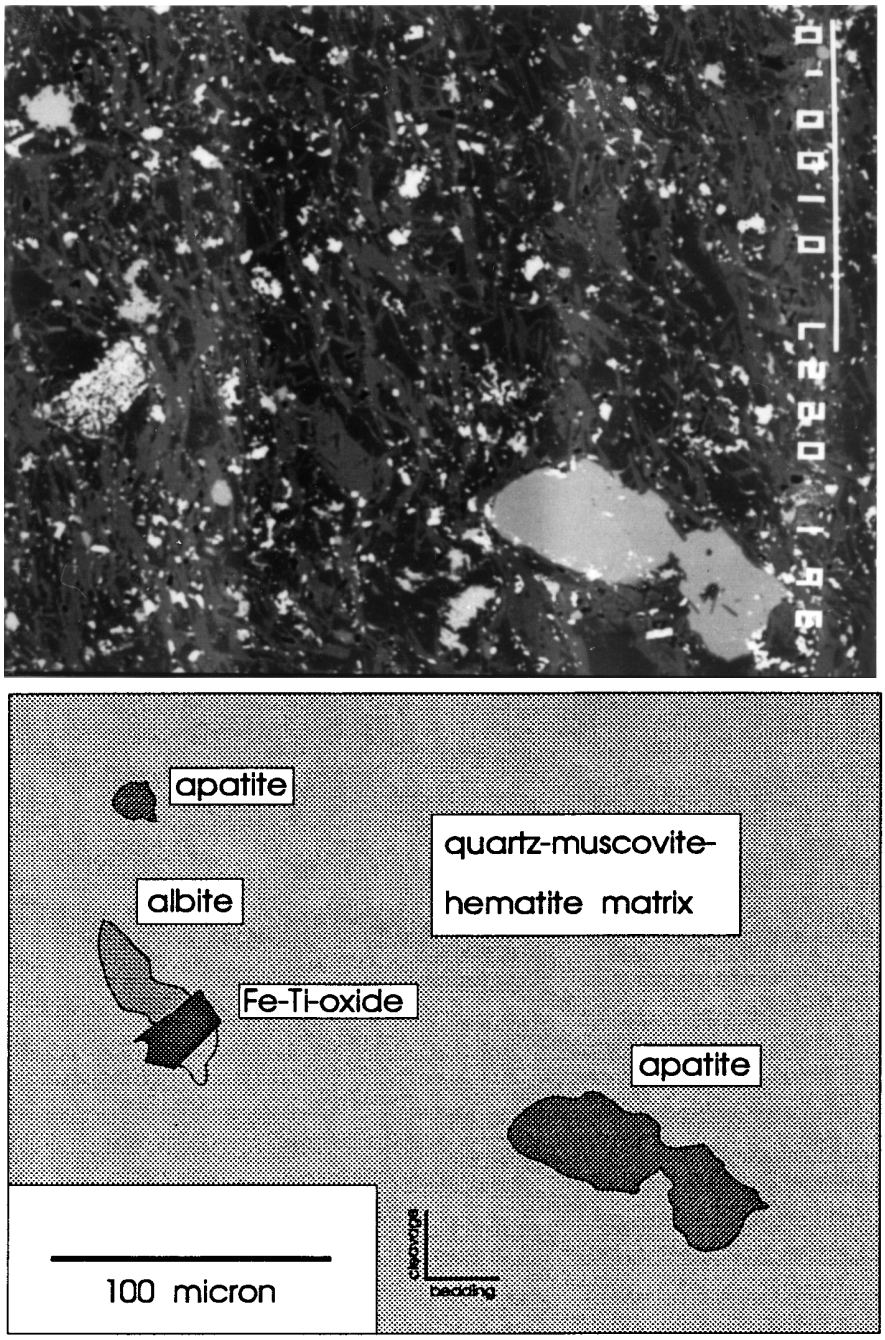

Figure 4.2: Backscattered electron image of red argillite (BB-10). Different grey tones indicate the mineral phases present. The accompanying sketch illustrates the most distinct phases on the image. Mineral phases were identified by energy dispersive spectra. Broad side of print is parallel to bedding. Scale bar indicates 100 microns.

images, the albite is represented as a medium- to dark-grey phase (Figure 4.2). The energy dispersive peaks of selected albite crystals appeared exclusively at the Na, Al and Si peaks, and indicated an almost pure albitic composition. Potassium feldspar is rare in the argillites of the Shoal Arm Formation. On backscattered electron images the potassium felspar is slightly brighter than the albite, and is commonly seen forming large euhedral crystals. These minerals were therefore interpreted as diagenetic K-spar. Ca-plagioclase is very rare. It is suggested that the unstable plagioclase was already rare in the originally deposited silty clay. During metamorphism, the remaining plagioclases were then altered to prehnite (and pumpellyite) and/or calcite and albite.

Prehnite forms small 10 - 20 micron crystals. Its identification using backscattered electron imaging was not conclusive, however. Nonetheless, the mineral can be identified with confidence under transmitted light.

Chlorite is present as a fine-grained constituent in the matrix. It is not considered to be an *in-situ* alteration product of ferromagnesian minerals (e.g., olivine or pyroxene), since no remnants of these minerals were detected. The energy dispersive spectra of selected chlorites indicated that they were Mg-rich, and contained only minor portions of Fe. A few, large chlorite minerals occurred as intergrowths with carbonate.

The backscattered electron images also showed larger, light-grey colored minerals. The energy dispersive spectra of these minerals showed two strong peaks at Ca and P, which indicated that the phases are likely to be apatite. In some cases, apatite forms large crystals up to 70 microns (Figure 4.2). Muscovite needles are enclosed in this mineral suggesting that the apatite is secondary. Small apatite crystals were found around some of the radiolarian grains (Figure 4.3). It is suggested that these small minerals are also of diagenetic origin. Presumably their formation is related to the neighbouring radiolarian. Biogenic material may be a conceivable explanation for the ultimate source of phosphorus (e.g., Froelich et al., 1982).

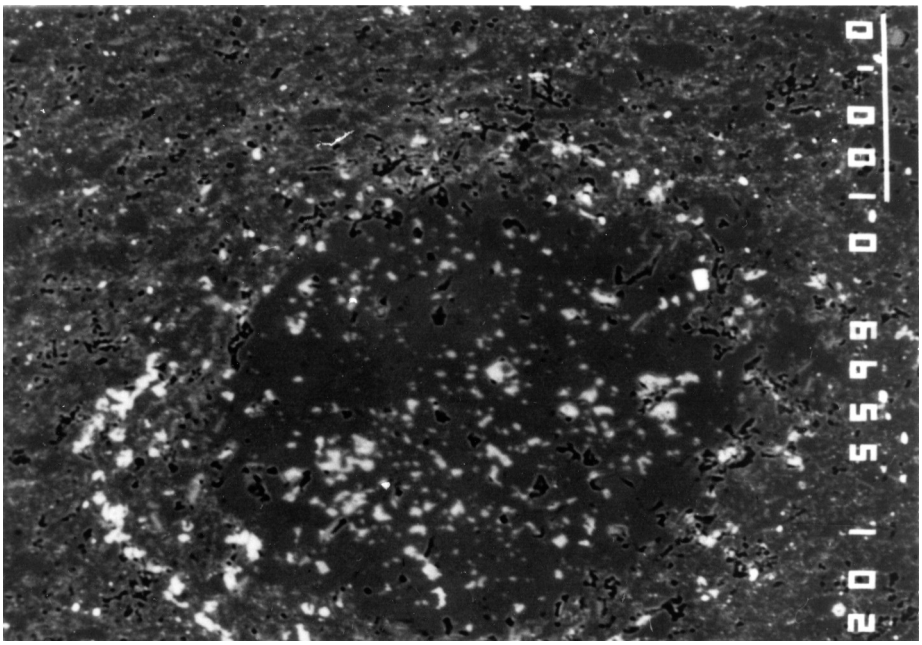

Figure 4.3: Backscattered electron image of a radiolarian and the surrounding matrix in thin section GI-22. The radiolarian interior consists of quartz (dark-grey) and apatite (light-grey), and minor Fe-Ti oxides (almost white). Small apatite crystals rim the radiolarian. Broad side of print is parallel to bedding. Scale bar is 100 microns long.

Carbonate is rare in the hematitic argillites. Where it appears, it forms large crystals, and replaces the quartz in the spherical or ellipsoidal former radiolarians. This observation strongly suggests a diagenetic origin.

Separate grains of the red, hematitic pigment could not be detected with the standard optical microscope. On backscattered electron images, using magnifications of 360, however, separate crystals/domains can be distinguished from the matrix. The hematite crystals have grain-sizes of $\leq$ 1 micron. At this scale, the hematite was found to be evenly distributed in the matrix (Figure 4.4). Other oxide minerals were also recognized containing Fe and Ti. Peak ratios of Ti:Fe up to 2:1 on the energy dispersive spectrum indicated that significant amounts of Ti are present in these oxides. Electron microprobe data of hematite in low grade schists described by Kawachi et al. (1983) showed abundances of TiO_2 in hematite between 0.35 percent and 4.52 weight percent. Major element analyses of hematite presented in Deer et al. (1985) also showed that TiO_2 in hematite does not exceed 5 weight percent. Consequently, it is more likely that the minerals examined here were either ilmenites or titaniferous magnetites which are known to contain up to 20 weight percent TiO_2 (Deer et al., 1985). The backscattered electron images showed that these minerals have in many cases euhedral square to rectangular shapes, and are larger than the hematite, between 4 and 5 microns (Figure 4.2, left side). The euhedral shape may indicate secondary growth. Some Fe-Ti oxides were found to be accumulated on one area (Figure 4.2). The origin of these features is unclear. They may represent an *in-situ* alteration product of a detrital Fe-Ti oxide mineral.

4.2.2 Sedimentary structures

The textures of the hematitic thin sections are variable. Channels filled with plagioclase-rich material and relatively large former radiolarians cut into the underlying

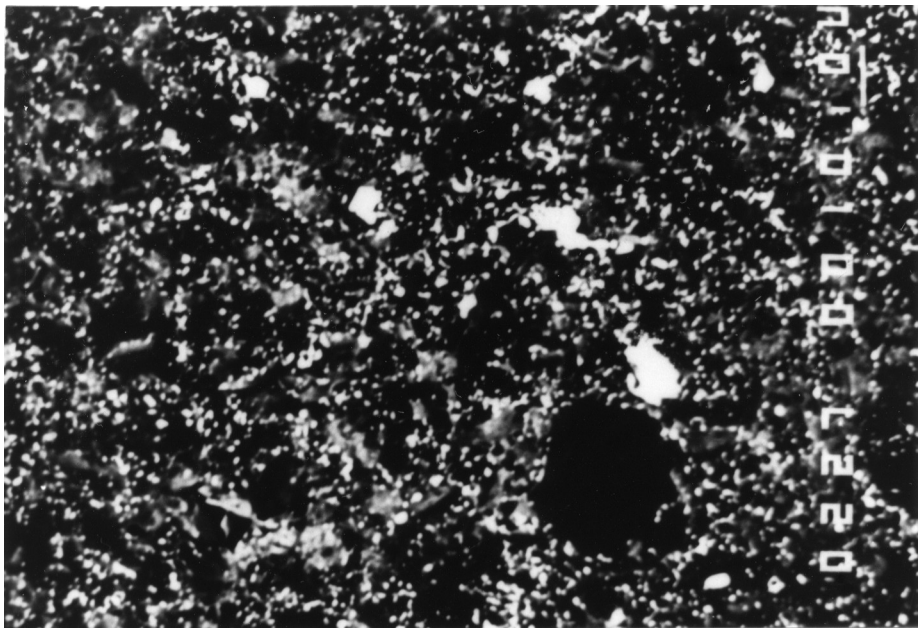

Figure 4.4: Backscattered electron microscope image of hematitic argillite GI-1. The smallest white phases are mostly Fe-oxides, larger white phases Fe-Ti oxides. Dark, large spherical body in the lower part of photograph is probably a recrystallized radiolarian. The rest of the matrix consists of quartz and muscovite. Broad side of print is parallel to bedding. Scale bar is 10 microns long.

clay-rich material. These features confirm the interpretation that the red argillites were deposited by silty turbidites. The silty intervals are less hematitic than the finer-grained tops. The presence of hematite is therefore not directly correlated with turbiditic deposition. The hematite appears to be more abundant in intervals of low sedimentation rate. This observation generally applies to laminations that result from changing abundances of hematite. In all cases, either the coarser grained, clastic component or the biogenic material have suppressed the hematite component. Color changes observed in the hematitic argillites are the result of varying abundance of hematite relative to the diluting detrital or biogenic component. Therefore, an independent Fe-source seems to be likely. These could have been Fe-oxyhydroxides that were dehydrated during compaction and formed hematite.

In the maroon and purple interval, which forms the lowest part of the red unit, fewer radiolarian spheres or ellipsoids were found in thin sections. In contrast to the rest of the red Shoal Arm Formation, relatively coarse-grained, matrix-supported, > 100 micron, angular quartz and plagioclase grains were present in the matrix. These are interpreted as volcaniclastic fragments. The thin sections were found to be particularly rich in hematite. The accumulation of biogenic material in this section may therefore have been minor, consequently the hematitic component was accentuated. The relationship between the angular mineral fragments and the increased abundance of hematite is unclear. It could be suggested that this interval marks increased, distal volcanic activity. Fragmented, ejected particles from volcanic eruptions may have settled through the water column and mixed with the hematitic clay.

Thin sections from samples located higher in the stratigraphic section of the red unit become progressively poorer in hematite, the grain-size of the matrix, however, remains constant. An increase in the detrital accumulation rate would possibly be paralleled by a slight grain-size increase, and a decrease in sorting. Increased accumulation of biogenic quartz does not necessarily require a grain-size increase,

because the radiolarians may be recrystallized as fine-grained quartz. It is also conceivable that the component from which hematite was formed became weaker in this interval. Therefore, it is suggested that two processes acted simultaneously. The hematitic component, or its predecessor, was continuously decreasing up-section, as the biogenic sedimentation rate increased. The gradation from bright-red to greyish-purple in the upper part of the red Shoal Arm Formation is attributed to an increased admixture of biogenic quartz coeval with a decreasing supply from the Fe-source.

4.2.3 Mn-micronodules

Mn-oxides and quartz are the dominating components of the 1 - 2 millimeter, black micronodules that were found in the mud tops of turbidites (Chapter 3). In backscattered electron images, Mn-oxides form the highly reflective components of the nodule interior (Figure 4.5). The energy dispersive spectrum of these oxides showed only Mn peaks. The high reflection and the absence of any other element at significant abundances (e.g. > 1 wt%) suggest that the minerals are Mn-oxides. The size of individual crystals is $\leq$ 5 microns. A second component is quartz, which is presumably derived from radiolarians. In the thin section of sample GI-17, which is derived from the middle part of the Gull Island Section in the bright-red unit, the nodules consist of coagulated spheres of radiolarians. The Mn-oxides are filling the interstices. Other nodules, e.g. in GI-8, do not show such a clear textural separation. The backscattered electron images showed that quartz and Mn-oxide form a fine-grained mixture. Few radiolarian spheres are preserved in these nodules. The electron microscope images revealed that a bedding parallel, layered structure is preserved in the interior of some of the nodules (Figure 4.5). The center of the nodule appears particularly metal-rich as evidenced by the white color. Another nodule in the thin section of sample GI-8, which is also taken from the bright-red unit in the Gull Island Section, showed a distinct,

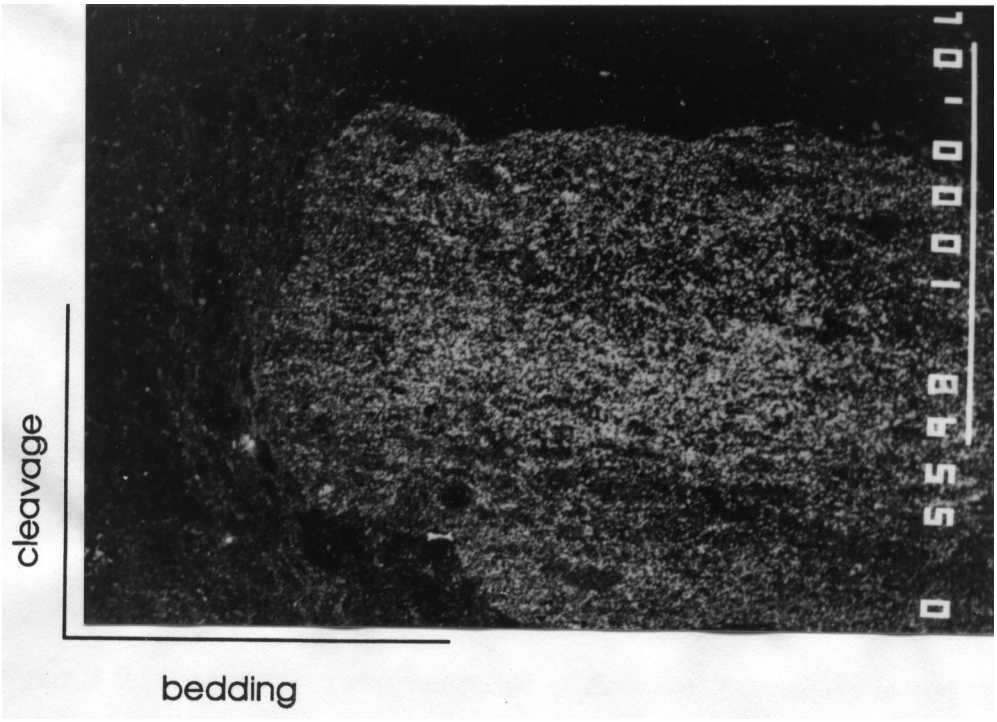

Figure 4.5: Backscattered electron image of Mn-nodule. Nodule interior displays layering that is parallel to bedding. The interior of the nodule consists mainly of Mn-oxides and quartz. Grey phases visible on the right side of nodule are anastomosing muscovite crystals that lie in the cleavage direction. Broad side of print is parallel to bedding. Scale bar is 1 millimeter long.

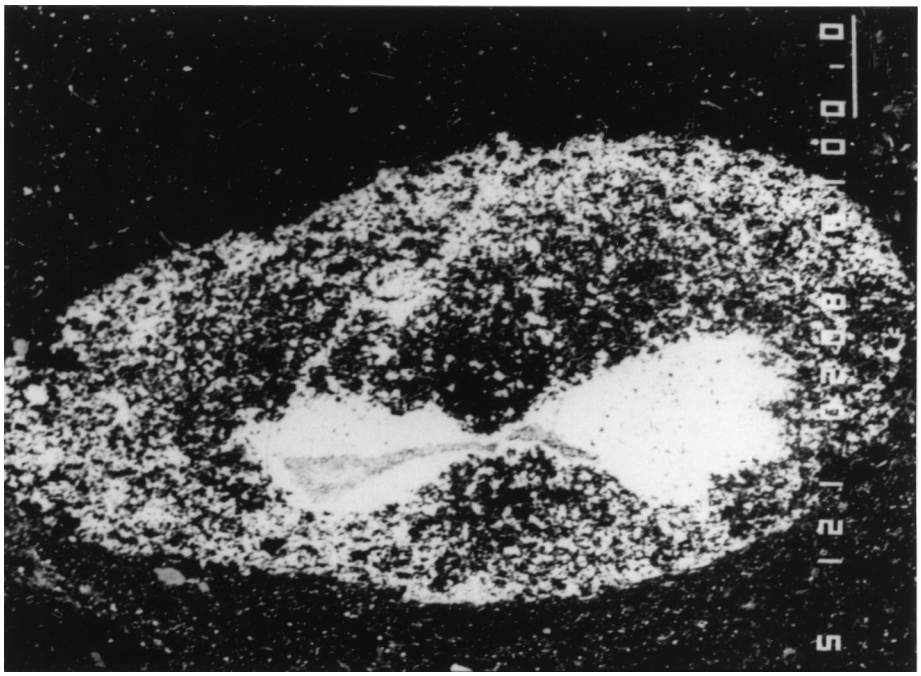

Figure 4.6: Backscattered electron image of "bow-tie" Mn-nodule in red argillite GI-8. The long side of the print is oriented parallel to bedding, and the nodule is in stratigraphically upright position. The center of the nodule is a slightly darker colored feature surrounded by the Mn-oxide-rich "bow-tie". Between bow-tie and outer rim, the nodule is less Mn-oxide rich. At the bottom of the nodule, a weak halo is visible, which is recognized by its slightly brighter colors compared to the top of the nodule. Scale bar is 100 microns long.

internal structure. An unidentified object forms the center of the nodule and is enclosed by Mn-oxides in a bow-tie fashion (Figure 4.6). This feature seemed to have served as the nucleus for the nodule. The rest of the nodule is a fine mixture of quartz and Mn-oxides. The nodules exhibit a pale halo up to 1 millimeter thick located at their bottom side. This halo shows fewer oxide minerals. The top of the nodules or the lateral ends never show a halo. These structural relationships suggest replacement or impregnation of a radiolarian-rich matrix by Mn-oxides. It is likely that Mn migrated upwards leaving a depleted halo on the lower side. Radiolarians or conodonts (?) may have served as nuclei for the nodules. A profile showing the variation of the geochemical composition across the nodule and the margins is described in chapter 5.5.

4.3 Green argillites

4.3.1 Petrography

The absence of a hematitic pigment in the green argillites allowed standard optical microscope observations using transmitted light. The backscattered electron images provided additional, textural information at large magnifications revealing phases that were not detected under transmitted light. The minerals in the green argillites are divided in two groups: (1) 5 - 20 micron minerals forming the silty to argillitic matrix, and (2) 10 to 50 micron minerals that appear to be of diagenetic origin.

Minerals of the first group are quartz, muscovite, chlorite, albite, minor potassium feldspar, prehnite, spessartine and epidote. This association indicates again that the metamorphic grade of the Shoal Arm Formation is low, ranging between prehnite-pumpellyite facies and lowest greenschist facies. Figure 4.7 shows a backscattered electron image of a typical green argillite. The muscovite is oriented subparallel to the cleavage, and forms small, elongated, medium-grey crystals. Energy

dispersive spectra of these minerals indicated that Mg and Fe occurred at abundances of ≤ 1 wt% thereby precluding a phengitic component in the muscovite. Radiolarians, although present, are rarer than in the hematitic thin sections. On the backscattered electron images, the radiolarians occur as dark-grey, round areas, free of the elongated muscovite (see accompanying sketch of back-scattered electron image in Figure 4.7). Fine-grained chlorite is more abundant in the green argillites than in the hematitic argillites. Energy dispersive spectra from selected minerals identify it as a Mg-Fe chlorite. (The black spots on the image are pits left by minerals that were torn out during polishing.)

The second group of minerals encompasses apatite, rhodochrosite, occasionally albite, and magnetite/ilmenite. Magnetite and/or ilmenite form ≤ 10 micron large, euhedral crystals, and are the only oxides present. On backscattered electron images, they can be identified by their almost white reflection color (Figure 4.7). Similar to the Fe-Ti oxides in the hematitic argillites, the oxides form discrete clusters, e.g., in the lower left corner of Figure 4.7.

Rhodochrosite is generally coarser-grained than the matrix. Figure 4.7 confirmed the initial characterization based on transmitted light microscopy that the phase was a carbonate. X-ray peaks at the Mn, Ca, and Sr wavelengths, in which Mn was the most intense peak, indicated that the phase is rhodochrosite. In several thin sections, the carbonates were found to replace radiolarians. These characteristics suggest that the large phases are secondary, and have been formed during diagenesis.

Apatite can be distinguished from rhodochrosite by its lighter grey color on backscattered electron images and by its energy dispersive spectrum which consists of X-ray peaks at Ca and P wavelengths. Muscovite needles can be found to be enclosed by the large phases. The grain boundaries of the large phases were irregular, and suggested grain boundary migration. This suggests that apatite was forming after

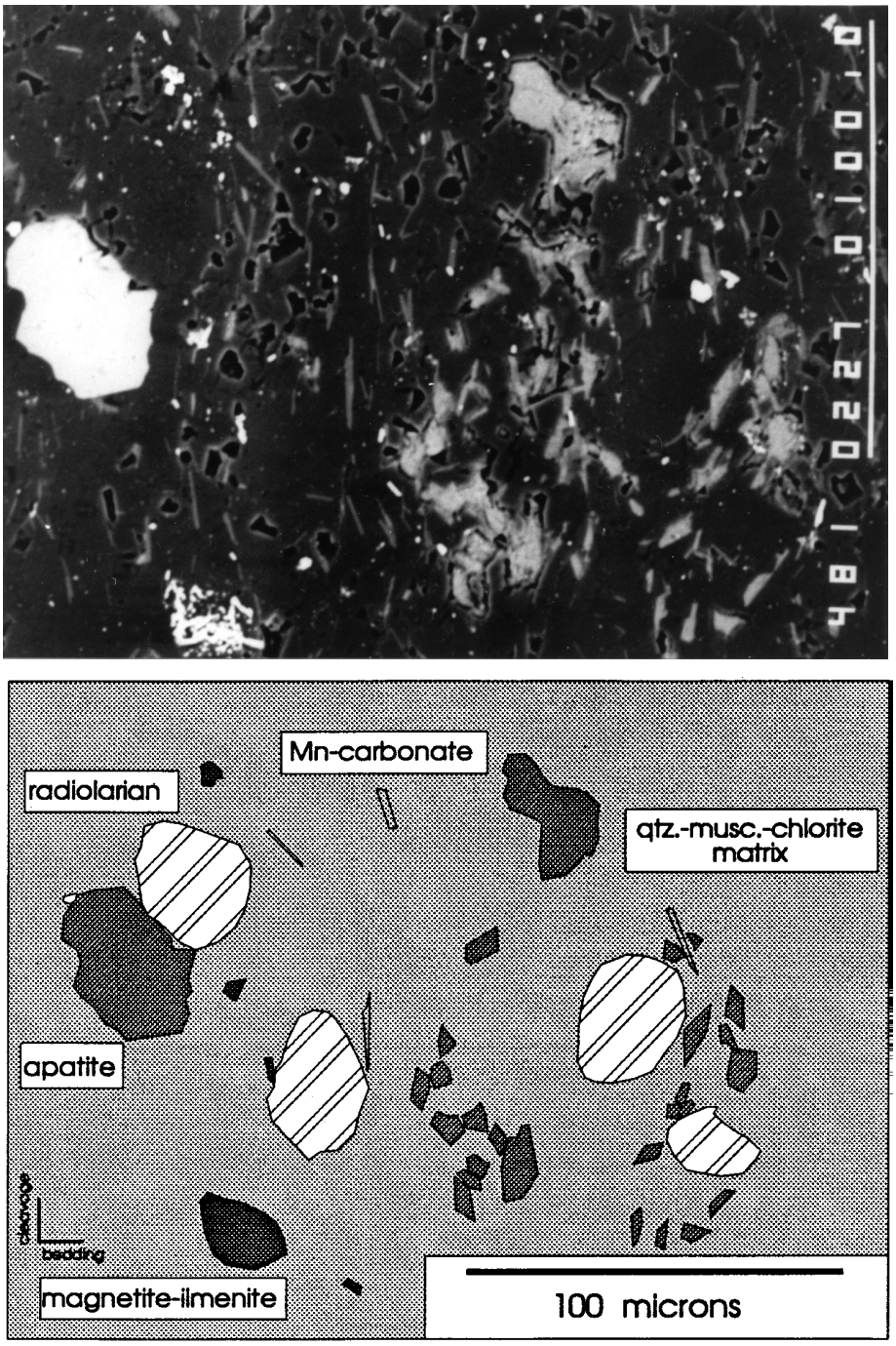

Figure 4.7: Backscattered electron image of green argillite BB-10. The accompanying sketch illustrates the most important features. The muscovite crystals lie in the direction of cleavage. Dark spots are crystals that were torn out during polishing. Long side of print is parallel to bedding. Length of scale bar is 100 microns.

deposition. It is, however, uncertain, whether the apatite represents a diagenetic or a metamorphic product.

4.3.2 Sedimentary structures

The grain-sizes of green argillites range from argillitic to silty-fine sandy. The coarser-grained examples are only present in samples of the uppermost Wild Bight Group. The grain-size decreases stratigraphically upward in the section. Primary sedimentary structures in the thin sections are not well-preserved because of considerable replacement of the clay matrix and the quartz by secondary carbonate.

A thin section of sample BB-10 (Beaver Bight Section, uppermost Wild Bight Group) exhibits thin, 1 millimeter thick laminae that appear to be slightly darker than the remaining thin section. These thin bands consist of coarser-grained carbonates. The origin of the carbonate is unclear. A secondary origin is favoured here, although the evidence is not strong. The grain-sizes of muscovite, quartz, or albite do not increase in these bands. In contrast, the carbonate crystals are large and euhedral, which suggests secondary growth. It appears that some of the carbonate has replaced the matrix. Potentially, the present structure resulted from an original thin band that was already calcareous, possibly a microturbidite. Although no definite explanation for this structure can be given, it supports the former statement (Chapter 3) that the green layers are most likely composite deposits from bottom currents (contourites?), and were not deposited as one event.

The color transitions of hematitic to green argillites were of particular interest. The field observations suggested an abrupt increase in grain-size at the contact of bright-red to green argillites. Thin sections that were prepared from color transitions could only partially confirm this hypothesis. A thin section of sample BB-10 (Beaver Bight Section; uppermost Wild Bight Group) exhibits a distinct grain-size increase from

the underlying purple argillite to the overlying green, silty argillite. The green part of the thin section contains coarse-grained plagioclase (albite), angular quartz grains and large chlorite minerals. Elliptical, quartz-filled bodies are occasionally present in the lower part of the green section. The underlying purple part is a distinctly finer-grained mixture of dominantly muscovite and quartz, and fine-grained albite. Thin sections from color transitions in the lower and middle part of the red unit do not exhibit such a clear-cut grain-size difference. At the contact, an abrupt grain-size increase was only noted by the appearance of large, secondary carbonate, presumably rhodochrosite. Carbonate is particularly abundant at the lower boundary of the green layers. Figure 4.8 is a photomicrograph of a green argillite close to a contact with a hematitic argillite. The photograph demonstrates that the rhodochrosite forms large, sometimes euhedral crystals replacing the matrix, and is thus likely to be a secondary phase. The grain-size of matrix minerals in the green part of the thin section was indistinguishable from the grain-size of the matrix of the hematitic part. Grain-sizes of matrix minerals were compared from several red and green colored thin sections. No major grain-size difference existed between the green and the hematitic argillites. Since recrystallization of the argillites during the metamorphic event has probably homogenized the mean grain-size, the few preserved, coarsest grained, detrital minerals in the two lithologies may be meaningful indicators of differing accumulation rates. A consistent difference in the coarsest grain-sizes between the two lithologies could not be observed confirming the previous statement that the mode of deposition of the green and the hematitic argillites was probably similar.

Thin sections of color transitions with basal rhodochrosite bands in the green argillites were also inspected. Again, the composition and the grain-size of the matrix do not change across the boundary. Hematite disappears abruptly at the color boundary, and is replaced by coarse-grained (>25 micron large) Fe-chlorite. The Fe-content was confirmed by the anomalous, blue interference colors of the chlorites. The size and

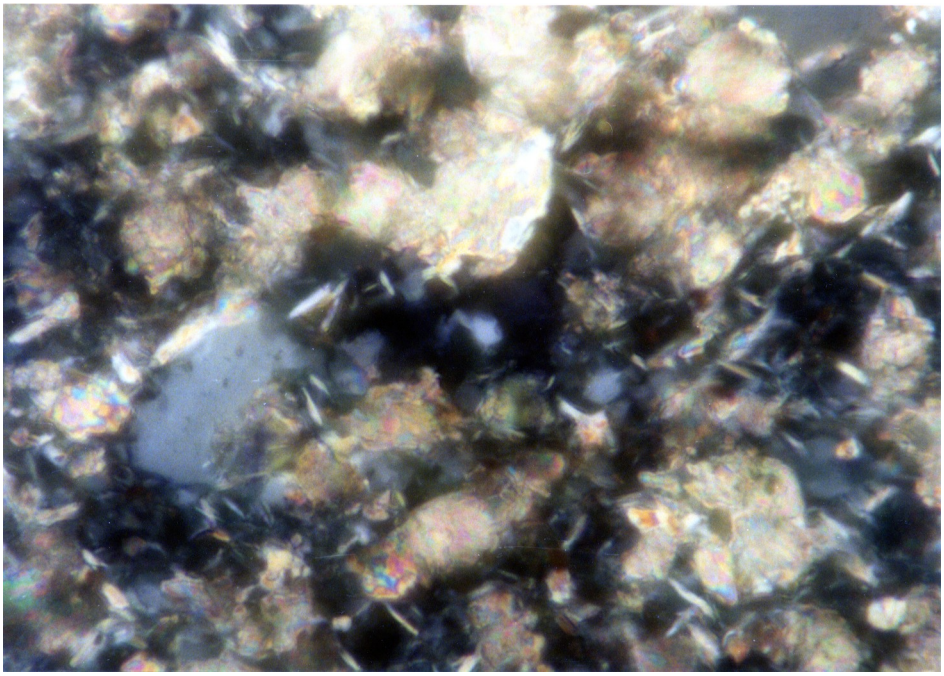

Figure 4.8: Thin section of Mn-rich argillite GI-5. Crossed polarizers. The yellow-golden phases are Mn-carbonate crystals. Mn-carbonate is interpreted as a secondary phase in the matrix. The matrix consists of small needles of muscovite crystals, and both fine-grained and coarse grained quartz. Haze on print is an optical effect that results from the relief of the thin section. Long side of print is about 150 microns. Magnification 100x.

texture of the chlorite suggest that it is a secondary phase. Coarse-grained carbonate is already present in the hematitic part. Here, the carbonate replaces former radiolarians. Across the boundary, the abundance of this phase significantly increases. Carbonate becomes the dominant phase in the pink rhodochrosite band. Overlying this band, carbonate remains the dominant phase for at least the next 3 centimeters, replacing the clastic matrix by approximately 75 percent.

4.4 Grey, cherty argillites and grey, laminated and mottled cherts

Field observations in the upper section of the Shoal Arm Section suggest that the grey, cherty argillites in the upper Shoal Arm Section strongly resemble the grey lithologies of the mottled and laminated grey unit. Based on this observation, the samples that formally belong to the upper, red Shoal Arm Formation are described together with the grey, laminated and mottled unit. The matrix composition of these lithologies can be described as a continuum. The two end-members of this continuum are an even mixture of chlorite, muscovite, albite, quartz, and a quartz-dominated lithology with only minor proportions of muscovite, albite and chlorite. The grey argillites of the Shoal Arm Section represent the first end-member, and the laminated, grey cherts form the other end-member. Intensely burrowed, grey cherts are generally less quartzose. All types show diffuse remnants of spherical bodies (i.e., radiolarians) filled with microcrystalline quartz. Some of the fillings are coarser-grained than the dispersed quartz in the matrix. It is suggested that most radiolarians were destroyed during diagenesis. The small quartz crystals may have formed as a result of recrystallization of the former tests. Where radiolarians retained their original structure, they are frequently replaced by a large, carbonate phase. The interior of the burrows of the grey cherts is distinctly darker grey than the surrounding substrate. Although this

suggested that compositional differences exist between the substrate and the filling, microscopic examination revealed no major mineralogical differences. Also, despite the fact that apatite may have been overlooked under transmitted light, it is possible that biogenic apatite is more frequent in the interior of the burrow. No backscattered electron images were produced from the grey cherts. Geochemical differences between the filling and the substrate cannot be ruled out.

4.5 Summary of characteristics

The microscopic work allows the following conclusions:

(1) There is no major and consistent grain-size difference between the matrices of the hematitic and the green samples. Although a coarser grain-size has been observed in one green, upper Wild Bight Group sample (BB-10), this characteristic disappears in the higher, stratigraphic units.

(2) The presence of secondary Mn-carbonate and the absence of hematite in the green argillites represent the only consistent difference between red and green argillites.

(3) The quantity of oxides that occur in the red argillites depend on the varying dilution by clastic and biogenic material.

(4) Mn-micronodules in turbidite tops appear to be replacements of radiolarian-rich zones that possibly nucleated from biogenic material. Pale, oxide-free haloes on the bottom sides of the nodules suggest localized element mobility.

(5) The texture of the rhodochrosite indicates that it is a secondary phase. The rhodochrosite may either be an *in-situ* alteration phase or the product of elemental migration into the lower part of the green argillites.

(6) Qualitatively, the clastic component does not change with deposition of the grey cherts. Fine-grained quartz is interpreted to be a recrystallization product of dissolved radiolarians, which effectively dilutes the clastic component.

5. GEOCHEMISTRY

Introduction

Analysis and interpretation of the geochemical composition of the Shoal Arm Formation is the center of this study. Whole-rock compositional data form one part, and compositional data from selected, fine-scale sedimentary structures form the other part of this investigation. The average chemical composition of the Shoal Arm Formation is compared to other metalliferous deep-marine sediments (Chapter 5.1), both ancient and recent, as well as to the underlying volcaniclastic sediments of the Wild Bight Group. Different, sedimentary sources of the Shoal Arm Formation are discriminated and characterized with respect to their origin. The compositional analysis is performed using elemental correlations, and a R-mode factor analysis. Particular attention is paid to the changes in the sedimentary sources progressing through the stratigraphy. The variation of the different sedimentary components is examined by a detailed investigation of the stratigraphic trends of key-elements of different sedimentary components. The aspect of metal enrichment and depletion by redistribution as a result of diagenetic mobility is examined on different scales: (1) to address the potential for large-scale elemental diffusion from the underlying Wild Bight Group; (2) to determine the localized, compositional variation within restricted intervals of the red Shoal Arm Formation. The red Shoal Arm Formation is given preference in this chapter. Not enough analyses of the grey unit and the black slates were obtained to allow for a similarly detailed investigation but, some significant geochemical differences between these units and the red unit are nevertheless recognizable. The results are compiled in Chapter 6 in two models that illustrate the geochemical evolution of the whole sequence starting from the deposition of the upper Wild Bight Group and ending with deposition of the greywackes of the Gull Island Formation.

Preparation of samples and analytical precision

To prepare the samples for whole-rock XRF analysis, they were crushed, milled, and finally ground in a tungsten-carbide shatter box. Depending on the grain-size, between 500 grams and 1.5 kilograms of a rock sample were crushed and ground. The whole-rock composition of a kilogram-sample can be expected to eliminate effects of primary sample heterogeneities, (e.g. laminations), and the effect of possible local, diagenetic or metamorphic, element diffusion on a millimeter-scale. Samples from the Badger Bay area have been most frequently analyzed, because the stratigraphic sequence is best known for this area. About 25 grams per sample were selected and sent to Geochemical Laboratories, McGill University, Montreal (analyst A. Ahmedali). The samples were analyzed for the major and minor elements Si, Ti, Al, Fe, Mn, Mg, Ca, Na, K, P, Ba, V, Cr, Ni, Co, Cu, and Zn, and the trace elements Nb, Zr, Y, Sr, Rb, Pb, Th, and U. Analytical precision was tested with a department-internal standard of the Austin Glen shale from the Ordovician Taconic Allochthon in eastern New York State (the duplicate analysis are listed in Appendix 2). The analytical precision given by McGill was < 0.3 weight percent for the major elements and < 8 ppm for the minor and trace elements. Zr abundances below 46.5 ppm had to be discarded until June 1991 because of a continuous analytical error in the McGill data when compared with analyses of the identical Austin Glen shale obtained at the University of Michigan at Ann Arbor and the University of Massachusetts at Amherst. After May 1991 the analytical precision for Zr was greatly improved, and did not require further correction. Detection limits given by McGill are 0.01 percent for the major elements, 15 ppm for Cr_2O_3, and 10 ppm for the other minor elements including Co, Cu, Zn. Detection limits for the trace elements were 5 ppm for all trace elements (until May 1990), 2 ppm for all trace elements, except Pb (4 ppm), since June 1991. The analyses are listed in Appendix 1.

5.1 General, geochemical characterization of the Shoal Arm Formation

Although a generalization, it is necessary to characterize the average composition of the argillites with regard to certain reference compositions of comparable ancient and modern sediments. This procedure gives a first-order insight into the particular geochemical composition of this formation. The characterization is subsequently refined by splitting the data set into smaller stratigraphic units. The following reference compositions are selected:

The Post-Archean Average Shale (PAAS) of Taylor and McLennan (1985). The North American Shale Composite (NASC) (Gromet et al., 1984) would also have served this purpose, but Taylor and McLennan (1985) present a more complete element collection for the PAAS. The composition of the two composites is similar. The chemical composition of this shale can be compared to the composition of the upper continental crust (Taylor and McLennan, 1985). Comparison of the Shoal Arm Formation with this standard can give a first-order indication of the characteristics of local sedimentary source areas.

Since the Shoal Arm Formation represents a deep-marine, apparently siliceous sediment that is potentially metal-enriched, the comparison with pelagic, siliceous and metalliferous sediments of recent and ancient age appears to be useful. For this purpose, the mean abundances of ancient pelagic and hemipelagic sediments from the literature were used. These are analyses of lower Cretaceous red siliceous mudstones in the top part of an ophiolite section in the Apennines, Italy (Barrett, 1981) and the Ordovician Poultney Formation in the eastern Taconic Allochthon of New York State. The latter are used to evaluate the differences to a clastic, passive margin sediment of similar age, that was also deposited in a slope and rise environment (Dewey and Bird, 1970).

Metal enrichment in recent, distal, pelagic sediments can largely be attributed to the dispersal of hydrothermally leached material from the oceanic crust onto the ocean

floor (Dymond, 1981; Glasby, 1991) (the hydrogenous enrichment is discussed below). In order to evaluate the potential of hydrothermal enrichment, I compare hydrothermal index ratios in various, modern sediments with the Shoal Arm Formation. I used the composition of an average pelagic clay (Chester and Aston, 1976), the average composition of a hemipelagic metalliferous sediment from the Cocos Plate (Leggett, 1982), and a ridge-crest metalliferous sediment (Marchig and Gundlach, 1982).

Additionally, the Shoal Arm Formation is compared to the local standard reference composition of 12 volcaniclastics from the upper Wild Bight Group. Comparison to this composition can indicate important changes in the stratigraphic sequence. The 12 samples are particularly useful, because they do not greatly differ in their grain sizes from the overlying Shoal Arm Formation lithology, thereby diminishing the importance of sorting effects. On the other side, some uncertainty derives from the fact that the volcanics of the Wild Bight Group, which must have served as sources for the volcaniclastics, are geochemically variable (Swinden et al., 1990). As a consequence, the geochemical composition of the source area of these volcaniclastics was probably heterogeneous, and also likely to have been variable through time. Indications of provenance may be obscured by the average composition.

It is not useful to compare the simple element compositions because of the varying potential of biogenic silica dilution. Therefore, the elements were normalized to Al_2O_3, assuming no primary variation in Al_2O_3. With the exception of few analyses in the Poultney Formation, which has CaO and LOI (loss of ignition) contents of about 5 wt.% , all analyses have low contents of CaO and LOI (e.g $\leq$ 5 wt.%. Therefore, recalculation on a CaO- and LOI-free basis appeared not to be necessary.

Results

Tables 5.1 to 5.7 show the various element/Al_2O_3 ratios normalized to the different reference compositions mentioned above. Ratios equal to one indicate equal

Table 5.1: Element/Al2O3 ratios normalized to average Wild Bight Group composition (Fine-grained volcaniclastics of upper Wild Bight Group)

	greywackes	black slates	grey cherts	green argillites	Mn-rich, green argillites	red argillites
TiO2/Al2O3	1.06	1.15	1.50	1.27	1.48	1.48
Fe2O3/Al2O3	0.90	0.45	1.55	1.44	1.40	2.22
MnO/Al2O3	0.10	0.03	0.75	1.76	24.16	2.59
SiO2/Al2O3	0.52	1.49	2.42	1.04	1.05	1.08
Cr2O3/Al2O3	2.50	3.87	2.03	1.35	2.97	1.96
Ni/Al2O3	1.37	2.01	4.32	1.67	3.04	2.43
Zr/Al2O3	0.57	0.66	0.74	1.17	0.74	0.85
Cu/Al2O3	0.63	1.69	1.81	1.35	1.59	0.95
Co/Al2O3	1.65	1.17	4.38	3.05	4.61	5.81
Pb/Al2O3	1.33	1.54	3.24	2.17	1.33	3.14
V/Al2O3	1.75	6.05	1.89	1.12	1.64	1.50
CaO/Al2O3	0.51	0.05	0.62	0.55	2.80	0.38
MgO/Al2O3	1.97	0.86	1.67	1.32	1.80	1.20
Na2O/Al2O3	0.59	0.33	0.37	0.97	0.56	0.79
K2O/Al2O3	1.19	1.53	1.45	0.47	1.18	1.12
BaO/Al2O3	1.12	3.64	8.15	1.69	3.44	1.70
Zn/Al2O3	1.04	0.89	1.27	1.01	1.04	1.05
Sr/Al2O3	0.86	0.39	1.17	1.12	1.10	0.64
Y/Al2O3	0.33	0.50	0.63	0.80	0.76	0.81
P2O5/Al2O3	0.73	0.53	1.25	0.87	1.08	1.52
Rb/Al2O3	1.52	2.22	2.06	0.61	1.73	1.49
Na2O/K2O	0.50	0.21	0.25	2.08	0.47	0.71

Table 5.2: Element/Al2O3 ratios normalized to Post-Archean Average Shale (Taylor and McLennan, 1985)

	greywackes	black slates	grey cherts	green argillites	Mn-rich, green argillites	red argillites	upper Wild Bight Group
TiO2/Al2O3	0.78	0.85	1.11	0.94	1.09	1.09	0.74
Fe2O3/Al2O3	1.10	0.55	1.89	1.76	1.71	2.70	1.22
MnO/Al2O3	0.92	0.31	7.15	16.78	230.48	24.69	9.54
SiO2/Al2O3	1.24	3.60	5.83	2.50	2.52	2.59	2.41
Cr2O3/Al2O3	1.23	1.91	1.00	0.67	1.46	0.97	0.49
Ni/Al2O3	1.16	1.70	3.66	1.41	2.57	2.06	0.85
Zr/Al2O3	0.70	0.81	0.92	1.44	0.92	1.05	1.24
Co/Al2O3	1.80	1.28	4.77	3.32	5.01	6.32	1.09
Pb/Al2O3	0.76	0.88	1.86	1.25	0.76	1.80	0.57
V/Al2O3	0.95	3.27	1.02	0.61	0.89	0.81	0.54
CaO/Al2O3	1.08	0.12	1.31	1.15	5.90	0.80	2.11
MgO/Al2O3	1.73	0.76	1.47	1.17	1.59	1.06	0.88
Na2O/Al2O3	2.60	1.43	1.60	4.27	2.44	3.45	4.38
K2O/Al2O3	0.91	1.17	1.11	0.36	0.90	0.86	0.77
BaO/Al2O3	1.08	3.52	7.89	1.64	3.33	1.65	0.97
Sr/Al2O3	0.73	0.33	0.99	0.95	0.94	0.55	0.85
Y/Al2O3	0.95	1.47	1.84	2.33	2.20	2.35	2.91
P2O5/Al2O3	0.82	0.60	1.41	0.98	1.22	1.71	1.13
Rb/Al2O3	0.67	0.97	0.90	0.26	0.76	0.65	0.44
Na2O/K2O	2.86	1.22	1.44	11.84	2.71	4.03	5.70

Table 5.3: Element/Al2O3 ratios normalized to average composition of Poultney Formation (fine-grained, Ordovician, clastic, passive margin sediment, N.Y.State); (Poultney analyses obtained by J.W. Delano)

	greywackes	black slates	grey cherts	green argillites	Mn-rich, green argillites	red argillites	upper Wild Bight Group
TiO2/Al2O3	0.95	1.03	1.35	1.14	1.33	1.32	0.90
Fe2O3/Al2O3	1.04	0.52	1.79	1.66	1.62	2.55	1.15
MnO/Al2O3	1.21	0.42	9.47	22.23	305.33	32.71	12.64
SiO2/Al2O3	0.87	2.52	4.09	1.76	1.77	1.82	1.69
Cr2O3/Al2O3	1.43	2.22	1.17	0.77	1.70	1.13	0.57
Ni/Al2O3	1.24	1.82	3.91	1.51	2.75	2.20	0.90
Zr/Al2O3	0.56	0.65	0.73	1.15	0.73	0.83	0.98
Pb/Al2O3	1.06	1.23	2.59	1.74	1.06	2.51	0.80
V/Al2O3	1.10	3.80	1.18	0.70	1.03	0.94	0.63
CaO/Al2O3	1.21	0.13	1.48	1.30	6.65	0.90	2.37
MgO/Al2O3	0.78	0.34	0.66	0.53	0.72	0.48	0.40
Na2O/Al2O3	2.20	1.21	1.35	3.61	2.07	2.92	3.70
K2O/Al2O3	0.56	0.72	0.68	0.22	0.55	0.53	0.47
BaO/Al2O3	1.07	3.50	7.84	1.63	3.31	1.64	0.96
Sr/Al2O3	0.95	0.43	1.29	1.23	1.21	0.71	1.10
Y/Al2O3	0.91	1.40	1.76	2.22	2.09	2.24	2.77
P2O5/Al2O3	0.88	0.64	1.50	1.04	1.29	1.81	1.20
Rb/Al2O3	0.61	0.89	0.82	0.24	0.69	0.59	0.40
Na2O/K2O	3.93	1.68	1.98	16.31	3.73	5.55	7.86

Table 5.4: Element/Al2O3 ratios normalized to average, Pacific, pelagic clay (Chester and Aston, 1976)

	greywackes	black slates	grey cherts	green argillites	Mn-rich, green argillites	red argillites	upper Wild Bight Group
TiO2/Al2O3	0.88	0.95	1.25	1.06	1.23	1.23	0.83
Fe2O3/Al2O3	0.91	0.46	1.57	1.46	1.42	2.24	1.01
MnO/Al2O3	0.14	0.05	1.11	2.60	35.72	3.83	1.48
SiO2/Al2O3	1.33	3.85	6.24	2.68	2.69	2.78	2.58
Cr2O3/Al2O3	1.42	2.20	1.16	0.77	1.69	1.12	0.57
Ni/Al2O3	0.27	0.39	0.84	0.33	0.59	0.47	0.20
Zr/Al2O3	0.93	1.08	1.21	1.91	1.21	1.38	1.63
Cu/Al2O3	0.38	1.01	1.07	0.80	0.94	0.56	0.59
Co/Al2O3	0.59	0.42	1.56	1.09	1.64	2.07	0.36
Pb/Al2O3	0.18	0.21	0.44	0.29	0.18	0.43	0.14
V/Al2O3	1.12	3.86	1.20	0.72	1.05	0.96	0.64
CaO/Al2O3	0.39	0.04	0.47	0.41	2.12	0.29	0.76
MgO/Al2O3	3.87	1.69	3.28	2.61	3.55	2.36	1.97
Na2O/Al2O3	1.93	1.06	1.18	3.16	1.81	2.56	3.24
K2O/Al2O3	0.96	1.26	1.19	0.39	0.97	0.92	0.82
BaO/Al2O3	0.29	0.94	2.11	0.44	0.89	0.44	0.26
Zn/Al2O3	0.70	0.60	0.86	0.68	0.70	0.71	0.68
Sr/Al2O3	7.66	3.49	10.42	9.99	9.83	5.74	8.92
Y/Al2O3	2.69	4.15	5.22	6.59	6.23	6.65	8.24
P2O5/Al2O3	0.89	0.65	1.52	1.06	1.31	1.84	1.22
Rb/Al2O3	0.91	1.34	1.24	0.36	1.04	0.90	0.60
Na2O/K2O	1.97	0.84	0.99	8.18	1.87	2.78	3.94

Table 5.5: Element/Al2O3 ratios normalized to siliceous, red mudstone composition, Apennines (Barrett, 1981)

	greywackes	black slates	grey cherts	green argillites	Mn-rich, green argillites	red argillites	upper Wild Bight Group
TiO2/Al2O3	1.15	1.24	1.63	1.38	1.60	1.60	1.08
Fe2O3/Al2O3	0.50	0.25	0.86	0.80	0.78	1.23	0.55
MnO/Al2O3	0.34	0.12	2.65	6.21	85.31	9.14	3.53
SiO2/Al2O3	0.31	0.91	1.47	0.63	0.64	0.66	0.61
Cr2O3/Al2O3	1.32	2.05	1.08	0.72	1.58	1.05	0.53
Ni/Al2O3	0.35	0.51	1.09	0.42	0.77	0.61	0.25
Zr/Al2O3	1.01	1.18	1.32	2.08	1.32	1.51	1.78
Cu/Al2O3	0.82	2.19	2.33	1.75	2.05	1.23	1.29
Pb/Al2O3	0.43	0.50	1.04	0.70	0.43	1.01	0.32
CaO/Al2O3	3.62	0.39	4.41	3.87	19.86	2.68	7.10
MgO/Al2O3	1.08	0.47	0.91	0.73	0.99	0.66	0.55
Na2O/Al2O3	17.51	9.65	10.76	28.71	16.45	23.24	29.46
K2O/Al2O3	0.70	0.91	0.86	0.28	0.70	0.66	0.59
BaO/Al2O3	1.99	6.47	14.49	3.01	6.11	3.03	1.78
Zn/Al2O3	0.59	0.50	0.72	0.57	0.59	0.59	0.57
Sr/Al2O3	1.89	0.86	2.57	2.46	2.43	1.42	2.20
Na2O/K2O	24.86	10.63	12.49	103.02	23.56	35.06	49.64

Table 5.6: Element/Al203 ratios normalized to average chert composition (Hein and Karl, 1983)

	black slates	grey cherts	green argillites	Mn-rich, green argillites	red argillites	upper Wild Bight Group
TiO2/Al2O3	0.93	1.22	1.03	1.20	1.20	0.81
Fe2O3/Al2O3	0.37	1.28	1.19	1.15	1.82	0.82
MnO/Al2O3	0.04	0.86	2.03	27.86	2.98	1.15
SiO2/Al2O3	0.35	0.57	0.25	0.25	0.25	0.24
Cr2O3/Al2O3	1.98	1.04	0.69	1.52	1.01	0.51
Ni/Al2O3	0.50	1.06	0.41	0.75	0.60	0.25
Zr/Al2O3	0.94	1.06	1.67	1.06	1.21	1.43
Cu/Al2O3	0.46	0.49	0.37	0.43	0.26	0.27
Pb/Al2O3	0.32	0.66	0.44	0.27	0.64	0.20
V/Al2O3	1.67	0.52	0.31	0.45	0.41	0.28
CaO/Al2O3	0.10	1.16	1.02	5.22	0.70	1.86
MgO/Al2O3	0.53	1.03	0.82	1.11	0.74	0.62
Na2O/Al2O3	1.17	1.30	3.48	2.00	2.82	3.57
K2O/Al2O3	1.27	1.20	0.39	0.97	0.92	0.83
BaO/Al2O3	0.13	0.30	0.06	0.13	0.06	0.04
Zn/Al2O3	0.22	0.32	0.25	0.26	0.26	0.25
Sr/Al2O3	0.17	0.50	0.48	0.47	0.27	0.43
Y/Al2O3	0.33	0.42	0.53	0.50	0.53	0.66
P2O5/Al2O3	0.20	0.46	0.32	0.40	0.56	0.37
Na2O/K2O	0.92	1.09	8.96	2.05	3.05	4.32

Table 5.7: Comparison of elemental ratios of the Shoal Arm Formation and several reference compositions to show potential hydrothermal influence

	Fe_2O_3/Al_2O_3	$(MnO/Al_2O_3)*100$	Fe_2O_3/TiO_2	$Al_2O_3/Al_2O_3+Fe_2O_3+MnO$	
black slates	0.21	0.18	4.67	0.83	this study
grey cherts	0.72	4.16	12.29	0.57	this study
green argillites	0.67	9.77	13.50	0.57	this study
Mn-rich, green argillites	0.65	134	11.29	0.33	this study
red argillites	1.03	14.37	17.86	0.46	this study
average, upper Wild Bight Group	0.47	5.55	11.89	0.66	this study
PAAS	0.38	0.58	7.22	0.72	Taylor and McLennan (1985)
red, siliceous mudstone	0.84	1.57	23.22	0.54	Barrett (1981); upper, siliceous, red mudstone in ophiolite sequence, Northern Apennines
average chert	0.57	4.81	11.77	0.62	Hein and Karl (1983); average of cherts from Nicoya Complex, Cyprus, and Sabana Grande unit, Costa Rica
average, pelagic clay	0.46	3.76	9.80	0.67	Chester and Aston (1976)
metalliferous, hemipelagic-pelagi sediment	0.75	19.45	28.00	0.56	Leggett (1982); Leg 66, DSDP, Cocos Plate; 0 - 145.7 meter sub-bottom depth
basal, metalliferous sediment	64	1871	978	0.01	Marchig and Gundlach (1982); basal sediment on the central oceanic ridge of the East-Pacific Rise

composition of the normalized element to the standard, ratios less than one indicate lower abundances, ratios greater than one indicate higher abundances of the normalized element. Averages of the Shoal Arm Formation, Wild Bight Group, and Gull Island Formation were calculated; the Shoal Arm Formation is separated into black slates, grey cherts, green argillites, Mn-rich green argillites, and red argillites.

Upper Wild Bight Group, red and green argillites of Shoal Arm Formation

The local reference composition of the volcaniclastics of the upper Wild Bight Group indicated an increased Fe_2O_3/Al_2O_3, MnO/Al_2O_3, Ni/Al_2O_3, and Co/Al_2O_3, and Pb/Al_2O_3 ratio in the red argillites (Table 5.1). Fe_2O_3 and MnO are also enriched relative to the other reference compositions. Green argillites, and in particular the Mn-rich argillites, are consistently enriched in MnO. Also notable is the P_2O_5/Al_2O_3 ratio of the red argillites which is enriched relative to all reference compositions. Similarly, TiO_2 in the red argillites is enriched relative to the Wild Bight Group composition and to the other standards; the enrichment disappears in the black slates.

The Mn-rich, green argillites show the highest CaO/Al_2O_3 ratios, and are enriched in CaO relative to all standards. The CaO/Al_2O_3 ratios also correlate with the highest MnO/Al_2O_3 ratios. Black slates, in contrast, are consistently depleted in CaO relative to all standards, and have the lowest CaO/Al_2O_3 ratios of the whole stratigraphic sequence.

The normalized SiO_2/Al_2O_3 ratios indicate that the Shoal Arm Formation is similar to the average, upper Wild Bight Group composition, and less siliceous than the siliceous mudstone analyzed by Barrett (1981). PAAS, pelagic clay, and Poultney Formation, on the other hand, are less siliceous than the Shoal Arm Formation.

The Zr/Al_2O_3 ratio may be used as an indicator of sedimentary sorting, since both elements are derived from the detrital fraction. The normalized Zr/Al_2O_3 ratio gives an indication of relative distance to the source area and the degree of sorting. The

red and green Shoal Arm Formation is enriched in Zr relative to the pelagic clay (Table 5.4), indicating that true pelagic conditions were not established. Similarly, the Apennine mudstone and the PAAS show lower Zr abundances resulting in higher, normalized Zr/Al_2O_3 ratios (Table 5.5 and 5.2, respectively). On the other hand, compared to the Ordovician Poultney Formation, the Zr/Al_2O_3 ratio is lower with the exception of some green argillites (see Chapter 5.4). It is concluded that the depositional environment of the Shoal Arm Formation is intermediate between a distal, pelagic setting and a slope and rise environment.

Na_2O/Al_2O_3, K_2O/Al_2O_3, and Na_2O/K_2O ratios show a strong deviation from the reference compositions. Stratigraphically upward, the Na_2O/K_2O ratio decreases mainly as a result of a decrease in the Na_2O/Al_2O_3 ratio. Whereas the compositional differences to the Wild Bight Group standard generally result in ratios of less than one (Table 5.1), the other standards consistently have lower Na_2O/Al_2O_3 and Na_2O/K_2O ratios. The origin of these ratios is discussed in Chapter 5.4.

Element ratios potentially diagnostic of hydrothermal components are Fe/Ti and Al/(Al+Mn+Fe). These ratios were proposed by Boström (1973) to indicate the mixing of hydrothermal component with a detrital component of mafic and/or continental origin. To differentiate the enrichments of the metals Fe and Mn, the Fe/Al and Mn/Al ratios are shown as well (Table 5.7). Red argillites, Mn-rich argillites, and green argillites show an Al/(Al+Mn+Fe) ratio that is modestly lower than the pelagic clay, the red, siliceous mudstone, the Poultney , and the PAAS ratios. On the other hand, the ratio is clearly higher compared to the ridge-crest, metalliferous sediments, and the hemipelagic sediment from the Cocos Plate. The latter is a good example of a sediment that formed in proximity to the two important end-members - the hydrothermal and the detrital component. Clearly, the hydrothermal component is much stronger in it than in the red and green Shoal Arm Formation. In conclusion, there is some modest indication of a hydrothermal component. The results are confirmed by the Fe/Ti ratio as well as the

Fe/Al and Mn/Al ratios. It has to be kept in mind that the ratios Al/(Al+Mn+Fe) and Fe/Ti have been used for sediments deposited at large distance from strong detrital source areas, and they assume a simple two-component mixture of detritus and hydrothermal component without secondary diagenetic enrichment. Figure 5.1 shows the whole data set of the Wild Bight volcaniclastics, Shoal Arm Formation argillites and cherts in order to examine how well the data variation can be represented by a simple two-component mixture model. The two end-members are represented by ridge crest hydrothermal sediment (data from Marchig and Gundlach, 1982) and the black slates of the Shoal Arm Formation. The large symbols indicate the reference compositions of the standards. Most of the Shoal Arm Formation data lie within the mixing trend. The red argillites appear to form the part of the Shoal Arm Formation with the strongest hydrothermal component. The Mn-rich, green argillites fall off that trend, because they do not show a corresponding, high Fe/Ti ratio which suggests that they are not Fe-enriched. Additional components or processes resulting in their present composition have to be considered.

As mentioned above, the hydrogenous component, partially representing the metal enrichment of Mn-nodules (e.g., Piper et al., 1984; Aplin and Cronan, 1985), is the other important contributing factor to the metal content of pelagic sediments. Bonatti et al. (1972b) proposed a ternary diagram for the discrimination of hydrothermal from hydrogenous sediments by plotting (Co+Cu+Ni)*10 versus Mn and Fe. The reasoning behind this element use is that hydrogenous sediments form in areas of very low sedimentation rate, where accumulation rates of adsorbed or seawater precipitated Ni, Co, and Cu become prevalent, since their accumulation is not diluted by high, hydrothermal or detrital accumulation rates. Although some criticism has been expressed with respect to the separation of the hydrothermal and the hydrogenous component, (i.e., the two components may in fact form a continuum (Fleet, 1983)), the diagram was used as a first-order device. The Shoal Arm Formation data are plotted in the ternary

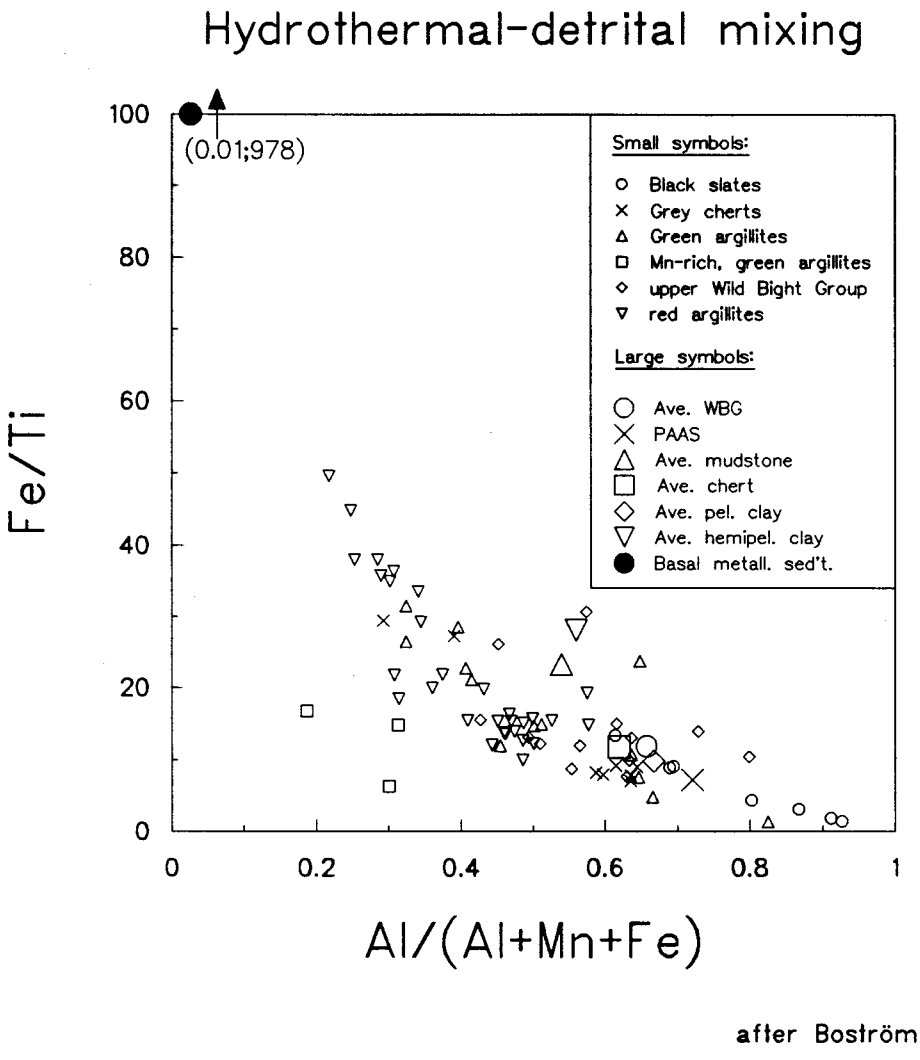

Figure 5.1: Fe/Ti versus Al/(Al+Mn+Fe) diagram introduced by Boström (1973) to indicate the mixing of a hydrothermal and a detrital source. Potential end-member compositions are indicated by a metalliferous, ridge-crest sediment (Marchig and Gundlach, 1982) and the PAAS (Taylor and McLennan, 1985) or the black slates of the Shoal Arm Formation.

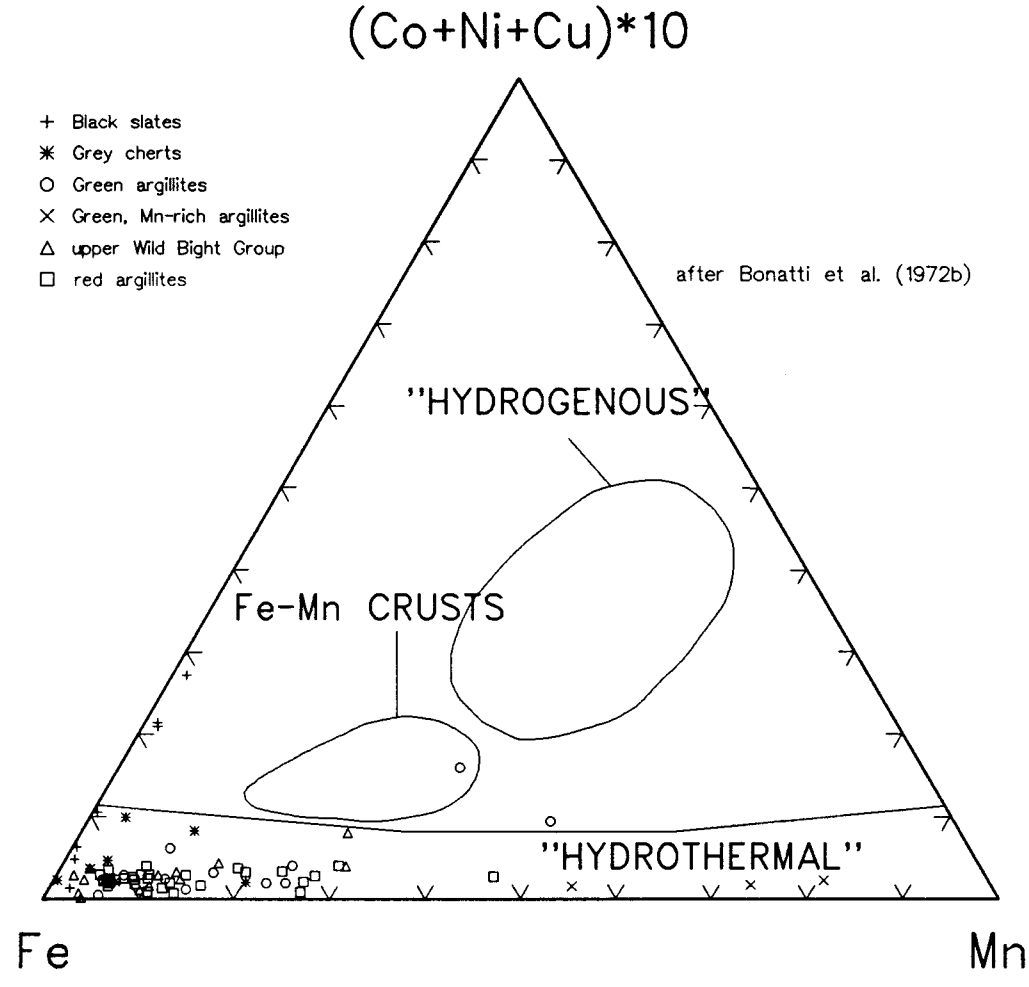

Figure 5.2: Ternary diagram introduced by Bonatti (1972) to discriminate hydrogenous sediments, hydrothermal sediments, and Fe-Mn crusts. The diagram suggests that the hydrogenous component in the Shoal Arm Formation was very minor, since no sample plots in the field of the hydrogenous sediments.

diagram in Figure 5.2. Except for the black slates and two green argillites, the samples lie within the "hydrothermal" field. It is concluded that a strong hydrogenous component was probably not present.

Grey cherts, black slates, and greywackes

Grey cherts of the Shoal Arm Formation are characterized by a higher BaO/Al_2O_3 and SiO_2/Al_2O_3 ratio compared to all standards except for the average chert by Hein and Karl (1983) (Table 5.6). The correlated increases are useful indicators of biogenic Si (e.g., Martin and Knauer, 1973). The high ratios decrease slightly in the black slates, and disappear in the greywackes. Minor enrichments relative to the average chert composition are noted for the elements Ti, Fe, Na, and K. The reason why all other elements listed have ratios less than one, is explained by the higher Al abundance in the Shoal Arm Formation grey cherts compared to the average chert. Another characteristic of the grey cherts is that the MnO/Al_2O_3, Ni/Al_2O_3, and Co/Al_2O_3 ratios remain elevated in the grey cherts when compared to the PAAS composition.

Cr_2O_3/Al_2O_3 and V/Al_2O_3 ratios increase in the black slates and greywackes being higher in the black slates than the greywackes. Conversely, MgO/Al_2O_3 ratios are higher in the greywackes. This indicates that a Mg-, Cr-, and V-rich source, which was likely to have been mafic detritus, became active with deposition of the black slates. The MnO/Al_2O_3 ratio in the black slates is very low, and contrasts to the comparably minor depletion of Fe_2O_3, Co, Pb, Cu, and Zn. Depending on which standard is used, the Ni, Co, and Cu ratios show slight enrichments or depletions. Compared to the underlying grey cherts, Co, Fe, Ni and Pb ratios are lower, whereas Cu and Zn remain relatively constant.

Standards like the pelagic clay, or the red, siliceous mudstone are oxic sediments, and may not be adequate for a compositional comparison with an anoxic sediment like the black slates, since it is well established that sediment diagenesis in oxic and anoxic

clays differ greatly (e.g., Berner, 1984). For this reason, the Al-normalized mean composition of the black Shoal Arm Formation is compared with a Cretaceous black shale, drilled during the DSDP leg 75 in the southern Atlantic (Site 530) (Dean and Parduhn, 1984). Additionally, the elemental ratios in the black slates were normalized to the average, pelagic clay used before (Chester and Aston, 1976) (Figure 5.3). The vertical and horizontal dashed lines in Figure 5.3 indicate ratios of one between black slates and the pelagic clay, and thus equal composition. Since Al is assumed to be relatively constant, both as the detrital component and during diagenesis, ratios deviating from one indicate the enrichment or depletion of the normalized element. The diagonal line denotes equal composition between the Cretaceous black shale composition and the average black slate composition of the Shoal Arm Formation. The small square in the upper right indicates relative enrichments of elements in both anoxic sediments. This field contains the elements Si, Cr, V, Mg, Zr, and K. Enrichment in Cu, Cr, V, Co, Pb, Ni, and Zn is a characteristic feature of black slates (e.g., Dean and Parduhn, 1984; Wedepohl, 1964; Vine and Tourtelot, 1970; Brumsack, 1986). These enrichments are interpreted as the result of bioconcentration, coprecipitation, or sorption and preservation with organic matter (e.g., Dean et al., 1984; Bruland et al., 1980; Vine and Tourtelot, 1970). Whereas Cr and V are enriched in both black shales, only the Cretaceous black shale shows an additional enrichment in Co and Zn. The Cu abundance is similar relative to the standard pelagic clay, whereas Ni and Pb are slightly depleted in the black shales, stronger in the Shoal Arm Formation than in the Cretaceous black shale. It is possible that the pelagic clay represents a slightly trace metal-enriched standard (see also Chapter 5.4.4).

The black slates of the Shoal Arm Formation are more strongly depleted in Mn and Fe than the Cretaceous black shale. These differences may be explained as a consequence of different degrees of diagenetic mobility in the different black shales. The Mn and Fe behaviour during diagenesis of black shales has been demonstrated to

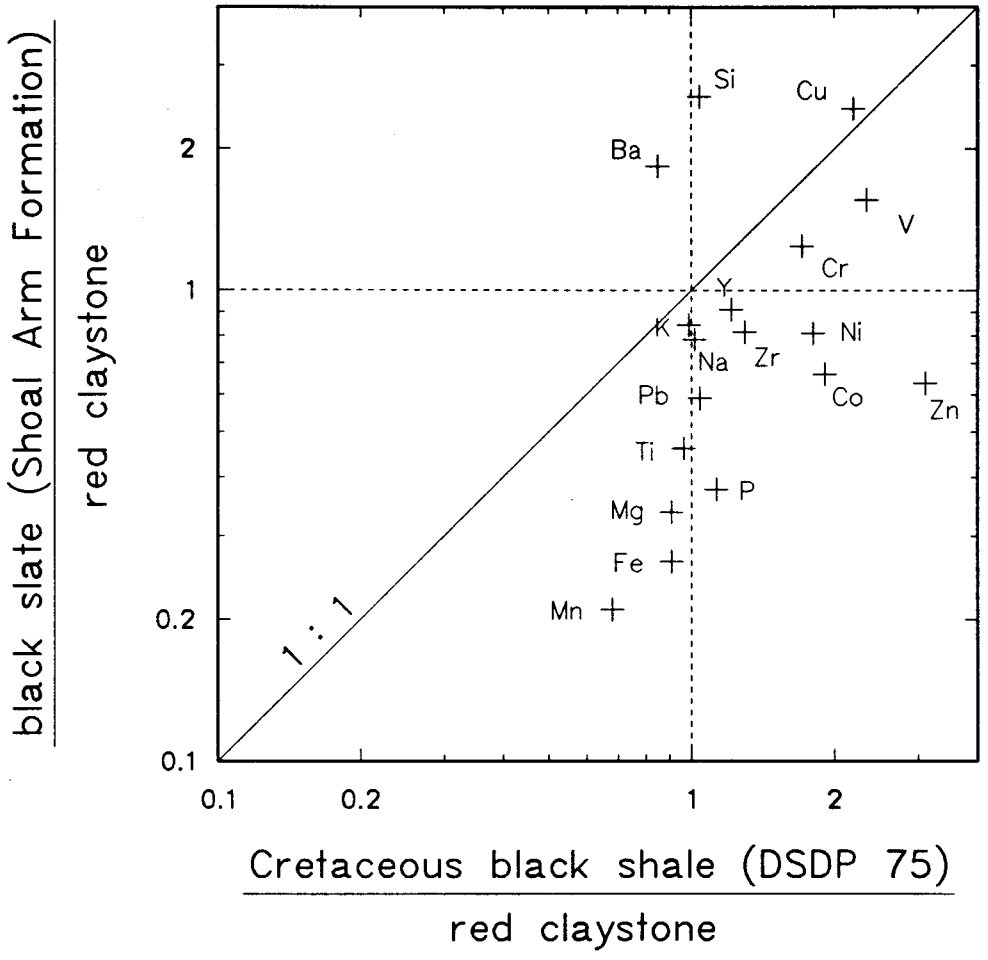

* elements are normalized to Al

Figure 5.3: Comparison of Shoal Arm Formation black slates with middle-Cretaceous black shales from Site 530 (DSDP 75) (Dean and Parduhn, 1984). Elements are normalized to Al and the pelagic clay (Chester and Aston, 1976). The Shoal Arm Formation shows black shale-typical enrichments in Cr and V, but not in Co, Zn, or Ni. Strong depletion in Mn is explained by loss during diagenesis to the overlying sea water.

contrast strongly (e.g., Elderfield, 1981; Suess, 1979). Fe is fixed to 80% by slowly diffusing, large organic complexes, whereas Mn does not show affinities to organic complexing (Elderfield, 1981), and therefore migrates much faster. Also, Mn^{2+} is not precipitated as a sulfide phase, whereas Fe^{2+} combines with S^{2-} to form pyrite. These differences may result in loss of reduced Mn from the sediment, assuming the absence of carbonate, which may facilitate precipitation as Mn-carbonate (Pedersen and Price, 1982). Dean et al. (1984) noted a good correlation of Ca with Mn in the middle Cretaceous black shales at Site 530, and suggested the presence of a Mn-carbonate phase. No Ca-Mn correlation was found in the black slates of the Shoal Arm Formation, and the CaO concentrations in the black slates are very low (< 0.04%). It is therefore concluded that Mn diffused out of the sediment, and was lost to the seawater. Instead, Fe was likely to have been precipitated as a sulfide phase, as evidenced by the pyritiferous appearance of the black slates (see chapter 3). The reason for the lack of a Zn, Co, Ni, and Pb enrichment in the Shoal Arm Formation can unfortunately not be answered with the available data set.

The Shoal Arm Formation is enriched in Si relative to the Cretaceous, black shales and the pelagic clay. The Si enrichment is probably due to the fact that the siliceous fraction makes up the bulk part of the pelagic, biogenic component in the Ordovician sediment, whereas in the Cretaceous black shale, both siliceous material and calcareous material was present in the biogenic component (e.g., Dean et al., 1984). It may also be that the total siliceous biogenic component in the Ordovician, black slates of the Shoal Arm Formation is larger than in the medial-Cretaceous black shales producing higher Si abundances.

Based on this general geochemical comparison, the following characteristics of the Shoal Arm Formation can be noted:

(1) Distal, pelagic conditions were probably not established during the deposition of the red Shoal Arm Formation.

(2) There is a moderate metal enrichment, which can be explained as the result of a hydrothermal component.

(3) Differences in the Na_2O/K_2O ratio to the reference compositions, but not to the Wild Bight Group average indicate the influence of local, detrital source areas that were different from passive, continental margin (e.g. Poultney Formation) sources, or the PAAS, which approximates average upper continental crust.

(4) The grey cherts are characterized by an increase in SiO_2 and BaO, which may be interpreted as biogenic silica. The elevated SiO_2-levels persist into the black shales.

(5) The black shales are enriched in elements like Cr, V, and possibly Cu, which is characteristic for black shales. The strong Mn-depletion is explained as the result of diffusion of mobilized Mn^{2+} back into the seawater.

(6) A more mafic, clastic source appeared to contribute to the greywackes, and possibly already existed during black shale deposition.

5.2. STATISTICAL APPROACH TO THE DATA SET

5.2.1 Introduction

The geochemical composition of a sediment is a mixture of several sediment sources. Each sediment source has a theoretical, pure, geochemical composition (the end-member composition), and can be recognized by the presence of certain elements and/or characteristic element proportions. The characteristic element correlations or groupings recognized by a compositional analysis can therefore be diagnostic of a specific component. Whether a sediment source can be successfully identified in a compositional analysis, may depend either on the quantity of this component present in the sediment, i.e., its amount may exert a complete compositional control on the sediment, or may depend on the unique, original composition of this particular sediment source. Since in most cases several sediment sources are present, the elements contained in a sediment have multiple sources as well. Any measured element abundance is therefore the sum of the element abundances in the sources. As a result of this mixture, it is necessary to partition the measured element abundance according to the relative proportions the different components appear to have contributed to the sediment. In the following chapters, an attempt is made to both identify the sediment sources of the Shoal Arm Formation (this chapter), and to semi-quantify the relative dominance of these components in stratigraphic order (Chapter 5.4).

For this compositional analysis, I use binary element relationships and a multivariate approach where the variation in each data set is analyzed simultaneously (R-mode factor analysis). It is shown that the binary approach, although seemingly simplistic, produces results similar to the multivariate approach. The petrographic variation of the whole stratigraphic sequence and the first-order, geochemical characteristics both suggest important compositional differences between the stratigraphic

units. Based on this observation, it seemed reasonable to separate the data set into different groups. This approach has the advantage that (a) compositional "noise" of evidently different lithologies is avoided, (b) the origin of a strong signal, not present in all lithologies, but still so strong that it would affect the variation of the whole data set, can be traced to the lithology solely responsible for the signal. Greywackes and black slates had to be treated as one group, because the number of samples of each lithology was too low for a statistical analysis. The whole data set was split into the following seven groups:

1. Greywackes and black slates
2. Grey mottled cherts
3. Zr-rich argillites of the upper Shoal Arm Formation
4. Green argillites
5. Bright red argillites
6. Fe-enriched argillites
7. Volcaniclastics of the upper Wild Bight Group

in stratigraphic order

5.2.2 Analysis of correlation coefficients

Pearson correlation coefficients were calculated for all pairs of variables in each of the lithologic groups. Since the separate data sets are small, statistical tests were run to establish the significance limit of a correlation coefficient. The limit was determined by calculating the high and low confidence limits for a correlation coefficient. The confidence limits depend on the number of samples in a data set. For positive correlation coefficients, the lower confidence limit had to be > 0.5. Correlation coefficients with confidence limits lower than this value were discarded. This procedure

was necessary, because small data sets like the Mn-rich argillites or the black slates yielded unusually frequent, high (> 0.9) or low (< -0.9) correlation coefficients. The scatter of two such elements in a binary diagram, however, was not lower than the scatter of two elements with a lower correlation coefficient from a larger data set. The lowest positive or highest negative, acceptable correlation coefficients for each data set are different, whereby small data sets have higher (respectively lower for negative correlation coefficients) acceptable correlation coefficients than larger data sets. Using the aforementioned confidence limits, the significant correlations could be successfully identified. Additionally, the binary relationships were checked by visual inspection of binary graphs. The elements in every data set were systematically plotted against Al_2O_3 and Fe_2O_3.

Elements that had high, positive correlation coefficients were combined into groups. Figures 5.4 - 5.6 illustrate the results of this analysis for each data set. Well-correlated elements are connected with tie-lines. The different groups are spatially organized in the figures in such a way that element groups with correlations just below the statistical cut-off are still located close to each other, in order to indicate their potential connection. Negative correlation coefficients were useful to confirm the different variances of groups of elements, which is expressed by spatial separation. Based on characteristic element associations, geologically plausible element groups were thus identified. The figures are organized in stratigraphic order, starting from the upper Wild Bight Group at the bottom of Figure 5.4, and ending with the greywackes of the Gull Island Formation at the top of Figure 5.6. Dotted lines are drawn around groups that appeared to be suggestive of a characteristic component.

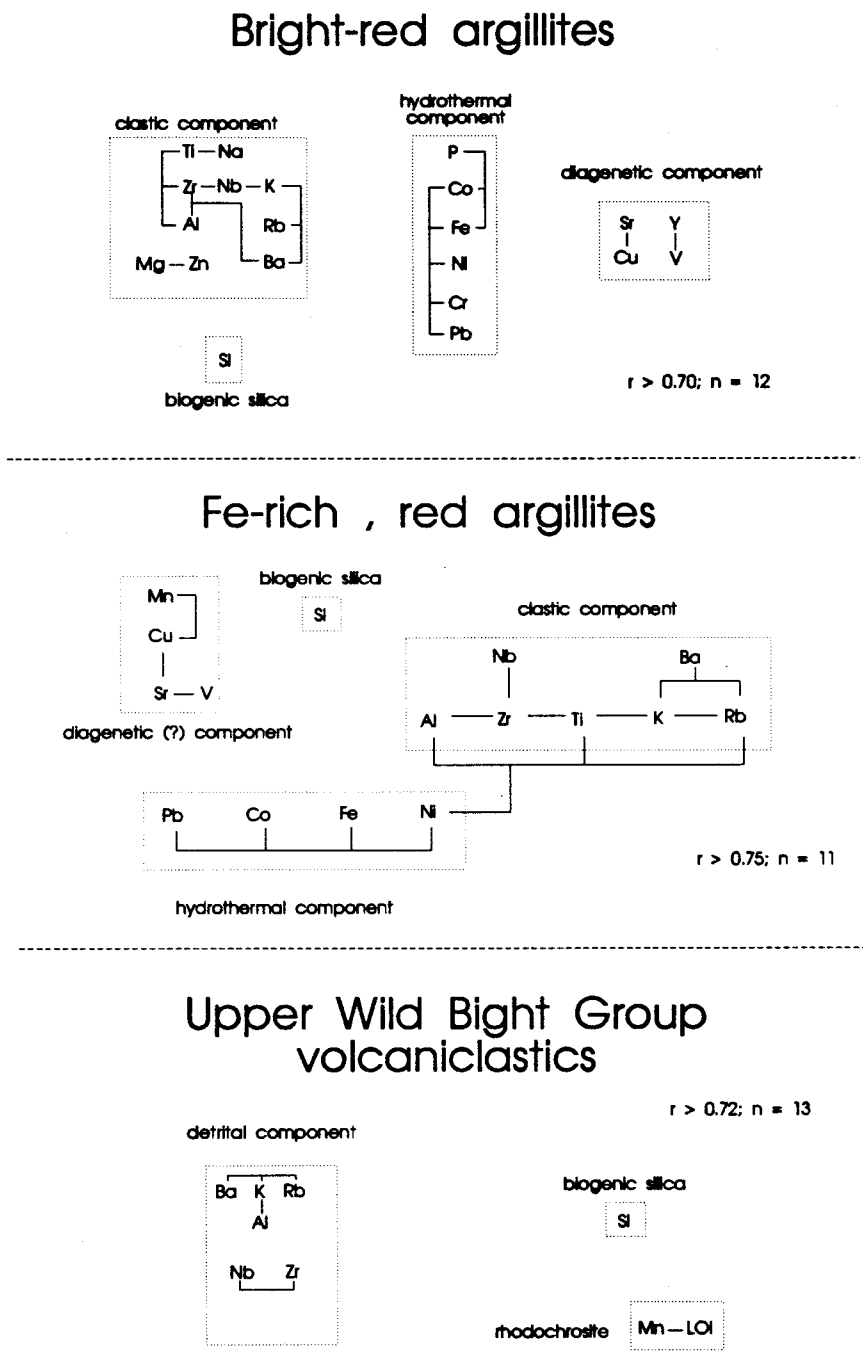

Figure 5.4: Illustration of the different sediment components in Wild Bight Group volcaniclastics, Fe-rich argillites, and bright-red argillites based on the analysis of element correlation coefficients. (r: correlation coefficient; n: number of samples used).

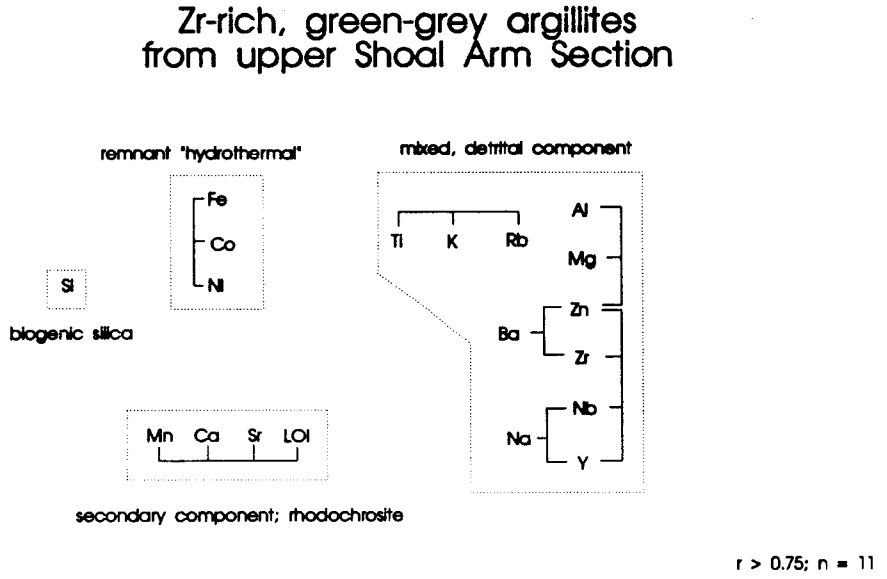

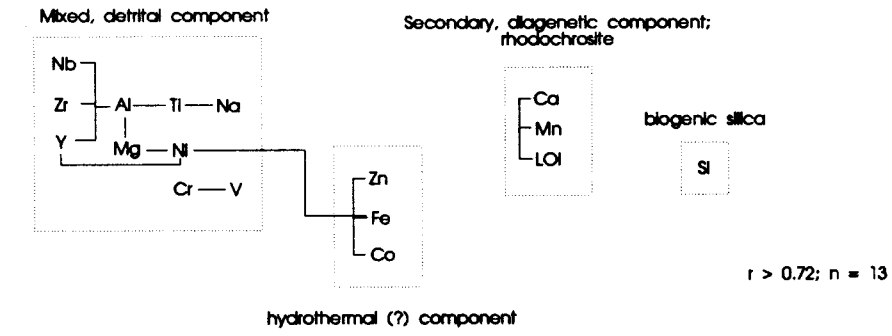

Figure 5.5: Illustration of different sediment components in green argillites and Zr-rich argillites based on the analysis of element correlation coefficients. (r: correlation coefficient; n: number of samples used)

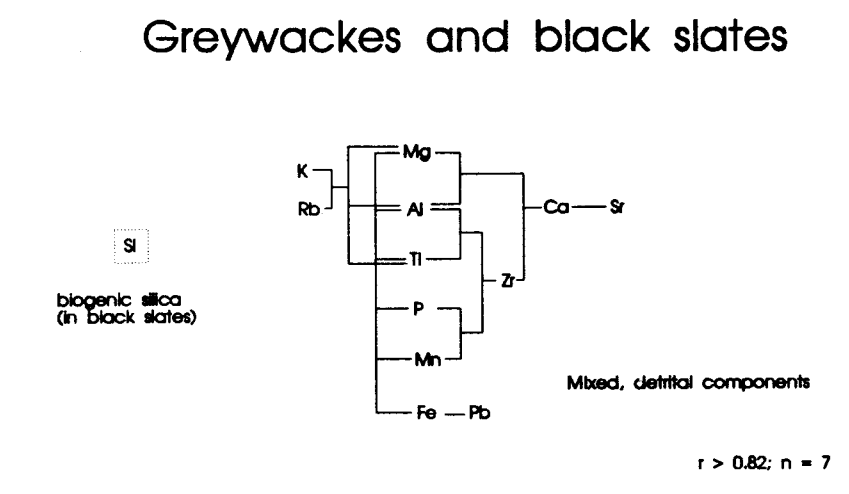

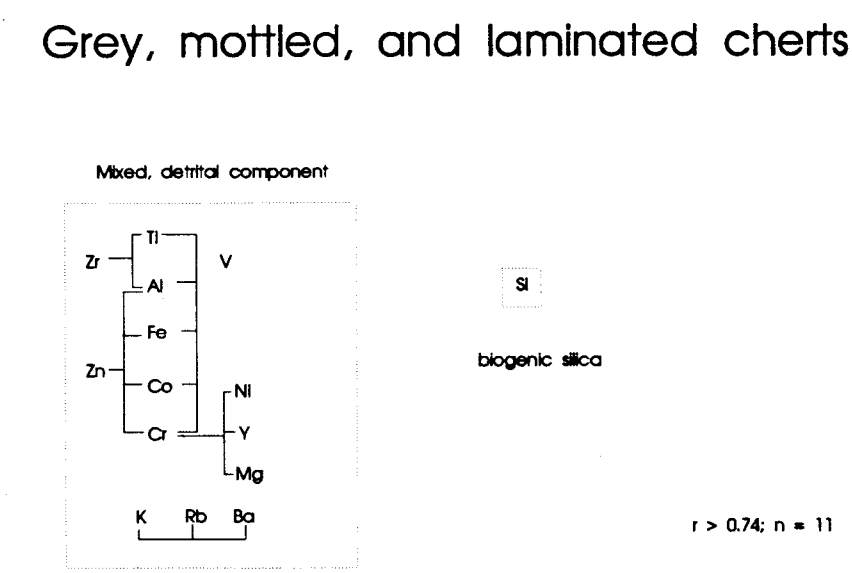

Figure 5.6: Illustration of the different sediment components in greywackes and black slates based on the analysis of element correlation coefficients. (r: correlation coefficient; n: number of samples used)

Results

A Si component, consistently unrelated to other elements, is present in all data sets except the greywackes. The black slates also show a negative Si correlation. Since Si shows no correlation with immobile elements associated with a clastic component, it is best described as biogenic Si derived from radiolarians.

Element associations with Al, Ti, or Zr are interpreted as clastic detritus. For the Shoal Arm Formation and the upper Wild Bight Group, this component includes the elements Al, Ti, Zr, Nb, Y, K, Rb, Na, Mg, and Zn. Zr, Nb, and Y as well as K, Rb, and Ba showed very strong correlations within this group. K, Rb, and Ba may replace each other in crystallographic positions because of their similar ionic radii (Deer et al., 1985), and may therefore be interpreted as the result of primary variation of the detrital source component containing feldspar or illite. Although the Zr, Nb, and Y correlation is not diagnostic, the correlation with Na may suggest an alkaline source. The association with immobile elements (e.g. Ti, Al and Zr) indicates that, in the Shoal Arm Formation, Na is still preserved in the original detrital fraction, and was, at least on the whole-rock scale, diagenetically not strongly mobile. No consistent negative correlation coefficients were found between ferromagnesian, compatible elements (e.g. Mg, Cr, Ni, and V) and more incompatible elements (e.g. Zr, K, and Rb). Since both groups show affinities to Al, they were compiled in the detrital component. Also, in the case of the red argillites and the upper Wild Bight Group volcaniclastics, the "compatible" elements do not always show good correlation coefficients among each other. A weak signal is only apparent from the set of the green argillites. On the other hand, in the upper parts of the stratigraphic sequence, within the black slates and greywackes, the detrital ferromagnesian contribution becomes more obvious. This suggests that a mafic, detrital source played only a minor role during the deposition of the Shoal Arm Formation. For the reasons discussed above, the box enclosing the immobile, clastic elements, is labelled as a "mixed, detrital component", since the elements may be derived from several,

compositionally different, detrital sources that had subsequently been blended into a single, undifferentiable component.

The Fe-rich, the bright-red, the green, and the Zr-rich argillites show associations of Fe, Co, and Ni, (± Pb and Zn). These elements can be discriminated from the other groups by low or negative correlation coefficients. The association can be interpreted to indicate a hydrothermal source, since these elements were found to be contained in hydrothermal fluids (e.g., Bischoff and Rosenbauer, 1983), emanating into the seawater at hydrothermal vents. The element group is particularly distinct in hematite-bearing argillites. Hydrothermally derived Fe in seawater is largely present in particulate form as Fe-oxyhydroxides (Hudson et al., 1986). Fe-oxyhydroxide particles have a large capability of adsorbing trace elements (e.g. Co, Ni, or Pb) onto their surfaces (Förstner 1982a). It is therefore suggested that the element association in this group reflects the primary adsorption of the trace metals Co, Ni, and Pb onto hydrothermally derived Fe-oxyhydroxides that were suspended in sea water. During diagenesis and metamorphism, the oxyhydroxides were dehydrated to form finely disseminated hematite. The hydrothermal component is not detectable in the upper Wild Bight Group, and may be blended into the mixed, detrital component in the grey cherts. Discrimination of this component in the green argillites is problematic, because the element Ni is apparently partitioned between a clastic and a hydrothermal component, thus lowering the correlation coefficient. This prevents an unambiguous identification of a hydrothermal component here.

Although present with Fe in the hydrothermal component (e.g. Leinen, 1987), Mn is not associated with Fe or any of the associated trace elements in either red or green argillites. Instead, a correlation with Ca, Sr, and LOI (loss of ignition) was found. Since the samples are fused before major element analysis, CO_2 is lost. Carbonate presence can therefore only be indirectly inferred from correlation of CaO with the percentage of LOI, which may include H_2O, or OH^-. The correlation of Ca with Mn,

Sr and LOI indicates the presence of Mn-carbonate. In Figure 5.4 and 5.5, this component is called "secondary". This attribute is given for the reason that in modern marine sediments, the occurrence of Mn-carbonate is generally related to diagenetic processes below the sediment-water interface (Thomson et al., 1986; Pedersen and Price, 1982; Minoura et al., 1991). A more detailed account of their occurrence is given in Chapter 5.5. The Mn-carbonate component is present throughout the red Shoal Arm Formation, and disappears with deposition of the grey cherts. The hematite-bearing argillites show no correlation between Mn and LOI. Instead, Fe-rich argillites show an association of Mn with Cu, which in turn is related to Sr and V (Figure 5.4; middle figure). Cu and LOI are uncorrelated (r = -0.01). The Mn, Cu, Sr, V group is uncharacteristic of commonly known sediment components, but the negative correlation coefficients to the members of the other sedimentary components distinguish this group. Since no correlation exists with a detrital element or an element from the hydrothermal group, diagenetic redistribution producing this new association appears to be the most likely process. Therefore, this group is also interpreted as a diagenetic component.

The following, most important changes can be noted in stratigraphic order:

(1) From the Wild Bight Group volcaniclastics to the Fe-enriched argillites, a hydrothermal component appears that is characterized by the elements Fe, Co, Ni, and Pb.

(2) The detrital source becomes more mafic in the black slates and greywackes, but is relatively constant in its composition throughout the upper Wild Bight Group and the red Shoal Arm Formation.

(3) Biogenic silica is always present in the Shoal Arm Formation, and disappears with greywacke deposition.

(4) A diagenetic Mn-carbonate component can be identified in hematite-free argillites of the red Shoal Arm Formation. With deposition of the grey cherts,

this component disappears. Hematite-bearing argillites show no Mn-carbonate component.

5.2.3 R-mode Factor Analysis

The most important shortfall of the previous analysis is that several, detrital components cannot be discriminated, although, based the variable geochemistry of the Wild Bight Group volcanics (Swinden et al., 1990) or the Robert's Arm Group volcanics (Bostock, 1988) which can be interpreted as the island arc volcanics, the presence of various clastic sources appears reasonable. In order to confirm and improve the present results, the data were subjected to a multi-variate statistical analysis (i.e., a R-mode factor analysis). The goal of a factor analysis is similar to the previous approach in that it tries to seek out the dominant sediment components. In contrast to the binary method previously applied, the data are now analyzed simultaneously for possible components that cause the variance of the data set. These components are described as orthogonal vectors in multidimensional space, and represent the "factors". The initial, principal vectors were rotated using a Varimax rotation. The Varimax rotation is one of the possible procedures that is used to improve the data representation by one factor. At the same time, the Varimax rotation may eliminate initial negative factor scores and factor loadings. Since negative values are unreasonable in compositional interpretations, this procedure appears justified. However, since the Varimax rotation rotates the principal component axes only to a direction where the maximum variability of the data set is achieved, the resulting rotated vectors may sometimes still have negative values. Unfortunately, the soft ware program (NCSS; Hintze, 1987) used here is not capable of other rotational procedures than the Varimax rotation. Accepting this shortfall, the analysis still has the advantage that an element which strongly contrasts to a particular

factor has a large negative loading therein. In the case of consistent negative loadings in all factors, the element(s) can therefore similarly be identified as a different component.

Results

Since the algorithm used requires more observations (i.e. samples) than variables for an analysis, larger data sets than previously used were necessary. The new groups consist of (a) bright-red argillites and Fe-rich argillites, and (b) green argillites, Zr-rich argillites, and green argillites of the uppermost Wild Bight Group. There is an insufficient number of analyses of greywackes and black slates present to run a successful analysis.

According to the factor analysis results, 69.4% of the data variance in the Fe-rich and bright-red argillites can be explained by 4 factors (Figure 5.7). This leaves approximately 30 percent compositional variation not accounted for. Factor 1, which accounts for 32.5 percent of the variance in the whole data set, contains the detrital elements Ti, Al, Na, K, Cr, Ba, Zr, and Rb. Therefore, the factor is interpreted as clay detritus. Factor 2, which explains 15.8 % of the data variance, contains the elements Fe, Mg, Ni, Pb, and Co. The factor may be a hydrothermal component, but the covariance of Mg in the same factor complicates this interpretation (Figure 5.7). Mg is not known to covary with metals in hydrothermal sediments (e.g. Leinen, 1987; Marchig and Erzinger, 1986). Normative partitioning of Mg by Q-mode factor analysis suggested that Mg has no preferred compositional end-member, and is equally partitioned (Leinen, 1987). The reason for the association of Mg with this factor is not understood. A Mg-rich clay has to be excluded, because Al has only small loadings in this factor. Factor 1 and 2 show a strong negative loading of Si, which indicates that the compositional variation of Si can be explained by neither of these two vectors, and has therefore to be interpreted as a separate component. Since no factor shows any element covarying with

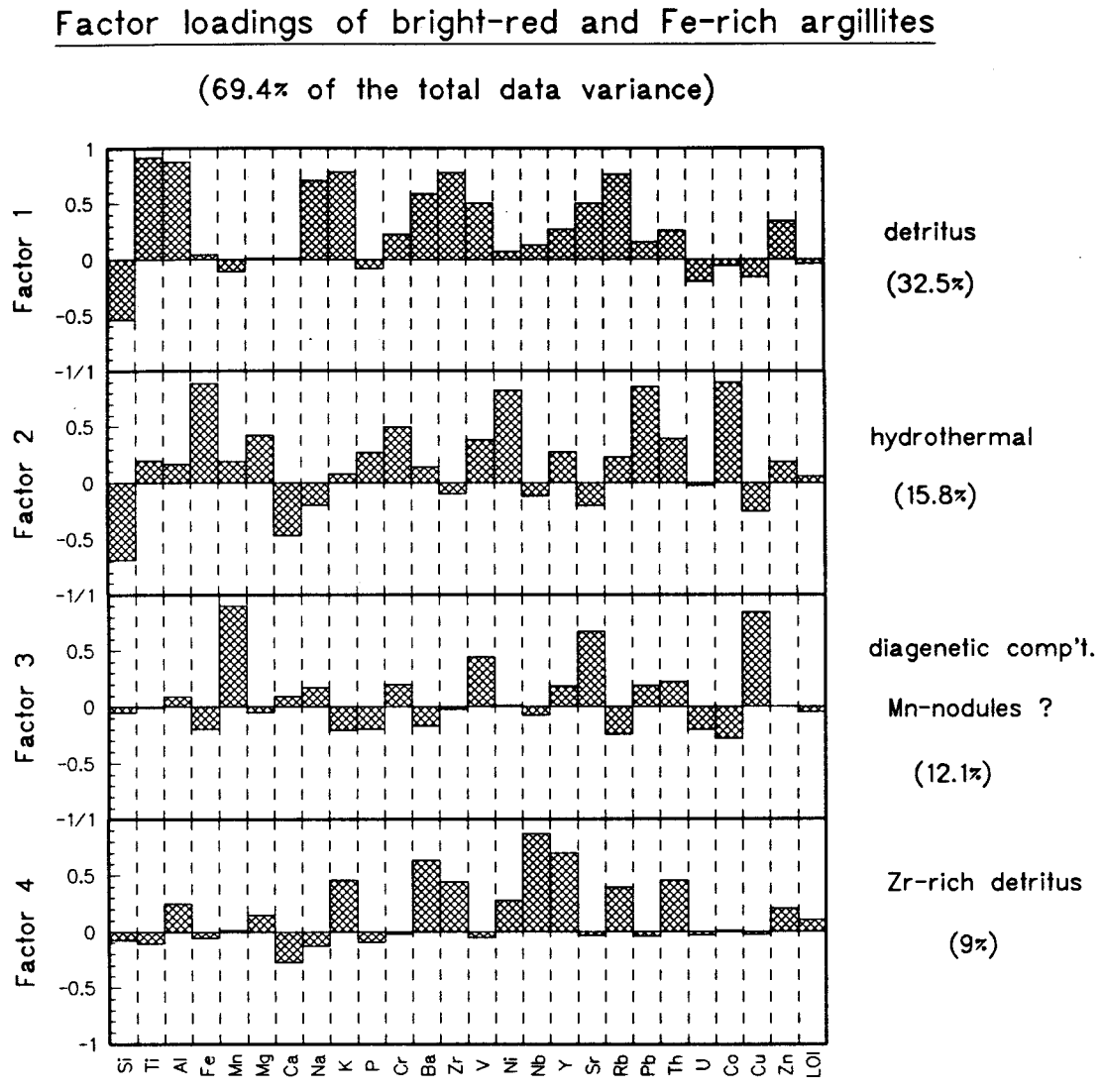

Figure 5.7: Factor loadings of a R-mode factor analysis from a sample set consisting of bright-red argillites and Fe-rich argillites. The percentages indicate the proportion each factor contributes to the total variance of the data set.

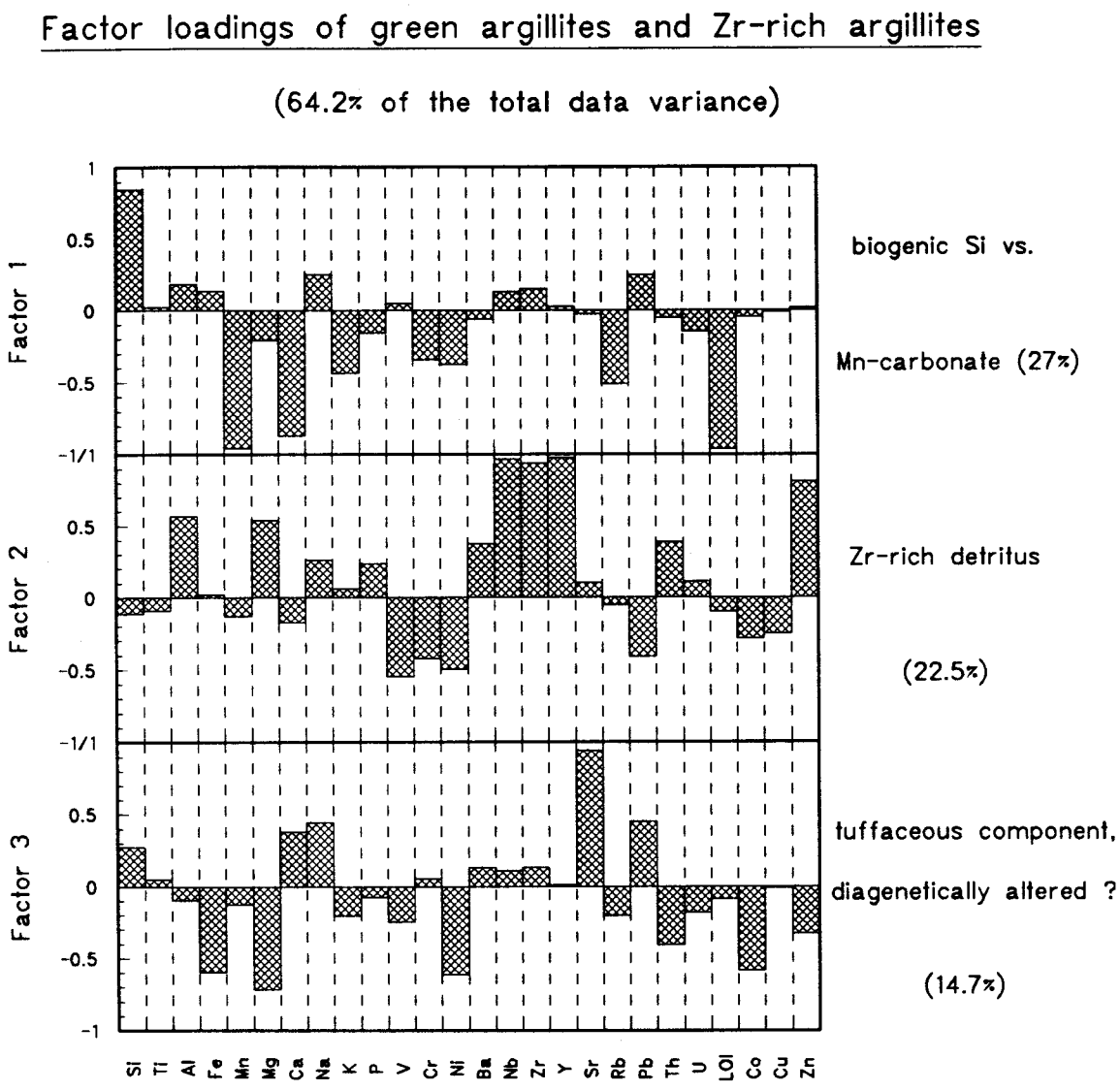

Figure 5.8: Factor loadings of a R-mode factor analysis from a sample set consisting of green argillites of the Shoal Arm Formation and uppermost Wild Bight Group and Zr-rich argillites. The percentages indicate the proportion each factor contributes to the total variance of the data set.

silica, a biogenic, siliceous component is suggested. Factor 3 depicts the covariance of Mn with Cu that was observed in the Fe-rich argillites (Figure 5.4). The factor scores calculated for factor 3 indicate that both Fe-rich and bright-red argillites share this factor. Factor 4 which accounts for 9% of the variance of this data set, shows larger loadings of K, Nb, Y, Zr, and Th. Possibly, this indicates the second, sedimentary component that is characterized by high Zr abundances.

3 factors explain 64.2% of the data variation in the group of green argillites (Figure 5.8). Si shows a strong loading in factor 1, which is not accompanied by other elements, suggesting Si is of biogenic origin. Mn, Ca, and LOI together have strong negative loadings in this factor (Figure 5.8). Factor scores calculated on factor 1 indicated negative scores (i.e., positive scores for negative loadings) in only the Mn-rich samples. The high abundance of Mn-carbonate in these samples is the main dilutent of Si, and counteracting the Si abundance. This may explain the strong, negative loading of only the Mn-carbonate component. Factor 2 depicts the Zr-rich detritus, which is associated with Nb, Y, Mg, and Zn (Figure 5.8). The set of Zr-rich argillites that were added to the green argillites may explain why this factor is stronger in this data set than in the red argillites. Since the covariance of Mg with Zr seems to exclude a silicic source, a mafic, alkalic source is suggested. The negative loadings in this factor (i.e. V, Cr, Ni, Pb, ± Co and Cu) are not diagnostic of a single sediment component, but it is possible that a hydrothermal component as well as mafic (non-alkaline) detritus show a negative variance relative to the Zr-rich detritus. Factor 3, accounting for 14.7% of the data variation, shows an element association that does not seem to be interpretable at first, since the elements Na, Ca, Sr, and Pb are not diagnostic of a particular sediment source (Figure 5.8). 5 samples (SA-11 top, SA-11 bottom, GI-14, SA-17, SA-14) showed high scores for this factor. SA-11 and SA-14 show elevated abundances of Na, Pb, Ca and Sr abundances. Samples SA-17 and GI-14 only have higher Na and Sr

abundances. An unusual combination of a detrital (tuffaceous ?) source and diagenetic redistribution may be responsible for the discrimination as a separate factor.

In conclusion, the R-mode factor analysis confirms the sedimentary components that were already identified from the analysis of correlation coefficients. Two, detrital sources are identified in both groups, one can be interpreted as clay detritus, the other derived from a Zr-rich source. The hydrothermal component is more distinct in hematite-bearing argillites, and a Mn-carbonate component could be recognized in green argillites.

5.3 EXAMINATION OF ELEMENT MOBILITIES IN THE WILD BIGHT GROUP

In a recent study, Swinden et al. (1990) presented a large data set on the geochemical composition of the Wild Bight Group volcanics. The data provide the opportunity to address following questions of interest with regard to the genesis of the Shoal Arm Formation:

(1) The geochemical composition of Wild Bight Group volcanics allows conclusions on the nature of specific detrital source areas identified in the Shoal Arm Formation.

(2) The degree of chemical alteration in the volcanics can give an indication of element diffusion out of the Wild Bight Group, and possibly into the Shoal Arm Formation.

The problematic of element mobility during low-grade metamorphism in volcaniclastics has been investigated by Viereck et al. (1982). Chemical alteration in volcanic rocks has been investigated by several authors (e.g., Alt and Emmermann, 1985; Coish, 1977). The general conclusion from this work can be summarized as follows:

(1) Volcaniclastics are more prone to alterations during low-grade metamorphic conditions than volcanic rocks because of their higher glass content, higher initial porosity and permeability.

(2) Up to low-grade metamorphism the large LIL ions Ba, K, Rb, and Sr are highly mobile in volcanic rocks. Al, Ti, Si, and Mg are only mobilized on a small scale. Zr, Sc, Y, Nb are essentially immobile, Na appears to become slightly enriched. Fe, Al, and Ti have not been observed to be subject to large compositional changes (Brey and Schmincke, 1980).

The fact that enhanced element mobility has been established for volcaniclastics, and the fact that large parts of the Wild Bight Group are epiclastic, opens the question of the potential of large-scale diffusion from the Wild Bight Group up to the Shoal Arm

Formation. Several lines of evidence indicate that the likelihood of such a scenario is low.

(1) Red slate samples were taken from a stratigraphic position in the lower to middle to middle part of the Wild Bight Group at Side Harbour. These slates strongly resemble the argillites of the Shoal Arm Formation, but the composition of these argillites showed no comparable Fe-enrichment.

(2) If uptake of Fe^{2+} from volcanics by diffusing pore fluids should have taken place, the Mg# (i.e., the ratio MgO/(MgO+FeO)) in the Wild Bight Group volcanics would be expected to have changed. Swinden et al. (1990) report linear relationships between the Mg# and the generally immobile elements Zr, Nb, P, Ti in petrogenetically related groups. This linear relationship would be expected to break down in the case of intense alteration and depletion of Mg or Fe. The data provided by Swinden et al. (1990) were used to test their statement of relative immobility. On a general basis, their assertion can be followed, although, when plotted against Zr, the Mg# showed a relatively wider scatter in all groups. The fact that some correlations are preserved supports the argument that Mg and Fe were not very mobile. It needs to be kept in mind that Swinden et al. (1990) did not analyze the volcaniclastics, which make up the majority of the 8 kilometer stratigraphic thickness of the Wild Bight Group (Nelson, 1979). Therefore, the possibility of some element depletion of the clastic sequence cannot completely be excluded. The detailed investigation of Viereck et al. (1982) on the geochemical alteration of coarse-grained volcaniclastics, however, indicated that the elements Al, Fe, and Ti showed only small changes.

Among the different lithologic groups that were identified by Swinden et al., (1990), the N1 group is of particular interest because of its Zr abundances and its high Na/K ratio which clearly is distinct from the other volcanics. Swinden et al. (1990) identified this source as alkaline basalts. Possibly, this rock type explains the Zr-rich clastic discriminated in Chapter 5.2.

5.4 Chemical stratigraphy

5.4.1 Introduction

The purpose of this chapter is to describe the stratigraphic relationships among the different sedimentary components that were identified in Chapter 5.2. It is very likely that the different sedimentary components varied in their relative importance with time. Stratigraphic variations among sediment components are the result of (a) change in provenance; (b) changes in the depositional process, i.e., changing accumulation rates, and/or a varying degree of sorting; and (c) diagenetic alteration. In some cases, the diagenetic alteration may be related to a sudden change in the depositional pattern. For example, it has been observed that the deposition of turbidites into an otherwise pelagic-clay dominated environment (Colley et al., 1984) produces secondary diagenetic changes. Therefore, a complex interrelationship exists among the depositional process, the chemical alteration during diagenesis, and the dominance of a particular sediment component. With these aspects in mind, I attempt to relate the geochemical variation observed to the varying physical sedimentary processes as well.

Figure 5.9 shows the frequency distribution of the samples in 20-meter intervals in the complete stratigraphic column. Except for the interval between 100 and 140 meters, the density of sampling ranges between 1 and 4 samples per 20 meters. This implies gaps as wide as 10 meters exist between some sample pairs, which leaves considerable space for undetected, primary and secondary, geochemical variation in unsampled intervals. Samples being enriched or depleted in diagenetically mobile elements may have had sinks or sources in these intervals. Also, the intervals that were not sampled may contain additional geochemical marker-horizons, which would further constrain the stratigraphic order and the correlation among the three sections, (i.e., the Beaver Bight, Shoal Arm and Gull Island Section). The frequency distribution indicates

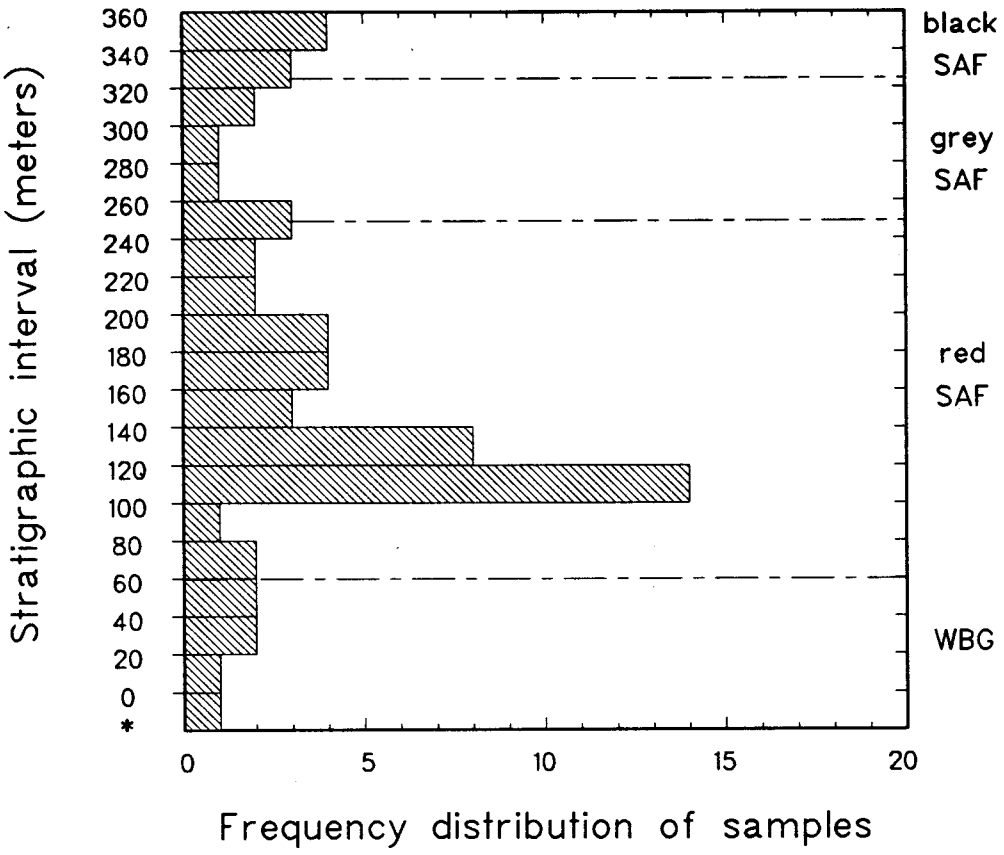

* below measured section

Figure 5.9: Frequency distribution of the Shoal Arm Formation samples in 20 meter intervals in the complete, stratigraphic column ranging from the upper Wild Bight Group to the black slates.

that the interval between 100 and 140 meters can be regarded as well-constrained by the number of samples, whereas interpretations of the other intervals are less-constrained.

5.4.2 Stratigraphic correlation based on chemical fingerprinting

The identification of geochemical markers in more than one section has important implications regarding the exactness of the stratigraphic correlation based on field observations, and on the geological interpretation of geochemical variations on a more regional scale. Important geochemical variations in one section do not necessarily imply that the cause of this variation was active on a regional scale. Although the original lateral distance between the three stratigraphic sections was probably not more than 2 kilometers, which is minor compared to the paleo-basin extent, correlatable geochemical changes in the three sections may still have some regional importance. In order to establish, whether distinct, correlatable geochemical markers exist in each section, the samples were divided into the three stratigraphic sections. The three sections were then aligned using the maroon/red color transition and the buckled rhodochrosite band as marker horizons. To equalize the thickness of the sections, the same principles as described in chapter 3 were applied (see chapter 3). The 0 meter marker was assigned to the maroon-red color transition, because it appears in each section.

The maroon parts below the maroon-red color transition show a distinct Fe enrichment with an Fe_2O_3/Al_2O_3 ratio that is five times the corresponding ratio in pelagic clays (Figure 5.10). This observation is important because it indicates that the color transition is not a local feature of only several meters lateral extent, but marks a significant, geochemical change on a lateral scale of at least 2 kilometers.

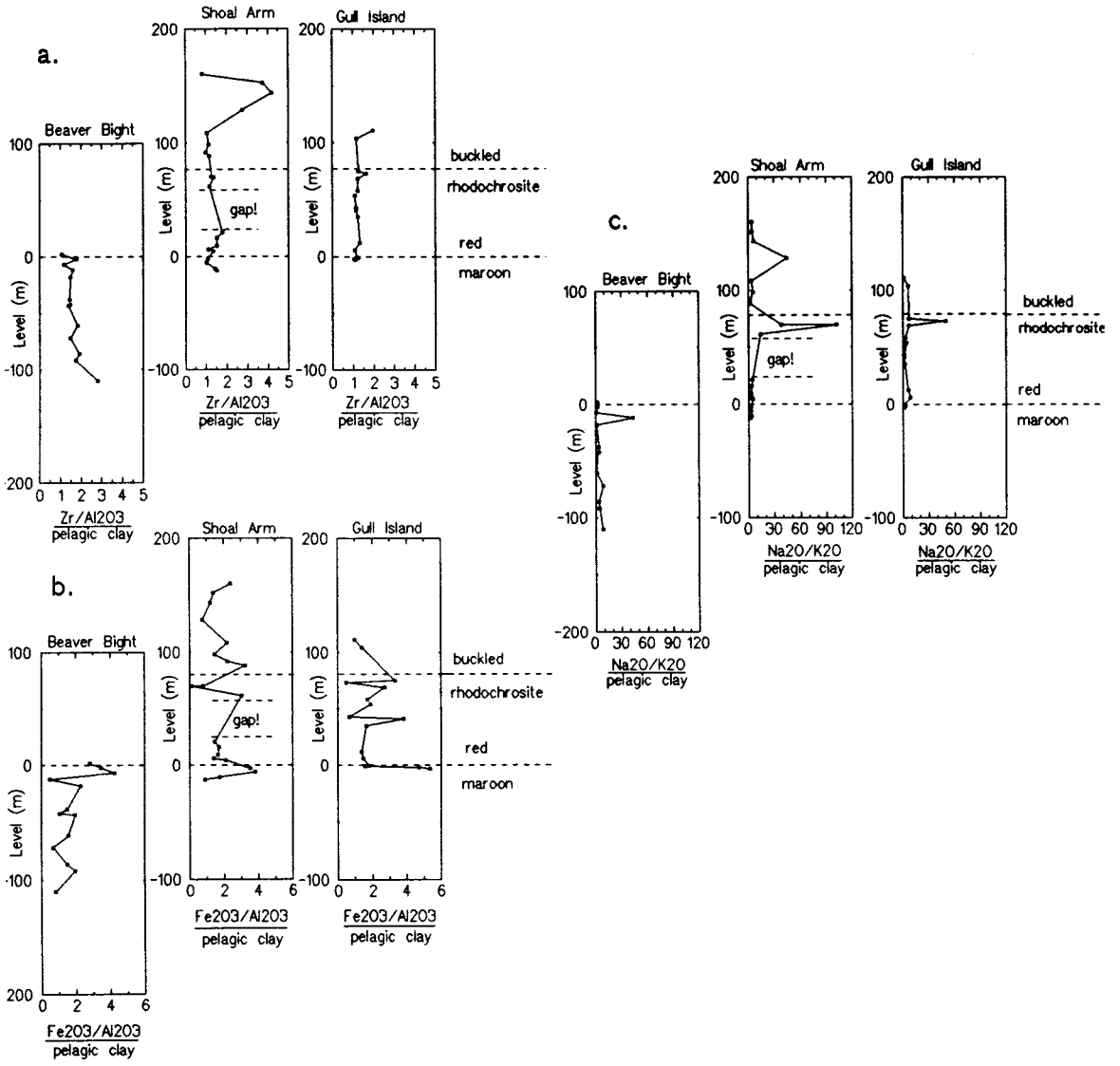

Figure 5.10: Geochemical correlation of Beaver Bight, Shoal Arm, and Gull Island Section. The correlation made in the field is confirmed by the following three geochemical characteristics: a. Correlation of the Gull Island and Shoal Arm Section based on the increase in the Zr/Al_2O_3 ratio; b. common peak in the Fe_2O_3/Al_2O_3 ratio in all three section at the maroon-red color transition; c. adjacent peaks in beds with anomalously high Na_2O/K_2O ratio in the Gull Island and Shoal Arm Section.

Elements that are immobile during diagenetic and low-grade metamorphic processes are the most appropriate to display any primary variation in the sediment. Zr and Al were used for this purpose. It is evident from Figure 5.10.a that the Zr/Al_2O_3 ratio increases in the top part of the Shoal Arm Section, and is very different from the rest of the stratigraphic section where the ratio remains fairly constant. The increase in Zr/Al_2O_3 in the uppermost sample in the Gull Island Section exactly fits the trend in the lower end of this interval in the Shoal Arm Section. This observation supports the recalculation procedure that placed the samples in the uppermost Shoal Arm Section above the samples in the uppermost Gull Island Section.

Five samples within the whole, stratigraphic column showed extremely high Na_2O/K_2O ratios. Three of these five analyses were derived from two beds that were located below the buckled rhodochrosite band. Alignment of the Shoal Arm and the Gull Island Section and stretching of the Shoal Arm Section, as required by the different thickness of the intervals between the marker horizons, caused these three samples to be placed very close to each other. This suggests that they represent (a) either the same bed, or (b) represent a stratigraphic interval that contains more than one of these geochemically peculiar beds. In both cases, their proximity or identity supports the method that was used to increase the thickness of the Shoal Arm Section, thereby also constraining the recalculated positions of other samples within the Shoal Arm Section. The observation also suggests that the deposition of these beds may have been laterally extensive.

5.4.3 Normalization

This chapter is mainly concerned with the variation of elemental abundances as a function of stratigraphic position. Dilution by biogenic SiO_2 is overcome by normalizing

the respective oxide abundances to Al_2O_3. Aluminum is well-suited, because it becomes mobile only under pH-conditions above 8 and below 5, which are usually not met in diagenetic pore fluids (Henderson, 1982). The Al_2O_3-normalization assumes that the accumulation of this element was constant through time, so that the variation in a ratio can always be attributed to the compositional variation of the normalized element. Additionally, this ratio is normalized to a reference composition in order to evaluate the deviation from a standard composition. Ratios are interpreted in the following way: $R = 1$ means sample and reference are equal; $R < 1$ means that the sample is depleted relative to the reference; and $R > 1$ means that the sample is enriched relative to the reference.

An average, modern pelagic clay composition from the Pacific ocean basin (Chester and Aston, 1976) was generally preferred as a reference over the composition of a shale composite. Based on the interpretation of its sedimentary structures, the Shoal Arm Formation was most likely deposited in a pelagic environment. Since the North American Shale Composite (NASC) or the Post Archean Average Shale Composite (PAAS) contain analyses of shales deposited in a variety of different environments (Taylor and McLennan, 1985; Gromet et al., 1984), the composites can be regarded as an average of all the specific geochemical characteristics that each environment produced. Compositional deviation from a shale composite only indicates the peculiarity of the Shoal Arm Formation composition, but allows little interpretation on potential hydrothermal activity, anoxic environments, enhanced detrital activity, or diagenetic disturbances of the Shoal Arm Formation. The pelagic clay, however, has a better defined sedimentary environment, and its sedimentary sources are relatively well-known (e.g., Bryant and Bennett, 1988; Leinen, 1989). The normalization to the pelagic clay composition therefore allows for a better environmental interpretation than the normalization to a shale composite.

5.4.4 Stratigraphic variation of compositional end-members

Each end-member has its own characteristic group of elements. By plotting the composition of each sample against its stratigraphic position, the trend of the characteristic elements represent the geochemical variation of each source component in stratigraphic order. In order to avoid deceptive effects of dilution by a third element (i.e., Si), a key-element of each end-member could be normalized relative to an element which is most likely constant through time. Again, the choice falls on aluminum, because this element is generally considered to be immobile and its abundance may be moderately constant in lithologies with consistently small grain-sizes. By comparison of several key-element trends normalized to Al_2O_3, we may be able to discriminate detrital components by their differing stratigraphic trends. Factor scores obtained from a R-mode factor analysis on the complete data set, excluding the greywackes, also give useful information on variations among source components. Factors can be interpreted to represent sediment source components. Since factor scores are an expression of the magnitude that these sediment components contribute to a sample, the magnitude of the factor scores indicate the relative magnitude of a particular component in the sample. In this respect, it is important to consider that samples which have a large factor score are dominating, or even establishing, a separate factor. The factor scores therefore also indicate whether a sediment component is actually contributing to the variation of the chemical composition in the *whole* data set, or whether this component is a dominating component in a limited stratigraphic interval that is insignificant, or not present, in the remaining part.

5.4.4.1 Detrital source variation

The immobile elements Ti, Cr, Zr, and Al were found to be associated with the clastic sediment component (Chapter 5.2), but they may not represent the same clastic source. Zr is chosen from the Zr-, Nb-, and Y-group, which has been shown to form a separate component (Chapter 5.2). Although a mafic component could not be discriminated in the data sets, the potential remains that certain intervals exist where such a source can be identified. The ferromagnesian element Cr was chosen to indicate a possible mafic source. All three elements (i.e., Zr, Ti, and Cr) were normalized to Al_2O_3, and additionally normalized to the respective element ratio in a modern pelagic clay. The following discussion refers to Figure 5.11.

The increase in Zr between 220 meters and 245 meters is most pronounced, but the lowermost sample of the stratigraphic section is similarly enriched in Zr. Two samples that are slightly enriched in Zr show a negative Ti-anomaly. Also, a negative Cr-anomaly exists for the most strongly Zr-enriched samples. One explanation may be that the Zr-rich component, which arrived at the source area, had low abundances of Ti and Cr and was dominating the integrated clastic component in the upper part of the Shoal Arm Formation. The increase in Zr cannot be explained as a result of a change in grain-size or as a result of sorting, because the Zr-rich samples show no obvious difference in grain-size to the other samples. Also, an increase in the Zr abundance by a grain-size increase appears to be related to the presence of the heavy mineral zircon in sandy and silty fractions (Van Weering and Klaver, 1985). Van Weering and Klaver (1985) suggested that hydraulic separation of zircon may be the cause for the drop of Zr abundances from sandy-silty to silty-clay and clay-size fractions. Instead of detrital zircon, the clay component may have been the carrier of Zr in the Shoal Arm Formation argillites. The increase in Zr/Al_2O_3 is associated with similarly strong increases in the Y/Al_2O_3 and Nb/Al_2O_3 ratios. Sorting trends examined in early Ordovician passive

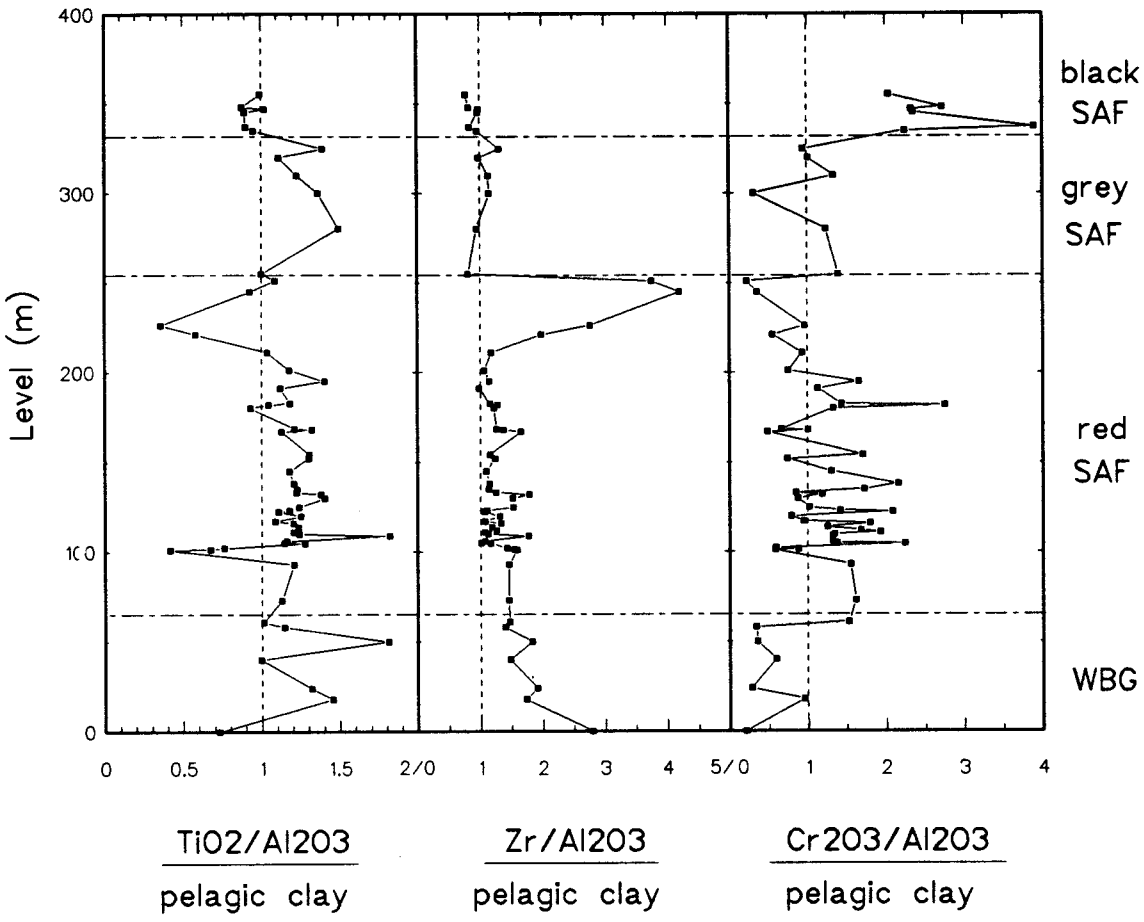

Figure 5.11: Stratigraphic variation of detrital key elements of different clastic sources. Discriminated clastic sources are represented by Zr, Ti and Cr. See text for discussion of the stratigraphic trends.

margin sediments of the Poultney Formation in New York State, and comparison of a sample set containing a wide range of grain-sizes of the Gull Island Formation greywackes shows that the correlation of the three elements Zr, Nb, and Y would break down if the sediment is subjected to intense physical sorting. The correlation of these three elements in the Shoal Arm Formation argillites supports the previous statement that Zr may be contained in the clay component. The Zr-Nb-Y-group is therefore interpreted to reflect the original source-rock composition. A volcanic source containing high Zr, Nb, and Y abundances is suggested to have been dominant in the upper part of the red Shoal Arm Formation and possibly also at the bottom of the measured stratigraphic section.

Both erosion of a volcanic complex and volcanic activity have to be considered as possible scenarios to explain the enrichment in Zr, Nb, and Y. The disappearance of the Zr-, Nb-, and Y-rich component with deposition of the grey cherts is fairly abrupt. This observation may constrain the interpretation that these argillites have a tuffaceous component, since it would be expected that the cessation of volcanic activity is a much more abrupt signal than the gradual erosion of a volcanic complex. This observation is particularly significant since (a) the transition to the grey, mottled cherts seems to be conformable and (b) this transition was also closely sampled. On the other hand, the proliferation of the Zr-, Nb-, and Y-rich signal over 40 meter of stratigraphic thickness, and the absence of discrete beds that could be interpreted as tuff layers and would be expected in an active volcanic period, favour the interpretation of erosion of a volcanic complex. The abrupt disappearance of the high-Zr argillites may alternatively be explained as the result of a depositional hiatus such that the top parts of the Zr-rich argillites have been eroded by scouring bottom currents.

The depositional interval from 30 meters to 220 meters is not characterized by high Zr, Nb, and Y abundances (Figure 5.11), which indicates that for this time period little material was derived from the Zr-Nb-Y-rich source. It is possible that either the

source areas of the high-Zr sample in the upper Wild Bight Group and those from the upper Shoal Arm Formation interval were different, or that the contribution from a single high-Zr source stopped for a long time period. The overall stratigraphic trend of the Zr/Al_2O_3 ratio may also be interpreted as a continuous decrease stratigraphically upward (excluding the high-Zr upper Shoal Arm Formation) from the upper Wild Bight Group to the grey Shoal Arm Formation. Such a trend is also observed for Y and Nb. A sorting effect is excluded for the reasons given above. The trend may suggest that the influence of the Zr-, Nb-, and Y-rich source may have rather become continuously weaker stratigraphically upward, but that this continuous evolution was interrupted by a final pulse in the upper Shoal Arm Formation.

The source-lithology of the Zr-, Nb-, and Y-rich component may have been alkaline basalts which contain as much as 1000 ppm Zr, 126 ppm Nb, and 50 ppm Y (e.g., Basaltic Volcanism Study Project, 1981). The Lawrence Head volcanics, which have been characterized as sub-alkaline to alkaline basalts (Swinden et al., 1990; Jacobi and Wasowski, 1985; DeLong, unpublished data) contain up to 526 ppm Zr, 85 ppm Nb, and 57 ppm Y (Swinden et al., 1990; DeLong, unpubl. data). No other analyzed volcanics in the Badger Bay - Seal Bay area or on the Fortune Harbour Peninsula have comparably high abundances of these elements. On the other hand, these basalts have generally high abundances of Ti (i.e., 2-3 wt% TiO_2), but two of the Zr-Nb-Y-rich argillites are characterized by low Ti abundances (i.e., 0.5 wt% TiO_2). An alternative source-lithology may have been dacitic porphyries (i.e., the Coaker porphyry), which form intrusions in the Dunnage Mélange. Dacites may contain high abundances of Zr (i.e., up to 250 ppm Zr, at TiO_2 abundances of < 0.8 wt%; Foden, 1983). Geochemical analyses of the Coaker porphyry show Zr abundances of < 191 ppm Lorenz (1985). It may therefore be argued that erosion of the Dunnage Mélange and its contained porphyries, as seen in the roughly coeval Cheneyville conglomerate, may similarly explain the high Zr abundances in these argillites. However, the likelihood that dacitic

porphyries served as a source area seems low for the following reasons: (1) Not only dacitic porphyries would have been eroded, but the surrounding lithologies, i.e., the mudstone matrix and the variety of lithologies contained in the Dunnage Mélange, would have been eroded as well. Fine-grained volcaniclastics of the New Bay Formation which is located in the eastern Exploits zone have Zr abundances of < 120 ppm (Wasowski, 1987). Since the Dunnage Mélange is considered to be a lateral equivalent of the volcaniclastic sequence of the New Bay Formation - Wild Bight Group, it is likely that its matrix composition is similar to the fine-grained lithologies of the New Bay Formation. The mudstone composition would have diluted the Zr-rich clastic component derived from the rhyodacite to a degree that the Zr abundances measured in the upper red Shoal Arm Formation could not have been achieved by erosion of this material. (2) Dacites generally have low abundances of Nb (< 15 ppm; Foden, 1983), but the Zr-rich argillites have Nb abundances up to 60 ppm (sample GI-28). Calc-alkaline rocks usually have Nb abundances < 15 ppm (Basaltic Volcanism Study Project, 1981). The high Nb abundances in the Zr-rich argillites make it generally difficult to argue for a calc-alkaline rock-source, i.e., a rhyolite or an andesite. The low Ti abundances may alternatively be explained by fractionation of heavy titano-magnetites during the hydraulic or subaerial transport of this material.

In contrast to Zr and TiO_2, Cr_2O_3 fluctuates in the interval between 100 meters and 200 meters. The fluctuation is unrelated to a particular rock type. The slight enrichment in Cr relative to modern pelagic clay in the red Shoal Arm Formation may suggest the influence of mafic, volcanic detritus. To test this hypothesis, "mafic", (i.e., compatible) ferromagnesian elements were plotted together with Cr in stratigraphic order. Figure 5.12 shows that MgO and Cr_2O_3 show similar trends in this interval, but the V/Al_2O_3-trend is different. Ni was not used because it may partly be derived from a hydrothermal component (see below). It remains speculative whether a mafic component was present. All samples of the upper Wild Bight Group have lower

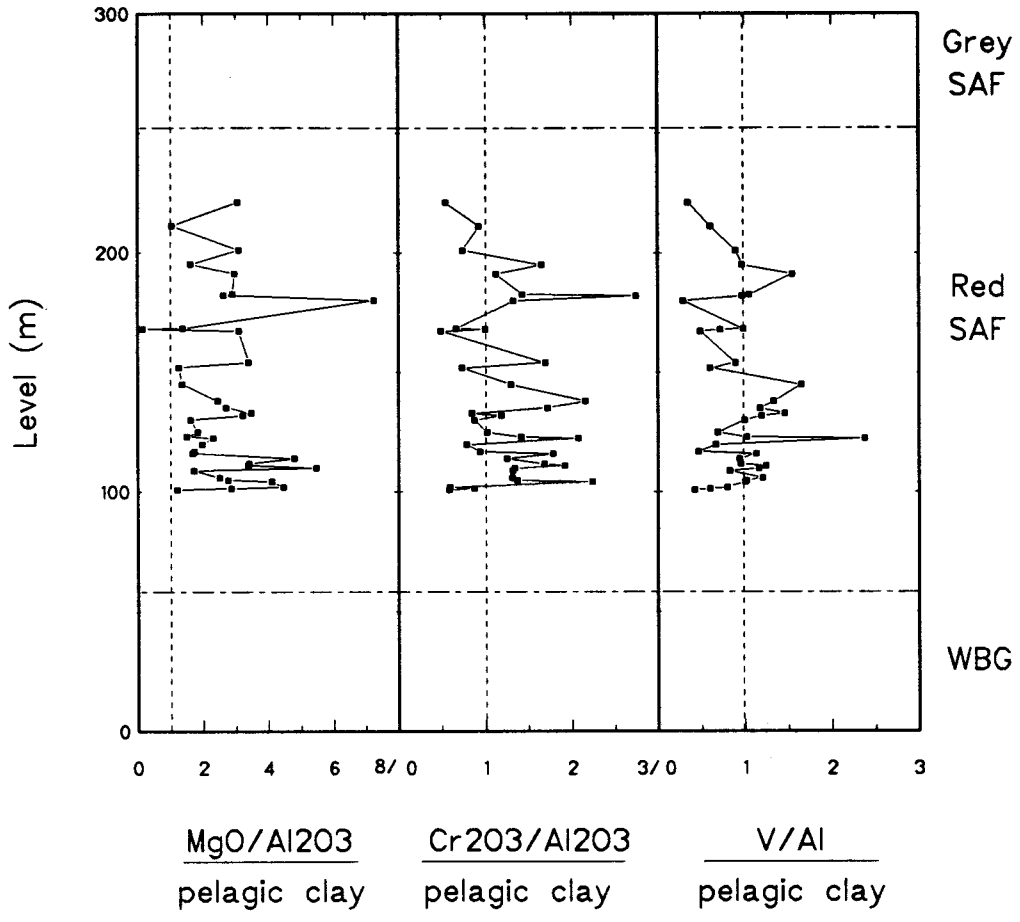

Figure 5.12: Stratigraphic trends of the "mafic" elements Cr, V, and Mg in the red Shoal Arm Formation. MgO and Cr_2O_3 display some correlation in contrast to the V trend. Relative to the pelagic clay, MgO is most strongly enriched.

Cr_2O_3/Al_2O_3 ratios than the Shoal Arm Formation and the modern pelagic clay. This result is surprising, because it has been assumed from petrographic work (Nelson, 1979) that the green volcaniclastics of the upper Wild Bight Group consist of mafic components. The present analyses do not support this interpretation and instead suggest a clastic source that was similar to the one seen in the upper Shoal Arm Formation between 220 and 250 meters. The sharp increase in Cr in the black slates can be explained as a typical characteristic of black shales, where elevated Cr abundances have been suggested to result from bioconcentration, biological sorption and precipitation processes under anoxic conditions (Vine and Tourtelot, 1970; Dean et al., 1984). Alternatively, the Cr-enrichment may be regarded as the first signal of the Cr-rich greywackes that were subsequently deposited on top of the black shales.

Ti and Al abundances are only well-correlated in the interval between 100 meters and 200 meters and in the black slates (Figure 5.11). In general, Ti is slightly enriched relative to the pelagic clay. It may be of importance that the TiO_2/Al_2O_3 ratio is approximately the same as in the interval between 100 and 200 meters and the grey Shoal Arm Formation. Possibly, similar detrital sources existed for these two intervals.

5.4.4.2 The hydrothermal component

Before discussing the influence of a potential, hydrothermal component in the Shoal Arm Formation, it is necessary to discuss a shortcoming resulting from the normalization to modern pelagic clay. It is observed that the pelagic clay of the Pacific basin has relatively high abundances of Ni, Pb, Co, Cu, and Ba - elements that are known to be contained in a hydrothermal component (e.g., Dymond, 1981; Leinen, 1987). The average pelagic clay composition provided by Chester and Aston (1976) is a compilation of numerous locations in the Pacific, and actually represents the relatively

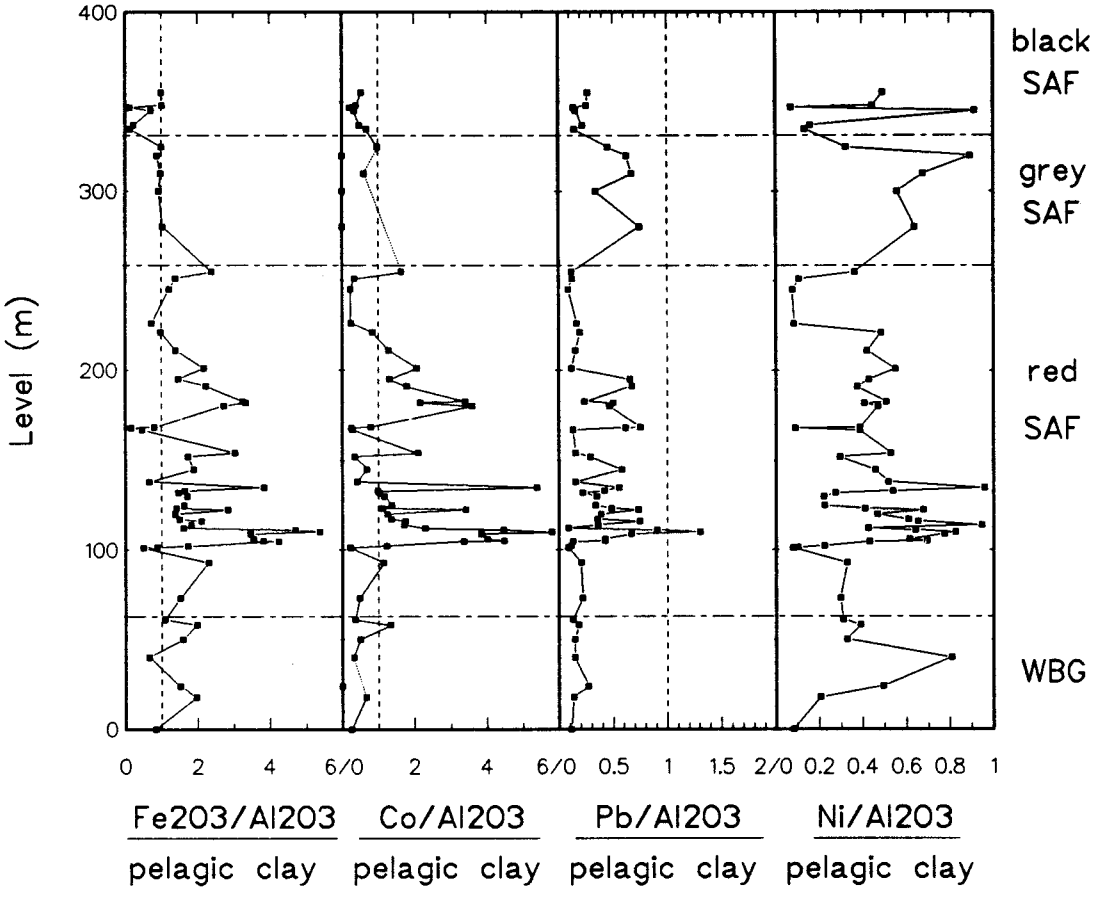

Figure 5.13: Stratigraphic trends of the "hydrothermal" elements Fe, Co, Pb, and Ni. The low Ni/Al_2O_3 and Pb/Al_2O_3 ratios are explained by anomalously high abundances of these elements in the average pelagic clay composition. Fe, Co, and Pb are well-correlated throughout the red Shoal Arm Formation, whereas Ni correlates only at 110 meters. The differing Ni-trend is interpreted as an additional contribution from a mafic source.

old data set established by Turekian and Wedepohl (1961). As was shown by Toyoda and Masuda (1990) and Leinen (1989), the composition of the pelagic clay is dependent on the distance from areas of hydrothermal activity. It is suggested here that the samples used by Turekian and Wedepohl (1961) could have been biased towards samples from locations in the realm of hydrothermal plumes (e.g., Lyle et al., 1986). Since the hydrothermal component may therefore be anomalously strong, normalization to this pelagic clay composition consequently results in normalized abundances of Cu, Ni, Zn and Ba in the Shoal Arm Formation samples that may seem to be too low to reflect their true nature. It may therefore be more important to examine the correlated trends of Ni and Pb with other, potentially hydrothermal elements than to directly compare their abundances to the pelagic clay.

The association of Fe, Co, Pb, and Ni was interpreted to represent a hydrothermal component (Chapter 5.2). Figure 5.13 shows that the metals Pb, Fe, Co, and Ni are enriched most strongly at the level 110 meters. The enriched samples belong to the dark maroon and purple part of the lower red Shoal Arm Formation. The maroon and purple part is therefore interpreted as the interval with the strongest hydrothermal influence. In the overlying bright-red part, the enrichment of the four elements is lower, and continues to decrease stratigraphically upwards. The Zr-rich argillites have the lowest abundances of these four elements in the red Shoal Arm Formation. Pb and Ni abundances in the grey Shoal Arm Formation remain elevated, but the association with Fe breaks down.

The metals Mn and Cu may also be contributed from a hydrothermal component (e.g. Heath and Dymond, 1977). The strongest Mn- and Fe-enrichments are closely associated in the stratigraphic section, i.e., within 50 cm (Figure 5.14). Although the reason for this fractionation is most likely the product of secondary mobilization, as is discussed in Chapter 5.5., the proximity of the Fe- and Mn-peak positions suggest that Mn is also of hydrothermal origin. The stratigraphic sequence, however, shows no clear

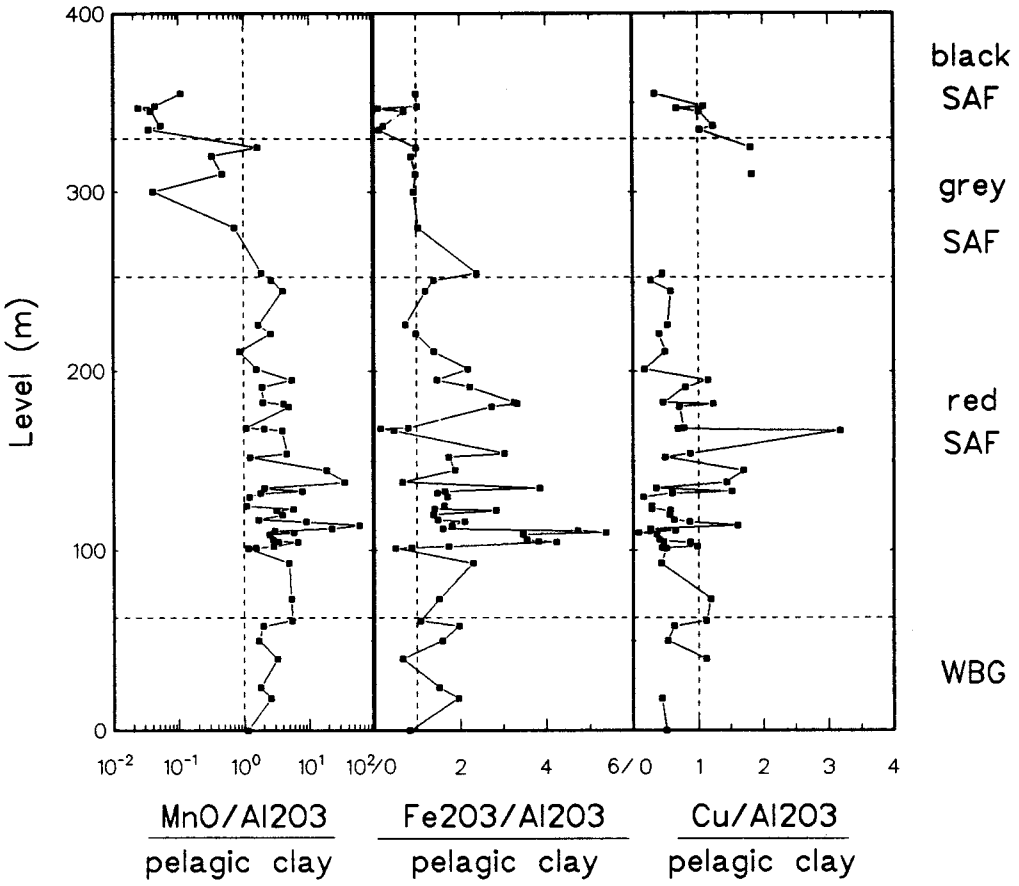

Figure 5.14: Comparison of the normalized stratigraphic trends of Mn, Cu and Fe. Mn and Fe show an enrichment in the same stratigraphic interval, which suggests a common, hydrothermal source. The Cu-trend shows no relationship to the hydrothermal enrichment.

relationship between Cu and the "hydrothermal" elements Fe, Ni, Pb, and Co. In oxic sediments, up to 96 percent of the Cu may be regenerated to the bottom seawater via diagenetic flux (Sawlan and Murray, 1983). Cu may therefore have been redistributed after deposition. In addition, since it is known that Cu has a biological affinity in recent sediments (Leinen and Stakes, 1979), it cannot be excluded that Cu in the Shoal Arm Formation may also be partly biogenic.

It was suggested in the previous chapter that a weak, mafic, clastic component may exist in the interval between 100 and 200 meters. It is conceivable that Fe is partly derived from this source. Comparison of the trends of Fe_2O_3/Al_2O_3 (Figure 5.14) and Cr_2O_3/Al_2O_3 (Figure 5.11) indicates that the strongest Fe-enrichments do not coincide with the strongest Cr-enrichments. A more detailed examination of the corresponding trends by comparing each sample also showed that there is no consistent relationship between Fe and Cr. This observation does not exclude the existence of a mafic contribution to the Fe abundances, but the quantity of this component cannot be extracted.

5.4.4.3 The origin of calcium carbonate in the red Shoal Arm Formation

The highest abundances of Ca in the red Shoal Arm Formation seem to indicate a general decreasing trend stratigraphically upwards (Figure 5.15). Figure 5.15 involves normalization to the Post-Archean-Average-Shale (PAAS) composition (Taylor and McLennan, 1985), because Chester and Aston (1976) gave no value for a loss of ignition (LOI) in their pelagic clay composition. Not surprisingly, the samples that are most enriched in Mn contain rhodochrosite, and therefore exhibit corresponding peaks of LOI, CaO, and MnO. The MnO abundances remain approximately constant in the red Shoal Arm Formation except for the two, markedly enriched intervals at 110 and 140

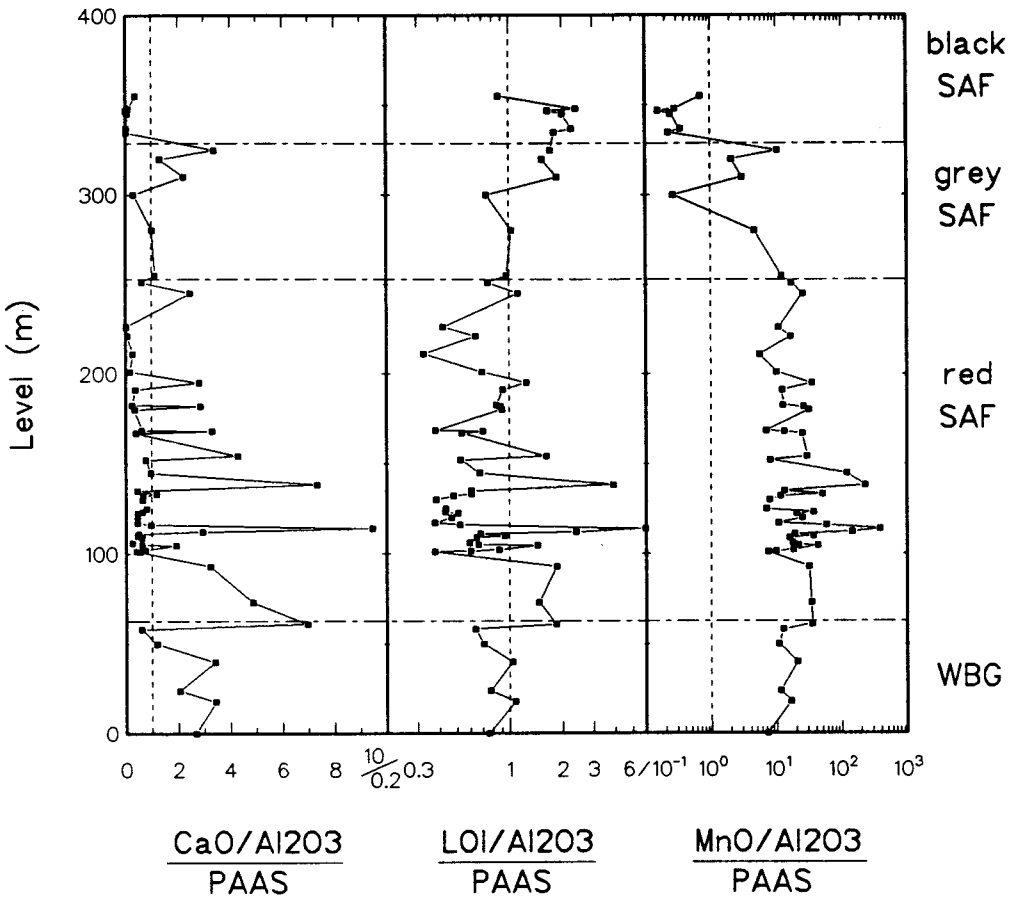

Figure 5.15: Diagram illustrating the stratigraphic variation of carbonate, represented by LOI (loss of ignition) CaO, and MnO. Note the different scales on the x-axes. Frequent rhodochrosite is present only in those samples that have elevated CaO and LOI abundances. Since MnO levels are high throughout the Shoal Arm Formation, carbonate is suggested to be the limiting parameter for rhodochrosite formation.

meters, whereas the high CaO- and LOI-normalized abundances appear to decrease steadily. Although three peak positions seen in the CaO-trend are missing from the LOI-trend, I am confident that the two curves both display a general decrease stratigraphically upward. The correlation of CaO and LOI in these samples is interpreted to represent $CaCO_3$. Less rhodochrosite is found in the upper Shoal Arm Formation than in the lower portions (Chapter 3). This may suggest that the formation of rhodochrosite depended on the availability of carbonate, since the Mn abundances were still relatively high in the upper stratigraphic levels of the red Shoal Arm Formation.

Figure 5.16 shows the CaO/Al_2O_3 trend again, but this time, the various lithologies are distinguished by using different symbols. The highest CaO abundances are restricted to the green argillites, whereas most of the red argillites and some of the green argillites in the red Shoal Arm Formation have similar Ca abundances which are generally lower than the PAAS composition. The sedimentary features of these carbonate-rich sediments suggest that they represent fine-grained turbidites (Chapter 3). Since pelagic, calcareous organisms are unknown for the Ordovician (Gray et al., 1982), the carbonate may have been transported as bioclastic turbidites from shallow-water environments. The reason for the CaO decrease may therefore be related to a change in the depositional regime landwards by a process that reduced the transport of $CaCO_3$ from shallower depths into the basin. Several scenarios could explain the decrease in the CaO- and LOI-content: (1) The source was gradually eroded and eventually disappeared; (2) the calcareous sediment was ponded in other parts of the basin; (3) fewer calcareous, biogenic particles reached this depositional site due to subsidence of the basin below the CCD.

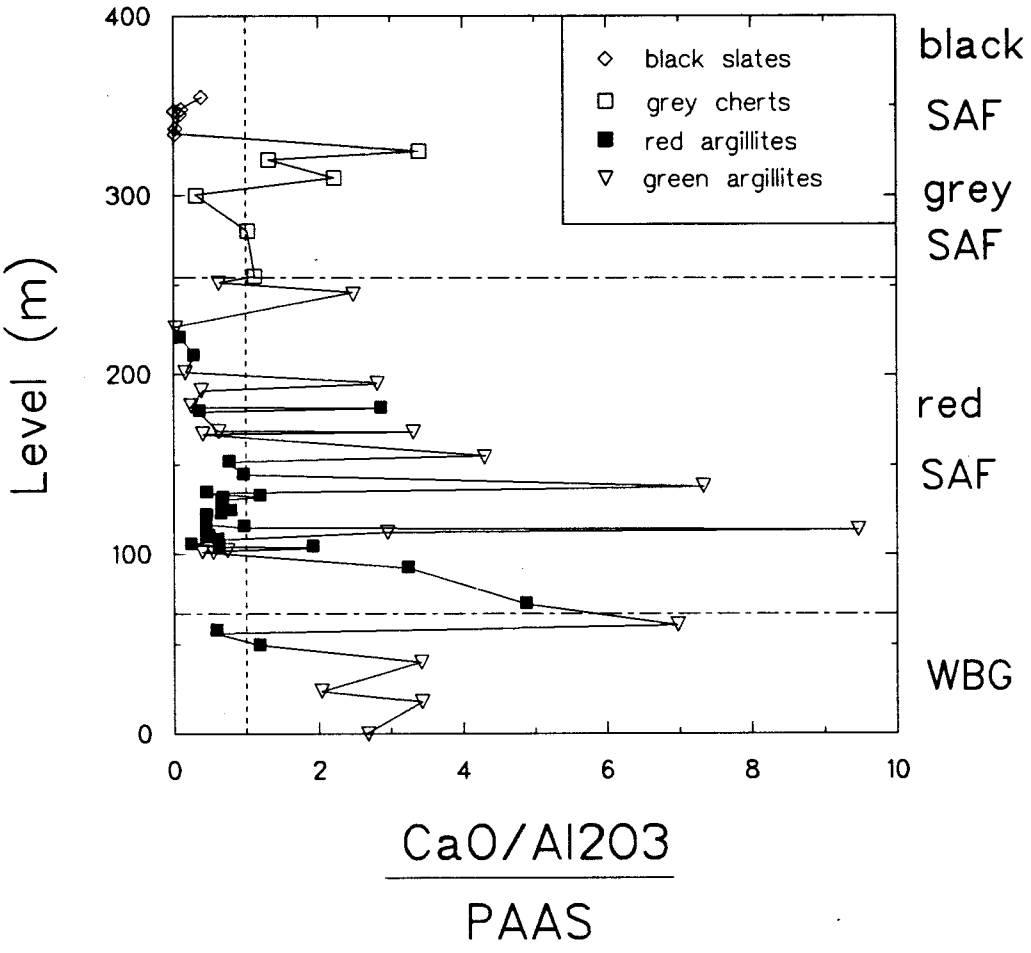

Figure 5.16: Normalized stratigraphic trend of CaO/Al2O3. Same diagram as in Figure 5.15, but each rock type is represented by a different symbol. With the exception of one purple argillite, only green argillites show higher Ca abundances. These argillites are interpreted to represent calcareous turbidites.

5.4.4.4 The Na/K ratio

The Na_2O/K_2O ratios of the Wild Bight Group and the red Shoal Arm Formation are higher than the PAAS composition by a factor of > 3. The origin of this high ratio can be attributed either to high Na abundances or low K abundances. In some intervals, the K abundances are similar to the PAAS composition, but there exist also intervals with very low K abundances (Figure 5.17 III). Since the grain-size of the stratigraphic section does not vary greatly, it is unlikely that the sediments display any sorting effects (e.g., Argast and Donnelly, 1987; Roser and Korsch, 1986). The variations of K may therefore either be attributed to K-loss during diagenesis (Hower et al., 1976; Blatt, 1985) or to rapid changes in provenance (Roser and Korsch, 1986). Na is consistently enriched relative to the PAAS composition (Figure 5.17 II). In order to explain the high Na_2O/Al_2O_3 ratio by diagenetic enrichment, samples should exist that are depleted in Na_2O. Since such samples have not been recognized, it is suggested that the high abundances of Na generally reflect the source-rock composition(s). Admittedly, the unsampled intervals leave enough space for Na-depleted intervals. Sorting trends observed between different grain-sizes of greywackes and mudstones generally suggest that the Na/K ratio decreases with grain-size (Argast and Donnelly, 1987; Roser and Korsch, 1986). This would require a source with an even higher Na/K ratio. Roser and Korsch (1986) used a discrimination scheme of active island arc, and passive continental margin settings by proposing that the Na_2O/K_2O ratio and the SiO_2-content of sandstone-mudstone suites can be used as maturity indicators. Since the SiO_2 abundances of the Shoal Arm Formation are likely to be contaminated by biogenic SiO_2, the tectonic discrimination diagram by Roser and Korsch appears to be of limited use. Based on the Na_2O/K_2O ratio alone, a quartz-intermediate to quartz-poor source area in an arc or active continental margin setting would have to be inferred. This correlates well with the general tectonic interpretation of Notre Dame Bay area (e.g., Dewey et al.,

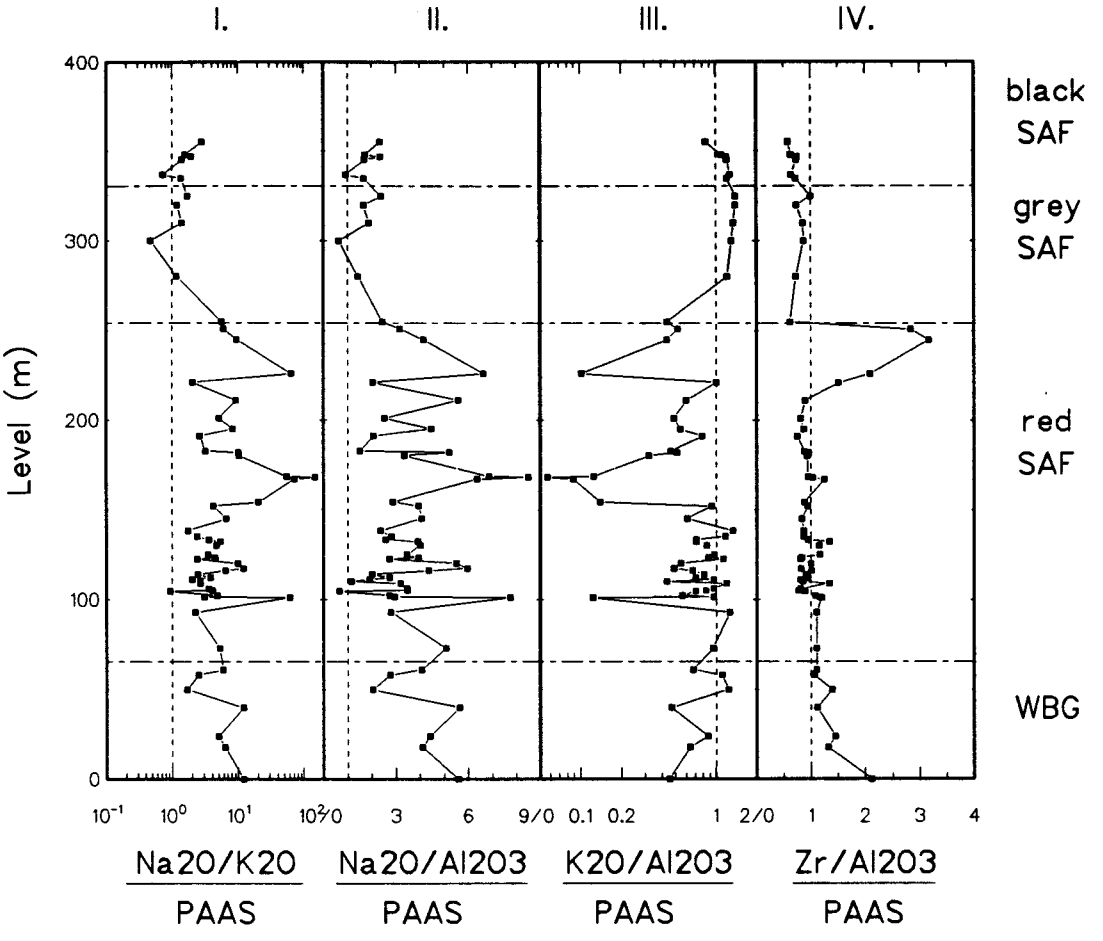

Figure 5.17: Comparison of the stratigraphic trends of Na, K, and Zr. Na and K are negatively correlated, but the two elements do not balance each other in their relative enrichments/depletions. A relationship to the Zr-rich component (IV) has to be excluded.

1983). However, since it has been pointed out by several authors that, under certain circumstances, Na and K can be mobile during diagenesis (e.g., Roser and Korsch, 1986; Argast and Donnelly, 1987; Hower et al., 1976), a further speculation on the nature of the source-rock seems not justified.

Three horizons display high Na/K ratios that differ significantly from most of the section. These horizons are very low in K, and high in Na (Figure 5.17), but the relative Na-enrichment does not compare to the relative K-depletion. The cause of these low K abundances may be explained by diagenetic loss of K and/or the presence a different primary source, (i.e., the beds may actually represent altered volcanic tuffs). Either hypothesis is difficult to prove with the present data. The sample SA-11 (stratigraphic interval: 168 meters) was split into an upper part and a lower part, which were analyzed separately. The analyses showed a decrease in the CaO- and Sr-content from 2.23 wt.% and 221 ppm, respectively, at the bottom to 0.42 wt.% and 84 ppm, respectively, at the top. Total Fe and Ba increase from 0.76 wt.% and 44 ppm, respectively, at the bottom to 3.63 wt.% and 118 ppm, respectively, at the top. While the increased CaO-content can clearly be attributed to thin layers of carbonate in the bottom part that are not present in the top part, the change in the Fe- and Ba-abundance is not understood. Detrital, immobile elements do not vary across the sample, and the grain-size appears to invariably small. Potentially, some element mobility is the cause for this compositional variation. On the other hand, the samples that exhibit high Na/K ratios also have other common characteristics. Relative to adjacent argillites, they are low in K, Rb and Ba, and high in Pb, Na, and Sr. Although it would be reasonable to argue that these elements are mobile, the consistency may indicate that they share a common, primary characteristic inherited from their clastic source.

A relationship to the Zr-rich interval must be excluded. This is illustrated in column IV of Figure 5.17. The Zr/Al_2O_3 ratio remains constant where the strongest Na-

and K-changes occur. Therefore, the supposed tuffs and the Zr-rich argillites of the upper, red Shoal Arm Formation probably did not have the same source.

5.4.4.5 Biogenic bloom in the grey cherts

Figure 5.18 shows the normalized compositional trends of SiO_2 and BaO. The SiO_2/Al_2O_3 ratio and the BaO/Al_2O_3 ratio increase in the grey unit. The BaO/Al_2O_3 ratio of the red Shoal Arm Formation is low relative to the abundance of BaO in the pelagic clay composition of Chester and Aston (1976). A study of the Ba-content of core-analyses from the central Pacific DSDP sites 576, 578, 580, and 581 (Heath et al., 1985) and a North-Atlantic pelagic clay composition (Thomson et al., 1984) indicated frequently lower Ba-contents than given by Chester and Aston (1976). Since the Ba content of pelagic clays is dependent on the biogenic productivity of the overlying waters (Chester and Aston, 1976; Glasby, 1991), it may be argued for similar reasons as discussed in Chapter 5.4.3 that a sample bias towards locations of high, biological productivity has resulted in an anomalously high Ba-content of the average pelagic clay composition. Relative to the PAAS composition, the Shoal Arm Formation would be enriched in Ba. Therefore, the low pelagic clay-normalized BaO/Al_2O_3 ratios in the red Shoal Arm Formation may be artifacts.

A correlation of Si with Ba in siliceous plankton is well-documented (Martin and Knauer, 1973). The increased abundance of these two elements in the grey unit suggests increased biological production in the seawater during deposition of the laminated and mottled, grey cherts. The increase in the SiO_2/Al_2O_3 ratio may mark an increase in the biogenic accumulation rate, although this hypothesis cannot be confirmed by paleontologic evidence. Figure 5.18 suggests that this biogenic bloom was disappearing with deposition of the black slates, since both the BaO/Al_2O_3 and SiO_2/Al_2O_3 ratio

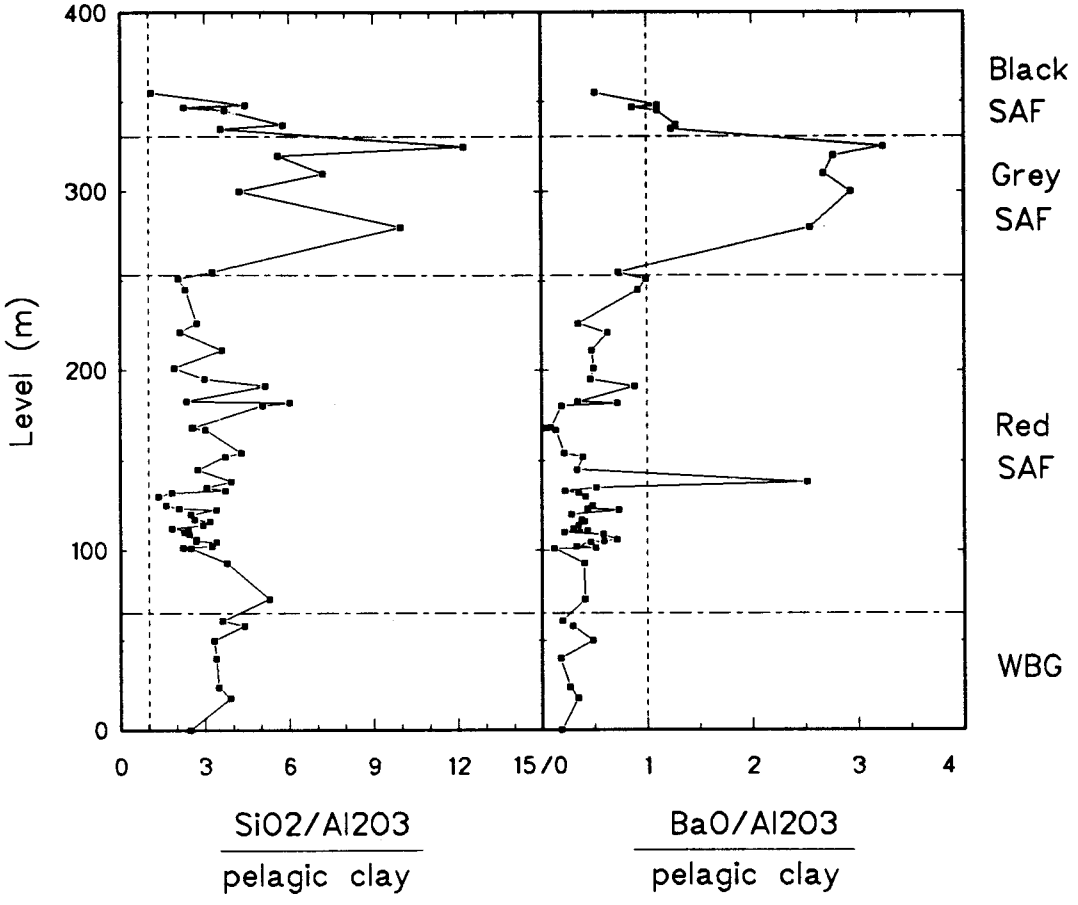

Figure 5.18: Normalized, stratigraphic trends of SiO_2 and BaO. The increase of SiO_2 and BaO in the grey cherts is interpreted as a biologic bloom. The low Ba ratios in the red Shoal Arm Formation are explained by anomalously high abundances of Ba in the average pelagic clay composition. The decrease of the Si and Ba abundances in the black slates suggests that the period of high biological productivity did not last until the deposition of the black shales.

decrease again in the black slates to the level of the red Shoal Arm Formation. Although clearly more data would be needed, the BaO/Al_2O_3 ratio appears to further decrease stratigraphically upward to the uppermost sample of the sequence. Since this sample is in fact a silty, black argillite, and may represent a distal greywacke, it may be suggested that the black slates form an intermediate stage where the biogenic component became continuously more suppressed by dilution with clastic material.

5.4.5 Stratigraphic variation of factor scores

An R-mode factor analysis was performed on 52 samples of the data set applying the same procedures as described in chapter in 5.2. The analyses of the black slates and the greywackes were excluded, since it was apparent from chapter 5.2 that the clastic sources of these lithologies were different from the underlying lithologies, and would have produced unnecessary noise in the data set. The analysis showed 5 factors with eigenvalues > 1.5. An eigenvalue of 1 is considered to be the significance limit in a factor analysis. Figure 5.19 illustrates the factor loadings of the 26 elements. Together the 5 factors account only for 71.3 percent of the compositional variation observed in the data set. This result is not good, because it leaves considerable compositional variation unaccounted for. The first 5 factors indicate consistent results with the conventional analysis of single element variations. In factor 1, which accounts for 26 percent of the total variation observed, the elements Fe, Co, Ni, and Pb are associated. Factor 1 is indicative of the hydrothermal component. Factor 2 shows a strong correlation of the elements Zr, Nb, Y, Zn, and Mg. This group is also known, and was interpreted to indicate a Zr-rich source. Factor 2 accounts for 16.8 percent of the compositional variation. Factor 3 shows a strong association of Mn, Ca, Sr, and LOI, and indicates the diagenetic rhodochrosite component. Factor 4 controls the variation of

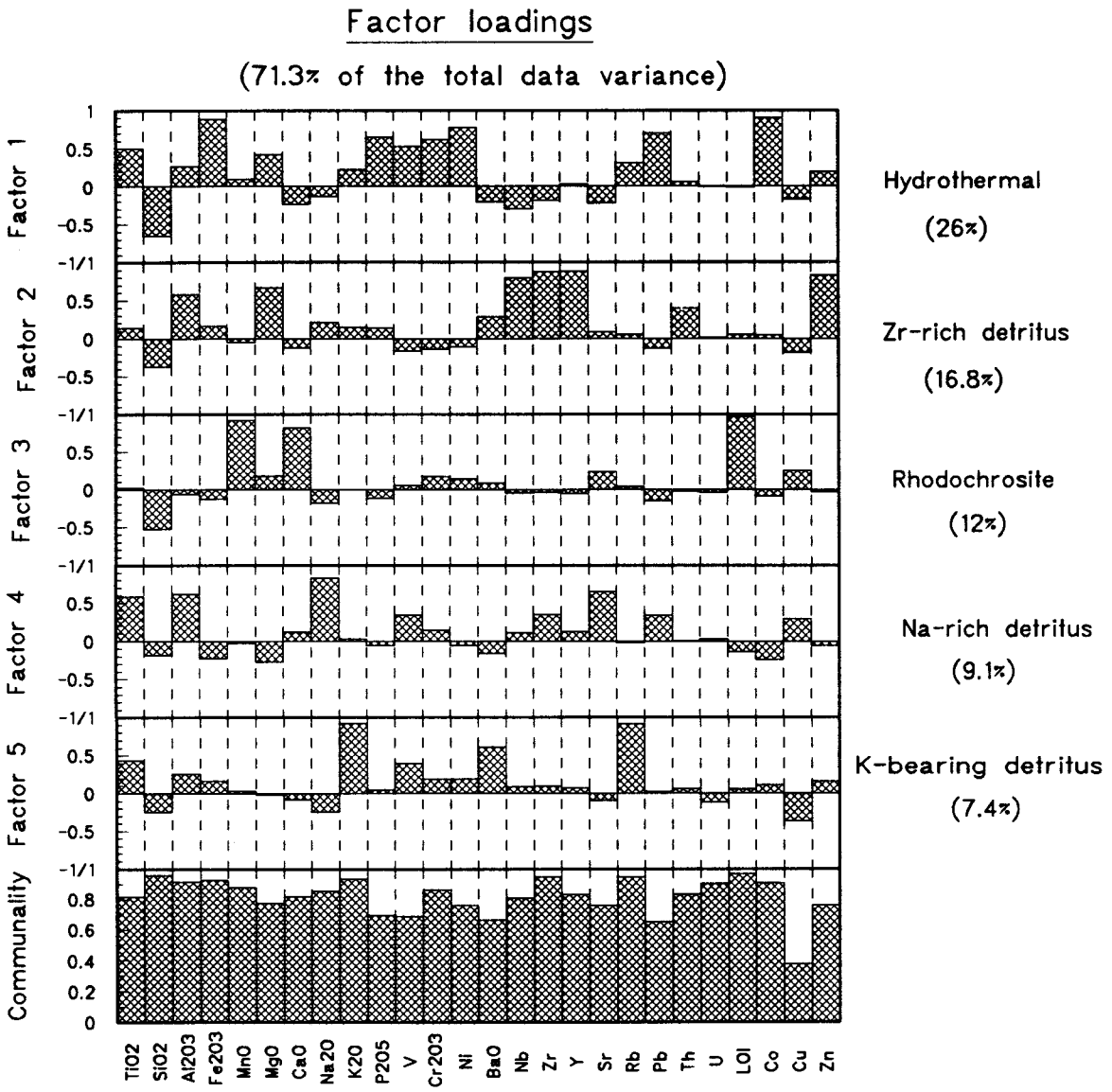

Figure 5.19: Factor loadings from a R-mode factor analysis on 52 samples of the upper Wild Bight Group, the red and grey Shoal Arm Formation. Five factors explain 71.3 percent of the compositional variation of the data set. Silica shows a consistent negative loading in all factors, and is interpreted as the biogenic dilutent. The communalities are a statistical parameter that indicates how well the factor loadings represent the compositional variations of any element. A value of "1" indicates 100% representation by the factors.

Na, Ti, Al, and Sr. The association of Na with immobile elements indicates the primary, detrital character of the element Na; the factor is therefore interpreted to represent a clastic component. Factor 5 finally shows a strong covariation of K, Rb, and Ba, with weak associations of the elements Al, Ti, and V. Because of their similar ionic radii and identical valency, the elements Ba and Rb can replace K in feldspar and clay minerals. The covariance of K, Rb, and Ba with Al and Ti also suggests a detrital component.

Factor scores of the five, first factors were calculated for each sample (Figure 5.20). The factor scores can be interpreted in the same way as elemental abundances, because they are an expression of the varying dominance of elemental groupings. However, it is important to bear in mind that the factor scores should not be understood as compositional data *sensu stricto*. The factor scores of the different factors do *not* have the same dimension, and cannot be regarded to represent the absolute proportions of the sediment components. The algorithm used excludes samples that do not have a complete set of elements. The gaps seen in the stratigraphic column of Figure 5.20 are the result of this omission. Analyses in these intervals were not analyzed for Co, Cu, and Zn.

The factor scores for factor 1 show a maximum at the stratigraphic level, where the strongest Fe-enrichment appears (110 meter) (Figure 5.20.a). The stratigraphic trend of the factor scores for factor 1 generally resembles the "hydrothermal" elements Fe, Co, and Pb. Interestingly, the factor scores of factor 1 are only positive above the level 110 meter, and remain positive to the top of the red Shoal Arm Formation. Possibly, the hydrothermal component did not start before the stratigraphic level 110 meter.

The second factor depicts the Zr-Nb-Y-rich argillites of the upper, red Shoal Arm Formation that were recognized by their high Zr/Al_2O_3 ratios. Factor 2 also shows a minor increase at 100 meters (Figure 5.20.b), which was not recognized before. The association of Mg and Zn may indicate that the two elements are derived from the same

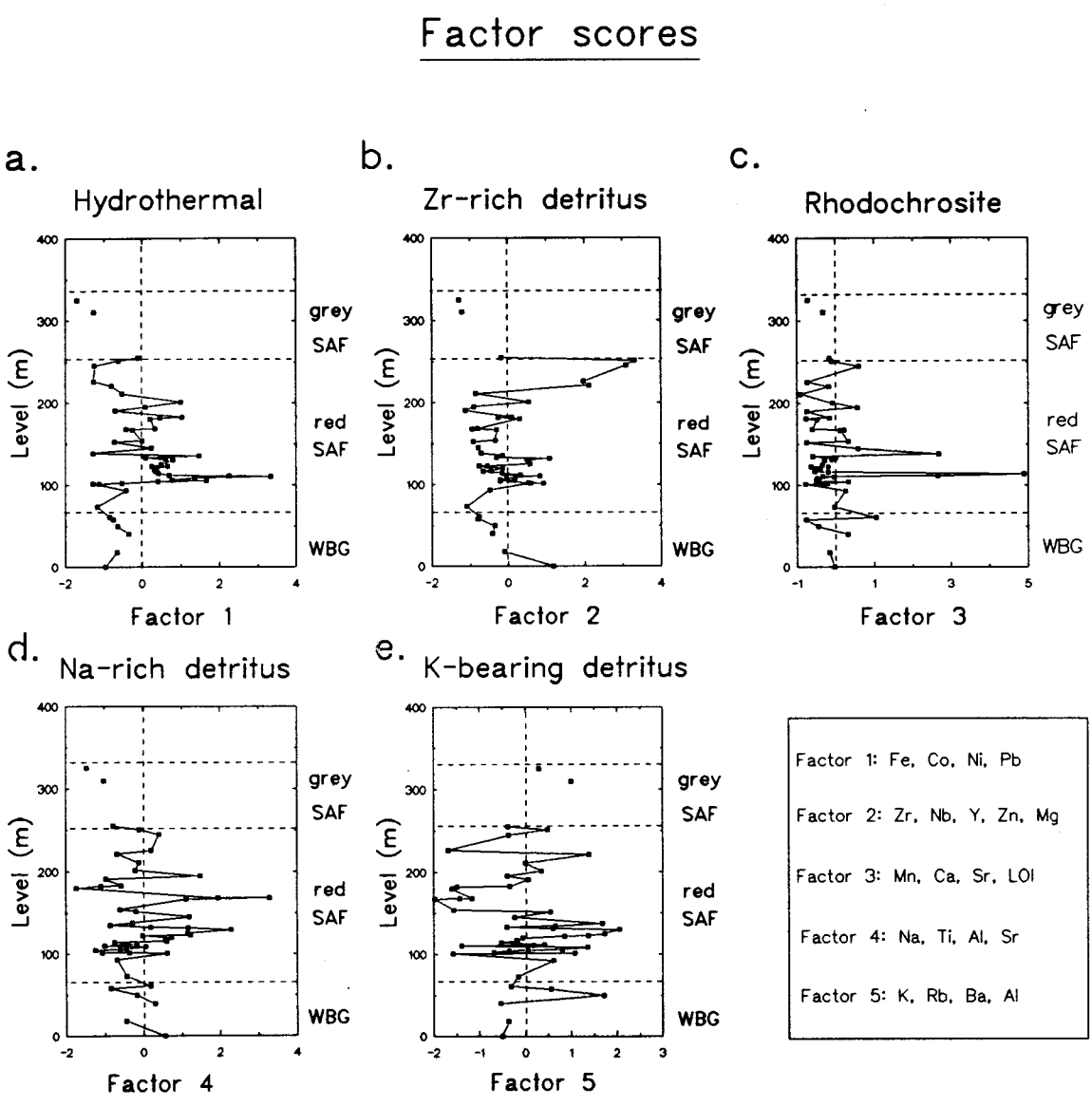

Figure 5.20: Stratigraphic trends of the factor scores. The magnitude of the score does not reflect their absolute compositional proportions, because the factor scores have also negative values. See text for discussion of the stratigraphic trends.

clastic source as Zr, Nb, and Y. It appears unlikely that different mineral grains of one clastic source could retain this element combination. It is therefore suggested that the five elements were all present in a clay component.

The factor scores for factor 3 achieve their maximum at the level of the rhodochrosite beds (Figure 5.20.c). Since the remaining stratigraphic levels have indistinguishable factor scores, it is concluded that few, distinct, rhodochrosite-bearing samples established a separate factor that may not have been significant in the remaining data set. This conclusion coincides with the observation that increased MnO-levels together with increased CaO- and LOI-levels appear only at the stratigraphic levels 110 meter and 138 meter, but are comparatively low throughout the rest of the stratigraphic column (see Chapter 5.4.4.3).

The factor scores for factor 4 seem to be influenced by the compositional variation of Na. Three peaks are present, which correspond to the highest Na_2O/Al_2O_3 ratios (compare Figures 5.17 and Figure 5.20.d). However, the general trend of factor 4 does not exactly reproduce the Na_2O/Al_2O_3-trend, which must be explained by the influence of the associated elements Ti, Al, and Sr. The repeated occurrence of factor 4 in distinct peaks in the red Shoal Arm Formation may indicate that this component was present for a longer time period, but was active in only short-term depositional events. This interpretation corresponds with a volcanic tuff origin.

The factor scores for factor 5 depict the strongly varying abundance of K and the associated elements Rb and Ba (Figure 5.20.e). At 168 meters, the lowest scores for factor 5 correspond to the highest scores of factor 4, but these low scores cover a thicker interval than the high scores of factor 4. Similarly, at 220 meters, the lowest scores of factor 5 are not reflected by higher scores of factor 4. This observation confirms the previous statement that the components that controlled Na and K appear to be independent of each other. This may preclude the hypothesis of diagenetic replacement of K by Na.

It was thought that the discrimination of factor 5 resulted from the fact that 9 out of 52 samples had K, Rb, and Ba abundances very different from the rest of sample set. The factor analysis may have established a separate factor based on the large compositional difference of these 9 samples, which is similar to what was suggested for the rhodochrosite in factor 3. Factor 5 may therefore have simply depicted the samples anomalously low in K, Ba and Rb. Exclusion of these samples in a test run did not change the results. The same, first five factors were established. Moreover, this test-run manifested the association of factor 4 and 5 with diagenetically immobile elements Ti and Al. The sediment components represented by these two factors therefore contribute to the variation of all Shoal Arm Formation argillites.

Notable is the consistent negative factor loading of SiO_2 in all 5 factors (Figure 5.20.a-e). This negative association can be interpreted as a separate component of diluting, biogenic silica. The biogenic component cannot be represented in either of the factor score diagrams, since the negative scores of any factor include the negative loadings of other elements than Si as well.

5.5 Fine-scale variation

As described in Chapters 3 and 4, many samples of the Shoal Arm Formation exhibit heterogeneities on a scale of few millimeters. It is not possible to examine the geochemistry of all the variations being observed under the microscope and in outcrop. The investigation is therefore restricted to sedimentary features that indicate an influence of either primary fluctuations in accumulation rates, or secondary, diagenetic mobility on the chemical budget of single beds. The geochemistry of three small-scale sedimentary structures is described here in more detail. The three features are each characteristic of common small-scale sedimentary structures in the Shoal Arm Formation. Three thin sections from the Shoal Arm Formation were analyzed and are briefly described below:

(1) Sample SA-4, a purple argillite from the maroon and purple part of the Gull Island Section (stratigraphic level: 106 meters). The thin section exhibits fine laminae of 1-3 millimeter thickness. Dark, purple, Fe-oxide-rich laminae alternate with light-purple laminae that are poorer in Fe-oxides. The different mineralogy was expected to be reflected by different geochemical compositions, particularly in Fe, if each layer were analyzed separately. The geochemical analyses of separate layers in this thin section would potentially give information on the following questions: (1) The origin of the laminae. The layers can be either primary or secondary. If a secondary origin of the oxide-rich layers could be demonstrated, this observation may have important implications for the small-scale mobility of Mn and Fe, and the alkaline elements in the purple argillites. (2) The detrital background composition. A variation of the geochemical composition of the detrital component on a millimeter-scale could be related to different sedimentation rates.

(2) GI-8, a thin section from a radiolarian turbidite in the bright-red part in the Gull Island Section (stratigraphic level: 120 meters) contains black Mn-micronodules. The

consistent halo at the bottom of these nodules, as well as indicators of original bedding in the interior of these nodules (Chapter 4) suggested replacement and diagenetic alteration. A geochemical profile across the nodule was necessary to provide information on the distribution of elements across the nodule.

(3) GI-3, a sample that encloses the color transition from purple to green argillites, including a rhodochrosite band in the lower part of the green argillite. Sample GI-3 is located in the maroon and purple part of the lower Gull Island Section (stratigraphic level: 111 meters). As previously mentioned, the consistent presence of the rhodochrosite band at the color transition is characteristic throughout the Shoal Arm Formation. Although the contrasting petrography at the interfaces already indicated geochemical variations at the interface, it could not be unequivocally demonstrated whether the rhodochrosite band is the result of migration of elements during diagenesis from the adjacent layers.

Setup:

The thin sections were analyzed with a JEOL Superprobe 733 at the Rensselaer Polytechnic Institute in Troy, New York. The microprobe was operated at 15 kV, using a beam current of 25 nA in order to avoid thin section damage and loss of the volatiles CO_2, H_2O and Na. The statistical cutoff for the maximum variation was set to 0.2%; the maximum count-time for each element was set to 40 seconds. The procedure for geochemical analysis of sedimentary features (e.g. laminae or nodules) had to be different from a standard, single-grain analysis. In every case, the goal was to obtain an average composition of the fine-grained matrix. A representative part of the matrix therefore had to be analyzed in one analysis including as many different, fine-grained components as possible. For this purpose, a beam diameter of 30 microns was chosen. Any larger beam diameter would have lowered the quality of the analyses. Large radiolarian spheres and phases > 30 microns in size were avoided. The pre-selection was

expected to have an impact on the completeness of the analyzed abundances, considering that some apatite, Fe-Ti-oxide or Mn-carbonate were also excluded. As a consequence, the analyses done on the microprobe could not *a priori* be expected to duplicate analyses done by X-ray fluorescence.

5.5.1 Geochemical composition of millimeter-scale banding in sample SA-4

Analytical strategy

Figure 5.21 illustrates the thin section prepared from sample SA-4. The lower 3 dark laminae were analyzed. Additionally, the composition of 2 pale intervals was obtained. The dashed lines on the thin section mark the rows along which the laminae were analyzed. Rows 1 through 5 refer to these layers. Each of these rows is $\leq$ 1 millimeter thick. The circles show the positions of single analyses within one row. As shown in Figure 5.21, each layer was analyzed in 4 groups of 3 analyses each within one row. Within each group, the analyses were positioned with a slight overlap to extend the size of one coherent area to a maximum area of 1500 - 2000 micron^2.

Analytical Precision

Each point was analyzed for Si, Ti, Al, Fe, Mn, Mg, Ca, Na, K, Ba and Cr. Backgrounds were collected on the first analysis, and used for all analyses. Data reduction was done using the empirical correction factors for electron microprobe analysis of silicates and oxides of Bence and Albee (1968). The microprobe was calibrated using natural and synthetic mineral standards. The calibration was checked by analyzing a Kakanui hornblende standard. Table 5.5.1 lists the analyses and their standard deviations and the published composition of the hornblende. Additionally, 3

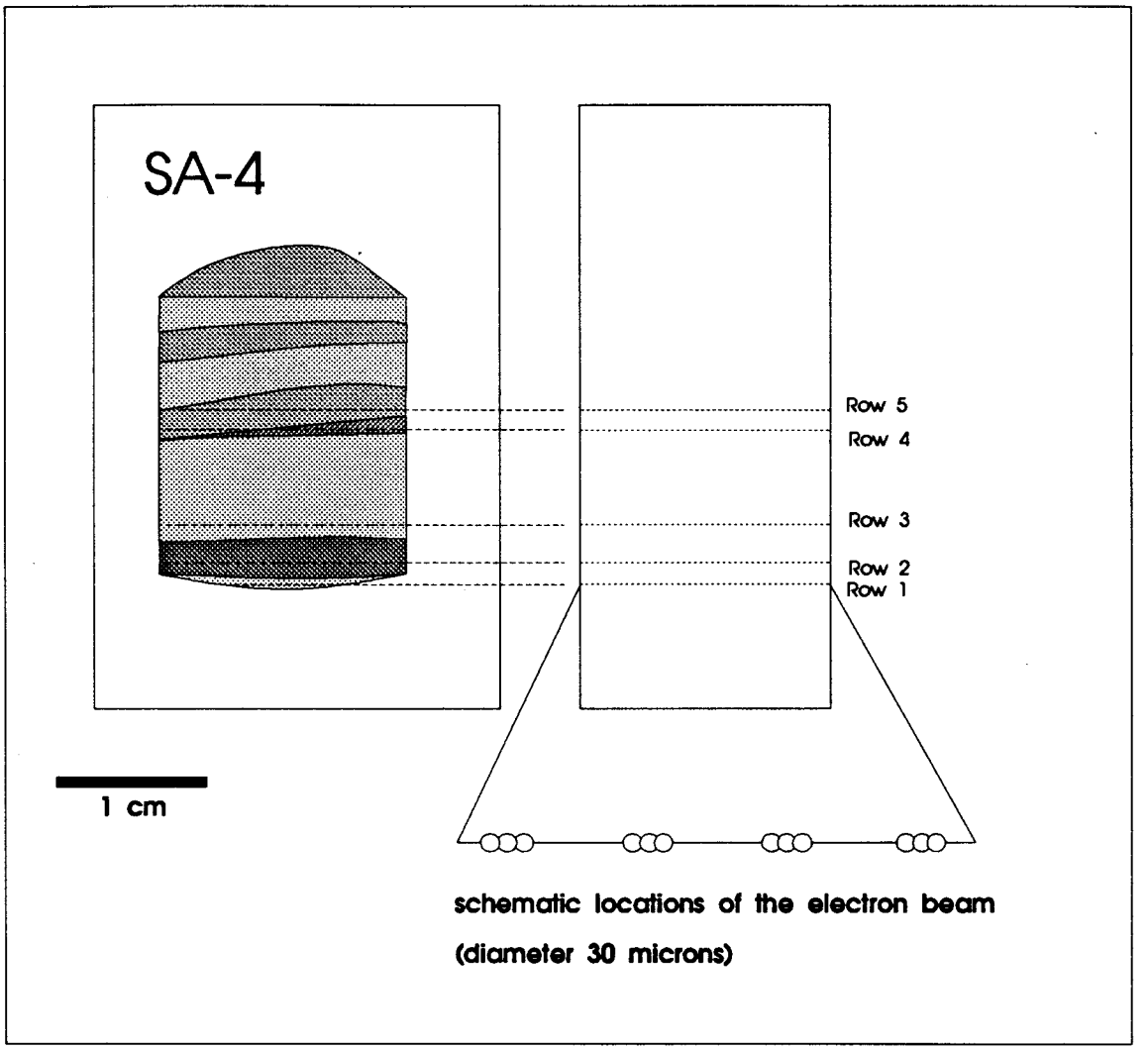

Figure 5.21: Illustration of the analytical setup for the analysis of the thin bands in thin section SA-4.

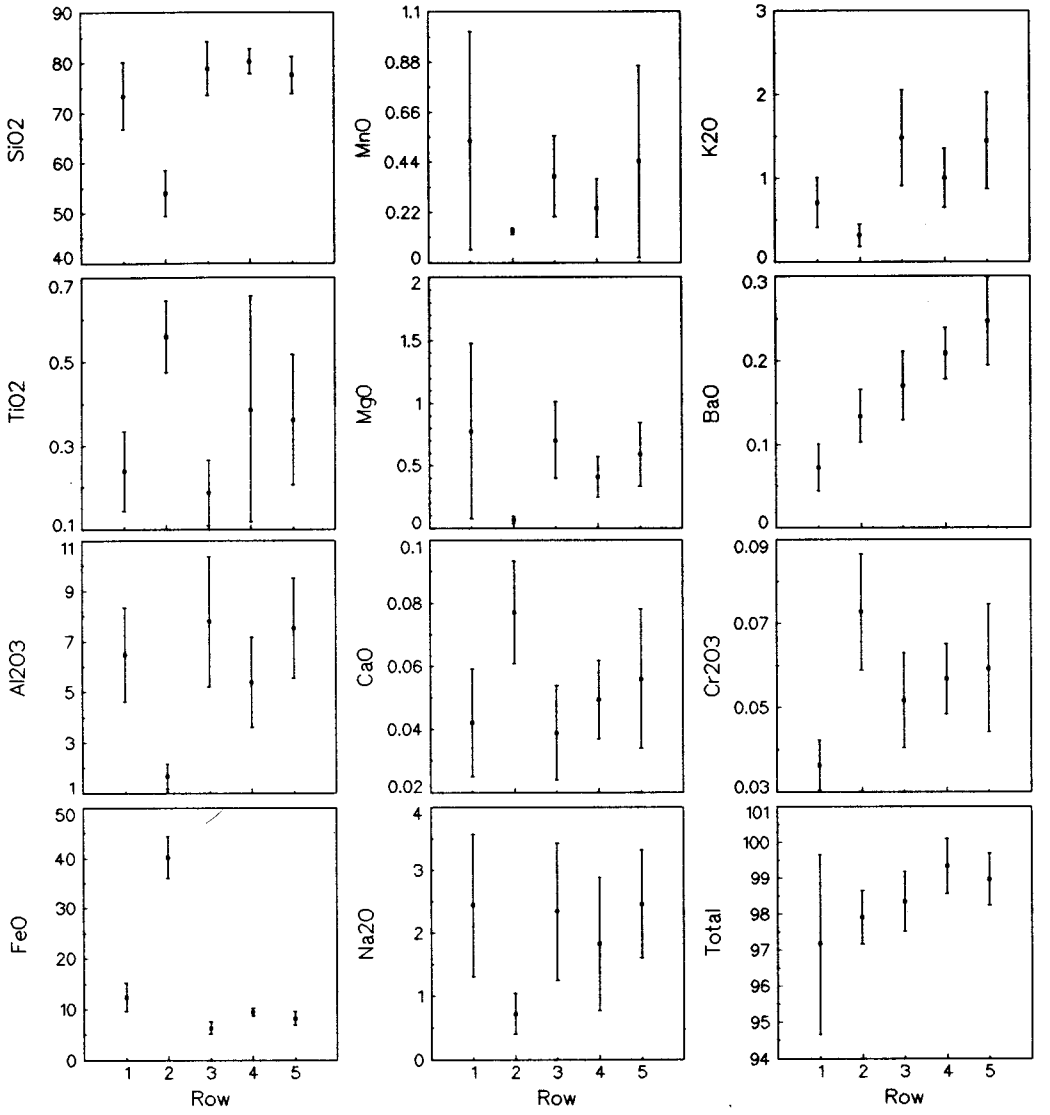

Figure 5.22: Mean abundances of element oxides (weight percent) per analyzed row and their standard deviations. Each data point is the mean +/- 1σ from 12 analyses on each row.

replicate analyses and their standard deviations of a selected point in sample SA-4 are listed.

Table 5.8: Replicate analysis of Kakanui Hornblende and replicate analyses on point #97 on sample SA-4

Element	Kakanui #1	Kakanui #2	Kakanui #3	Kakanui #4	Published value
SiO_2	40.04	40.16	40.08	39.98	40.37
TiO_2	4.64	4.76	4.60	4.60	4.72
Al_2O_3	14.2	14.22	14.09	14.20	14.30
FeO*	10.69	10.57	10.78	10.73	10.9
MnO	0.1	0.05	0.05	0.11	0.09
MgO	12.51	12.60	12.58	12.60	12.60
CaO	10.15	10.29	10.03	10.23	10.30
Na_2O	2.77	2.74	2.77	2.79	2.60
K_2O	2.17	2.14	2.13	2.13	2.05
Σ	97.30	97.61	97.21	97.43	97.93

* Total Fe expressed as FeO

Replicate analysis sample SA-4

Element	#97	#98	#99	Std. dev. of mean
SiO_2	77.85	77.14	77.20	+/- 0.32
TiO_2	0.24	0.23	0.24	+/- 0.004
Al_2O_3	7.42	7.45	7.39	+/- 0.024
FeO*	8.82	8.90	8.77	+/- 0.05
MnO	0.35	0.34	0.34	+/- 0.01
MgO	0.69	0.68	0.69	+/- 0.002
CaO	0.07	0.06	0.07	+/- 0.001
Na_2O	2.25	2.24	2.24	+/- 0.003
K_2O	1.47	1.47	1.48	+/- 0.002
BaO	0.26	0.27	0.32	+/- 0.03
Cr_2O_3	0.07	0.06	0.07	+/- 0.006
Σ	99.49	98.86	98.82	+/- 0.31

* Total Fe expressed as FeO

Results

For each set of 12 analyses per row, the mean and the standard deviation were calculated. Figure 5.22 lists the mean abundances of the 11 elements in each of the 5 rows, and their standard deviations. The data quality is variable, and clearly a result of the size of the phases analyzed by the beam. Unusually large error bars in one row when compared to the rest of the rows can best be explained by the presence of a larger phase within the area of one beam which consequently increased the standard deviation of the row. In general, it is one single, strongly deviating analysis which causes the large deviation. For example, one analysis in row 4 contained 1.12 weight percent TiO_2 in contrast to the other analyses of the same row which varied between 0.27 and 0.49 weight percent. Similarly, the large standard deviations of MnO and MgO in row 1 are the result of one very different analysis. The standard deviations for each element in the rows 3, 4 and 5 overlap. The rows 3, 4, and 5 may be regarded as compositionally similar, so that few interpretations can be made from the compositional trends of the mean abundances of these rows. In contrast, the compositional variation between rows 1, 2 and 3 clearly exceeds the internal compositional variation of each row. This allows for unequivocal interpretations of the inter-row relationships.

Inter-row variations

The oxide abundances were normalized to Al_2O_3 to avoid deceptive effects of dilution by a third element. Al_2O_3 is interpreted to represent the finest-grained detrital fraction in the sediment and was assumed not to have changed over the length of the thin section observed. Also, Al is usually immobile during diagenesis. For reference, the composition of the whole-rock XRF analysis of sample SA-4 corresponding to each elemental ratio is shown on the bottom x-axis of the diagrams in Figure 5.23.

Row 2 shows a distinct compositional difference to the rest of the rows. The oxides Ca, Ti, Cr and Fe, when normalized to Al_2O_3, show a maximum in the second

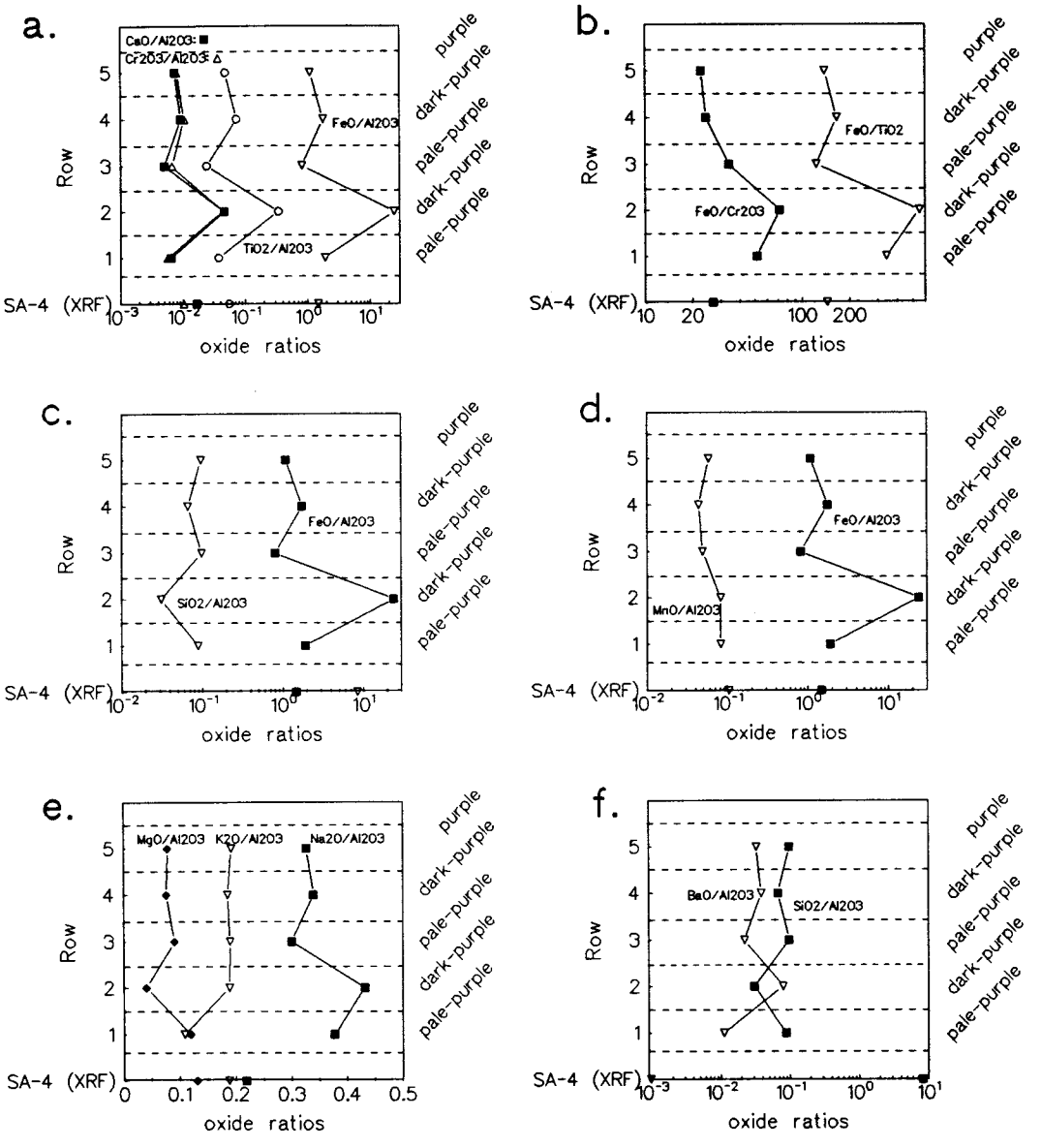

Figure 5.23: Al_2O_3 normalized oxide abundances of the row averages. The markers on the bottom x-axis show the reference abundance of the whole-rock analysis of sample SA-4.

row (Figure 5.23.a). The correlation of Ca with the metals Fe, Cr, and Ti precludes an interpretation of a metal oxide source as the single cause for the enrichment. The carrier phase of Ca is unclear. The totals for the analyses, in particular when recalculated for ferric iron, sometimes exceed 100 percent and thereby preclude the presence of significant amounts of carbonate (Table 5.5.2).

Table 5.9 Totals recalculated assuming all Fe to be present as ferric Fe

Row	new total
Row 1	98.55
Row 2	102.38
Row 3	99.10
Row 4	100.39
Row 5	99.38

The value of 102 percent in Row 2 indicates that Fe is not entirely present in the trivalent state. The presence of titaniferous magnetites having both valence states of iron supports this view. No sphene was detected under the microscope, but a few grains of prehnite are present in the lower dark-purple laminae. The abundance of Ca is generally very low, i.e., less than 0.08 percent. The addition of few % Ca from prehnite would have significantly affected the total amount of Ca present, but would have had a minor effect on the total Al abundances. The correlation of Fe with Ti and Cr reflects the presence of Cr-bearing Fe-Ti-oxides. However, Ti and Cr are probably not derived from the same source as Fe. This interpretation is based on the fact that the FeO/TiO_2 and the FeO/Cr_2O_3 ratios increase in row 2 (Figure 5.23.b). If Cr and Ti would have been associated with Fe in the component that caused the strong Fe-enrichment, no change in the FeO/TiO_2 and FeO/Cr_2O_3 ratio would be expected. It is therefore unlikely that the Fe-Ti-oxides are primary phases. The enrichment in FeO seen in the FeO/Al_2O_3 ratio in Figure 5.23 a. in row 2 can be interpreted as an increase in intensity of a primary source, since the average composition of sample SA-4, indicated by the XRF-analysis, equals the trend of rows 1, 3, 4, 5. The SiO_2/Al_2O_3 ratio of the

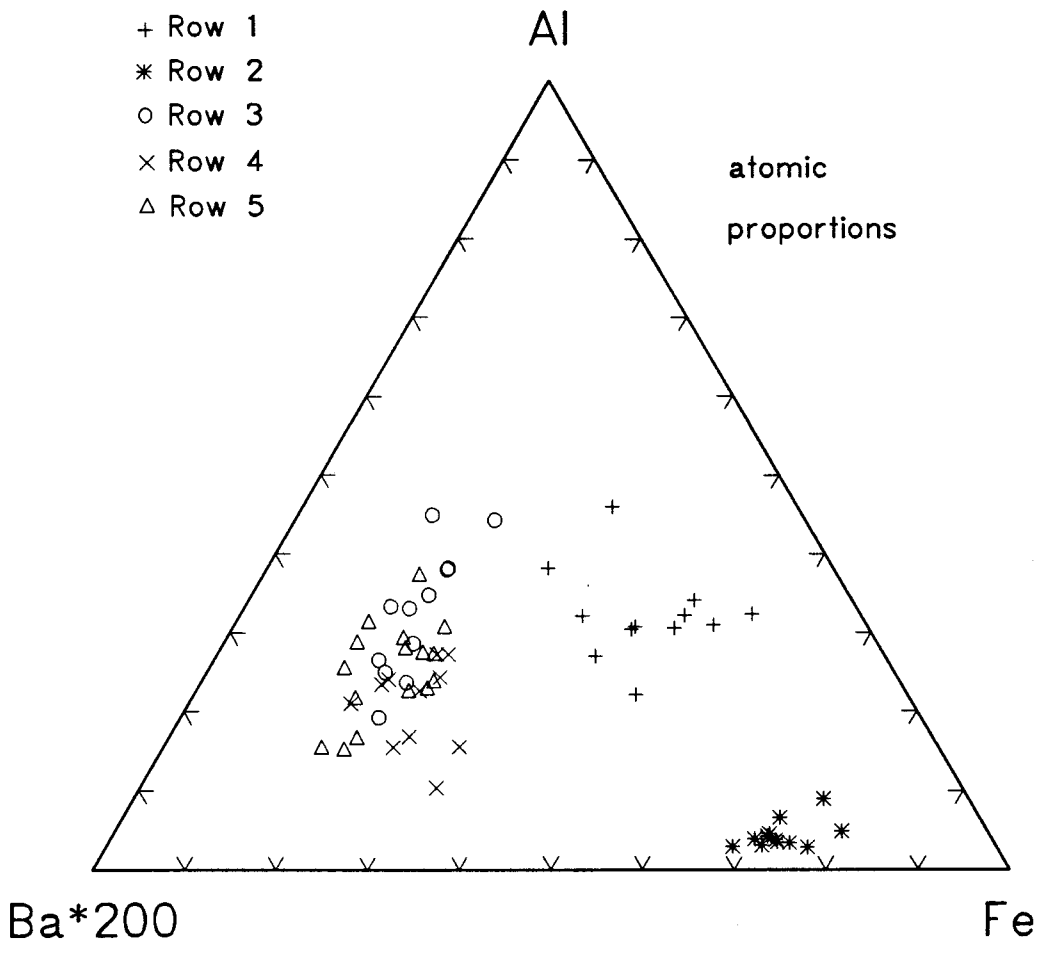

Figure 5.24: Ternary plot of the atomic proportions of Al, Ba, and Fe. Viewed from the Fe apex, the Ba*200/Al ratio of row 2 does not significantly differ form row 1, 3, and 4. The Fe enrichment is thus independent of Ba. The whole sample set is enriched relative to PAAS.

microprobe analyses from row 1 to row 5 is consistently lower than the XRF-analysis, and is explained as a result of the exclusion of radiolarian spheres (i.e. silica-rich domains) from the microprobe analyses. A negative SiO_2/Al_2O_3 excursion in row 2 corresponds to the FeO/Al_2O_3 peak (Figure 5.23.c). Therefore, a rapid decrease of the silica component in row 2 accentuated the FeO/Al_2O_3 peak. This observation supports the interpretation that three major components are present in this sample: (1) A clay component, represented by Al_2O_3, (2) a metal oxide component, represented by FeO, and (3) a siliceous, biogenic component, represented by SiO_2. Whereas the clay component can be viewed as relatively constant, the two other components vary antithetically. The fact that Fe is decoupled from the other major elements supports the interpretation of a hydrothermal source of Fe. This interpretation would be better constrained by the presence of a similar Mn-trend, but the MnO/Al_2O_3 ratio shows no peak in row 2, and is generally only slightly varying between the analyzed rows (Figure 5.23.d). Mn therefore appears to be closely associated with the aluminous fraction of the sample. The average MnO/Al_2O_3 ratio of the XRF-analysis indicates a higher Mn abundance in the bulk sample (Figure 5.23.d). The reason for this discrepancy is interpreted as the result of exclusion of large Mn,Ca-carbonates phases which occasionally occur as replacements of radiolarian spheres in this thin section.

Diagenetic mobility of redox-sensitive elements on the thin section-scale was not observed. The constancy of the MnO/Al_2O_3 ratio precludes mobility of Fe, because Fe mobilization requires even more reducing conditions for mobilization than Mn. Mn, however, seems to have been immobile. The alkaline elements Na and K do not vary significantly relative to Al (Figure 5.23 e.). Mg deviates in its behavior from these elements showing a distinct depletion in row 2 relative to Al. Whether this depletion is a diagenetic effect, or the reflection of a primary, lower Mg abundance in this band, cannot be answered with the present data. The BaO/Al_2O_3 ratio is also different from the rest of the elements. The association of Ba with Si can be a useful indicator to

identify biogenic Si (Martin and Knauer, 1973). This correlation does not hold true in the present case where Ba is apparently associated with the group of elements that were not diluted by the Fe-enrichment in row 2. The BaO/Al_2O_3 ratio of all 5 rows is antithetical to the SiO_2/Al_2O_3 ratio (Figure 5.23.f). The ternary diagram in Figure 5.24 shows the relationship between the 5 rows using the original analyses. It is apparent that the Fe-enrichment is independent of Ba, although Ba is enriched relative to a Post-Archean Average Shale (PAAS) composition. Taking the Ba/Al ratios of rows 1, 3, 4 for reference, Ba is enriched in row 2 and slightly depleted in row 1. This variation in Ba may reflect some diffusion of Ba from row 1 into row 2.

5.5.2 Geochemical profile of Mn-nodule in sample GI-8

Analytical strategy

Figure 5.25 is an illustration of the Mn-nodule made from a backscattered electron image. The length of the nodule is 0.87 millimeter. The feature and the surrounding matrix can be divided in several units. From bottom to top these are: The "standard" matrix of the red argillite of sample GI-8; the pale halo at the bottom of the nodule; the outer nodule; the inner nodule known as the "bow-tie"; the core. The diagonal line in Figure 5.25 shows the location of the profile along which 32 points were analyzed for the major element analyses plus Ba and Cr. Figure 5.26 illustrates the detailed locations of the electron beam for each analysis according to the coordinates of the sample on the microprobe stage. The lines separate the different units of the nodule. The 15 kV electron beam had a diameter of 30 microns, the current used was 25 nA.

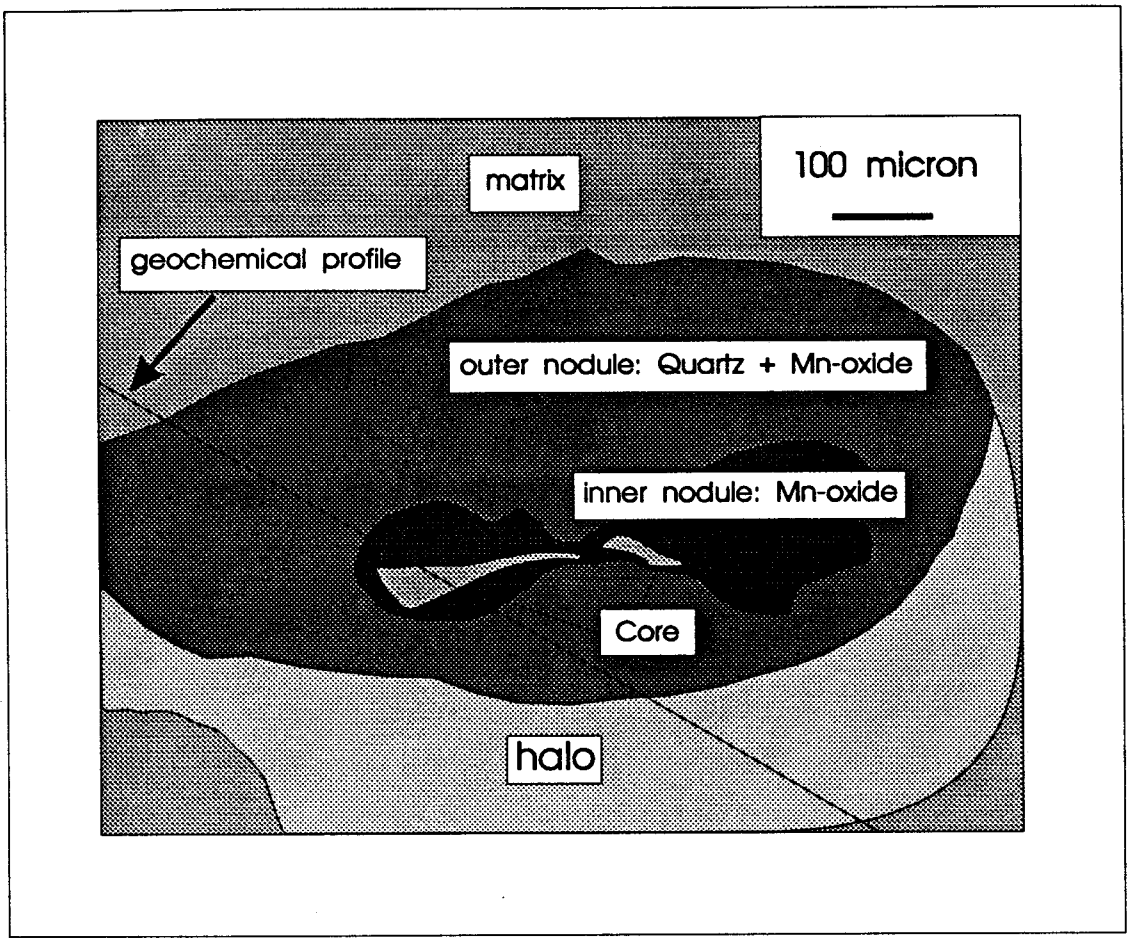

Figure 5.25: Illustration of Mn-nodule and surrounding matrix in thin section GI-8. The diagonal line marks the geochemical profile.

Analytical precision

The microprobe calibration is the same as described in section 5.5.1. Additionally, three (3) replicate analysis were obtained for the bow-tie. Table 5.5.3 lists the measured abundances, and the standard deviations from the mean.

Table 5.10: Replicate analyses in bow-tie of Mn-nodule

	Analysis #1	Analysis #2	Analysis #3	Std. dev. of mean
SiO_2	15.28	15.42	15.32	+/- 0.054
TiO_2	0.7	0.71	0.63	+/- 0.035
Al_2O_3	7.43	7.43	7.49	+/- 0.028
FeO*	9.42	9.58	9.64	+/- 0.092
MnO	47.23	47.14	46.59	+/- 0.282
MgO	6.24	6.25	6.29	+/- 0.021
CaO	1.63	1.61	1.65	+/- 0.016
Na_2O	0.03	0	0	+/- 0.014
K_2O	0.04	0.01	0.02	+/- 0.012
Cr_2O_3	0.04	0.02	0	+/- 0.016
Σ	88.04	88.16	87.64	+/- 0.22

* Total Fe expressed as FeO

The data are background-corrected. Two sets of reference backgrounds were collected, one for the matrix, and one for the nodule. Analyses of the matrix and the halo are corrected according to the backgrounds collected on the matrix, analyses of the nodule are corrected for the backgrounds collected on the nodule. Bence-Albee procedures were used for on-line data reduction.

Results

Figure 5.27.a and 5.27.b summarize the chemical variation of each element oxide across the nodule and the matrix. For reference, the abundance of each element obtained by whole-rock XRF analysis of sample GI-8 is shown with the arrow on the

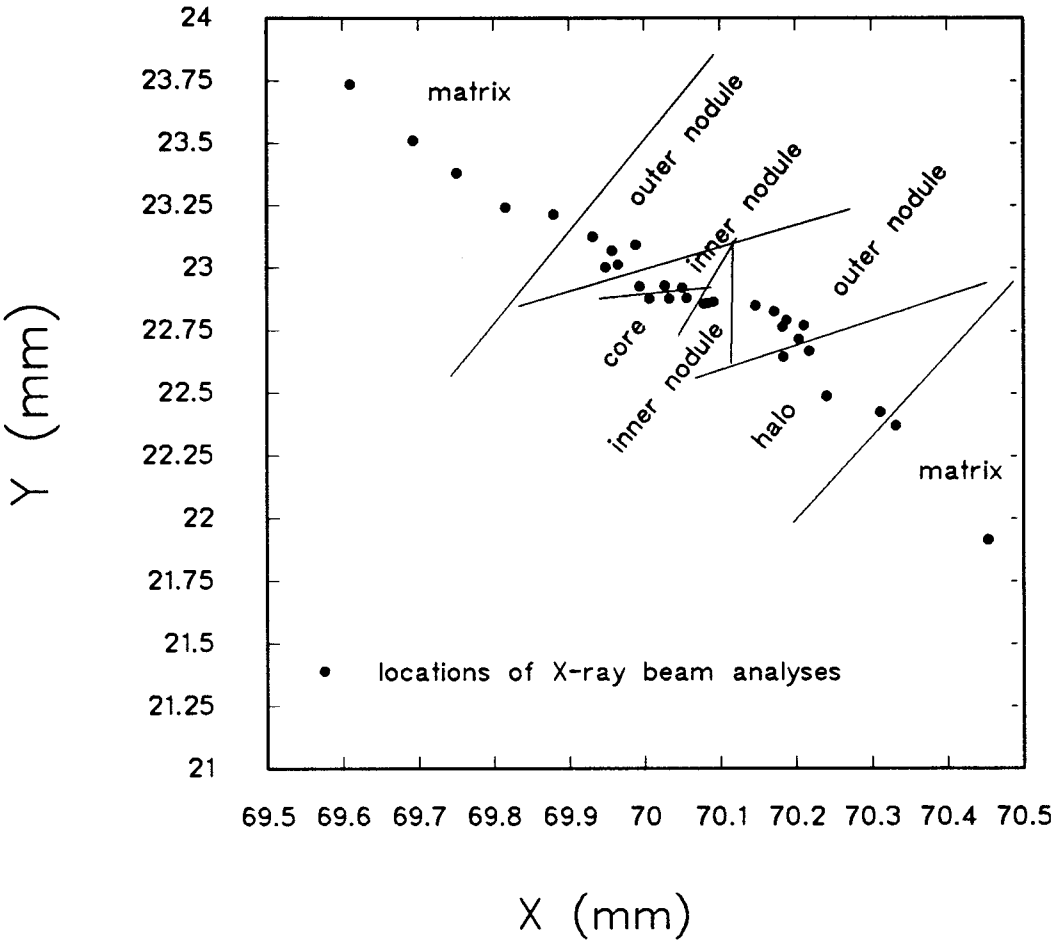

Figure 5.26: Location of X-ray beams along the geochemical profile. The lines represent the boundaries between the subunits.

left side of the profile. The elemental distribution across the profile is very symmetrical. The abundances of SiO_2, MgO, CaO, and MnO are relatively constant in the matrix. The FeO and TiO_2 peak in the left matrix interval is attributed to an Fe-Ti-oxide dominating the analyzed area of this point. The outer margin of the nodule marks a sharp compositional boundary. MnO increases from less than 2 weight percent to over 40 weight percent. Mn hereby dilutes the abundances of all elements except for Ca which also increases at the boundary. The increase at this boundary is equal on both sides of the nodule. The Mn abundance symmetrically decreases again to the interior of the outer nodule, corresponding to an increase in the Al_2O_3 and Na_2O content. The CaO behaviour is inconsistent with MnO in this interval. At the boundary to the inner nodule ("bow-tie"), MnO increases again, accompanied by CaO, FeO, TiO_2, and Cr_2O_3. MnO abundances increase to over 60 weight percent. The core of the nodule is very different from this composition. Whereas MnO drops to the center, FeO and CaO achieve their peak abundances together with MgO and Al_2O_3.

The chemical composition of the halo is not indicative of a particular trend. It was assumed that the pale habit of the halo observed under transmitted light would indicate metal depletion accompanied by corresponding metal enrichment within the nodule. Based on the analysis obtained on the halo, this assumption cannot be confirmed. FeO remains elevated in this interval, and MnO returns to the level of the original matrix composition. Strong variations of Al_2O_3 are accompanied by K_2O and Na_2O, indicating a felspar and clay component. Contrasting trends between SiO_2 on one side, and Al_2O_3, K_2O, and Na_2O on the other side indicate two different sources. The variation in this interval is therefore interpreted as the interplay of the biogenic SiO_2 and the detrital component.

The bottom diagram of Figure 5.27.b shows the variation of the oxide totals across the profile. The interval of the inner nodule and the core mark a distinct "valley". The oxide abundances of the core add up to a maximum of only 84 weight

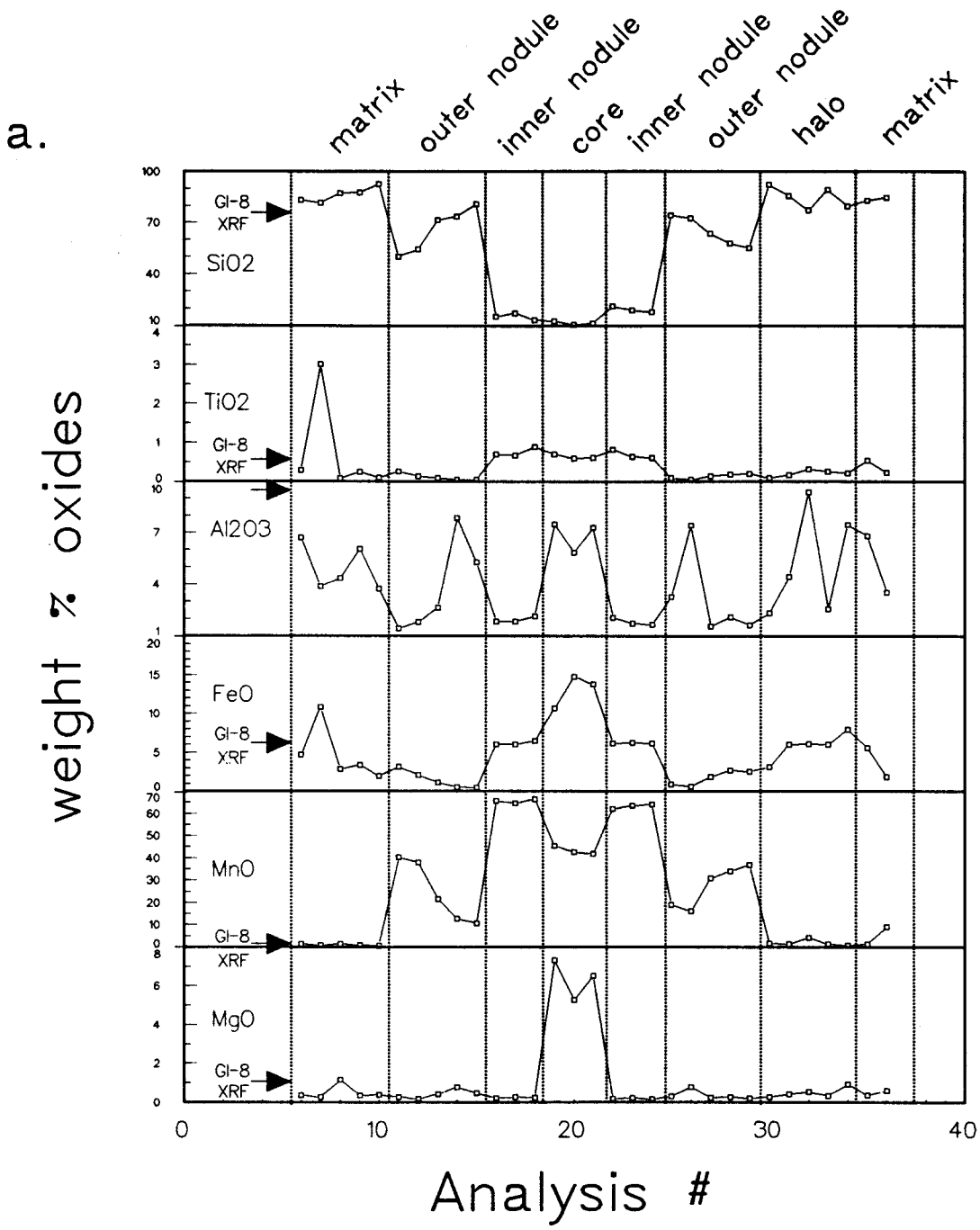

Figure 5.27.a: Summarized element oxide abundances across the nodule. The arrows on the left side of the figure show the abundances observed in the whole-rock XRF analysis of sample GI-8.

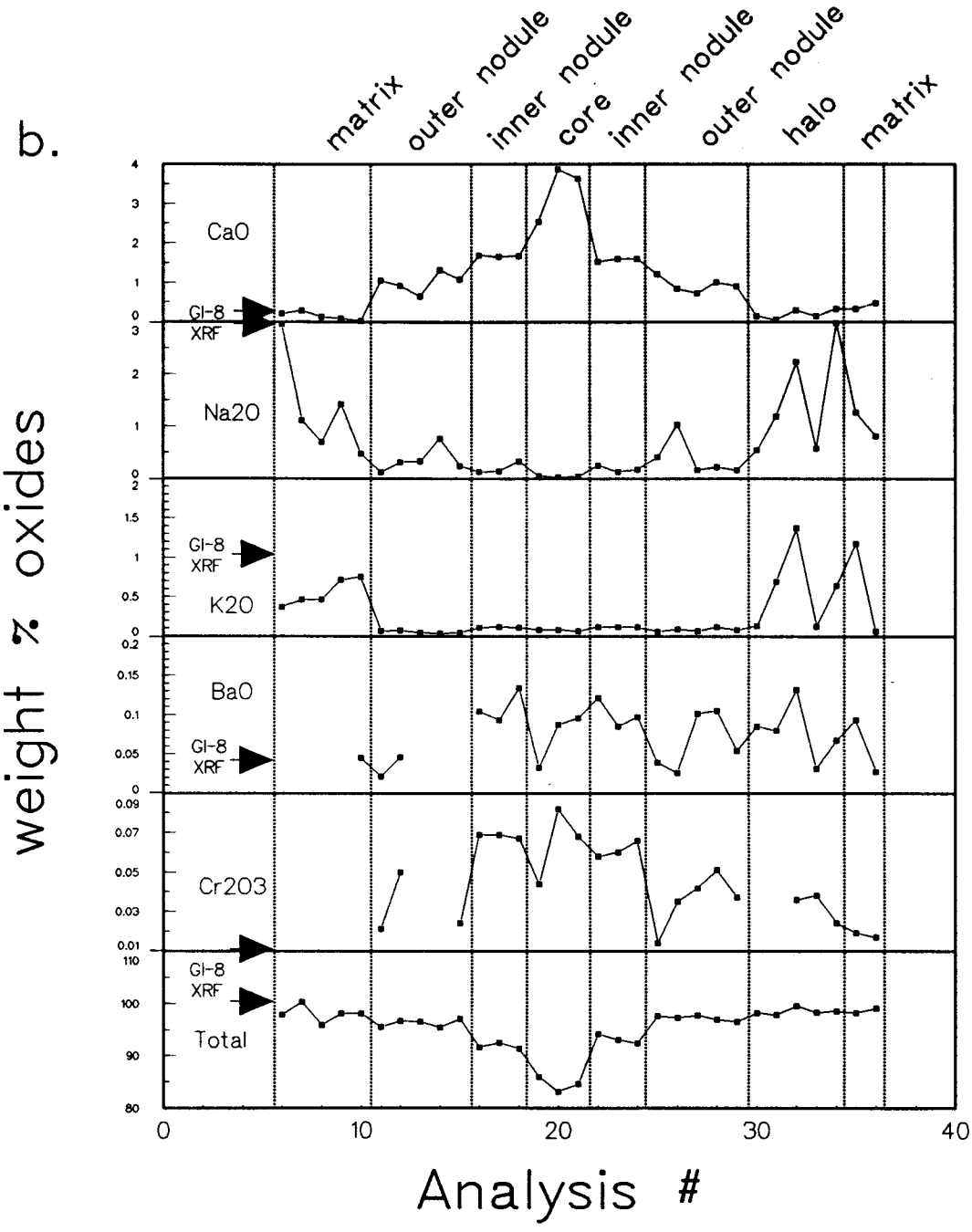

Figure 5.27.b: Summarized element oxide abundances across the nodule. The arrows on the left side of the figure show the abundances of the whole-rock XRF analysis of sample GI-8.

percent. Since energy dispersive spectra of the core showed that no other element is present in significant abundances, the deficiency is probably due to significant amounts of CO_2 and/or H_2O that cannot be observed directly by the electron microprobe. Although the low totals correspond to an increased abundance of CaO, which is suggestive of CaO being present as a carbonate phase, the resulting totals including CO_2 for the carbonate formation still do not exceed 85.2 weight percent. The presence of a carbonate is also not confirmed by the observation under transmitted light: The interior of the nodule appears completely opaque. On the backscattered electron image, the core appears darker (see Figure 4.5), which indicates a lower mean atomic number of the elements present in the core when compared to the surrounding inner nodule. Unfortunately, this does not give any unique information on the phase(s) present. Alternatively, therefore, the presence of H_2O cannot be excluded as a contributor to the observed deficit (i.e. about 16 weight percent).

Different oxidation states of Mn and Fe can account for some of the deficits of the oxide totals in the core and the inner nodule. Totals for the inner nodule reach only a maximum of 95 weight percent. In the inner nodule, the Mn is present in an opaque phase, and clearly forms an oxide. Most Mn present in naturally occurring Mn oxides is in the tetravalent state (Murray et al., 1984). Therefore, Mn which is expressed in the analyses as divalent MnO had to be recalculated to MnO_2. The amount of the oxide totals had to be corrected for the new MnO_2 value. Figure 5.28 illustrates the recalculated total oxide abundances of the analyzed points assuming all Mn is present as MnO_2. The recalculated totals of the analyses of the inner nodule and the outer margin of the outer nodule exceed 100% by more than 5 weight percent, indicating that MnO cannot be present exclusively as MnO_2. It is therefore concluded that part of the Mn is present as Mn^{2+} or even in the rare Mn^{3+} form. The identity of the Mn-phase can only be speculated with the available data. Clearly, X-ray diffraction data of the nodule would help to resolve this problem. The minimum amount of Mn_2O_3 required to satisfy

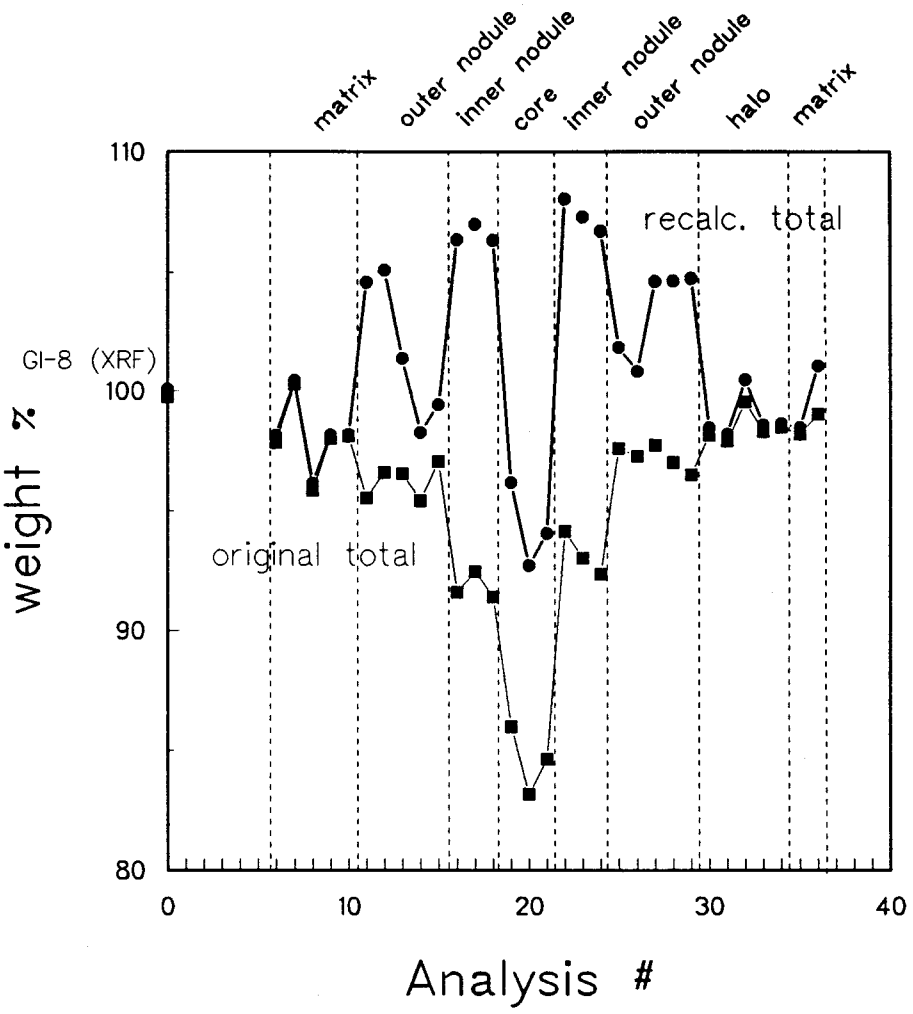

Figure 5.28: Geochemical profile showing the original totals and the recalculated totals assuming all MnO is present as MnO_2.

the requirement of 100 weight percent total is 13 percent of the measured MnO abundance assuming only Mn^{3+} and Mn^{4+} are present. The minimum amount of MnO necessary in order not to exceed the 100 weight percent limit, is 8.7 percent of the measured MnO abundance. Possible phases that contain such large amounts of trivalent or divalent Mn include silica-poor braunite ($3Mn_2O_3 \cdot Mn_{0.62}Fe_{0.08}Ca_{0.3}SiO_3$; Maynard (1983), p.126), but this phase has never been reported in recent and ancient Mn-nodules (Piper et al., 1984), or todorokite, the main Mn-oxide contained in deep-sea Mn-nodules, which is known to host minor amounts of Mn^{3+}, and Mn^{2+} for reasons of charge compensation (Burns and Burns, 1977b). The possibility of the presence of phases containing only divalent Mn has to be precluded, since divalent Mn in natural systems requires additional components to form minerals. This is the case for silicates, e.g., chlorite, for rhodochrosite, which requires CO_2, or MnS_2, which requires sulfide for the formation. In every case, the original oxide totals in all analyses of the inner nodule are already close to 100% (Figure 5.28), which precludes the presence of significant amounts of either CO_2 or sulfide that would be necessary to form a phase containing divalent Mn. The degree of reflection of the mineral phase under backscattered electron imaging precludes this phase as being a silicate. On a similar basis, it must be argued that at least part of the Fe present in the nodule analyses is present as Fe^{3+}, and consequently would have to be recalculated to Fe_2O_3. This would also increase the original abundance of the totals. However, based on the data present, it is not possible to uniquely budget the different oxidation states of Fe and Mn, because the relative amounts of the different phases with these elements in different oxidation states are not known. Also, since chlorite may occur in the detrital component and holds divalent and trivalent Fe, this further complicates an assessment of the Fe^{2+}/Fe^{3+} ratio in the sample. In conclusion, different oxidation states of Mn and Fe can only partially resolve this problem. CO_2 and H_2O in the core are suggested to be responsible for the measured low total-abundances in the core of the nodule.

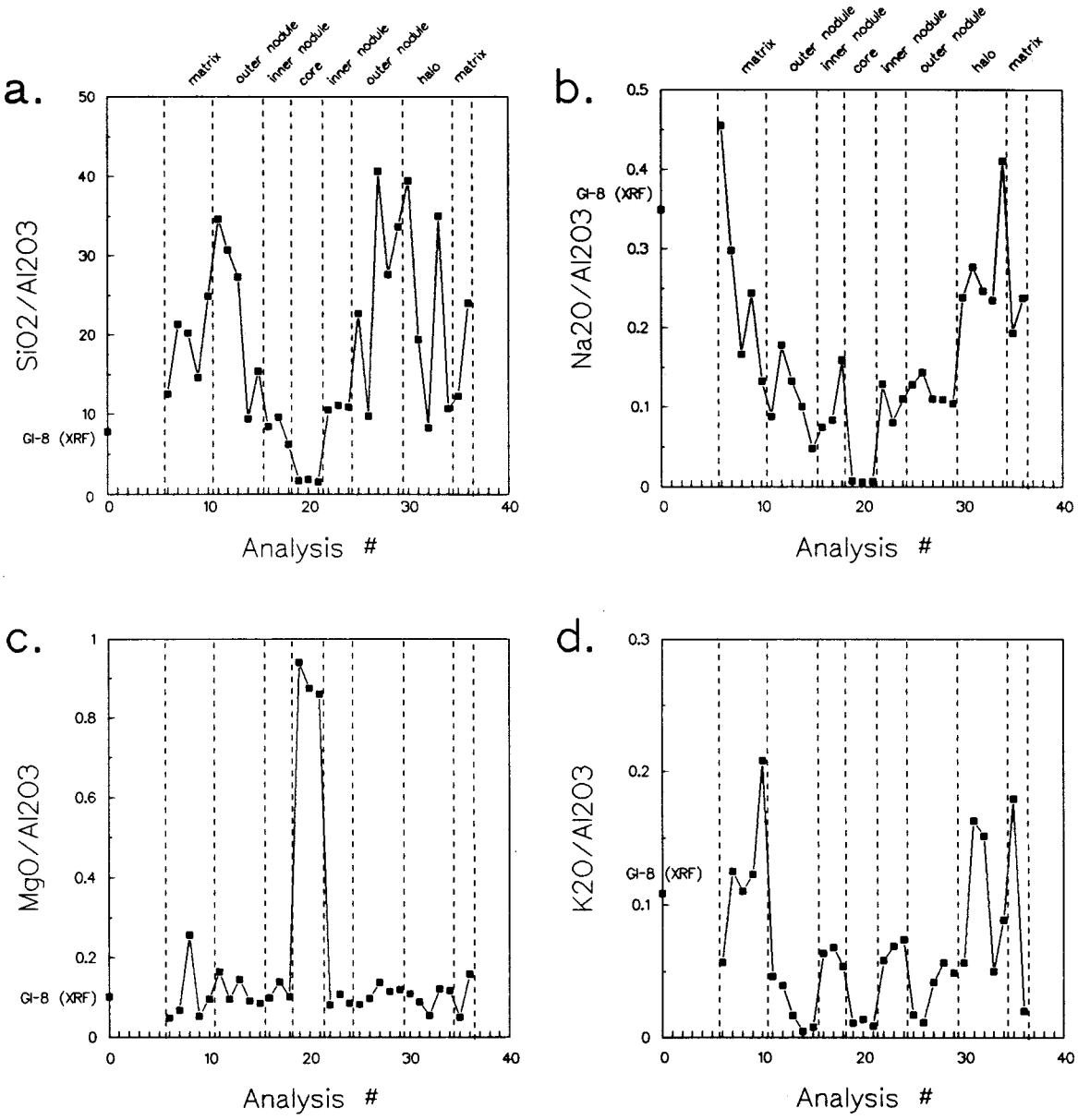

Figure 5.29: Al_2O_3-normalized oxide abundances across the nodule. For reference, the XRF composition of the GI-8 whole-rock is shown on the left y-axis.

In order to examine the relative enrichments and depletions of various elements and to further establish element groupings, the element oxides were normalized to Al_2O_3 (Figure 5.29). For reference, the Al_2O_3-normalized whole-rock composition of GI-8 which hosts the nodule, is plotted on the left side of the diagrams. Normalized to Al_2O_3, most element distributions retain their strong symmetry across the nodule. Except for the halo and matrix, all subunits show sharp, compositional boundaries. The normalization to Al_2O_3 results in a negative excursion for each element ratio in the core relative to the inner nodule, except for MgO/Al_2O_3. This consistency can be explained in two ways: (1) An increase in Al_2O_3 as a result of the additional presence of a Mg-containing aluminous phase in the core. (2) Diagenetic depletion of the elements SiO_2, Na_2O, K_2O, MnO, FeO, CaO, and *even* TiO_2 from the core. The likelihood of this latter case in which all these elements were mobilized and diffused out of the core, seems low. Therefore, the first mechanism is given preference, although limited diffusion of some elements cannot be excluded.

The SiO_2/Al_2O_3 ratio demonstrates a distinct depletion of SiO_2 in the inner parts of the nodule, being sharpest in the core (Figure 5.29.a). The matrix and the outer nodule have higher SiO_2/Al_2O_3 ratios relative to the whole-rock XRF analysis of sample GI-8, whereas the core has a lower ratio relative to the whole-rock XRF analysis. Since this lower SiO_2/Al_2O_3 ratio in the core region cannot balance the apparent excess SiO_2 in the outer parts (Figure 5.29.a), it appears that the nodule has formed in a silica-rich, or respectively Al_2O_3-poor part of the sample. Possibly, more radiolarian shells were present here. This view is supported from the observations of other nodules under transmitted light that showed accumulations of radiolarians in oxide-rich (possibly Mn-oxide) domains. The small peaks in the outer nodule can be interpreted to indicate minor silica mobility outwards from the core, but these peaks do not account for the difference in the SiO_2/Al_2O_3 ratios.

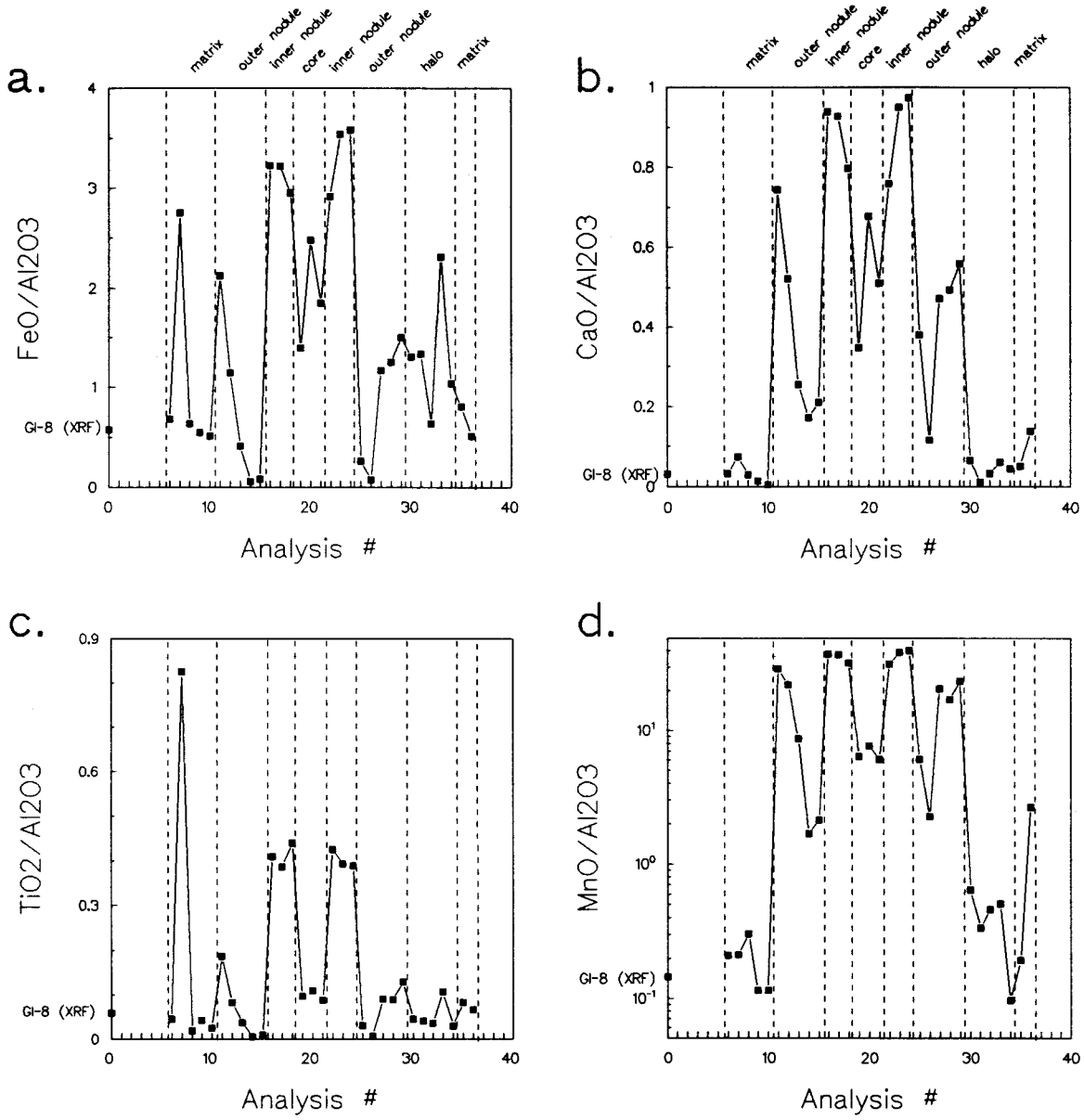

Figure 5.30: Al_2O_3 **normalized oxide abundances across the nodule. For reference, the XRF composition of the GI-8 whole-rock is shown on the left y-axis.**

The alkaline elements Na and K are also depleted in the nodule, but when examined in more detail, their trends differ (Figure 5.29.b and 5.29.c). Relative to the whole-rock, the Na-depletion is more prominent than the K-depletion. Both elements show an excess abundance in the surrounding halo and matrix. Possibly, the deficit of each element is balanced by an equivalent surplus in the surrounding matrix. The K_2O/Al_2O_3 ratio shows two distinct peaks in the inner nodule, which contrasts to the depletion in the immediately adjacent area. It may be that the peaks are the result of diffusion of K from these adjacent areas.

The FeO/Al_2O_3 ratio in the core is lower compared to the adjacent areas, and suggests a stronger clay component in this interval. At the margin from outer to inner nodule, FeO is depleted below the whole-rock GI-8 reference level (Figure 5.30.a). Since corresponding excess ratios exist at the outer margin of the outer nodule as well as in the inner nodule, the sink for this depletion cannot be exactly defined. CaO/Al_2O_3 (Figure 5.30.b) shows a generally similar trend to that of FeO/Al_2O_3 in the outer nodule, inner nodule, and the core. The ternary diagram Fe-Ca*5-Ti*10 confirms this relationship, but furthermore reveals a strong Ca-enrichment at the outer margin of the nodule, which is unparalleled by Fe (Figure 5.31.c). Besides the high MnO abundances, it is the CaO-enrichment that distinguishes the Mn-nodule from the halo and the matrix. This effect becomes apparent in a ternary plot of Al-Ca*5-Si/10 where a continuous Ca-enrichment relative to Si occurs from the matrix to the interior of the nodule (Figure 5.31.a). The data do not allow one to determine whether this enrichment is primary or secondary.

The MnO/Al_2O_3 ratio shows an enrichment at the outer margin similar to the CaO/Al_2O_3 ratio, and also a similar minimum at the boundary of the outer nodule to the inner nodule (Figure 5.30.d). An examination of the relationship of Ca to Mn showed that the Ca/Mn ratio in the strongly Mn-enriched parts of the nodule is constant (Figure 5.31.b). This suggests a common source of Mn and Ca, although in the present

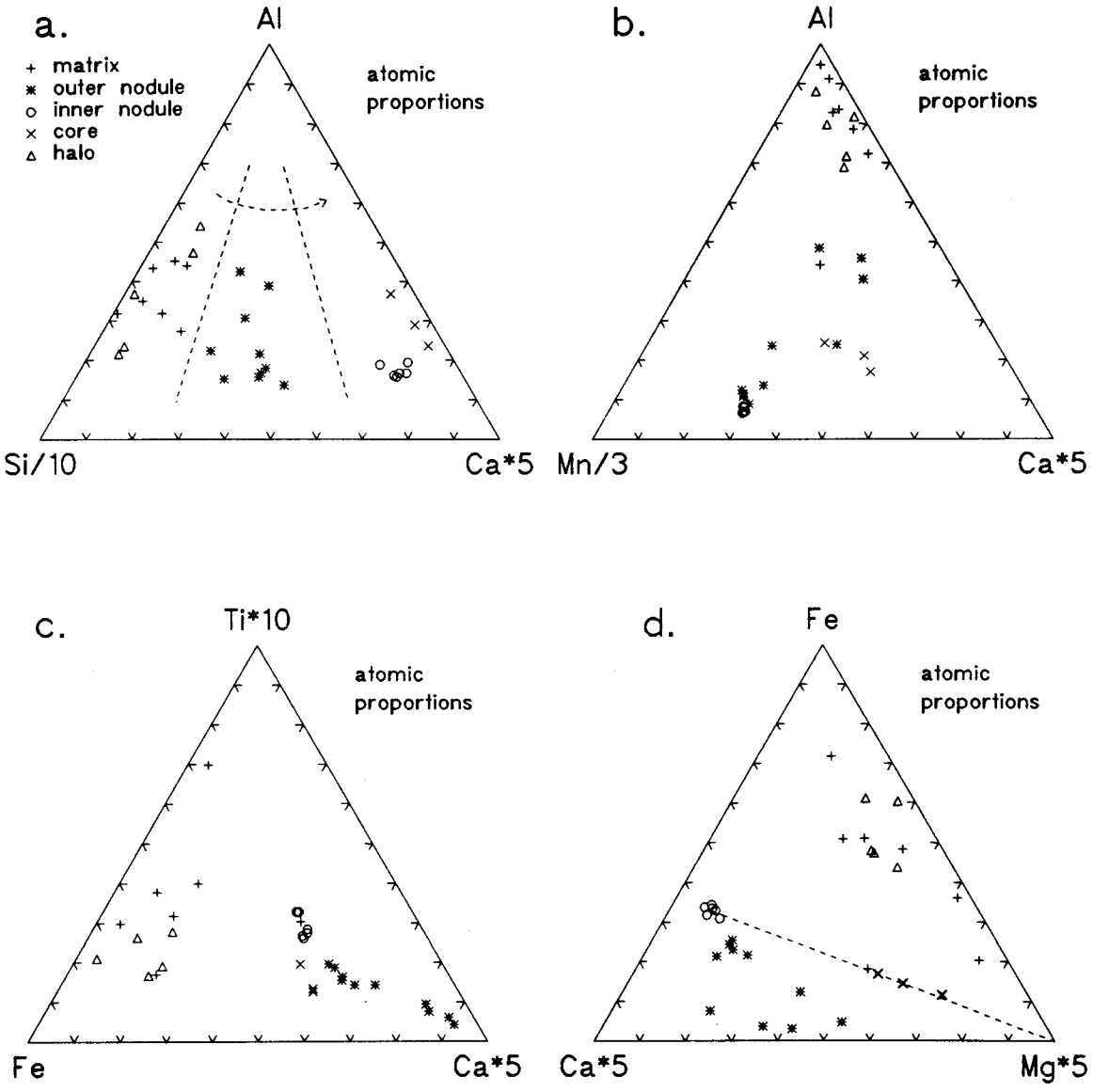

Figure 5.31: a. Ternary plot demonstrating the calcium enrichment of the Mn-nodule. b. Ternary plot of Al, Ca, and Mn. The Mn/Ca ratio in the strongest enriched parts of the nodule is constant. c. Ternary diagram demonstrating that the Ca enrichment is discriminating the nodule from the matrix. d. Mg is uncorrelated to Ca and Fe, and is independently enriched relative to the adjacent inner nodule.

state, the two elements do not share the same carrier phase. It may be speculated that there was a predecessor of MnO_2 in which Ca^{2+} and Mn^{2+} coexisted. Possibly, this was a Ca,Mn-carbonate. Under later, more oxic conditions, the Mn was oxidized, and the carbonate phase became unstable. The incompleteness of this oxidation process is reflected in the totals that exceed 100 weight percent when MnO is recalculated to MnO_2. The sink of the CO_2 is uncertain, but possibly reflected in the low totals of the core.

The MgO/Al_2O_3 ratio is relatively constant across the nodule with the exception of a sharp increase in the core (Figure 5.29.c). This ratio resembles the ratio derived from the whole-rock XRF analysis of sample GI-8 and suggests that in all parts, except for the core, Mg is associated with the detrital clay component. It is assumed that the MgO/Al_2O_3 peak in the core indicates a primary feature, because bulk sample and adjacent parts show no evident depletion. The association of MgO with low totals in the core supports an interpretation of either a hydrous or a CO_2-bearing phase as the Mg-carrier. MgO, CaO, and FeO together show maxima in the core of the nodule (Figure 5.27.a and b). The ternary diagram Fe-Mg*5-Ca*5 examines this relationship (Figure 5.31.d). The dotted line connecting the analyses of the core and the inner nodule indicates independent Mg-enrichment. This enrichment is generally independent of any of the elements analyzed. The origin of the MgO peak in the core remains unclear. Possibly, under high magnifications a distinct phase might be identified in the core. Single phases could then be analyzed with a narrower electron beam than used in this current procedure.

5.5.3 Red-green color transitions: GI-3

Analytical strategy

Figure 5.32 illustrates two overlapping thin sections of sample GI-3, which cover the color transition and a diffuse rhodochrosite band at the bottom of the green layer. Similar to sample SA-4, points were selected along rows parallel to bedding. Eleven (11) points within one row were selected in order to obtain the average composition per row. 5 rows were analyzed in the red part and 4 rows in the green part. The total length of the analyzed interval was 4.7 centimeters. The analyses were clustered in order to increase the analyzed area. The electron beam diameter was 30 microns, the current used 25 nA. The maximum counting-time per element was set to 40 seconds, or to a maximum analytical variation of 0.2%, respectively. Before storage in a points table, selected points were checked for their qualitative composition with the energy dispersive spectrum; if the point did not show almost pure SiO_2, then the position was stored in the points table for later analysis (still 3 analyses out of 99 were apparently quartz analyses). Whole-rock XRF-analyses were present for a red bed located 40 centimeter below these thin-sections (sample GI-2: red argillite), and the adjacent green layer above (GI-4: green argillite). The data of these two analyses are plotted on the right and the left y-axis as reference points on the distance versus composition diagrams (Figure 5.34 -36).

Analytical precision

The secondary standard was a Kakanui amphibole. Two analyses of an identical spot on the thin section GI-3 were obtained in order to estimate a typical variation due to counting variation. Table 5.5.4 lists the element composition of point #10 (in the green part of thin section GI-3).

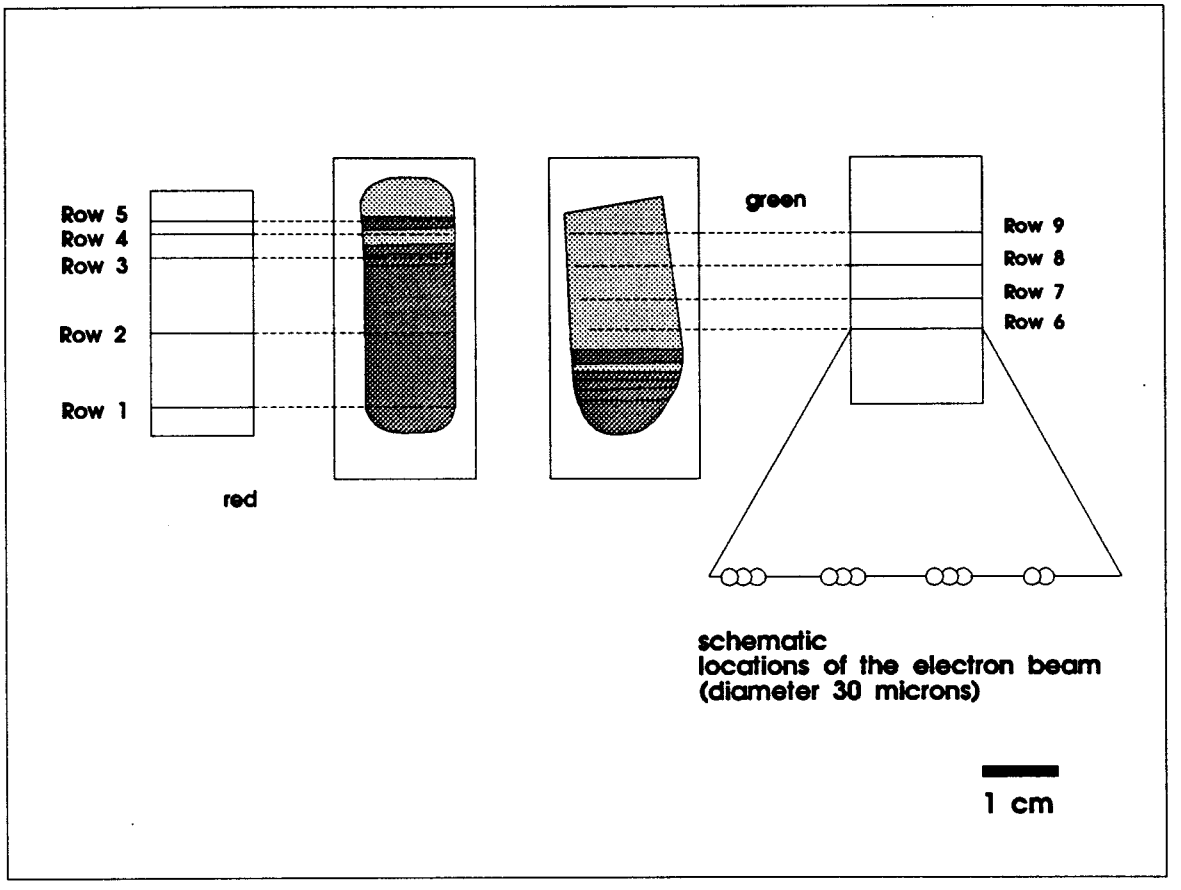

Figure 5.32: Illustration of thin section sample GI-3 and the analytical setup. The thin, green band in the top part of the red argillites serves as the marker horizon.

Table 5.11: Composition of replicate analyses point #10 and standard deviation

Element	#1	#2
SiO_2	45.59	45.72
TiO_2	0.06	0.02
Al_2O_3	3.05	3.00
FeO*	5.23	5.11
MnO	22.39	22.66
MgO	1.1	1.07
CaO	1.14	1.11
Na_2O	0.05	0.03
K_2O	0.04	0.05
BaO	0.13	0.10
Cr_2O_3	0	0.02
Σ	78.68	78.89

* Total Fe expressed as FeO

Backgrounds were collected on the first analysis of this sequence and automatically used for all subsequent analyses. For each set of 11 analyses in each row, the mean and the standard deviation were calculated. Figure 5.33 shows the mean abundances of the 11 elements plus the total abundances in each of the 9 rows, with their standard deviations. Although the standard deviations for most elements are too large to permit an interpretation of detailed trends *within* the green and the red part based on element abundances alone, SiO_2, MnO, and CaO show a compositional change at the color boundary that is larger than the compositional variation within the respective rows. Analyses of the red argillite generally have high totals of > 94 weight percent, but analyses of the green part, in particular Mn-rich samples have totals of only 70 - 80 weight percent. The weight percentage CO_2 necessary for the formation of pure $MnCO_3$ was calculated from the measured MnO abundance assuming rhodochrosite is the only Mn-carrier. The recalculated total weight percentage is shown in Figure 5.34. In some cases, the new total exceeds 100 weight percent by a considerable amount (e.g., 7 weight percent in GI-4). This indicates that Mn is not solely represented by rhodochrosite and may be contained in other phases (e.g., chlorite, spessartine). The

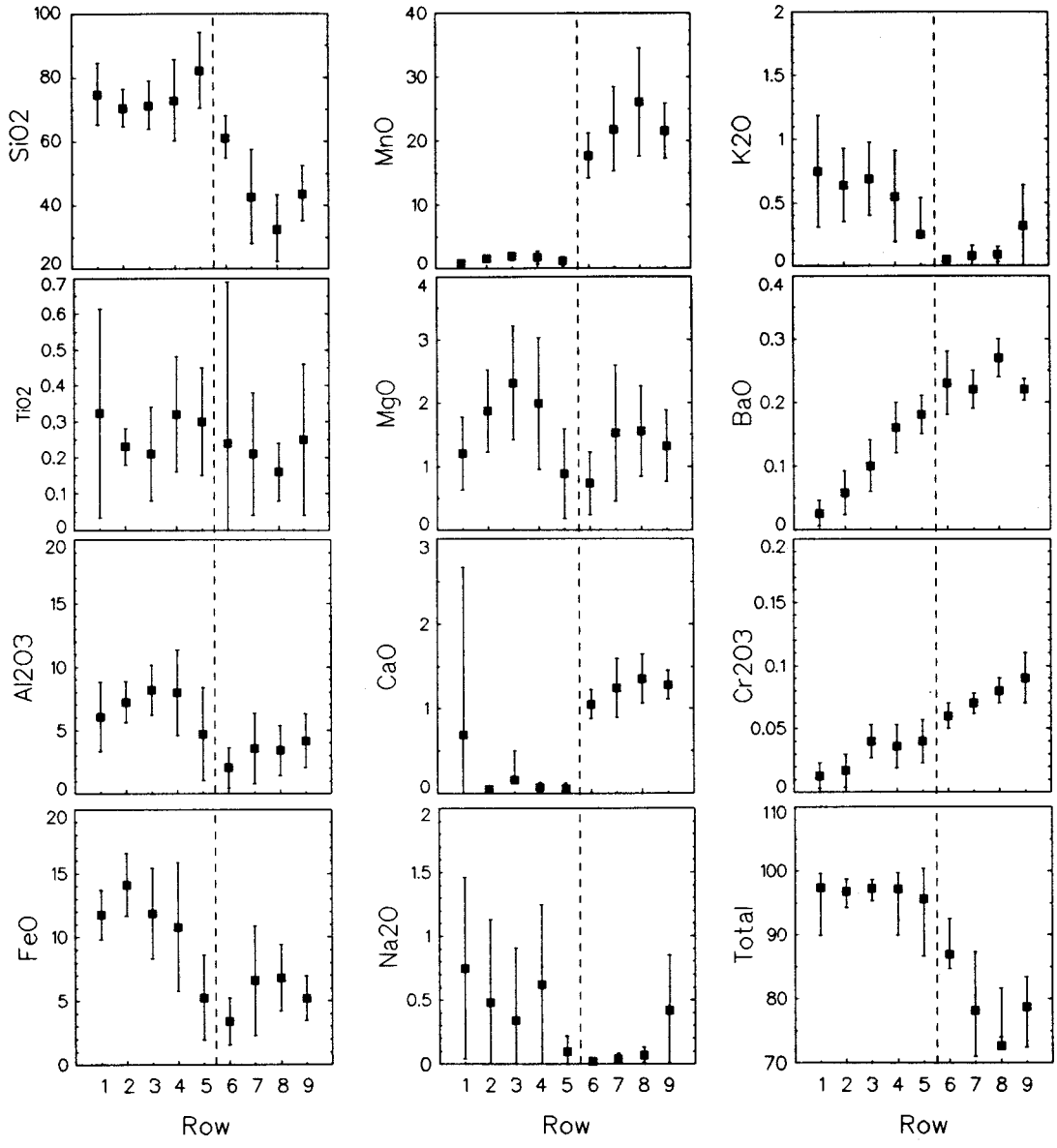

Figure 5.33: Mean abundances of element oxides per analyzed row and their standard deviations. The main color boundary occurs between rows 5 and 6 (see Figure 5.32).

totals in the range of 95 weight percent in the red argillite indicate that the presence of volatiles, most likely CO_2, hydroxide and water from the Mn- carbonate and hydrous silicates.

Results

Figures 5.35 a-d and Figure 5.36 a-c show plots of the Al_2O_3-normalized compositions versus distance across the color boundary. Al_2O_3-normalization was used to avoid deceptive effects of SiO_2-dilution, and to establishes the relative enrichments or depletions relative to the immobile element Al. The marker "0" millimeter represents row 1. The two symbols on the left and the right y-axis represent whole-rock XRF analyses of the adjacent red (GI-2) and green (GI-4) argillitic beds.

The color boundary between the rows 5 and 6 at 27 millimeter is marked by a sharp increase of two orders of magnitude in the MnO/Al_2O_3 ratio (Figure 5.35 a). The ratio already increases gradually in the red part as the color boundary is approached. In the green part, the MnO abundance then gradually decreases with increasing distance from the color boundary. If the samples GI-2 and GI-4 were directly connected, the analyzed rows in the red part would lie close to that line, whereas the green argillite adjacent to the color boundary show a major enrichment in MnO. Since it does not seem likely that this excess Mn can be derived from the adjacent red argillite, an additional (perhaps external) source of MnO is needed, or a mobilization of reduced Mn^{2+} over a thicker section in the red argillite than analyzed is required.

The CaO/Al_2O_3 (Figure 5.35.b) trend resembles the MnO/Al_2O_3 trend. CaO also shows a minor depletion in the uppermost part of the red argillite, which does not balance the excess CaO present at the bottom of the green bed. The correlation of CaO and MnO confirms the microscopic observation that rhodochrosite occurs at the bottom of the green layer.

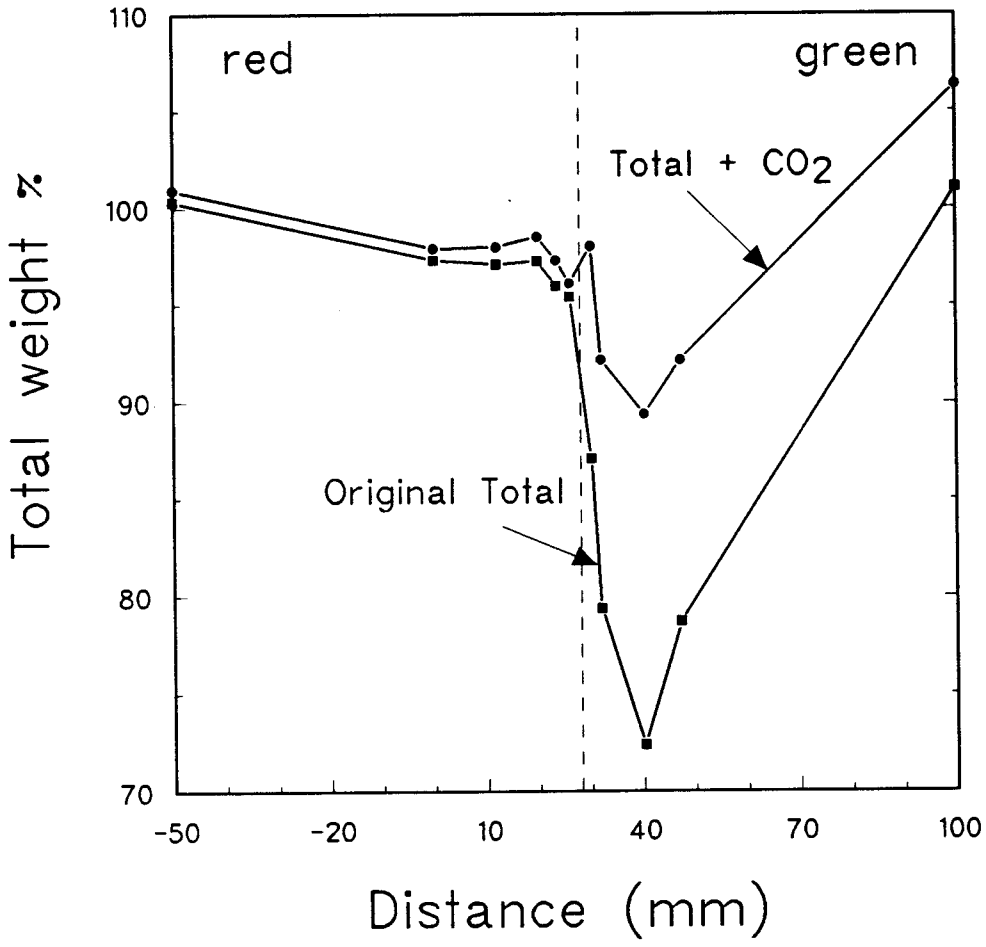

Figure 5.34: Diagram showing the original and the recalculated total abundances of the row averages. Recalculation was performed by addition of the amount of CO_2 necessary for rhodochrosite formation assuming all CaO and MnO are located in the rhodochrosite. Whole-rock XRF-analysis of red argillite GI-2 and green argillite GI-4 occur at -50 and +100 on this figure, respectively.

The $SiO2/Al_2O_3$ ratio also shows a maximum at the color boundary (Figure 5.35.c). Constraints on the biogenic origin of SiO_2 derive from the similar trend of the BaO/Al_2O_3 ratio that shows a peak at the same position. Despite the low count rate for BaO at the low current and acceleration potential (15 kV) used, the BaO/Al_2O_3 ratio increases by an order of magnitude and is probably far beyond the limits of analytical uncertainty. BaO was found to be well correlated with the SiO_2 abundances in siliceous plankton (Martin and Knauer, 1973). Further constraints derive from the SiO_2/Al_2O_3 correlation coefficient for the whole data set, which is -0.83. This supports the interpretation of a biogenic origin of SiO_2. The silica-rich bottom of the green argillite is therefore interpreted as the result of a former radiolarian-rich bed. It is probably not a coincidence that the CaO, SiO_2, and BaO peak all occur at the same position. They may mark the increased accumulation of biogenic material, e.g., a turbidite. The subsequent oxidation of the associated organic matter may have induced the diagenetic reduction and mobilization of Mn (Froelich et al. 1979) from the underlying red bed, as well as partial dissolution of carbonate (Jarvis and Higgs, 1987). Mn may then have been precipitated in the lower green part meeting conditions that favoured rhodochrosite formation, when an excess of HCO_3^- derived from the dissolution of $CaCO_3$ was present (Thomson et al., 1986). A analogous situation has been reported by Thomson et al. (1986) where Mn-oxyhydroxides underlying a calcareous turbidite served as a source for Mn. Upon reduction, the Mn diffused upwards into the turbidite, where it was fixed by adsorption on calcite.

The FeO/Al_2O_3 ratio (Figure 5.36.a) continuously decreases from sample GI-2 to GI-4, but the color boundary interrupts this trend. The loss of FeO in the red argillite is apparently complemented by an excess in the green argillite suggesting a mass transfer of FeO from the upper red argillite across the color boundary into the lower green argillite. The diagenetic mobility for FeO was therefore localized and only active on a scale of 3 centimeters, which contrasts to the larger-scale mobility of Mn. The

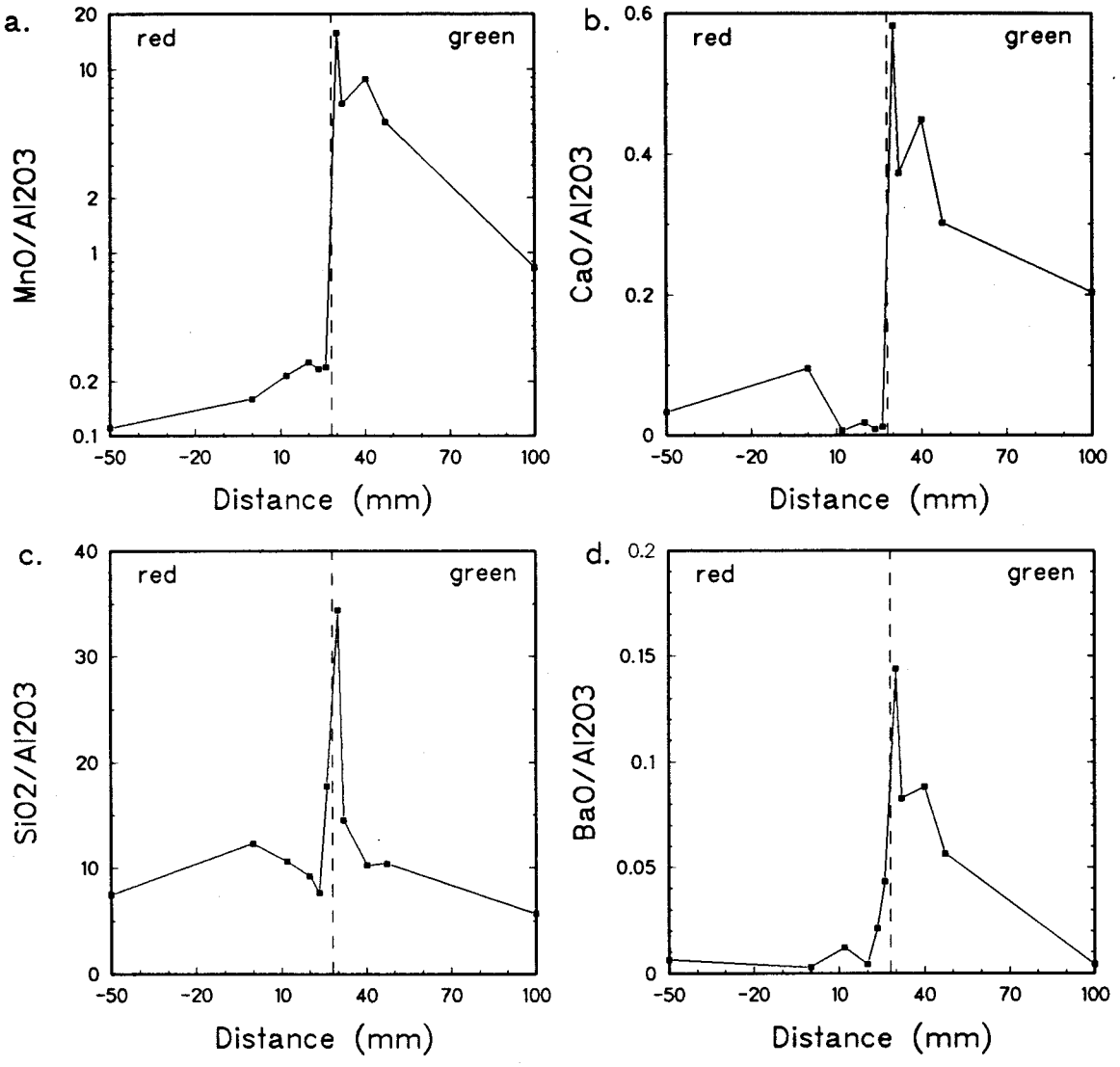

Figure 5.35: Plot of the Al_2O_3 normalized element oxide composition versus the distance across the thin sections. a. and b. MnO and CaO achieve their maximum abundances in the basal rhodochrosite band. c. and d. SiO_2 and BaO also reach their maximum abundances at the color transition. The peaks indicate the presence of biogenic-rich material at the bottom of the green argillite, which was possibly deposited as a biogenic turbidite.

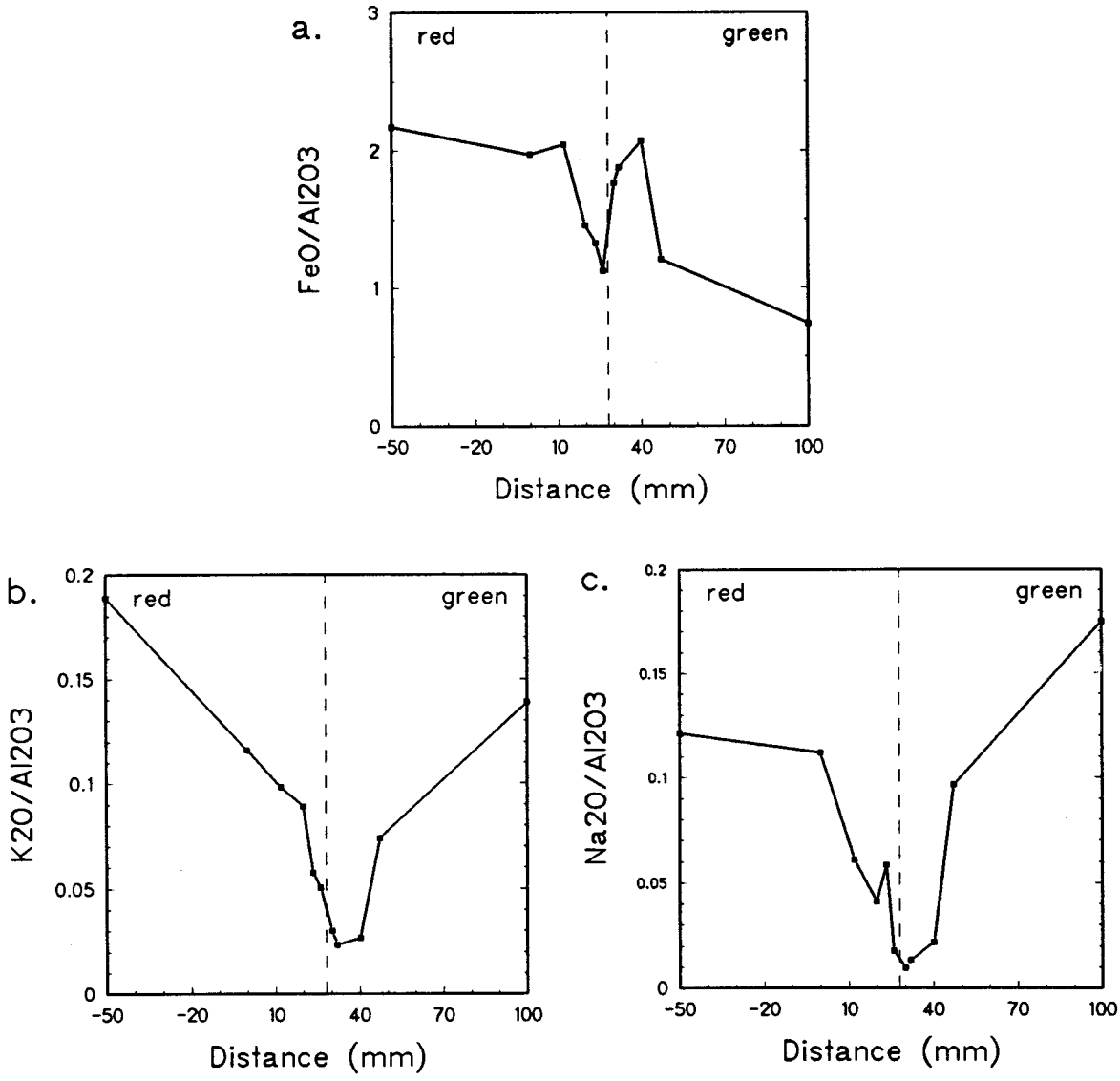

Figure 5.36: Plot of the Al_2O_3 normalized element oxide composition versus the distance across the thin section. a. limited diagenetic mobility of Fe. b. and c. alkaline depletion at color boundary.

cause for the Fe mobility was probably also diagenetic reduction and upward diffusion along a downward-migrating oxidation front resulting from the emplacement of the biogenic turbidite.

The Na_2O/Al_2O_3 and K_2O/Al_2O_3 ratios indicate that both elements are markedly depleted at the color transition. No complementary enrichment was detected. It cannot be excluded that the elements were immobilized farther away from the color transition, which is supported by the trend of increasing K_2O/Al_2O_3 and Na_2O/Al_2O_3 ratios toward the XRF analyses on either side.

Matrix composition

Sample GI-3 was chosen from a stratigraphic interval showing a marked enrichment in Fe and Mn (see Chapter 5.4). While the strongest enrichment in Mn is restricted to green, calcareous argillites, the enrichment in Fe occurs in the red, hematitic argillites. Based on the discussion in the previous section, it seems reasonable to attribute this separation to diagenetic mobilization of Mn^{2+} from the red argillites into the green argillites. The question arises what the composition of the rock may have been excluding this metal enrichment. Figure 5.37 shows that Mn-enrichment in green argillites takes place at a constant Fe/Mg*5 ratio, and Fe-enrichment takes place at a constant Mn/Mg*5 ratio, respectively. Therefore, both cases indicate that the enrichment is independent of the third major element Mg, which would be expected to be contained in a Mn-Fe-bearing silicate (e.g, chlorite). Consequently, this observation supports the conclusion of an individual metal source, which was likely to be hydrothermal (see Chapter 5.4). Both data sets converge to one point where their metal enrichment is minor. It may be speculated that this point represents the composition of the non-hydrothermally enriched matrix. For reference, the composition of a composite shale (PAAS) is plotted in Figure 5.37, indicating that this hypothetical composition would also have been enriched in Mn and Fe. The carrier phase of this metal

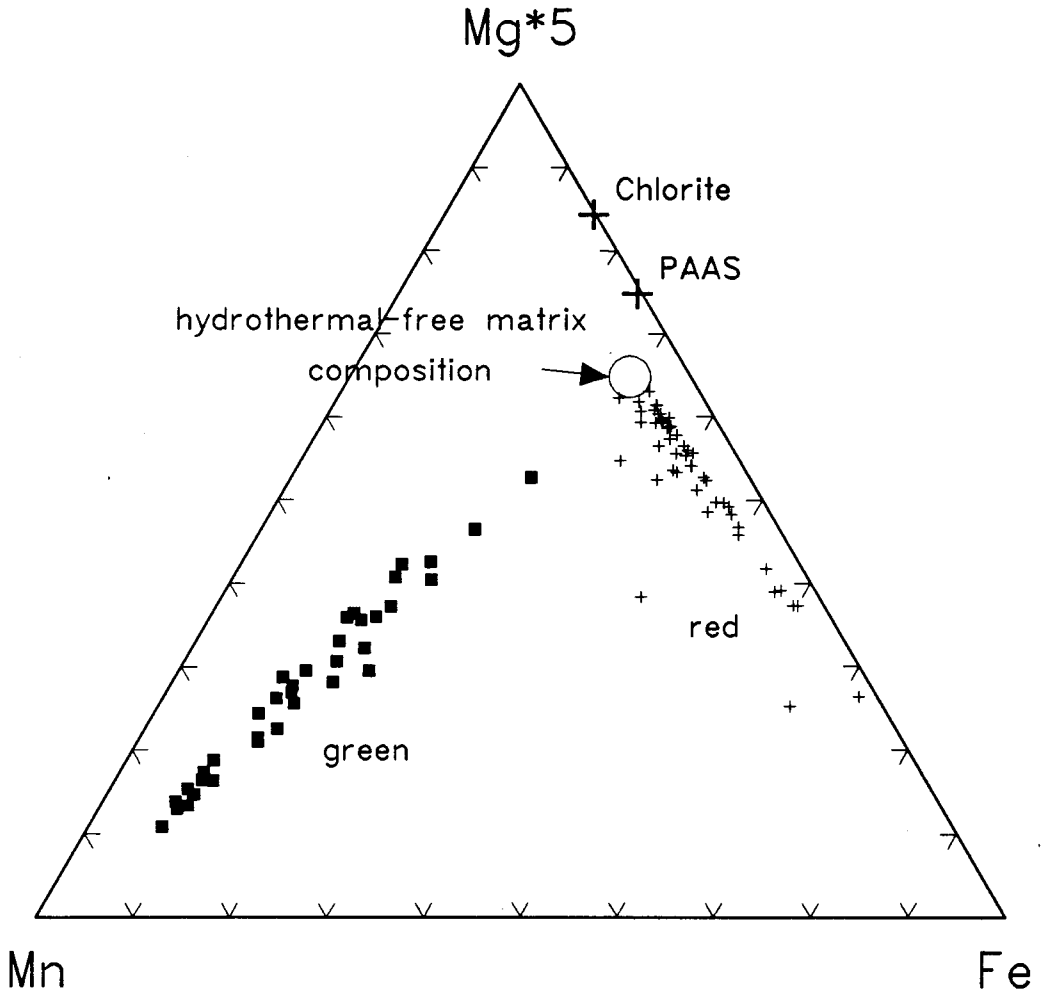

Figure 5.37: Ternary showing the respective metal enrichments in the red and green part of the thin section. Point of convergence is assumed to represent the non-hydrothermally enriched sediment composition.

component was probably polymineralic, since a chlorite composition plots toward the Mg*5 apex. Other phases like spessartine for Mn, and phengitic muscovite and prehnite for Fe, respectively, are also likely to be present as metal carriers, and may have caused the trend away from the Mg*5 apex.

Comparison of whole-rock XRF analyses with microprobe analyses

The applied method of matrix analyses with a 30 micron diameter opens the question whether the data acquired for this scale of analysis are compatible with those obtained by whole-rock XRF analyses. In order to test whether micron-scale (respectively micro- or even nanogram-scale) microprobe and kilogram-scale XRF analyses are compatible, a set of Fe-rich, hematitic argillites from all three sections of the Badger Bay area were selected for comparison. The elements K, Mg, and Mn were chosen, because they represent elements most likely to be controlled by the chemical composition of the fine-grained fraction. Figure 5.38 shows Al and K*10 plotted against Mn and Mg. Both the whole-rock XRF and the microprobe analyses show the same trend of variation. The data approach the K*10/Al side of the triangle at a K*10/Al ratio of about 75:25. This is very close to the K*10/Al ratio for an ideal muscovite. The compositional variation of the data may be interpreted (a) as a result of compositional control by single minerals of more-or-less fixed composition (i.e., controlled by the phases muscovite and chlorite) that vary in their relative proportions or (b) as a result of compositional variation in the whole-rock composition. In the first case, the results are less surprising, because the chemical composition of individual phases would be the same on both scales of analyses. The petrographic and associated chemical homogeneity on the different scales remains significant. In the second case, the coincidence of the data is remarkable considering the scale of comparison between less than square millimeter sized, nanogram analyses in *one* sample and a *set* of kilogram-sized whole-rock analyses from samples that may be horizontally separated by

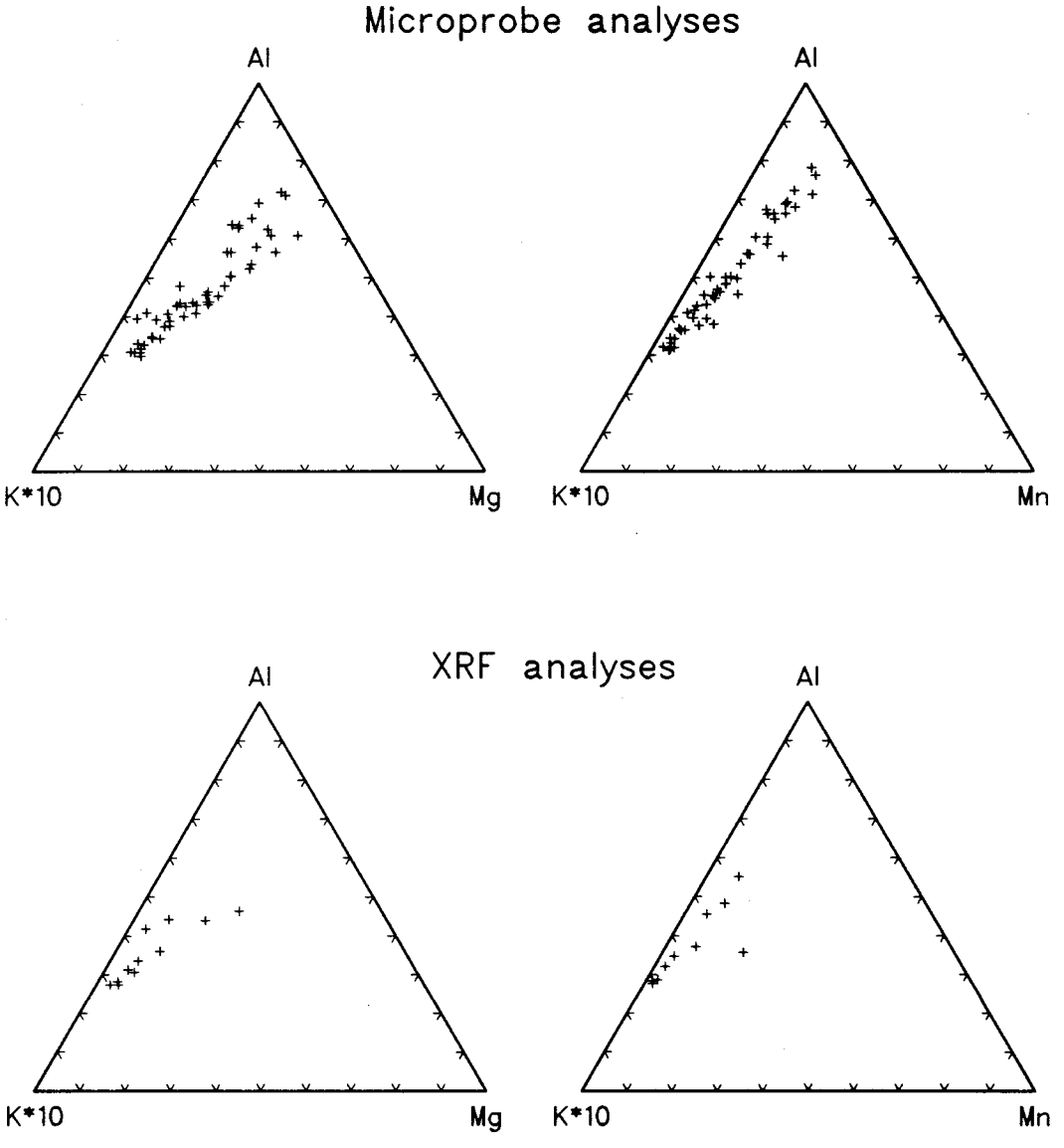

Figure 5.38: Comparison of the geochemical composition of the fine grained matrix from analyses of the red, hematitic part obtained on the microprobe with whole-rock XRF analyses of Fe-enriched hematitic argillites from the Shoal Arm Formation.

2 kilometers, and by > 50 meter stratigraphically. The results imply that the geochemical variation of K, Al, Mn and Mg can be observed on widely differing scales, but the magnitude of variation remains the same and displays the same trend within one sample and between samples.

6. SUMMARY AND DISCUSSION

This chapter briefly summarizes the previous sections to emphasize the most important sedimentological, petrographical, and geochemical changes that occurred during the deposition of the Shoal Arm Formation. Following this summary, two tectonic models are proposed that relate the evolution of the Shoal Arm Formation to the general, early Ordovician - early Silurian geologic history of the Exploits zone.

The depositional history of the Shoal Arm Formation may be divided into seven stages. Stage 1 includes the deposition of sediments of the upper Wild Bight Group and the lower Shoal Arm Formation, and is characterized by the subsidence of a basin southeast of the Ordovician island arc. In the stratigraphic column, this stage reaches to the level 100 meters. The basin received fine-grained, silt-size to clay-size green and purple volcaniclastics. Intermittent, sandy, green-colored turbidites interrupt the continuous deposition pattern. Geochemically, the fine-grained sediments appear to be derived from a mixed clastic source, since no element association could be found that unambiguously characterized a single source. Potentially, alkalic volcaniclastics or volcanic tuffs are mixed into the sediment, as indicated by a component in which Zr, Nb, Y, Mg, and Zn are associated. The intermittent, coarser layers may have a stronger mafic component, which is interpreted from the higher Cr_2O_3/Al_2O_3 ratio in two coarser-grained samples in the upper Wild Bight Group. Analysis of correlation coefficients, factor analysis, and characteristic element ratios indicated that a hydrothermal component was either not present or was suppressed at the time of upper Wild Bight Group deposition.

The change from stage 1 to stage 2 is characterized by the additional supply of hydrothermally derived material. In contrast to the previous stage, fewer green layers are intercalated into the maroon argillites. Stage 2 reaches to the level 115 meters. The oxic, maroon sediments in this stratigraphic interval are enriched in Fe, Pb, Co, and Ni,

whereas the corresponding green argillites are strongly enriched in Mn, and show higher CaO- and LOI-contents. The green beds are interpreted as calcareous turbidites, which, upon deposition, apparently produced reducing conditions in the underlying oxic sediment, and caused reduction and mobilization of Mn. Mn^{2+} then was reprecipitated as $MnCO_3$ in the adjacent, overlying green bed.

The strong hydrothermal component seems to recur in short pulses, but shows a generally decreasing trend upsection (stage 3). This new stage is characterized by deposition of bright-red argillites in contrast to the dominantly maroon argillites in the previous stage. The stage occupies the stratigraphic interval from 115 meters to 160 meters. A biogenic component is represented by the deposition of radiolarian-rich turbidites. Three main sediment sources may be distinguished in stage 3: (a) radiolarians (biogenic Si); (b) hydrothermal Fe-Mn oxyhydroxides; (c) fine-grained clay-sized detritus of multicompositional, volcanic origin. Slight fluctuations of different, clastic components can be recognized. In particular the Cr-source interpreted as a weak, mafic component, shows varying influence. The top parts of the turbidites are burrowed, and contain Mn-nodules, eventually indicating an interval of low sedimentation rates that permitted Mn-nodule formation. The mechanism of the Mn-nodule formation is, however, not exactly understood, since they show a remnant carbonate component, which is not typical for deep-sea nodules.

With stage 4, the abundances of "hydrothermal elements" decrease indicating that the hydrothermal activity faded. Stage 4 occupies the stratigraphic interval from 160 to 252 meters. Purple argillites and more frequent green argillites than in the stage 3 characterize this interval. The deposition of radiolarian turbidites continued. Apparent in this interval is a continuous decrease in the $CaCO_3$-content of the green argillites, which may indicate the gradual disappearance of a shallow-water (shelf?) carbonate source. Concurrently, a source (re)appeared which is characterized by high Zr, Nb, and Y abundances. The source material may have consisted of alkaline/sub-alkaline basalts.

Two samples with high Zr abundances show low abundances in Ti, which appears unusual considering that alkaline basalts are generally enriched in Ti. However, the high Nb abundances of all Zr-rich argillites make it unlikely that erosion of acidic calcalkaline material, e.g., dacites contained in the Dunnage Mélange (Coaker porphyry), is responsible for this Zr-signal.

Deposition of the distinctive grey, mottled and laminated cherts defines stage 5. This stage reaches from 255 meters to 325 meters. The interval shows increased accumulation of biogenic material, which is indicated by the increased abundances of Ba and Si. The hydrothermal component disappeared. Accumulation of Zr-rich material did not continue into the grey cherts, since the Zr/Al_2O_3 ratio abruptly decreases at the boundary of green argillites to grey cherts. The grey cherts are low in CaO and have low LOI's, which indicates the virtual absence of a calcareous component. The intense burrowing of parts of the grey cherts indicates a vital, benthic environment on an oxygenated sea floor. Intermittent thin, black shale layers in the upper grey cherts indicate a transitional stage from dysaerobic to anaerobic conditions.

Black shale deposition (stage 6) must have taken place in a markedly different environment. The sediments were apparently deposited in an oxygen-deficient environment, since the black slates carry some general characteristics of black shales (i.e., an enrichment of Cr and V, and possibly of Cu) which has been recognized among other Phanerozoic black shales. These black shales have been deposited either in anoxic basins or in parts of basins where an oxygen minimum zone presumably intersected with the basin margin. The strong biogenic influence in the previous stage decreases again. The black shales are strongly depleted in Mn and Ca, and slightly depleted in Fe and P (Tables 5.1.1 - 5.1.6). The Fe-depletion is unusual for black shales because, in anoxic sediments, the dissolved Fe^{2+} is commonly thought to be precipitated with S^{2-} to form pyrite (Berner, 1984). Although the Shoal Arm Formation is pyritiferous indicating that the diagenetic reaction sequence reached sulfate reduction (Froelich et al., 1979), part of

the Fe was apparently lost. It can only be speculated what the reason of this depletion could have been. Under the assumption that the low Ca abundances actually represent a very low $CaCO_3$-content, it may be argued that $CaCO_3$ had been dissolved under acid conditions. Dissolution and removal of the carbonate and bicarbonate ions would have produced a low pH and a low pore fluid alkalinity. A low pH would be required to be outside the stability field of pyrite and siderite at low Eh (Hem, 1972), so that Fe^{2+} remained dissolved. Similarly, this low pH and the low alkalinity would have prohibited $MnCO_3$-formation. Since both reduced elements could not form a solid phase, they diffused upwards into the seawater, and were at least partly lost from the sediment. Possibly, the pore-water conditions were close to the pyrite stability field, so that eventually some metastable pyrite formed. The low pH may also explain the P-depletion of the black slates, because the phosphate phase (probably apatite) would have been unstable under such conditions (Roden, pers. comm., 1992).

Greywacke deposition defines stage 7 (> 350 meters). The clastic source is characterized by element associations of both compatible elements Cr, V, Ni, Mg, and Fe and incompatible elements, e.g. K and Rb, with Al. This indicates that both mafic detritus and more silicic detritus were contributed to the basin. These sources may have first appeared during black shale deposition. If so, the clastic fraction of the black shale may be the distal equivalent to the greywackes.

Figure 6.1 and 6.2 attempt to illustrate the evolution of the depositional basin using the work of others authors on the regional geology of the Exploits zone, in particular the work of Nelson (1979), Kusky (1985), Arnott et al. (1985), van der Pluijm and van Staal (1988), Pickering et al. (1988), and Swinden et al. (1990). Two models are proposed, since the geologic information available allows for different scenarios. The essential difference between the two models hinges on the problem of whether (a) the deposition of the red and grey unit ended simultaneously with beginning of deposition of the black shales in every part of the basin, or whether (b) deposition of the top parts

Figure 6.1: Tectonic model illustrating the evolution of the Shoal Arm Formation from early Ordovician to early Silurian times. The model assumes that deposition of the red and grey Shoal Arm Formation was finished by the time the black shales were deposited. Thus, the model assumes a synchronous deposition across the basin. A global anoxic event is thought to be responsible for the black shale deposition (see text for discussion).

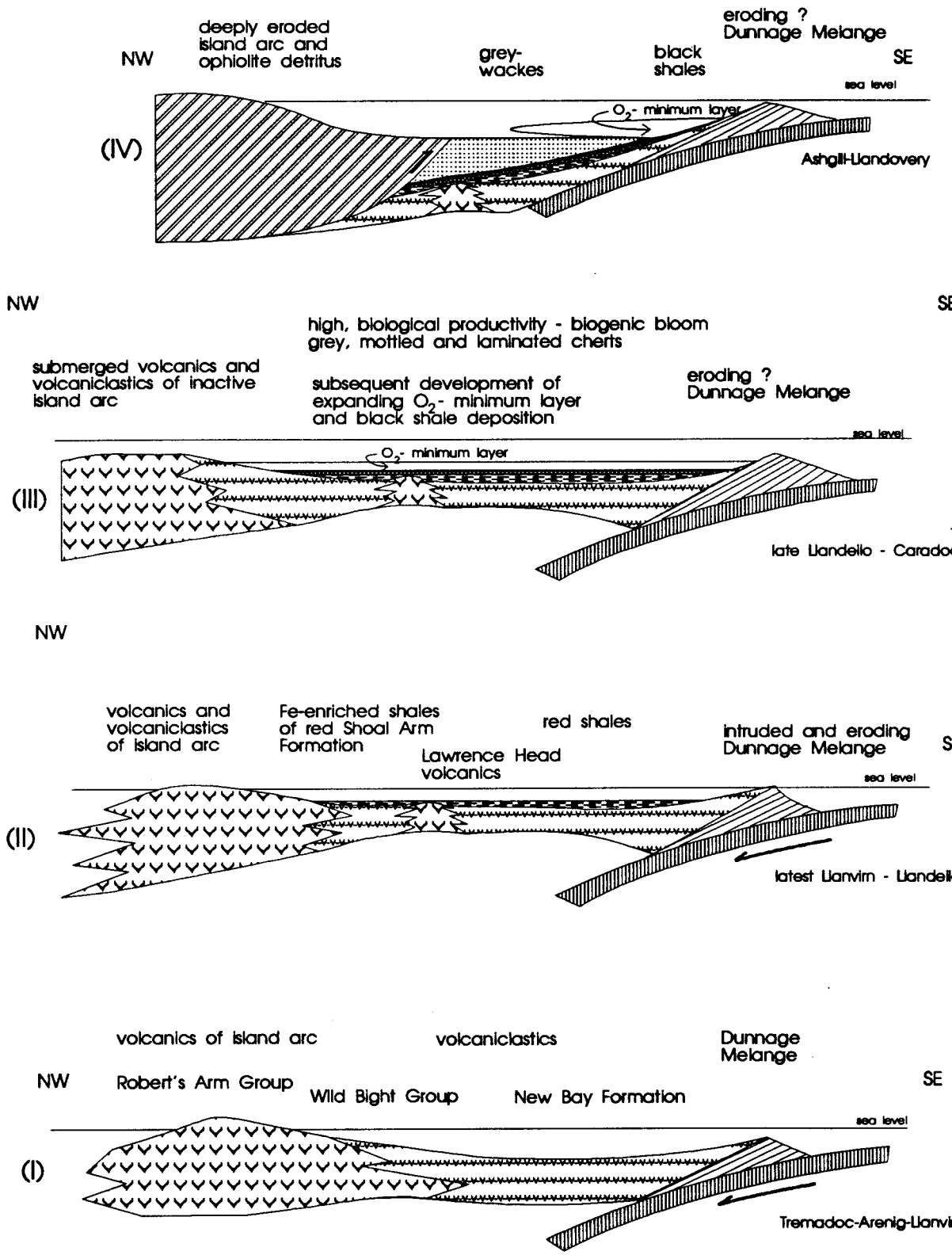
eroding ?
Dunnage Melange
deeply eroded
island arc and
ophiolite detritus
NW
grey-
wackes
black
shales
SE
sea level
O_2- minimum layer
(IV)
Ashgill-Llandovery
NW
SE
high, biological productivity - biogenic bloom
grey, mottled and laminated cherts
submerged volcanics and
volcaniclastics of inactive
island arc
subsequent development of
expanding O_2- minimum layer
and black shale deposition
eroding ?
Dunnage Melange
sea level
O_2- minimum layer
(III)
late Llandello - Caradoc
NW
volcanics and
volcaniclastics
of island arc
Fe-enriched shales
of red Shoal Arm
Formation
red shales
Lawrence Head
volcanics
intruded and eroding
Dunnage Melange
SE
sea level
(II)
latest Llanvirn - Llandello
volcanics of island arc
volcaniclastics
Dunnage
Melange
NW
Robert's Arm Group
Wild Bight Group
New Bay Formation
SE
sea level
(I)
Tremadoc-Arenig-Llanvirn

of the red Shoal Arm Formation, and the grey and black Shoal Arm Formation was a time-transgressive, diachronous sequence that took place as a result of thrust-loading induced subsidence migrating from the northwest.

The early Ordovician (i.e., Tremadoc-Arenig-Llanvirn) sedimentation in the basin is characterized by subduction proposed to be from the southeast, resulting in an active volcanic arc (Figure 6.1.I and 6.2.I). At that time, the basin was supplied with sandy volcaniclastics. Since the proportion of volcanics to volcaniclastics decreases to the east, it is assumed that the detrital source was located to the north or northwest. The volcaniclastics are represented by the Wild Bight Group and New Bay Formation, respectively.

In the Llandeilo (Figure 6.1.II and 6.2.II), the activity of the island arc was fading, and the relief became continuously less pronounced as the result of erosion. Sedimentation rates were therefore lower. At this time, oxic, red shales were deposited in an environment intermediate between hemipelagic and pelagic conditions. Volcanic activity at this time period is noted in the Lawrence Head volcanics. Based on the chemistry of these volcanics which show an E-MORB signature (Swinden et al., 1990; Jacobi and Wasowski, 1985; Kidd et al., in prep.), it can be said that the Lawrence Head volcanics were probably not part of the arc complex. The actual, tectonic environment of the Lawrence Head volcanics still has to be clarified (see Chapter 2: General Geology). Several field observations support the argument that the Lawrence Head volcanics were most likely extruded in a submarine environment and active at a time when the red shales of the Shoal Arm Formation were deposited in other parts of the basin: (a) these volcanics are the only ones that directly underlie middle Ordovician red shales equivalent in age to the red Shoal Arm Formation; (b) only a thin veneer of red shales is overlying the Lawrence Head volcanics (Kidd, pers. comm.); (c) maroon argillites comparable to the red Shoal Arm Formation occur in the lower part of volcanics that are lateral equivalents of the Lawrence Head volcanics (Kidd, pers.

comm.). Based on these observations, it is suggested that hydrothermal activity in the Lawrence Head volcanics is responsible for the hydrothermal enrichment observed in the Shoal Arm Formation. This interpretation is supported by the observation of blue chert and calcite interstices associated with sulfide minerals in pillow lavas of the Lawrence Head volcanics (Kusky, 1985). Kusky (1985) suggested that these features resemble those found near submarine hydrothermal springs along ridge axes.

Based on the available data, the island arc (i.e., Robert's Arm Group) is not considered to be the likely source of the hydrothermal activity. Sediments in the Side Harbour Formation (Nelson, 1979), which is located within the Wild Bight Group, were not found to be hydrothermally enriched (see chemical composition of samples SB-2, SB-9; Appendix 1). These samples are also red argillites, probably had the same general source area as the Shoal Arm Formation, and are also likely to have been deposited at low sedimentation rates.

Since the hydrothermal component fades in the upper part of the Shoal Arm Formation it appears that the Lawrence Head volcanism had ceased by the end of deposition of the red Shoal Arm Formation. However, the exact timing of this cessation is uncertain. Consequently, the Zr-, Nb-, and Y-rich component in the argillites of the upper red Shoal Arm Formation may be explained either by erosion or by continued volcanic activity of equivalents of the Lawrence Head volcanics. In the beginning, this volcanic complex may have been restricted to large water depths and thus contributed little clastics to the Shoal Arm Formation. With time, it may have been gradually built up to shallower depths so that its clastic contribution into the adjacent basin increased in importance.

Equivalents of the Lawrence Head volcanics may have been eroded from the middle to late Llandeilo on. Unfortunately, since isotopic ages of these volcanics are not available, age estimates are dependent on fossil finds, which only exist for the overlying black slates. The age is derived from an estimation of the time required for deposition

of 100 meters of stratigraphic thickness (i.e., from the level 225 meters, where the increase in the Zr/Al_2O_3 ratio is noted (Figure 5.4.3), to 325 meters - the base of the black Shoal Arm Formation, which has a Caradocian age. Assuming sedimentation rates of 5 - 10 $cm/10^3$ a (compare Nares Abyssal Plain; Kuiypers et al., 1987), the time required for deposition of the Zr-, Nb-, and Y-rich argillites would have been between 1 and 2 Ma. This places the age of the red Shoal Arm Formation into the middle to late Llandeilo (Harland et al., 1982). However, since the Shoal Arm Formation may have been shortened by 50% (Nelson, 1979), this age estimate is considered to be the minimum.

Alternatively, with time the Lawrence Head-type volcanic edifice(s) may as well have been built up above sea level while being active. In this scenario, the Zr-, Nb-, and Y-rich material may represent a tuffaceous component. However, it is surprising that the later inevitable erosion of this complex is not noted anywhere in the Exploits zone. In this tectonic setting, where the different clastic sources may have been more or less proximal, it may be expected that the erosion of such a characteristic lithology is noted in the resulting sediments. For this reason, it seems more likely that the spike in Zr, Nb, and Y in the upper red Shoal Arm Formation is derived from erosion of a Zr-, Nb-, and Y-rich alkaline/sub-alkaline volcanic source that had been built up to shallow-water depth and then ceded to be active.

Subsequently, the tectonic evolution of the basin is interpreted in two different ways. The first model indicates further subsidence of the basin with the development of quiet, pelagic conditions (Figure 6.1.III). Since the late Llandeilo-Caradoc marks a time of high sea level, the arc would have been submerged and subject to minor erosion. This is evidenced by continued low, clastic sedimentation rates. Several authors argue for a global, eustatic sea-level rise of substantial magnitude in the Caradocian (e.g., Leggett, 1980; Leggett et al., 1981; McKerrow et al., 1977). Leggett et al. (1981) proposed a model that relates the deposition of black slates in the Caradoc to global "G"

(greenhouse) effects - time periods of high sea level stands, higher marine temperatures, reduced oceanic circulation, stratified waters, and a high biological diversity. Essentially applying this model to the Shoal Arm Formation, it could be argued that nutrient-rich waters in upper mid-water levels allowed a flourishing phytoplankton community. This high biological productivity is evident from the enhanced accumulation of biogenic material (i.e., Si from radiolarians) on the seafloor at the time of grey chert deposition. The period of high biological productivity and rapid accumulation of biological matter ended the mainly oxic, diagenetic conditions seen in the red shales. It is furthermore assumed that a thermocline existed below the wave base that prohibited O_2-renewal in the zone of high biological productivity. Due to density stratification, restricted circulation, and O_2-drain by organic carbon oxidation in the zone of high biological productivity, the deep water became increasingly depleted in O_2. This O_2-depletion eventually resulted in the development of anoxic conditions and black slate deposition. According to this model, the deposition of the black shales may be coincident with a worldwide "Oceanic Anoxic Event" (e.g., Schlanger and Jenkyns, 1976), since black shales of similar age have also been reported from other parts of the world (e.g., Leggett, 1981). Continuous O_2-depletion was possibly enhanced by the topography of the basin, where the Dunnage Mélange, interpreted as the inactive (?) accretionary prism, served as a barrier for influxing open-ocean, O_2-rich seawater. The deposition of grey cherts and black slates therefore took place in a period of tectonic and volcanic quiescence - similar to what has been proposed by other workers (e.g., Nelson, 1979; Arnott et al., 1985; Dewey et al., 1983) for the Caradocian. The deposition of the greywackes of the Gull Island Formation then marks a change from the previous environment by the renewal of a clastic source that progrades over the basin from northwest to southeast (Figure 6.1.IV).

Arnott et al. (1985) suggested that the duration of the fine-grained sedimentation in the Notre Dame Bay may have been very variable from place to place. In particular,

Figure 6.2: Alternative tectonic model illustrating the evolution of the Shoal Arm Formation from early Ordovician to early Silurian times. In contrast to the previous model, the grey and black Shoal Arm Formation were deposited diachronously to the southeast and preceded a migrating, greywacke-filled trough (see text for discussion).

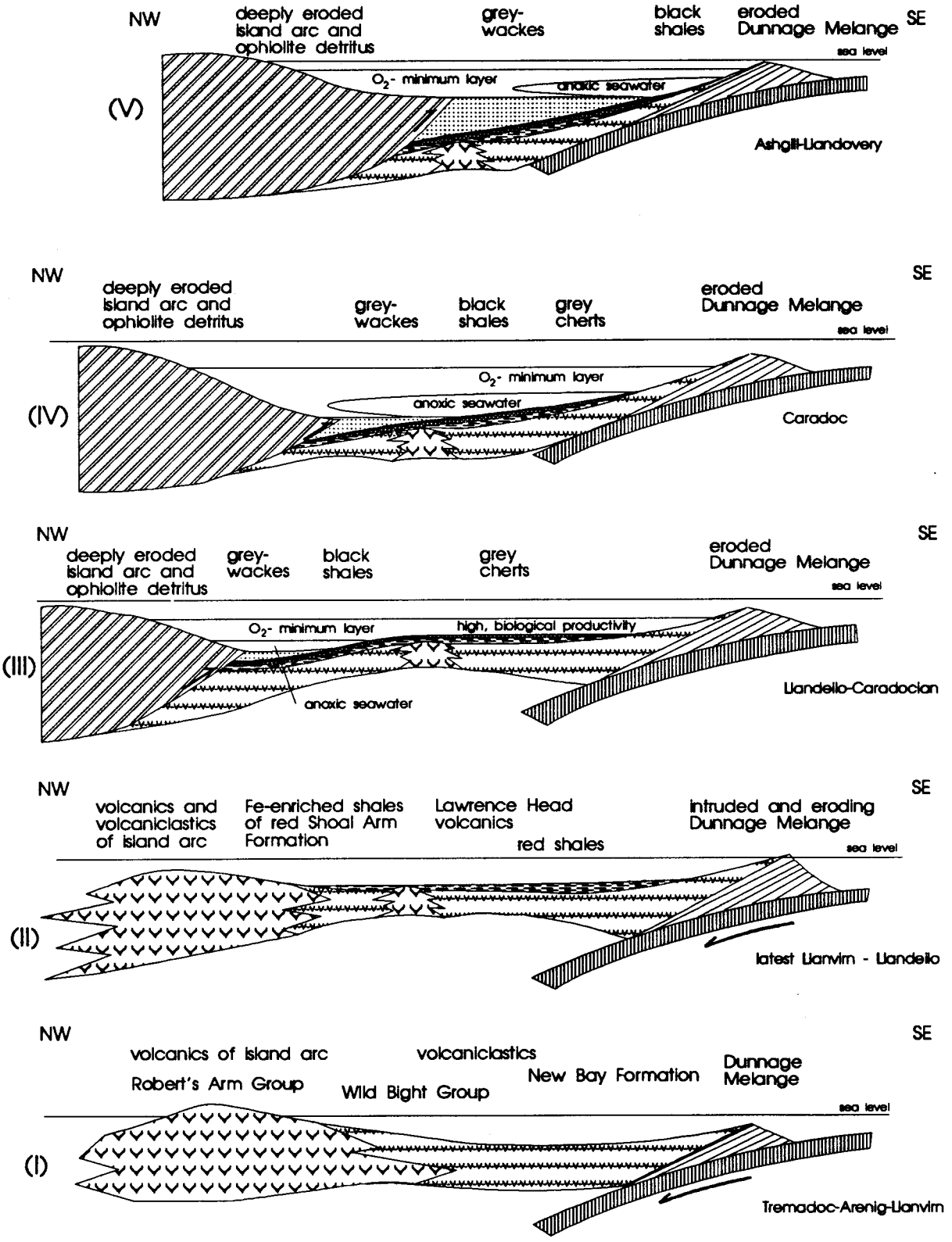
NW
deeply eroded island arc and ophiolite detritus
grey-wackes
black shales
eroded Dunnage Melange
SE
sea level
(V)
O_2- minimum layer
anoxic seawater
Ashgill-Llandovery
NW
deeply eroded island arc and ophiolite detritus
grey-wackes
black shales
grey cherts
eroded Dunnage Melange
SE
sea level
(IV)
O_2- minimum layer
anoxic seawater
Caradoc
NW
deeply eroded island arc and ophiolite detritus
grey-wackes
black shales
grey cherts
eroded Dunnage Melange
SE
sea level
(III)
O_2- minimum layer
high, biological productivity
anoxic seawater
Llandello-Caradocian
NW
volcanics and volcaniclastics of island arc
Fe-enriched shales of red Shoal Arm Formation
Lawrence Head volcanics
red shales
intruded and eroding Dunnage Melange
SE
sea level
(II)
latest Llanvirn - Llandello
NW
volcanics of island arc
Robert's Arm Group
volcaniclastics
Wild Bight Group
New Bay Formation
Dunnage Melange
SE
sea level
(I)
Tremadoc-Arenig-Llanvirn

they referred to the differing fossil ages that were found for the Caradocian black slates (p.613, Arnott et al., 1985). Although the geochemical information is ambiguous, a similar clastic source appears to have existed for the black shales and the greywackes. If this is true, the black shales may have been deposited diachronously to the southeast similar to the overlying greywackes. Since the onset of the black shale deposition reflects anoxic bottom water conditions, the different ages of the black slates would indicate that these anoxic conditions also developed diachronously in the direction of greywacke progression. These aspects are emphasized in model 2 and are illustrated in Figure 6.2.III - 6.2.V. The model includes the subsidence effect that an approaching thrust stack from the northwest would have imposed on the basin. As the thrust stack migrated to the southeast, it probably caused the basin to founder and to form a prograding trough in the direction of thrust movement.

Similar to the previous model, the deposition of red shales was largely completed by the time this process started. The climatic effect of the Caradocian transgression is reflected in high biological productivity and the development of an expanding oxygen minimum layer in mid-water depths. The Dunnage Mélange acted as a topographic barrier limiting water exchange with the open ocean. As a result of the high biological productivity, grey cherts had started to accumulate on top of the red shales. The southeastward directed thrusting of a deeply eroded arc and ophiolite fragments caused the northwestern part of the basin to subside first. These deepest parts of the basin may have had restricted water-circulation, so that anoxic bottom-waters developed and black shales were deposited. This anoxic water layer migrated southeastward in front of the deep trough. The deepest parts of the trough were filled with greywackes being derived from the uplifted terrane in the north and northwest. Possibly, the deepest parts of the basin were ventilated again with greywacke deposition, assuming that the turbulent currents contained O_2-rich waters from shallower depths. On the lower southeastern side of the trough, the basin was still anoxic, and sedimentation rates remained low. In

these parts, black shale deposition continued. Farther up-slope, the sea floor was still located within a dysaerobic zone characterized by high biogenic accumulation. Here, grey cherts accumulated.

It is therefore proposed that the amount of biogenic material being supplied to the basin floor at the time of highest biological productivity controlled the change from oxic conditions (red argillites) to suboxic conditions (grey cherts). Anoxic conditions were then achieved as the basin floor subsided into the euxinic, stagnant deep-water layer. With continued basin subsidence as a result of thrust progression, the parts of the basin located to the southeast were also subject to this transition.

Since the Dunnage Mélange appears to have been locally exposed to submarine/shallow-water erosion in the Llandeilo (as demonstrated by the Cheneyville conglomerate; Arnott et al., 1985), sedimentation rates towards the Dunnage Mélange should have been higher than in the coeval red Shoal Arm Formation. No red and green shales are found overlying the Dunnage Mélange. However, grey, burrowed cherts were deposited on top of the Dunnage Mélange immediately following the Cheneyville conglomerate; at this time, the Mélange may have been considerably eroded, so that low sedimentation rates returned to this area. Subsequently, deep-water, anoxic conditions prevailed, indicated by the deposition of black shales onlapping over the Dunnage Mélange.

In a sense, the model requires coeval deposition of grey cherts and greywackes, but the source areas of the two lithologies appear to be different (Chapter 5.2). This discrepancy is best explained by the fact that the early greywackes, shed into the basin, were most likely derived from the upthrusted part of the Robert's Arm Group - and therefore not very different in their composition from the Shoal Arm Formation. Later, when more Cr-rich greywackes accumulated (the addition of ophiolite detritus to the clastic source), grey chert deposition took place far to southeast or had eventually been succeeded by black shale deposition. It is also possible that the Lawrence Head volcanics

and their equivalents acted as topographic highs in the earlier basin history so that the first greywackes were ponded in the northwest. The late stages of the basin evolution were then presumably similar to the first model where greywackes prograded over the grey cherts and black shales to the southeast, and subsequently filled the basin.

7. COMPARISON OF THE SHOAL FORMATION WITH THE MEDIAL ORDOVICIAN SEQUENCE OF THE TACONIC ALLOCHTHON, EASTERN NEW YORK STATE AND VERMONT

As mentioned in the general introduction, the medial Ordovician part of the Taconic sequence of eastern New York State and western Vermont, and the Shoal Arm Formation exhibit a similar stratigraphic sequence. The two sequences are displayed in Figure 7.1. In the Taconic Allochthon, red argillites are represented by the Indian River Formation (Rowley at al., 1979). The overlying Mt. Merino Formation consists of bedded, occasionally mottled cherts intercalated in graptolitic slates in the lower part, and dominantly black slates in the upper part (Rowley et al., 1979). The major difference to the Shoal Arm Formation is the dominantly, siliciclastic, early Ordovician and older substrate and a thinner, mottled grey chert unit. The thickness of the Mt. Merino Formation ranges from 25 - 70 meters, typically 50 meters (Rowley et al., 1979), which is less than the thickness of the two units in the Shoal Arm Formation (80 and 30 meters for the grey cherts and black slates, respectively). The red and green slates of the Indian River Formation have a thickness of about 50 meters. With reference to Wood (1974), Rowley et al. (1979) indicate that the slates of the Taconic sequence were shortened by at least 75% perpendicular to the slaty cleavage. Nelson (1979) suggested a finite shortening also between 50% and 75% for the Wild Bight Group. It therefore appears that the medial Ordovician stratigraphic sequence before deformation in the Taconic Allochthon was thinner than in the Shoal Arm Formation.

55 samples have been analyzed by J.W. Delano from the Poultney Formation, the red and green slates of the Indian River Formation, and the black slates and cherts of the Mt. Merino Formation. It is the purpose of this chapter to compare the geochemistry of the Indian River Formation and the Mt. Merino Formation with the red

Stratigraphic correlation of the Newfoundland sequence and the middle Ordovician part of the Taconic sequence, New York

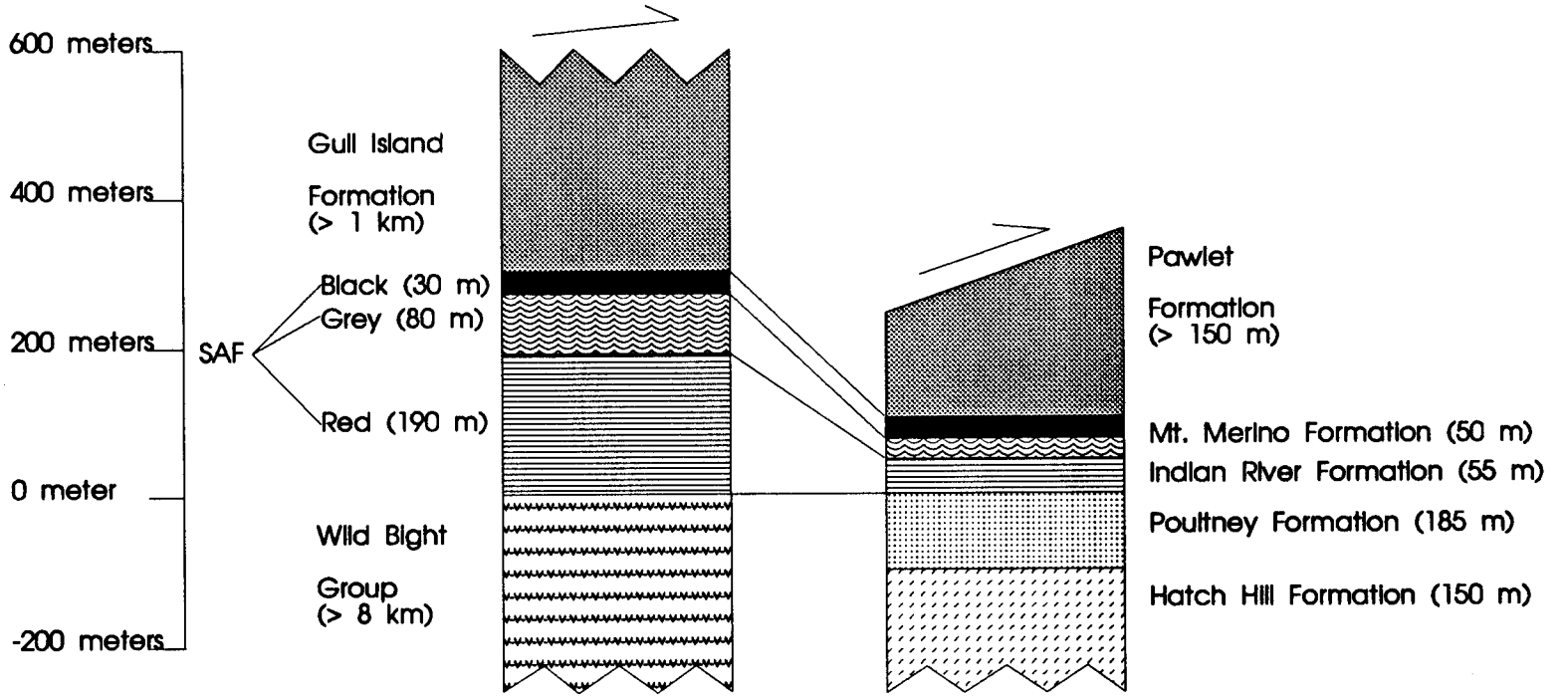

Figure 7.1: Comparison of the Ordovician stratigraphic thicknesses in the Badger Bay area of Newfoundland and the Taconic Allochthon. Thicknesses for the Taconic Allochthon are from Rowley et al. (1979).

argillites and the black slates of the Shoal Arm Formation. The geochemistry of these rocks will not be evaluated in the same detail as was done in the Shoal Arm Formation. An attempt is made to determine whether (a) a comparable metal enrichment exists in the red slates of the Indian River Formation; (b) the Mt. Merino Formation bears characteristics that make it comparable to the grey and black cherts and/or slates of the Shoal Arm Formation; (c) the models created based on the geology of the Shoal Arm Formation can be applied to the medial Ordovician strata of the Taconic Allochthon of New York State as well.

7.1. The sedimentary environment of the Poultney, the Indian River, and the Mt. Merino Formation based on interpretations of their geochemical composition

Principal sediment components

The three sample sets of the Poultney Formation, the Indian River Formation and the Mt. Merino Formation were subjected to a R-mode factor analysis in order to discriminate the principal sediment components in these three formations. The Varimax-rotated factor loadings of each formation are displayed in Figures 7.2 through 7.4. The results of the factor analysis can be summarized as follows:

(1) A clay component is present in all three formations, which is interpreted from a factor with loadings of Ti, Al, Zr ± Na, K, Cr, and Rb. This factor generally has the strongest loadings, which suggests it is the dominant sediment component. Fe is associated with this factor in the Poultney and Indian River Formation, but this association breaks down in the Mt. Merino Formation.

(2) A Si-component is consistently negatively correlated with most other elements. In the Shoal Arm Formation, petrographic evidence confirms the interpretation as biogenic Si. It is suggested that biogenic Si in the New York State Taconic Allochthon data sets

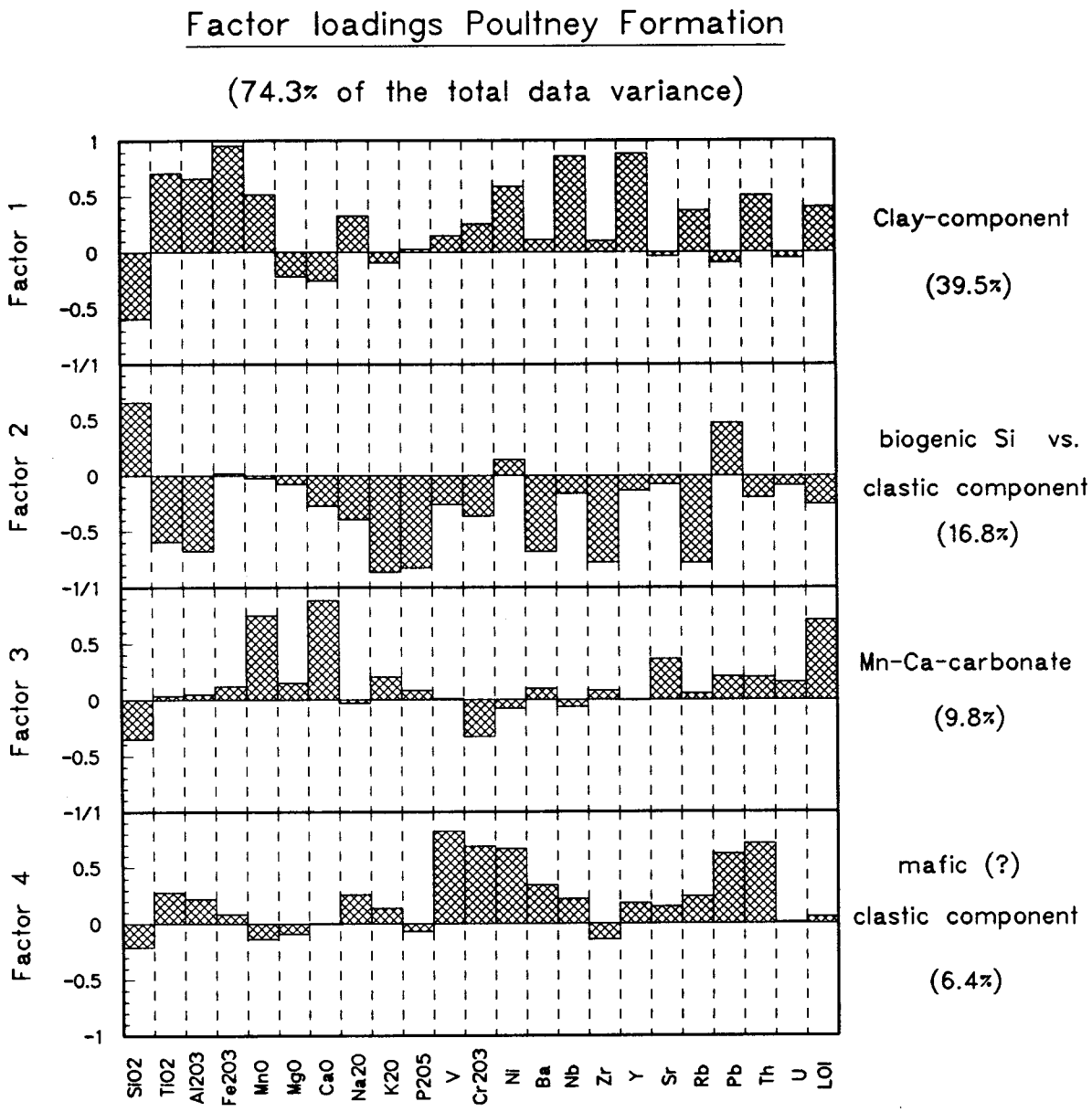

Figure 7.2: Factor loadings from a R-mode factor analysis of 16 samples of the Poultney Formation. Four factors explain 74.3 percent of the compositional variation of the data set. See text for discussion of the different factors.

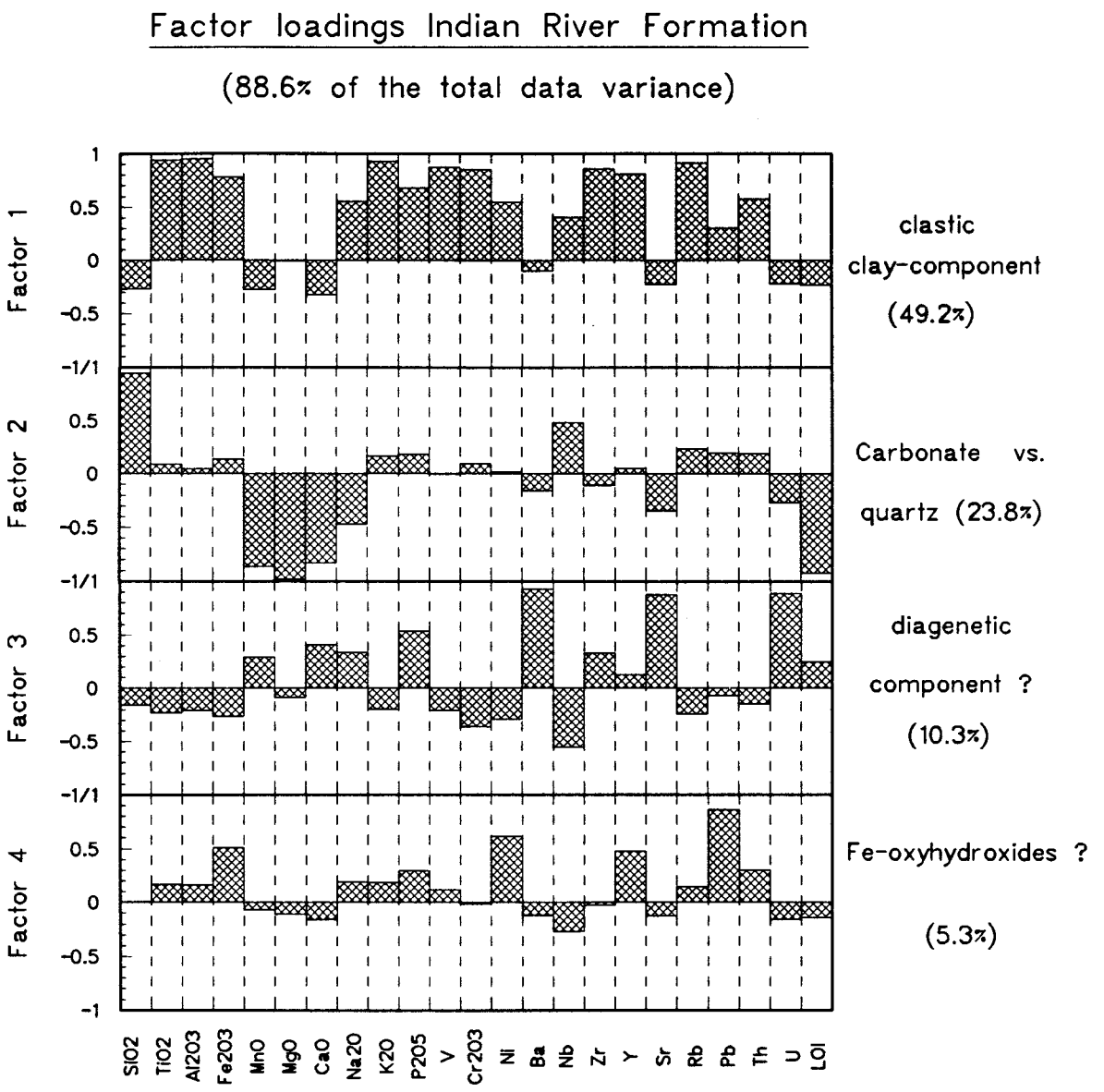

Figure 7.3: Factor loadings from a R-mode factor analysis of 17 samples of the Indian River Formation. Four factors explain 88.6 percent of the compositional variation of the data set. See text for discussion of the different factors.

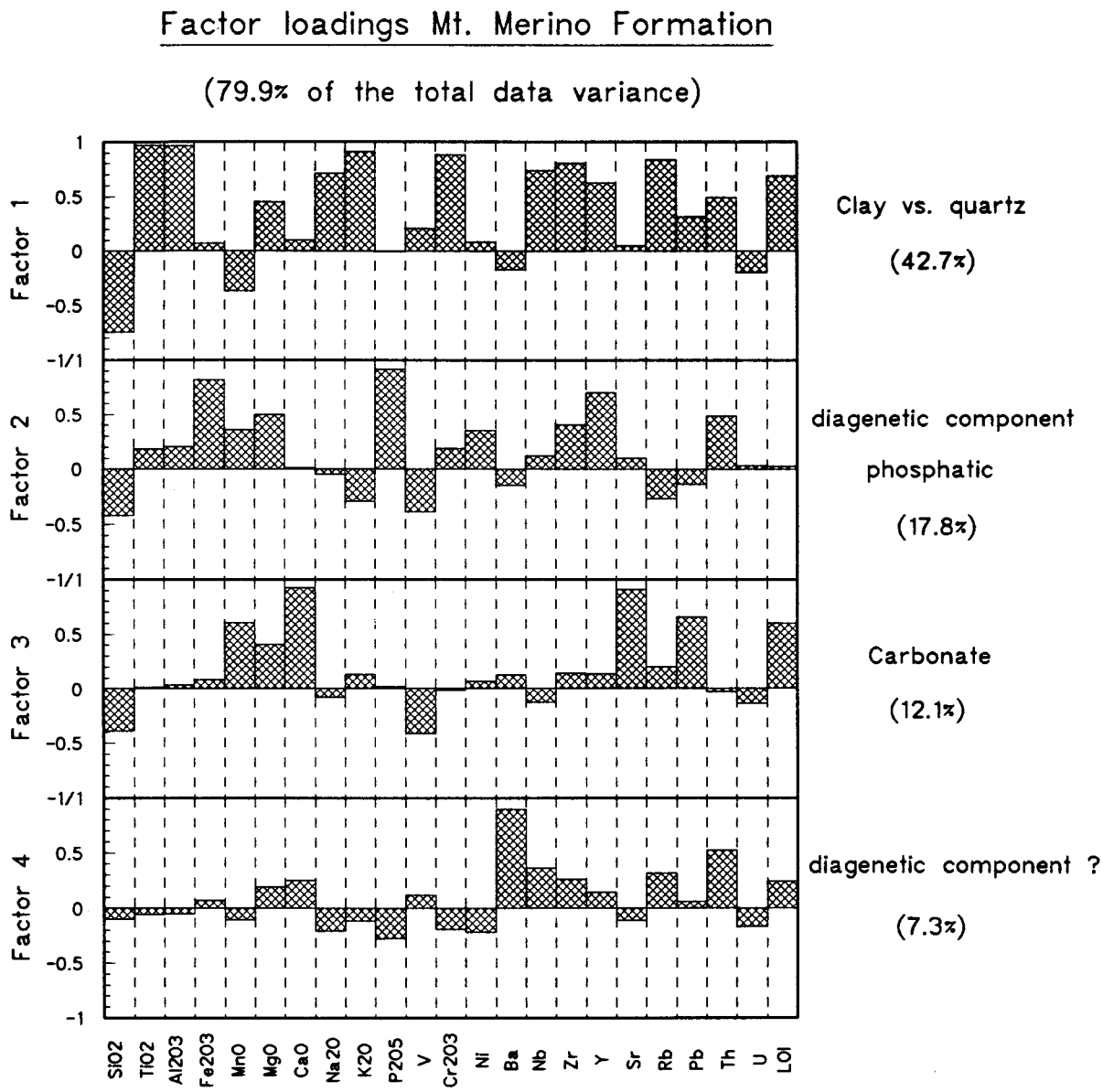

Figure 7.4: Factor loadings from a R-mode factor analysis of 21 samples of the Mt. Merino Formation. Four factors explain 88.6 percent of the compositional variation of the data set. See text for discussion of the different factors.

may similarly be responsible for a separate Si-component. Round and ellipsoidal, 0.1 millimeter large poly-crystalline quartz grains seen on cleavage surfaces in the red slates of the Indian River Formation suggest the original presence of radiolarians (Rowley et al., 1979).

(3) Mn, Ca, LOI, ± Mg appear together in factors of all three data sets. This covariance is interpreted to represent Mn-Ca-Mg-carbonate. It is important to note that the carbonate component is present in the Mt. Merino Formation as well.

(4) Only the Indian River Formation shows a weak component that is characterized by the covariance of Fe, Ni, Pb, ± Y. This component suggests that these elements have an additional sediment source. Except for Y, this factor is similar to the one interpreted as a hydrothermal component in the red Shoal Arm Formation.

(5) In the Mt. Merino Formation, Fe is represented by a separate factor, where it is correlated with P and Y. Possibly, the establishment of Fe in a separate factor in the Mt. Merino Formation is related to element redistribution during the anoxic diagenesis of the Mt. Merino Formation (J.W. Delano, pers. comm., 1990).

Factor 3 of the Indian River Formation sample set and factor 4 of the Mt. Merino Formation sample set show element associations that did not allow straightforward interpretations (i.e., Ba, Sr, U ± Ca and P - a phosphatic component ?, and Ba with Th, respectively). These factors may also result from diagenetic alteration.

Sorting and grain-size

The Zr/Al ratio decreases stratigraphically upward from the Poultney to the Indian River Formation, and remains approximately constant in the Indian River and Mt. Merino Formation (Figure 7.5). This decrease in the relative Zr/Al, or respectively, relative Ti/Zr ratio may be attributed to loss of zircon from the detrital fraction during sediment sorting (van Weering and Klaver, 1985). Under the assumption that the constant ratio between the three elements Ti, Al, and Zr is an indicator of homogeneous,

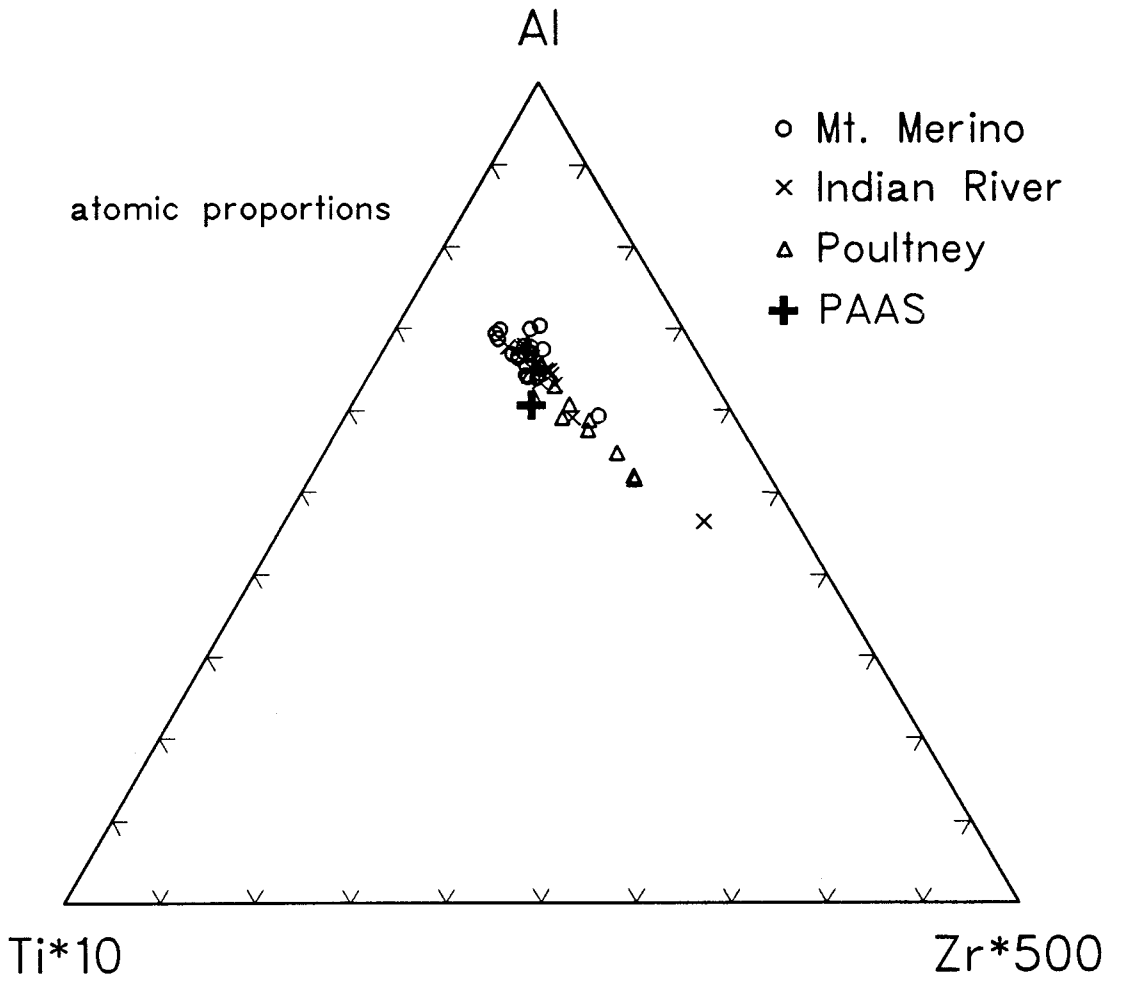

Figure 7.5: Ternary diagram illustrating the compositional relationships of the immobile, detrital elements Ti, Al, and Zr in the three Middle Ordovician formations of the Taconic Allochthon. The decrease in Zr relative to Al and Ti is attributed to a grain-size decrease from the Poultney to the Indian River and the Mt. Merino Formation. The PAAS composition (Taylor and McLennan, 1985) is plotted for reference.

clay grain-size, there appears to be a decrease in grain-size from the Poultney to the Indian River Formation. Since the relative proportions of the three elements do not vary greatly between the Indian River Formation and the Mt. Merino Formation, the clastic grain-size of these two formations may have been similar.

Metal content

The relative changes of metal contents between the three formations were evaluated by plotting Fe, Mn, Cr, Ni, V, and Pb against Al and Zr (Figure 7.6). These metals have similar or slightly lower abundances in the Poultney Formation relative to the PAAS composition, whereas the Indian River Formation (except for V) and the Mt. Merino Formation are both enriched relative to the PAAS composition. It is observed that Fe, Ni, and V have higher abundances in the black slates and cherts of the Mt. Merino Formation than in the red slates of the Indian River Formation. Changes in the Zr/Al ratio are restricted to the Poultney Formation (except for one Indian River Formation sample), and seem to vary at a constant metal/Al ratio. Referring to the previous paragraph, the metal-enrichment of the Mt. Merino Formation and the Indian Formation therefore appears to have been independent of the grain-size. It is concluded that an additional metal component appeared with deposition of the Indian and the Mt. Merino Formation.

Biogenic Si-content

A similar procedure was applied to examine the variation in the biogenic Si-content. The two ternary diagrams in Figure 7.7 demonstrate that the Si-enrichment is restricted to the Indian River Formation and the Mt. Merino Formation. Si is unlikely to be of detrital origin, because the strong Si-enrichment is not accompanied by a variation in the Zr-content. Except for two cherts of the Indian River Formation, the Mt. Merino Formation shows the strongest Si-enrichment. Therefore, the biogenic

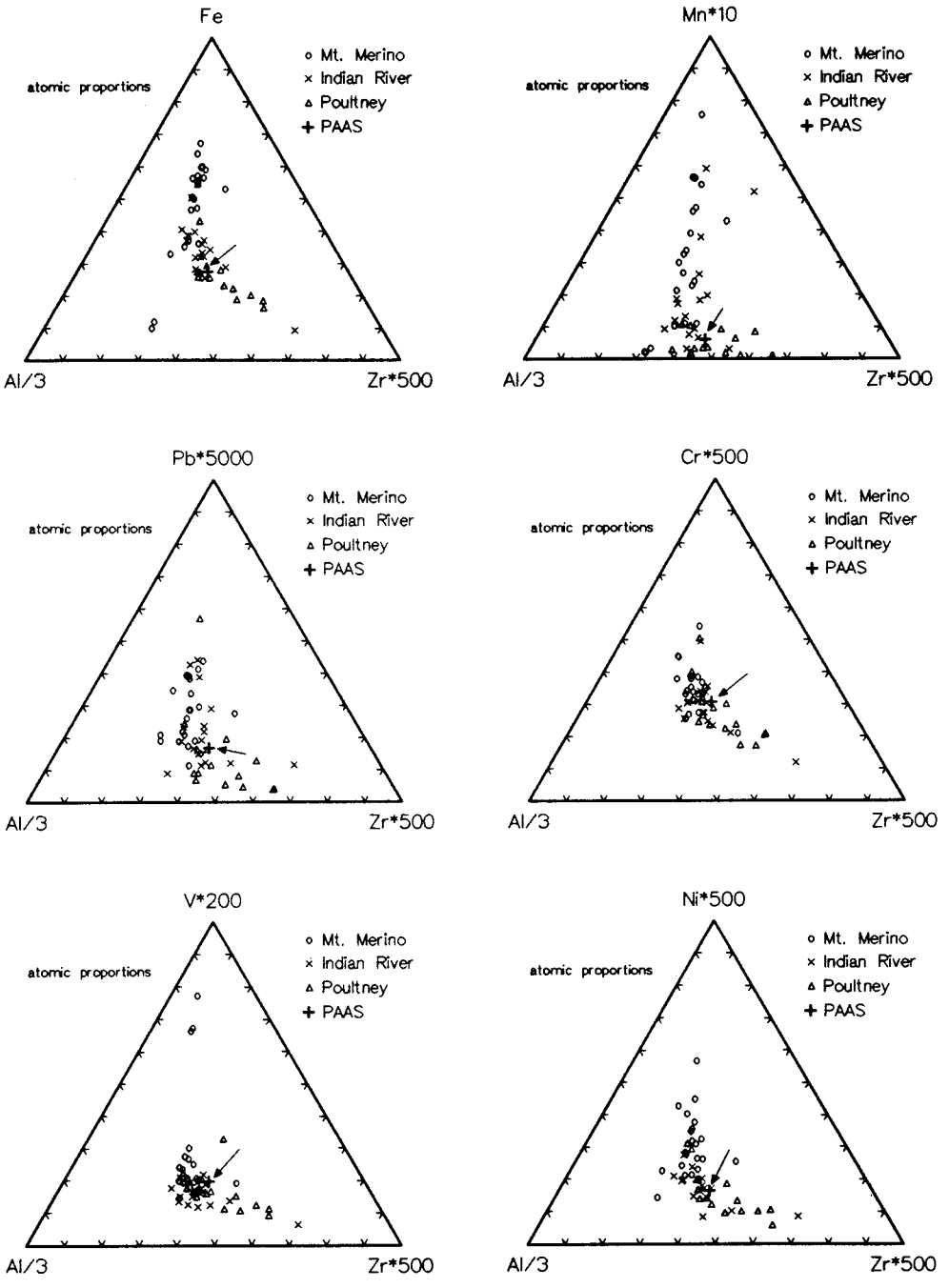

Figure 7.6: Ternary diagrams illustrating the enrichment of Fe, Mn, Cr, Ni, Pb, and V in the Mt. Merino Formation and the Indian River Formation relative to the Poultney Formation and the PAAS composition (arrowed). In general, the enrichment in the Mt. Merino Formation appears to be stronger than in the Indian River Formation.

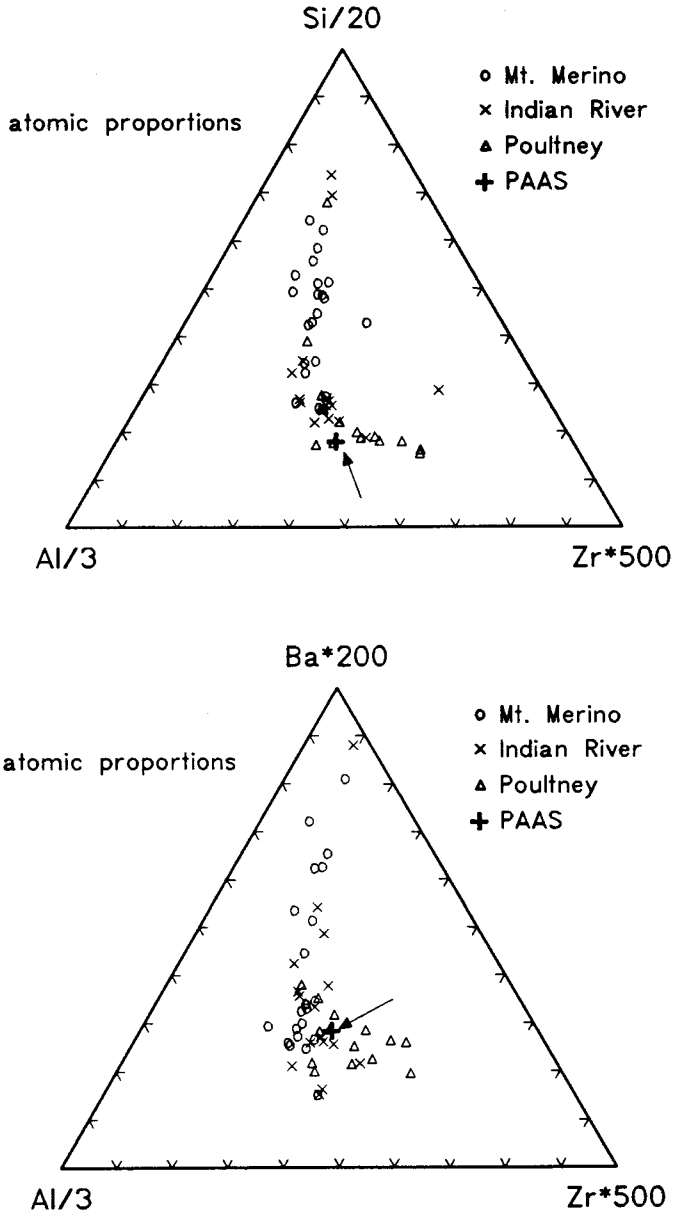

Figure 7.7: Ternary diagrams illustrating the enrichment of biogenic Si and Ba in the Mt. Merino Formation and the Indian River Formation relative to the Poultney Formation and the PAAS composition. The biogenic component appears to be strongest in the Mt. Merino Formation.

Si-content seems to have increased from the Poultney Formation through the Indian River Formation into the Mt. Merino Formation. In the Shoal Arm Formation, the increase in Si was accompanied by an increase in the Ba-content, and served as a constraint for a strong biogenic contribution. Similarly, the Ba-content of the Mt. Merino Formation and the Indian River Formation is elevated (Figure 7.7). There is, however, no consistent trend apparent, since several analysis plot close to the PAAS composition, or are even depleted relative to the PAAS composition. This suggests that Ba may have been remobilized during diagenesis (Brumsack, 1986).

7.2 Comparison of mean elemental abundances of the Taconic sequence and the Shoal Arm Formation

Selected Post-Archean-Average-Shale (PAAS)-normalized mean elemental abundances of the Indian River Formation and the Mt. Merino Formation are compared with the composition of the red argillites, the grey cherts and the black slates of the Shoal Arm Formation (Figure 7.8). The top diagram compares the oxic (grey cherts: suboxic) sediments, and the bottom diagram compares the anoxic sediments. Since the grey cherts appear to occupy an intermediate position with respect to their diagenetic history and/or sedimentary environment, they are displayed in both diagrams. Of particular interest were the metals and the elements of potential biogenic origin. Figure 7.8 compairs the six metals (i.e., Fe, Mn, Cr, Ni, V, Pb) that were found to be enriched in the Indian River Formation (except for V) and the Mt. Merino Formation. Also shown are the mean abundances of Zr and the potentially biogenic elements Si and Ba.

The normalized Zr abundances in all five formations are similar, and suggest minor grain-size differences. The Zr-rich argillites of the upper Shoal Arm Formation were excluded from this comparison. For the remaining argillites, it appears that the

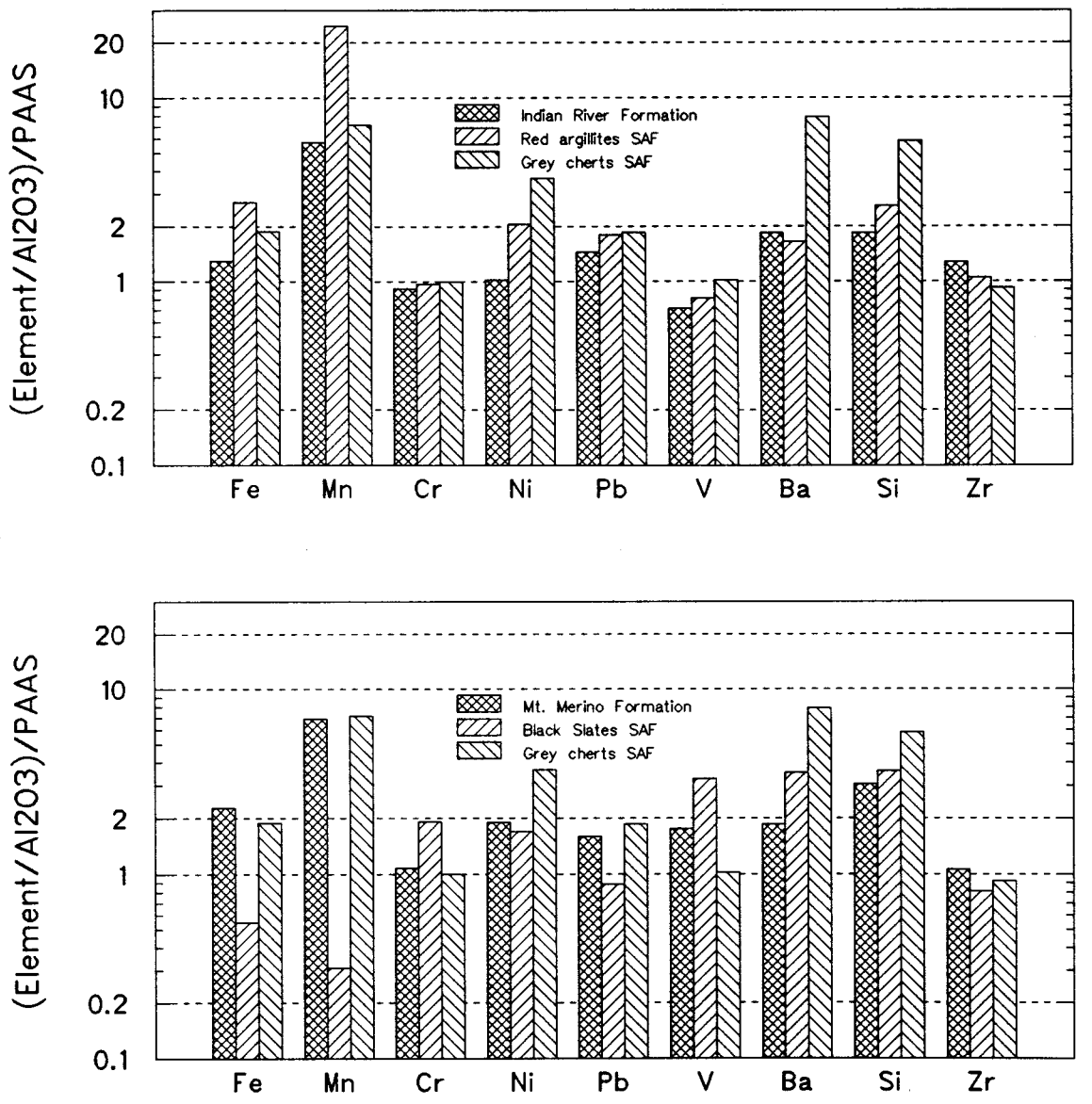

Figure 7.8: Diagram illustrating the mean Al-normalized compositions of Fe, Mn, Cr, Ni, Pb, V, Ba, Si, and Zr relative to the PAAS composition in formations of the Taconic sequence and the Shoal Arm Formation. Bars above "1" indicate higher mean abundances of the normalized element relative to the PAAS composition, bars below "1" indicate lower abundances, respectively. See text for discussion of the relationships between the different formations.

formations of the Taconic Allochthon have slightly higher Zr abundances. Since provenance as well as sorting will affect the Zr/Al ratio, it is uncertain which parameter is responsible for this subtle difference.

In contrast to the red argillites of the Shoal Arm Formation, the Indian River Formation shows only a significant enrichment in Mn. Fe and Pb abundances are also slightly elevated, but clearly lower than in the red argillites of the Shoal Arm Formation. Average V abundances are lower in the oxic sediments compared to the PAAS composition. On the other hand, when comparing anoxic sediments, the Fe, Mn, and Pb abundances of the Mt. Merino Formation are higher than in the black slates of the Shoal Arm Formation. As previously stated, the mean Fe abundances of the Mt. Merino Formation are higher than in the Indian River Formation. In the Shoal Arm Formation, these abundances decrease upwards from the red to the grey to the black Shoal Arm Formation. The Mn abundances in the Indian River Formation and the Mt. Merino Formation remain approximately constant. To explain these differences, the following considerations have to be taken into account:

(1) Differences in duration of the additional source of metals.

(2) Mobilization of Mn and Fe during anoxic diagenesis.

(3) Presence of anions, i.e., S^{2-} and CO_3^{2-} that could precipitate the reduced, dissolved Mn^{2+} and Fe^{2+} either as Mn-carbonate, siderite, pyrite, or as Mn-sulfide (e.g., albandite).

The factor analysis of the Mt. Merino Formation indicates the covariance of Mn with Ca and LOI (factor 3, Figure 7.4). Therefore it seems that at least some of the Mn^{2+} formed Mn-carbonate. Ternary diagrams including Mn and LOI, or Mn with Ca show no clear linear relationships between such element pairs as it might be expected in the case when Mn is exclusively associated with a carbonate phase. The presence of Mn in silicates and MnS (albandite) therefore cannot be excluded. Coexistence of albandite with Mn-carbonate has been demonstrated in anoxic sediments of the Baltic Sea (Suess,

1979). In contrast, in the Shoal Arm Formation, CaO and LOI abundances in the black slates are very low, and Mn is unlikely to be present as Mn-carbonate. It is not clear whether some MnS formed instead, but clearly the sulfide present did not retain all of the available reduced Mn, so that part of the Mn^{2+} was regenerated to the seawater.

Figure 7.6 shows that more analyses of the Mt. Merino Formation are enriched than are depleted in Fe. The net Fe-enrichment suggests that an additional metal source existed into the Mt. Merino Formation. Fe was most likely reduced to Fe^{2+}, and, since the diagenetic reactions probably involved sulfate reduction (e.g Berner, 1984; Froelich et al., 1979), Fe was subsequently precipitated with pyrite. The Shoal Arm Formation is also pyritiferous, suggesting that bacterially mediated sulfate reduction and subsequent pyrite precipitation was probably active in these black slates as well. However, similar to Mn as already discussed in Chapter 6, Fe is depleted in the black slates of the Shoal Arm Formation. In the Mt. Merino Formation, Fe has been observed to be more concentrated in chert beds, whereas the corresponding slate is depleted in Fe (J.W. Delano, unpublished data). Possibly, these cherts served as an important sink for mobilized Fe. Since similar chert beds are not found in the black Shoal Arm Formation, the reduced Fe may have diffused back to the seawater. Alternatively, it may be argued that the underlying grey Shoal Arm Formation served as the sink for the mobilized Fe and Mn. Although the Mn- and Fe-enrichment of the grey Shoal Arm Formation may also be regarded as a continuation of the underlying red Shoal Arm Formation, it is noteworthy that the depletion in Mn and Fe in the black slates corresponds well to the enrichment in Mn and Fe in the grey Shoal Arm Formation (Figure 7.8).

It remains to be answered why the Mt. Merino Formation is more strongly metal-enriched than the underlying Indian River Formation, a characteristic that contrasts with the equivalent units in the Shoal Arm Formation. A continental, detrital source of Fe appears unlikely, because Fe is enriched independently of Zr and Al (Figure 7.5).

For the lower Shoal Arm Formation, a hydrothermal source has been proposed as the

cause for the metal enrichment. Although the factor 4 in Figure 7.3 resembles the factor loadings and the element correlations that were interpreted as a hydrothermal component for the Shoal Arm Formation, independent indicators of hydrothermal activity are missing from the New York State Taconic Allochthon. Therefore, a hydrothermal component in the Indian River Formation may not be excluded as a possible mechanism, but other sources need to be considered as alternatives. Mn-enrichment in deep-sea continental margin sediments has been suggested to result from lateral advection of reduced Mn in O_2-minimum zones (Jenkyns et al., 1991; Force and Cannon, 1988). The Mn is apparently remobilized from continental slope sediments (Heggie et al., 1987; Martin and Knauer, 1984) and reprecipitated at the oxic/anoxic interface. For lateral Fe-advection, a stronger O_2-deficiency is required in the O_2-minimum layer (Spencer and Brewers, 1971; Jacobs et al., 1987). In present-day oceans, only the lateral transport of dissolved Mn has been demonstrated to have a notable effect on the Mn-abundances in coexisting sediments (e.g. Martin and Knauer, 1984; Landing and Bruland, 1987). The concentrations of dissolved Fe (1- 10 nmol/l) (Saager et al., 1989; Landing and Bruland, 1987) in these suboxic oxygen minimum zones seem to be too low to significantly enrich continental margin sediments in Fe. It is unlikely that a present-day O_2-minimum zone could account for the two-fold Fe-enrichment observed in the Taconic rocks. On the other hand, anoxic, silled basins, e.g., the Cariaco trench or the Black Sea, may have sufficiently high dissolved Fe-concentrations, but the water circulation patterns in these basins may not be comparable to the Ordovician foreland basin. Warmer, nutrient-rich seawater and more sluggish circulation in the Middle Ordovician sea seem to be required to produce a severely O_2-depleted water layer. Assuming that an oxygen-depleted mid-water layer existed in the Middle Ordovician ocean, reduced elements from continental slope sediments could have been recycled to the seawater. With time, the O_2-minimum layer may have expanded, and became increasingly anoxic, thus enhancing the transport capabilities of reduced metal species.

At the oxic/anoxic interface of this oxygen minimum zone, Fe and Mn were oxidized to form oxyhydroxides and scavenged trace metals, e.g., Pb and Ni, from the seawater.

Unfortunately, no Indian River Formation-correlative, middle Ordovician continental slope lithologies, which might enable testing of this hypothesis, are exposed in the Taconic Allochthon. A continuously increasing metal enrichment from the Indian River Formation into the Mt. Merino Formation may further constrain the hypothesis of an expanding O_2-minimum layer. This is not possible with the present data, because detailed information of the relative stratigraphic relationship of samples from these two formations is not available.

Chert beds in the lower Mt. Merino Formation have been interpreted as siliceous turbidites derived from shallower parts of the basin (J.W. Delano, pers. comm., 1990). Some of the grey chert beds that are intercalated in the black slates of the Mt. Merino Formation show a mottling, which probably resulted from burrowing organisms. This suggests that episodic, dysaerobic conditions existed during deposition of the Mt. Merino Formation. The bedded chert in the Mt. Merino Formation can be compared to the mottled grey cherts of the Shoal Arm Formation. Although the mean Ba and Si abundances are elevated in the Indian River and the Mt. Merino Formation, these abundances are not as high as the ones seen in the grey Shoal Arm Formation (Figure 7.8). Siliceous and Ba-rich cherts of the Indian River Formation may also be radiolarian turbidites derived from the continental slope. The bioclastic turbidites could be derived from the section of the continental slope that intersected the O_2-minimum layer. The biological productivity would have been highest in this depth zone. Since radiolarian turbidites are more frequent in the lower part of the Mt. Merino Formation, their increased abundance could be interpreted as a reflection of a further increase in the biological productivity with time, whereby increased organic carbon oxidation lead to a gradual expansion of the oxygen minimum zone.

In the Shoal Arm Formation, the grey cherts are considered to represent a transitional facies between the red and green argillites and the black slates. This "buffer" zone is much thinner in the Taconic sequence, and indicates a very abrupt change in the pore-water and/or seawater O_2-content. The different thicknesses may be interpreted as the result of different accumulation rates in the two units. In order to better address this problem, a detailed geochemical profile that also includes the variation in organic carbon content would have to be taken over the transition from Indian River Formation to the Mt. Merino Formation.

7.3 Application of the geologic models to the Taconic sequence

The comparable lithology and the similar tectonic environment and age of the Ordovician Taconic Allochthon in New York State/ Vermont and the Shoal Arm Formation in Newfoundland has already been pointed out in Chapter 1. Based on this similarity, the two models that have been proposed for the Shoal Arm Formation (Figure 6.1 and Figure 6.2) can be tested on the Taconic sequence. In order to establish whether these models appropriately explain the geologic history of the Taconic Allochthon, the important, stratigraphic, lithological and geochemical characteristics are discussed in the following. In particular, this discussion refers to the stages III, IV, and V in Figure 6.1, and the stages III and IV in Figure 6.2.

Synchroneity/ diachroneity;

Similar to the Shoal Arm Formation, no dateable fossils have been reported from the Indian River Formation, and age estimates are based on fossil finds in the Poultney and the Mt. Merino Formation. The upper boundary is constrained by graptolites of the Nemagraptus gracilis zone, which were found at the base of the Mt. Merino Formation

(Rowley et al., 1979). The youngest fossils found in the Poultney Formation have an upper Arenigian age (Landing et al., 1992). Deposition of Indian River-type lithologies could therefore have taken place from the Llanvirn to the upper Llandeilo. Based on these fossil finds, it cannot be demonstrated whether the contact between the Poultney Formation and the Indian River Formation, or the Indian River Formation and the Mt. Merino Formation is diachronous or synchronous. This uncertainty allows that both models proposed in Chapter 6 may be examined.

Sedimentation rates

The existence of a red, oxic, deep-marine sediment requires low bulk sedimentation rates (Kuivila and Murray, 1990). Both in model 1 and model 2 topographic conditions may have existed that favoured oxic sedimentation. Geologic mapping in the Taconic Allochthon suggests that the thickness of the Indian River Formation decreases to the west (Rowley et al., 1979). At some localities in the west, the Mt. Merino Formation is found directly on top of the Poultney Formation. Comparable information is not available to the east. Similar to the red Shoal Arm Formation, it may therefore be argued that closer to the clastic (and bioclastic) sources of the continental slope, oxic sedimentation could not take place.

Landing et al. (1992) pointed out that the continental margin sediments had to surpass a peripheral bulge that migrated westwards in front of the approaching thrust stack. According to Landing et al. (1992), the peripheral bulge would have acted as a barrier to continent-derived detritus, which was ponded to the west of the peripheral bulge. The red shales of the Indian River Formation are assumed to represent a condensed sequence that accumulated under very low clastic sedimentation rates when the continental rise migrated through the peripheral bulge. After passage over the bulge, Mt. Merino shales and cherts were deposited on top of the red shales. Both the diachronous and the synchronous model remain applicable assuming the existence of a

peripheral bulge, since it is not known whether there is a direct relationship between the development of anoxic conditions and the presence of a peripheral bulge. It is alternatively possible that the Indian River Formation was deposited behind the peripheral bulge, and the Mt. Merino Formation developed subsequently as a result of change in ocean water conditions (see below).

Biological productivity, climate, and basin configuration

The highest Si and Ba abundances in the Mt. Merino Formation suggest the strongest biological productivity for the Caradocian. This is consistent with occurrences of black shales in other parts of the world at the same time (Leggett et al., 1981). The black shales may therefore reflect a downward-expanding O_2-minimum zone as a reflection of increasing amounts of organic carbon oxidation in the mid-water depths. High biological productivity is the controlling factor for gradual euxinification of the basin and black shale deposition in the synchronous model (compare Figure 6.1.III-IV).

In the diachronous model, on the other hand, the deepest parts of the basin had developed due to thrust-loading, and may have been separated from free water circulation. The fact that the Mt. Merino Formation is less enriched in Si and Ba than the grey cherts of the Shoal Arm Formation may suggest that the euxinification was not only the result of a biogenic bloom, but was instead influenced by the basin configuration as well. It appears that one process alone may have been insufficient to produce the basin euxinification. Enhanced, biological productivity and the locally humid climate, which could have produced a strong density stratification, may have been the basis for the development of an expanded O_2-minimum layer. Thrust-loading induced subsidence may have resulted in the development of a deep trough with restricted water-circulation. Black shale deposition may have first taken place in this zone. With continued subduction and basin shortening, this zone would have migrated continentwards - analogous to what has been illustrated in Figure 6.2.III-V.

Metal source and mode of transport

Referring to the discussion in Chapter 7.2, an O_2-deficient layer may have developed during the Llandeilo in mid-water depths, and provided metals in increasing amounts to the Indian River Formation and the Mt. Merino Formation. During deposition of the Indian River Formation, an oxidized water layer must have been maintained above the red shales.

In the synchronous model, it appears conceivable that the O_2-deficient layer expanded continuously. Fe and Mn were recycled from the continental slope, laterally advected in the O_2-minimum layer, and recycled to the sediment on the continental rise. The gradual downward-expansion of the O_2-minimum layer continuously thinned the oxidized deep-water layer, so that by the late Llandeilo, the oxidized zone above the red shales had disappeared.

In the diachronous model, the strongest O_2-depleted water mass would have been located above the black shales, and prograded to the west (Figure 6.2.III-V). However, the black shales are enriched in metals (Figure 7.7), and cannot have served as a source. It would be very difficult to demonstrate whether the metals could be derived from sediments in the accretionary stack located to the east. In this context, it is interesting to note that increased concentrations of dissolved Mn have been noted in the seawater above accretionary prisms (e.g., the Barbados ridge, T.H. Donnelly, pers. comm., 1992). Possibly, dissolved Mn contained in fluids that are emanated from the accretionary prism contributes to these elevated Mn-concentrations. On the other hand, if it is assumed that the metal source was located on the continental slope, a second O_2-minimum is required, which existed in mid-water depths and which intersected the continental slope. During deposition of the Indian River Formation, an O_2-saturated zone must have been sandwiched between these two O_2-deficient layers. Such a geometrical configuration would be very complex, and independent lines of evidence are required to constrain such an hypothesis. It would be necessary to recognize two anoxic/suboxic sediment facies of

the same age that accumulated (a) on the continental slope and (b) on the outer trench slope. The limited preservation of the Middle Ordovician strata in the Taconic Allochthon may prohibit a solution of this question.

7.4 Summary

Summarizing the previous discussion, it appears that the two models established for the Shoal Arm Formation are largely applicable to the Taconic Allochthon in New York State/Vermont. Several factors may have acted more or less synchronously to produce a gradual euxinification of the depositional basin. Due to insufficient fossil evidence and preservation of Middle Ordovician strata, the problem of depositional synchroneity or diachroneity cannot be resolved. Depositional diachroneity of the black shales would be consistent with a similar observation on the continental shelf, where the Utica Shale was unquestionably deposited time-transgressively to the west (e.g., Bradley, 1989; Bradley and Kusky, 1986; Cisne et al., 1982). The diachronous model implies that the depositional environment in the flexural foredeep is more important than climatic and biogenic factors, whereby the latter two factors may only have enhanced the euxinification process. The variable thickness of strata rich in biogenic Si (i.e., the grey cherts of the Shoal Arm Formation and the bedded cherts of the lower Mt. Merino Formation) suggest that biological productivity may not have been the determining factor.

The source and mode of transport of Fe, Mn, Cr, Pb and Ni in the Indian River Formation and the Mt. Merino Formation is not entirely clear. The diachronous model requires a complex, stratified O_2-distribution for the time when the Indian River Formation was deposited. If this hypothesis is not accepted, then either no expanded O_2-deficient layer existed during that time, or the diachronous model has to be discarded. Alternatively, the observed enrichment may be explained by a distal

hydrothermal component. This possibility requires no expanded O_2-minimum layer. The hydrothermal component did also not have to stop with Mt. Merino deposition, because this formation is enriched in the same metals as the Indian River Formation.

In every case, the presented data require a revision of the karst hypothesis for the red coloration of the Indian River Formation (Bird and Dewey, 1970). According to this hypothesis, terra rossa soils have been admixed to the continental rise sediments being derived from subaerially exposed shelf lithologies. If this were the case, Fe *and* Al, Th, Ti, Zr as the residual components in such a depleted soil should have been transported together. However, Fe shows independent behavior of these elements (Figure 7.3 and 7.6), and is contained in a independent sedimentary component that has no affinities to detrital, immobile elements. Therefore, it is considered unlikely that the red coloration is derived from eroded terra rossa soils.

8. COMPARISON OF THE MIDDLE ORDOVICIAN ARGILLITES WITH PRECAMBRIAN SEQUENCES CONTAINING BANDED IRON-FORMATIONS

8.1 Introduction

The Fe-enriched hematitic units of the two Middle Ordovician sequences studied occupy the same kind of stratigraphic position as large units of Precambrian, Lake Superior-type banded iron-formations. Figure 8.1 compares the two Ordovician sequences with a generalized Precambrian sequence taking the Lake Superior region as an example. In many of the Precambrian sequences, a shallow-water, transgressive substrate (either very pure quartzites, dolostones, and/or arenite-shale clastics underlie the cherty iron-formations (Morey, 1983; Ojakangas, 1983, Gross and Zajac, 1983). The fact that the Superior-type banded iron-formations show no sedimentary structures indicative of wave action (e.g., ripples or cross bedding) suggests that their deposition took place below the wave base (Simonson, 1985). Therefore, the shallow-water substrate must have been drowned prior to or during deposition of the iron-formations (Beukes, 1989; Simonson, 1985; Ojakangas, 1983).

Drowning and iron-formation deposition could have been accomplished by a eustatic sea level rise (as suggested for iron-formations in "platform"-type settings as the Transvaal Supergroup (Klein and Beukes, 1989)). However, as shown in Figure 8.1, a deep-water euxinic shale and a flysch sequence frequently overlie the iron-formations (Simonson, 1985; Hoffman, 1987; Morey, 1983). From a comparative study of various stratigraphic sequences of early Proterozoic age and their tectonic environment, Hoffman (1987) concluded that these sequences are likely to have been deposited on the outer trench slope of early Proterozoic foredeeps. In his model, the Superior-type banded iron-formation was deposited as the continental margin migrated into the outer trench slope in front of an approaching fold and thrust belt. This tectonic setting would thus

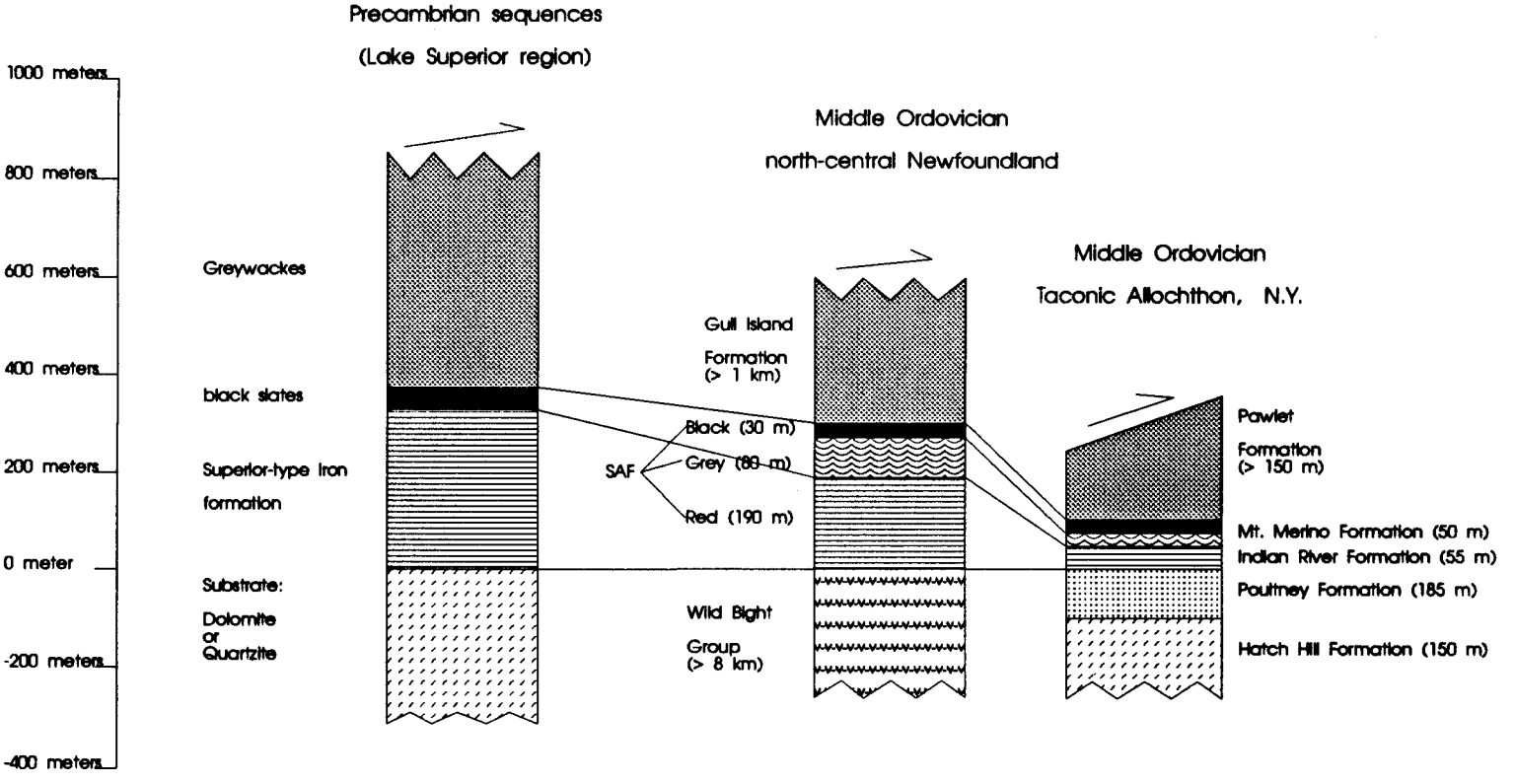

Figure 8.1: Comparison of the stratigraphy of Precambrian sequences containing units of Superior-type banded iron-formations and the two medial Ordovician sequences of north-central Newfoundland and the Taconic Allochthon. The Precambrian sequences of the Lake Superior region are taken as an example . Stratigraphic thickness of units in the Precambrian sequence are from Morey (1983).

be analogous to the Middle Ordovician Utica shale in front of the advancing Taconic sequence (Rowley and Kidd, 1981). However, the Ordovician hematitic units occur exclusively on top of deep-water, continental rise-type sediments. Adjacent Ordovician continental shelf environments show a direct transition from shelf carbonates to black shales (Bradley, 1989). Thus, it appears that environmental conditions during shelf drowning in the Ordovician were unfavourable to iron-formation deposition. Only earlier, when the deep-water continental-rise substrate migrated into the outer trench slope position, were comparable conditions for Fe-enriched sediments produced in these Paleozoic examples.

Based on these general similarities, it appears justified to compare the geochemical composition of the metalliferous argillites of the red Shoal Arm Formation and the Indian River Formation with the composition of Superior-type banded iron-formations some of which seem to occupy a similar stratigraphic position.

This geochemical comparison with banded iron-formations has some shortcomings. For those Precambrian banded iron-formations which display a similar stratigraphic sequence to the Ordovician formations (e.g., the Mesabi Range and the Gunflint Range in the Lake Superior Region (Morey, 1983), or the Kaniapiskau Supergroup in the Labrador trough (Hoffman, 1987)), a satisfactory data set was only available for the major element composition of iron-formations. Recent publications of Klein and Beukes (1989) and Dymek and Klein (1988) of banded iron-formations in the Transvaal Supergroup and the Isua Belt of Greenland provide a wide range of major, minor, trace, and rare earth elements, but the complete stratigraphic sequence in these cases appears less well-established. Also, the study of Dymek and Klein in the Archean Isua Belt of Greenland indicates that the sequence had gone through multiple deformation events and passed metamorphic peak temperatures of 600^{o}C. Here, the original stratigraphic sequence is unclear and considerable secondary alteration has to be accounted for. Another disadvantage is that particular attention was usually paid to the

iron-formations themselves, and not to the surrounding sediments. As a consequence, few analyses of black shales or the underlying substrate are available from the literature.

For the reasons discussed above, a firm geochemical comparison of Superior-type banded iron-formations and their stratigraphic sequences with the Ordovician sediments is not possible. Instead, a similar strategy to the one applied in Chapter 7 is used. First, factor analysis results from a variety of iron-formations are interpreted with respect to their principal sediment components. Then, by using the detailed chemical data set on chert-magnetite and siderite iron-formations of the Kuruman iron-formation of the Transvaal Supergroup (Klein and Beukes, 1989) and the banded iron-formations from the Isua Belt (Dymek and Klein, 1988), the mean abundances of selected major and trace elements in these and the Ordovician formations are examined to further constrain the nature of possible sedimentary sources. Finally, there is a discussion of whether the tectonic models established for the Shoal Arm Formation can be or cannot be applied to the Precambrian sequences.

8.2 Principal sediment components

A data collection of 126 samples analyzed for major elements from the Biwabik iron-formation (Lake Superior Region) (Lepp, 1966), the Sokoman iron-formation (Labrador trough) (Klein, 1978), the Marra Mamba iron-formation (Hamersley Basin, Western Australia) (Klein and Gole, 1981), the Brockman iron-formation (Hamersley Basin, Western Australia) (Ewers and Morris, 1981), the Kuruman iron-formation (Transvaal Supergroup, South Africa) (Klein and Beukes, 1989), an Archean banded iron-formation from the Yilgarn Block, Western Australia (Gole, 1981), and a quartz-magnetite iron-formation from the Isua Belt (West Greenland) (Dymek and Klein, 1988) were used for a factor analysis in order to establish the principal components that may

have controlled iron-formation composition. The ages of these iron-formations range from about 3.8 Ga of the Isua Belt to 1.8 Ga in the Sokoman iron-formation (James, 1983). As for the other factor analyses presented in this work, the factor loadings were rotated using the Varimax rotation. The following discussion refers to Figure 8.1. and Figure 8.2, which display the factor loadings and the factor scores of the analysis, respectively.

Results

Factor 1 depicts the peculiar geochemical composition of a group of Mg-rich iron-formations from the Isua Belt (Figure 8.1). Factor scores of all other iron-formations indicated a constant negative value on this factor (Figure 8.2). This compositional contrast to the rest of the analyses may be the reason why this is the strongest factor of the factor analysis. Dymek and Klein (1988) suggested that the high Mg-content in this iron-formation is the result of admixture of volcanic material. Factor 1 is of no general importance for the other iron-formations.

Factor 2 was established based on higher Ca and LOI abundances in the sideritic iron formations of the Transvaal Supergroup (Kuruman), the Sokoman (Labrador Trough) and Marra Mamba Formation (Hamersley Group). The factor is interpreted to represent a carbonate component. It is important to note that Fe is not associated with the carbonate component, although siderite is probably the dominating Fe-phase in these formations. The other iron-formations, in particular the Brockman iron-formation, show only little variation in this factor.

Factor 3 is interpreted as the clastic component, and is most likely clay. The relative constancy of most of the analyses is surprising. Only few analyses in the Marra Mamba iron-formation and the iron-formation from the Yilgarn Block show higher scores indicating a stronger clastic component in these samples.

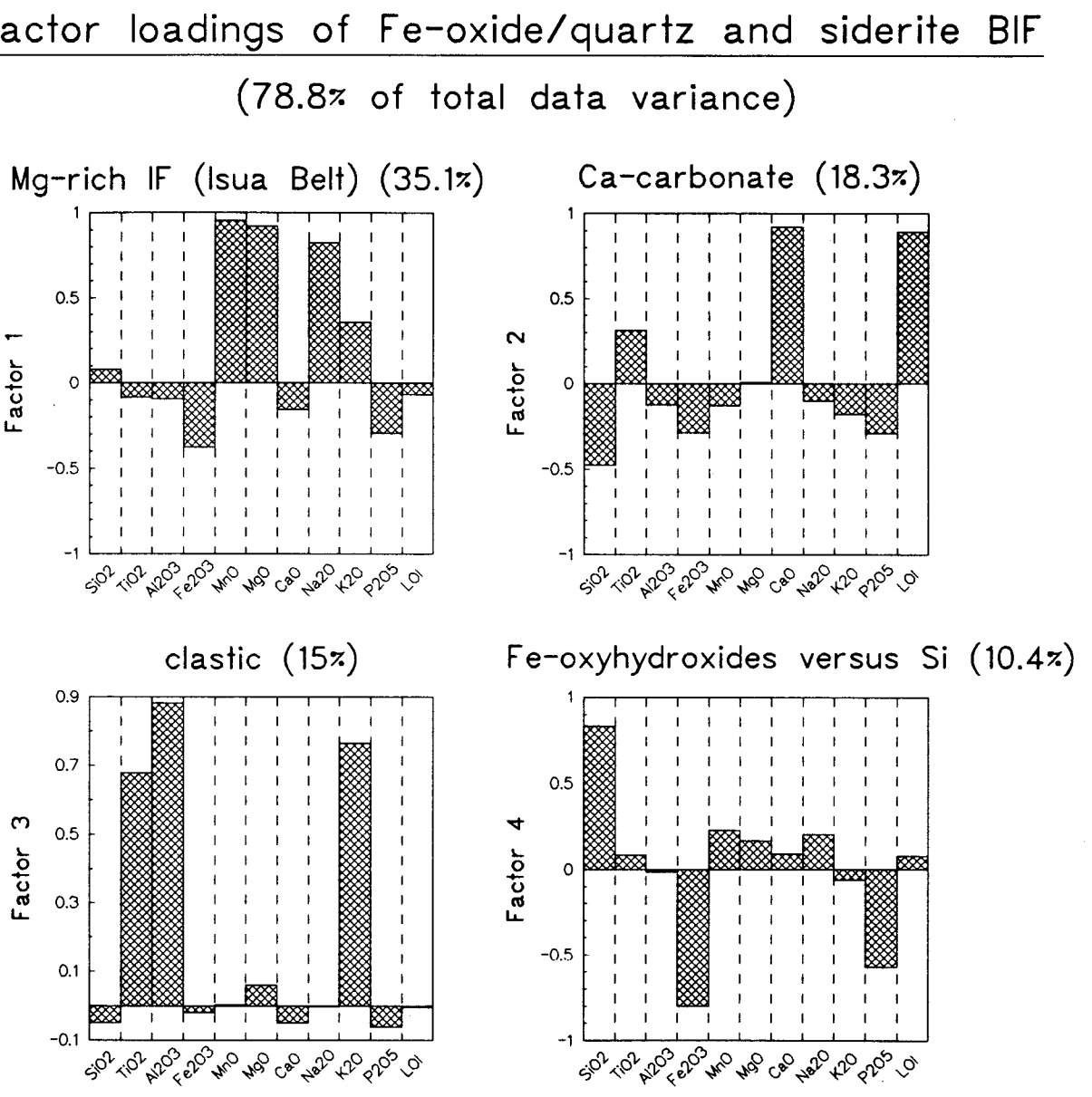

Figure 8.2: Factor loadings of a R-mode factor analysis from a sample set consisting of 126 samples of different Archean and Proterozoic iron-formations. 4 factors explain 78.8% of the total data variance. The percentages indicate the proportion each factor contributes to the total variance of the data set. See text for discussion.

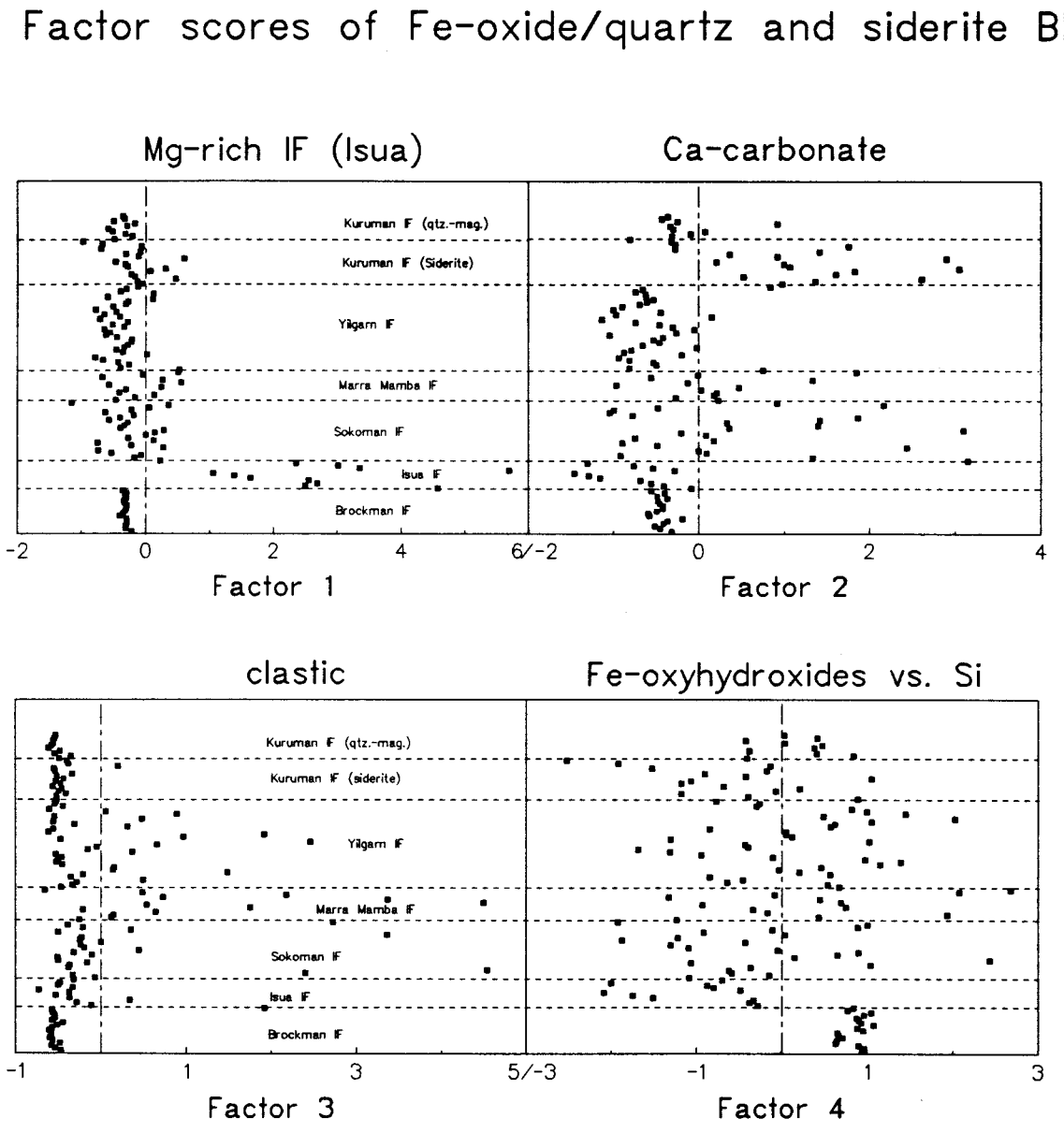

Figure 8.3: Factor scores of the four factors displayed in Figure 8.2. The different iron-formations are displayed on the y-axis. The diagram illustrates that the positive scores of factor one and factor two are limited to some iron-formations, and are not important for the compositional variation in the whole data set.

The variance of Fe, P and Si is represented by factor 4. The contrasting loadings of Fe-P and Si can be interpreted as mutually exclusive abundances of these two groups. Although it may be somewhat speculative, factor 4 could be a reflection of the alternating, Fe-rich versus Si-rich banding that is characteristic of banded iron-formations. Factor scores of the sideritic types showed generally lower values of factor 4, but the general distribution of all samples indicates that factor 4 represents the data variance of the whole data set and is not based on the very different composition of only few iron-formations. It thus appears that factor 3 and factor 4 are represented in all of these groups from which iron-formation analyses were used. The association of P with Fe in factor 4 suggests a primary association of these two elements. Possibly, the precursor of the hematite and/or magnetite were Fe-oxyhydroxides that adsorbed P on their surfaces (Berner, 1973). The factor loadings in factor 4 also preclude an association of Fe with detritus because detrital elements, e.g., Ti and Al, should show only minor loadings.

The factor analysis results thus indicate the omnipresence of competing Fe-P and Si-sources. A shale-like detrital source can also be recognized. These results are insufficient (a) with respect to a clear identity of the source components, and (b) with respect to the genesis of the iron-formations in the context of the general stratigraphic sequence. The minor and trace element analysis provided by Dymek and Klein (1988) and Klein and Beukes (1989) are used to better address these problems. Since these two studies also provide analyses of the related black shale facies, a geochemical comparison with the Ordovician hematitic argillites and black shales is possible.

Elements of interest are Si, Ti, Fe, Mn, K, P, Cr, Ni, Co, Pb, and Zr. The elements Ti, Zr, Cr, and K were chosen to compare the clastic component of the different formations, and Si and Fe because they are the dominating elements of banded iron-formations. The elements Mn, Ni, Co, and Pb have been used because they can be

indicative of hydrothermal or hydrogenous components, and tend to adsorb on Fe-oxyhydroxides.

Figure 8.3 compares the mean abundances of the red Shoal Arm Formation and the Indian River Formation with two oxide iron-formations and a ferruginous shale. Elements have been normalized to Al_2O_3, and these ratios have been divided by the same element ratio of the PAAS-composition (Taylor and McLennan, 1985). The diagrams therefore display the enrichments relative to the reference PAAS-composition. The information illustrated in Figure 8.3 may be summarized as follows:

(1) Si and Fe abundances are much higher in Precambrian banded iron-formations than in the Ordovician argillites.

(2) Other distinctly enriched elements in banded iron-formations include Mn, P, Ni, Pb, ± Co but, relative to Fe, their enrichment is lower.

(3) In the Precambrian examples, the Si abundances are lower in the black shales compared to the iron-formations. In contrast, in the Ordovician examples, the Si abundances increase from the hematitic argillites to the black shales.

(4) Precambrian black shales have generally higher Fe-abundances than Ordovician black shales, and are also more strongly enriched in Ni, Co, and Pb.

(5) The relative abundances of immobile detrital elements in all formations, e.g., Ti, Zr, Cr, K (except for K in the ferruginous shale) are similar to the PAAS-composition, and suggest a shale-like clastic component.

Simple comparison of the composition of the Ordovician examples and Precambrian iron-formations indicates that the detrital component in the Ordovician argillites must have been stronger than in the Precambrian iron-formations. However, it cannot be said whether the high Si and Fe abundances of the Precambrian iron-formations are the result of high accumulation rates of Fe and Si, or whether the clastic

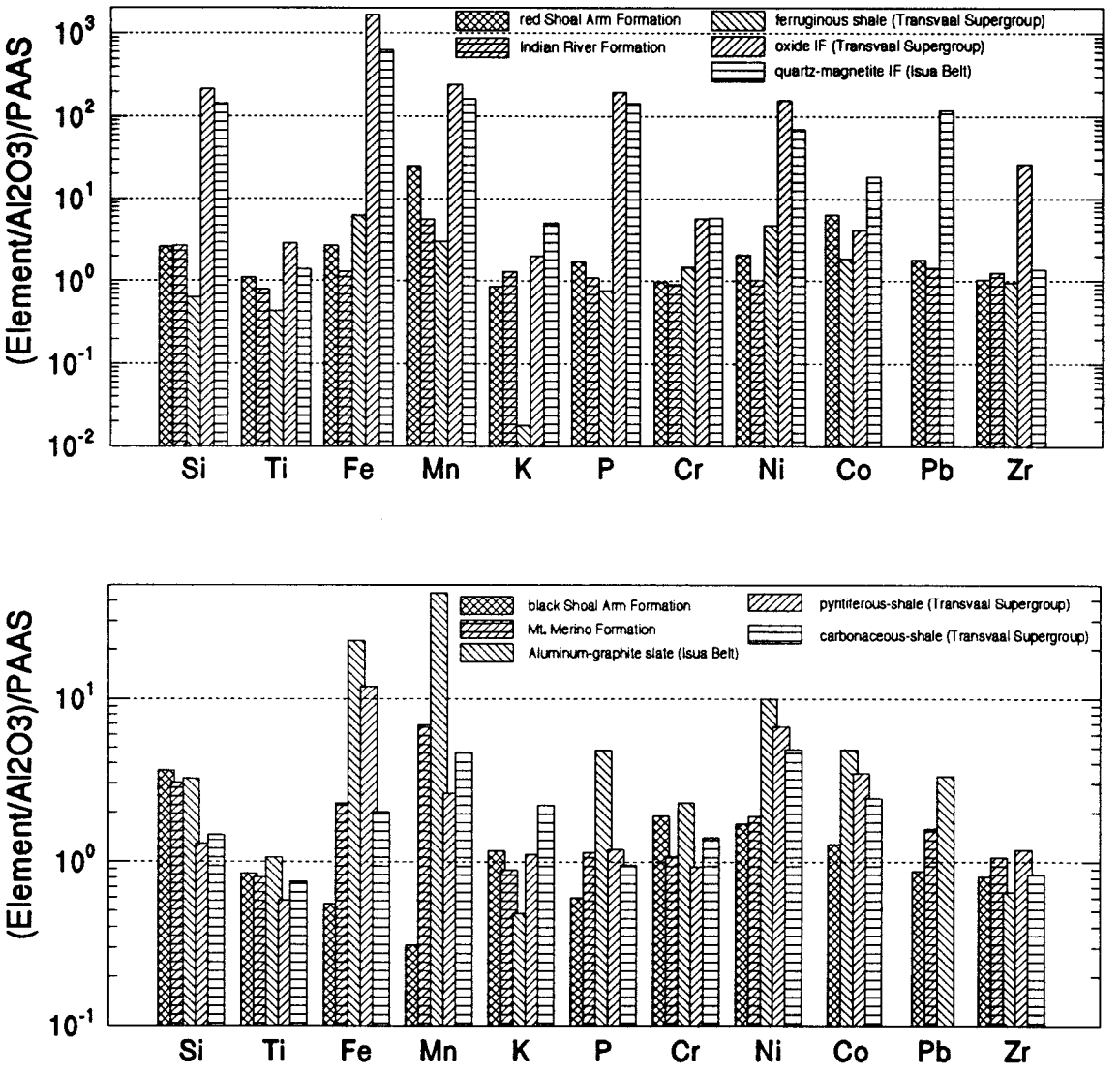

Figure 8.4: Comparison of the relative element enrichments in the hematitic argillites and black slates of the Middle Ordovician Indian River Formation, Mt. Merino Formation and Shoal Arm Formation with Precambrian ferruginous shales, oxide-quartz banded iron-formations and black shales. The elements were normalized to Al_2O_3 and then to the corresponding PAAS-composition. The oxic sediments are shown in the top diagram, the anoxic sediments are shown in the bottom diagram.

component was strongly suppressed in these intervals. Possibly, both mechanisms acted in concert.

The observation that Fe, Ni, Co, Pb, and Mn are enriched in iron-formations correlates well with the observation that P and Fe were found to be associated in one factor (Figure 8.1). The common enrichment constrains the previous interpretation that precursor Fe-oxyhydroxides may have existed, which adsorbed P, Ni, Pb, and Co. Together, these elements could indicate the presence of a hydrothermal component. However, Co, Ni, and P are not enriched to the same degree as Fe. A possible explanation may be that Fe was not immediately oxidized after emanation into the seawater, and remained dissolved as Fe^{2+}. After being oxidized in relatively shallow water, the oxyhydroxides settled rapidly to the seafloor and were buried, which left a relatively short time for the adsorption of Ni, Co, Pb, and P. The smaller enrichment of Mn may be explained by incomplete oxidation of Mn after entering the seawater environment. Alternative explanations for the lower abundances of Mn, Ni, Co, and Pb may be related to diagenetic redistribution, or recycling to the seawater, but a detailed account of such mechanisms is beyond the scope of this chapter.

The different Si abundances in the Precambrian formations and the Ordovician sequences suggest a fundamentally different relationship. In the Shoal Arm Formation and the Middle Ordovician Taconic sequence, the Si abundances increase in the hematitic argillites, but reach their maximum in the overlying black shales. This Si-enrichment was related to an increased accumulation of biogenic Si from dead siliceous plankton. In the Precambrian sequences, however, the strongest Si-enrichment corresponds to periods of strongest Fe-enrichment in oxic sediments, but is lower in the anoxic sediments. On the other hand, the high carbon content of the Precambrian black shales (Klein and Beukes, 1989) suggests that microorganisms were present. The difference is most easily explained by the commonly held view that organisms with Si-skeletons did not exist in the Proterozoic or the Archean oceans (Ewers, 1983; Cloud,

1983). The increased Si abundances of the iron-formations are therefore unlikely to be derived from biogenic material. Inorganic precipitation of Si from the seawater is the most favoured mechanism, although the details of this process are debated (Ewers, 1983; Mel'nik, 1982). In order to determine whether the biological productivity changed during deposition of the iron-formations and the black shales, other chemical indicators are required. As an alternative biogenic element, P may be used to indicate the presence of increased accumulation of organic matter but, except for the Aluminium Graphite slate of the Isua Belt, the black shales are not particularly enriched in P (Figure 8.3). Stable isotope studies $\rho\partial\ \ \partial^{13}C$ and $\partial^{34}S$ may be helpful to further clarify this problem.

8.3 Conclusions

In conclusion, with the presented geochemical data, little supports the notion that the Ordovician hematitic argillites are comparable to Precambrian banded iron-formations. The ultimate source of iron by hydrothermal activity may have been the same in the different formations, but there is little additional evidence to further constrain the origin of the banded iron-formations. A few interesting aspects may, however, be pointed out.

It may be argued that in order to investigate the possibility of reduced metal-transport in Precambrian oceans by comparison with Phanerozoic oceans, it is more instructive to examine the element Mn than the element Fe. A similar suggestion has been made by Force and Cannon (1988). This hypothesis is based on two observations: (a) when comparing the Precambrian and the Ordovician argillites, it becomes apparent that the Fe-enrichment in the Ordovician argillites is low, whereas the Mn-enrichment, although not as strong as in banded iron-formations, is significant. The comparison of a variety of other Phanerozoic stratabound Fe-Mn deposits from similar stratigraphic

positions indicates that, in general, a Mn-enrichment in the Phanerozoic replaces the strong Fe-enrichment in the Precambrian (Jenkyns et al., 1991; Wonder et al., 1988; Force and Cannon, 1988; Crerar et al., 1982). The other argument is that in present-day oxygenated oceans, lateral, long-distance transport of reduced metals has best been demonstrated for Mn (Martin and Knauer, 1984). Truely anoxic conditions would be required for effective dissolved Fe-transport. Long-distance, lateral transport of Fe appears to have been necessary, because banded iron-formations show little or no evidence of proximal volcanic activity. Therefore, because sufficient oxygenation of open Phanerozoic oceans apparently prevented large amounts of dissolved Fe from being transported, Mn, which is transported, should be used for comparison instead. The degree of deoxygenation of the transporting medium (i.e., a seawater layer) may be the most important factor that determined why the Ordovician formations are less enriched in Fe and relatively more strongly enriched in Mn.

The prerequisites to develop a stratigraphic sequence that consists of a succession from oxic to anoxic sediments may have been very different in the Precambrian compared with the Ordovician. In the Ordovician, it may be assumed that the deep-water was sufficiently oxidized (red Shoal Arm Formation). Thus, red shale deposition could occur, wherever bulk sedimentation rates were low enough for oxic diagenesis. Anoxic conditions developed under special circumstances, as a result of different factors, e.g., increased biological productivity, climatic changes, restricted basin circulation and the development of stratified water columns. In contrast, for the Precambrian, it is not clear whether hemipelagic or pelagic sediments accumulated under oxic or anoxic conditions. Only if anoxic conditions existed in larger water depths would material produced at hydrothermal vents have remained in a reduced state and could have been transported by deep ocean currents. Conditions that would have permitted dissolved metal transport may have involved (a) permanent, deep, anoxic waters, or (b) episodic anoxia in restricted water layers. In the following, these two conditions are discussed

for (a) the "platform"-type setting and (b) the outer trench slope setting as the site of iron-formation deposition. Figure 8.5 (a) and (b) illustrate these two possible settings.

The first case envisions permanently anoxic conditions in greater water depths. For iron-formations, where the stratigraphic information is insufficient to argue for a foredeep setting (i.e., the Transvaal Supergroup), a second mechanism, for example upwelling, would be required to transport the dissolved metals from the anoxic layer onto the shelf platform, where O_2-levels in the water may have been high enough for Fe-oxidation and precipitation (Drever, 1974; Klein and Beukes, 1989; Holland, 1984) (Figure 8.5 a).

As mentioned in the introduction of this chapter, Superior-type iron formation may have been deposited in the outer trench slope (Hoffman, 1987), i.e., in much greater water depths. In order to precipitate the vast amounts of iron in the position of an outer trench slope, sufficient O_2-levels in more substantial water depths would have been necessary. Assuming that permanent anoxic conditions prevailed in the deeper parts of the oceans, there is no obvious reason why iron oxidation and precipitation should have occurred on the outer trench slope. Short-term ventilations of the oceans perhaps would have been necessary to provide O_2 to greater depths, but the mechanism or the reason for a ventilation are unclear.

Alternatively, mildly oxic conditions in the Precambrian oceans may have to be envisioned. Lateral transport of dissolved Fe and Mn of potential hydrothermal origin would have been restricted to time periods where expanded, anoxic water layers existed. Conditions that would have favoured the development of a thick anoxic water layer include increased spreading rates, increased volcanic activity, increased CO_2-output, ocean warming, development of a density stratification, and the expected larger propensity of Archean and Proterozoic oceans to turn anoxic in the case of suitable environmental changes. In such time periods, the sea-level should have been high and probably wider shallow-water shelf areas may have developed. These places would have

a.

Drowned shelf platform during transgression

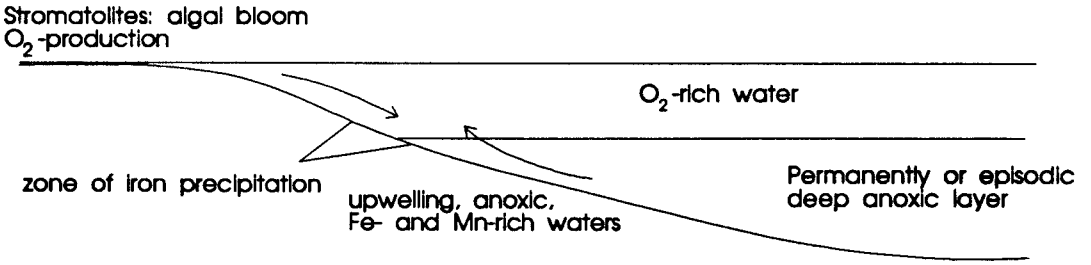

modified after Klein and Beukes (1989)

b.

Drowned shelf as a result of thrust-loading

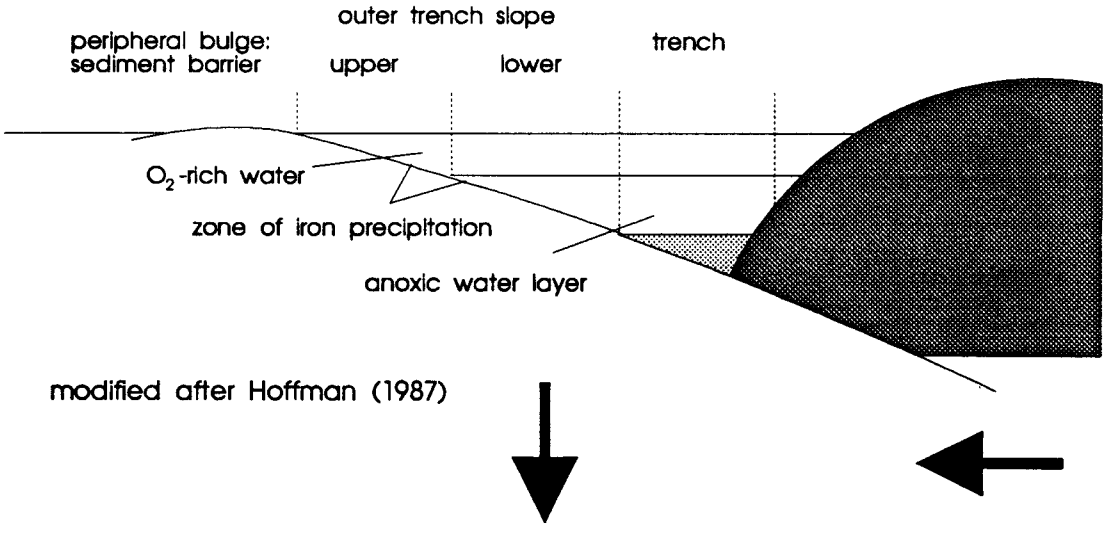

modified after Hoffman (1987)

Figure 8.5: Comparison of the "platform"-type model and the outer trench slope model as the possible sites of iron-formation deposition.

been favourable for an algal bloom, which would have increased the O_2-production in the surface waters. In such a situation, the surface water layer should have been well-oxygenated and separated from an anoxic water layer below. At the oxic/anoxic sediment interface, large quantities of iron could have been oxidized and precipitated.

Similar to the permanent anoxic conditions, the "platform"-type setting for iron-formation deposition requires a second mechanism to transport dissolved metals upwards - eventually in upwelling currents (Drever, 1974) (Figure 8.5 a). If, on the other hand, the iron-formations were deposited as the continental shelf migrated into the position of the outer trench slope, a second mechanism may not be required. Fe-precipitation could have taken place time transgressively in the direction of migration of the foredeep at the point where the oxic/anoxic interface intersected the drowned platform (Figure 8.5 b). With continued subsidence of the shelf platform, the O_2-producing organisms could not exist anymore, the O_2-supply from the atmosphere by wind and waves vanished, and the platform was finally buried under deep-water black shales. The peripheral bulge that would have migrated in front of the trench could have served as a barrier to pond clastic sediments derived from the continent (Figure 8.5 b). To an extent, such a mechanism resembles the proposed tectonic models of the Ordovician sequences, but it is clear that additional work is required to test this model. It is therefore concluded that the tectonic model of a thrust-loading induced shelf drowning sequence in connection with other climatic and tectonic factors may further explain the stratigraphic sequences that contain banded iron-formations. At present, this model is largely based on field relationships, and needs more geochemical evidence, which cannot be given with the available presented data.

REFERENCES

Alt J.C. and Emmermann R. (1985). Geochemistry of hydrothermally altered basalts: Deep Sea Drilling Project Hole 504b, Leg 83. *Initial Reports Deep Sea Drilling Project*, **83**, 249-262.

Aplin A.C. and Cronan D.S. (1985). Ferromanganese oxide deposits from the central Pacific Ocean, II. Nodules and associated sediments. *Geochimica Cosmochimica Acta*, **49**, 437-451.

Argast S. and Donnelly T.W. (1987). The chemical discrimination of clastic sedimentary components. *Journal of Sedimentary Petrology*, **57**, 813-823.

Arnott R.J., Mc Kerrow W.S., and Cocks L.R.M. (1985). The tectonics and depositional history of the Ordovician and Silurian rocks of Notre Dame Bay, Newfoundland. *Canadian Journal of Earth Sciences*, **22**, 607-618.

Barrett T.J., Fralick P.W., and Jarvis I. (1988). Rare earth element chemistry of some Archean iron formations north of Lake Superior, Ontario. *Canadian Journal of Earth Sciences*, **25**, 570-580.

Barrett T.J. (1981). Chemistry and mineralogy of Jurassic bedded chert overlying ophiolites in the Northern Apennines, Italy. *Chemical Geology*, **34**, 289-317.

Basaltic Volcanism Study Project (1981). *Basaltic volcanism on the terrestrial planets.* 1286 p. Pergamon Press, New York.

Bence A.E. and Albee A.L. (1968). Empirical correction factors for the electron microanalysis of silicates and oxides. *Journal of Geology*, **76**, 382-403.

Bergström S.M., Riva J., and Kay M. (1974). Significance of Conodonts, graptolites, and shelly faunas from the Ordovician of western and north-central Newfoundland. *Canadian Journal of Earth Sciences*, **11**, 1625-1660.

Berner R.A. (1973). Phosphate removal from seawater by adsorption on volcanogenic ferric oxides. *Earth and Planetary Science Letters*, **18**, 77-86.

Berner R.A. (1984). Sedimentary pyrite formation: an update. *Geochimica Cosmochimica Acta*, **48**, 605-615.

Bhatia, M.R. (1983). Plate tectonics and geochemical composition of sandstones. *Journal of Geology*, **91**, 611-627.

Bird J.M. and Dewey J.F. (1970). Lithosphere-plate continental margin tectonics and the evolution of the Appalachian Orogen. *Geological Society America Bulletin*, **81**, 1031-1060.

Bischoff R.J. and Rosenbauer J.L. (1983). Uptake and transport of heavy metals by heated seawater: A summary of the experimental results. In *Hydrothermal processes at seafloor spreading centers* (eds. P.A. Rona, K. Bostroem, L. Laubier, and K.L. Smith), pp. 177-196, Plenum, New York.

Blatt H. (1985). Provenance studies and mudrocks. *Journal of Sedimentary Petrology*, 55, 69-75.

Bonatti E., Kraemer T., and Rydell H. (1972b). Classification of and genesis of submarine iron-manganese deposits, in *Ferromanganese deposits on the ocean floor* (ed. D. Horn), pp. 149-165, National Science Foundation.

Bostock H.H (1988). Geology and Petrochemistry of the Ordovician volcano-plutonic Robert's Arm Group, Notre Dame Bay, Newfoundland. *Bulletin Geological Survey of Canada*, 86 p.

Bradley D.C. (1989). Taconic plate kinematics as revealed by foredeep stratigraphy, Appalachian Orogen. *Tectonics*, 8, 1037-1049.

Bradley D.C. and Kusky T. M. (1986). Geologic evidence for rate of plate convergence during the Taconic arc-continent collision. *Journal of Geology*, 94, 667-681.

Brey G. and Schmincke H.U. (1980). Origin and diagenesis of Roque Nublo breccia, Gran Canaria (Canary Islands) - Petrology of Roque Nublo volcanics, II. *Bulletin Volcanology*, 43, 15-33

Bruland K.W. (1980). Oceanographic distributions of cadmium, zinc, nickel, and copper in the north Pacific. *Earth and Planetary Science Letters*, 47, 176-198.

Brumsack, H.J. (1986). The inorganic geochemistry of Cretaceous black shales (DSDP, Leg 41) in comparison to modern upwelling sediments from the Gulf of California. In *North-Atlantic Paleooceanography* (eds. C.P. Summerhayes and N.J. Shackleton), pp. 447-462, Geological Society Special Publications No. 21.

Bryant W.R. and Bennett R.H. (1988). Origin, physical and mineralogical nature of red clays. The Pacific ocean as a model. *Geomarine letters*, 8, 189-249.

Burns R.G. and Burns V.M. (1977b). Mineralogy. In *Marine manganese deposits* (ed. G.P. Glasby), pp. 185-249, New York, Elsevier.

Chester R. and Aston S.R. (1976). Geochemistry of deep-sea sediments. In *Chemical Oceanography*, Vol.6 (eds. J.P. Riley and R. Chester), pp. 281-390, New York, Academic Press,.

Cisne J.L., Karig, D.E., Rabe, B.D., and Hay, B.J. (1982). Topography and tectonics of the Taconic outer trench slope as revealed through gradient analysis of fossil assemblages. *Lethaia*, 15, 343-363.

Cloud P.E. (1983). Banded iron-formations - a gradualist's dilemma. In *Banded iron-formations - facts and problems.* (eds. A.F. Trendall and R.C. Morris), pp. 401-416, Elsevier, Amsterdam.

Coish R.A. (1977). Ocean floor metamorphism in the Betts Cove ophiolite, Newfoundland. *Contributions Mineralogy Petrology*, 60, 255-270.

Colley S., Thomson J., Wilson T.R.S. and Higgs N.C. (1984). Post-depositional migration of elements during diagenesis in brown clay and turbidite sequences in the Northeast Atlantic. *Geochimica Cosmochimica Acta*, 48, 1223-1235.

Coombs D.S., Dowse. M., Grapes S. Kawachi Y., and Roser B. (1985). Geochemistry and origin of Piemontite-bearing and associated manganiferous schists from Arrow Junction, Western Otago, New Zealand. *Chemical Geology*, **48**, 57-78.

Crerar D.A., Namson J., Chyi, M.S., Williams L., and Feigenson M.D. (1982). Manganiferous cherts of the Franciscan assemblage, I. General geology, ancient and modern analogues and implication for hydrothermal convection at oceanic spreading centers. *Econ. Geology*, 77, 519-540

Dean W.E., Arthur M.A. and Stow D.A.V. (1984). Origin and geochemistry of Cretaceous black shales and multicolored claystones, with emphasis on Deep Sea Drilling Project site 530, southern Angola Basin. *Initial Reports Deep Sea Drilling Project*, **75**, 819-843.

Dean W.E. and Parduhn N.L. (1984). Inorganic geochemistry of sediments and rocks recovered from the Southern Angola Basin and adjacent Walvis Ridge, sites 530-532, Deep Sea Drilling Project Leg 75. *Initial Reports Deep Sea Drilling Project*, **75**, 923-958.

Deer W.A., Howie, R.A., and Zussman J. (1985). *An introduction to the rock-forming minerals*. 528 p., Longman, Harlow.

Derry L.A. and Jacobsen S.B. (1990). The chemical evolution of Precambrian seawater: Evidence from REEs in banded iron formations. *Geochimica Cosmochimica Acta*, **54**, 2965-2977.

Dewey J.F., Kennedy, M.J., and Kidd W.S.F. (1983). A geotraverse through the Appalachians of northern Newfoundland. In *Profiles of orogenic belts*, Geodynamic Series 10, American Geohysical Union, 205-241.

Drever J.I. (1974). Geochemical model for the origin of Precambrian banded iron-formation. *Geological Society America Bulletin*, **85**, 1099-1106.

Dymek R.F. and Klein C. (1988). Chemistry and Petrology from the 3.8 By Isua supracrustal belt, Western Greenland. *Precambrian Research*, **39**, 247-302.

Dymond J. (1981). Geochemistry of Nazca Plate surface sediments: An evaluation of hydrothermal, biogenic and hydrogenous sources. In *Nazca plate: Crustal Formation and Andean Convergence* (eds. L.D. Kulm, J. Dymond, E.J. Dasch and D.M. Hussong), pp. 133-173, *Geological Society America Memoir 154.*

Elderfield H. (1981). Metal-organic associations in interstitial waters of Narrangansett sediments. *Am. J. of Sci.*, **281**, 1184-1196.

Ewers W.E. (1983). Chemical factors in the deposition and diagenesis of Banded Iron Formation. In *Iron Formation: Facts and Problems* (eds. A.F. Trendall and R.C. Morris), pp. 491-512, Elsevier, Amsterdam.

Ewers W.E. and Morris R.C. (1981). Studies on the Dales Gorge member of the Brockman Iron formation. *Econ. Geology*, 77, 1929-1953.

Fleet A.J. (1983). Hydrothermal and hydrogenous ferromanganese deposits: Do they form a continuum? The rare earth element evidence. In *Hydrothermal processes at seafloor spreading centers* (eds. P.A. Rona, K. Bostroem, L. Laubier and K.L. Smith), pp. 535-555, Plenum, New York.

Foden J.D. (1983). The petrology of the calcalkaline lavas of Rindjani volcano, east Sunda arc: a model for island-arc petrogenesis. *Journal of Petrology*, **24**, 98-130.

Förstner U. (1982a). Chemical forms of metal enrichment in recent sediments, in Ore genesis (ed. G. Amstutz), pp. 191-199. Springer Verlag, Heidelberg.

Force E.R. and Cannon W.F. (1988). Depositional model for shallow marine Manganese deposits around black shale basin. *Econ. Geology*, **83**, 93-117.

Frey, M. (1987). Very low-grade metamorphism of clastic sedimentary rocks. in *Low Temperature metamorphism* (ed. Frey M.), pp. 9-58. Blackie, Glasgow.

Froelich P.N., Klinkhammer G.P., Bender M.L., Luedtke N.A., Heath G.R., Cullen D., Dauphin P., Hammond D., Hartman B., and Maynard F. (1979). Early oxidation of organic matter in pelagic sediments of the eastern equatorial Atlantic: suboxic diagenesis. *Geochimica Cosmochimica Acta*, **43**, 1075-1090.

Froelich P.N., Bender M.L., Luedtke N.A., Heath G.R., and de Vries (1982). The marine phosphorus cycle. *American Journal of Sciences*, **282**, 474-511.

Garrels R.M. (1987). A model for the deposition of the microbanded Precambrian iron-formations. *Amer. J. Sci.*, **287**, 81-106.

Glasby G.P. (1991). Mineralogy, geochemistry and origin of Pacific red clays: a review. *New Zealand Journal of Geology and Geophysics*, **34**, 167-176.

Gole M. (1981). Archean banded iron formations, Yilgarn Block, Western Australia. *Econ. Geology*, **76**, 1954-1975.

Gray J., Massa D., Boucot A.J. (1982). Caradocian landplant microfossils from Libya. *Geology*, **10**, 197-201.

Gromet L.P., Dymek R.F., Haskin, L.A., and Korotev R.L. (1984). The "North American Shale Composite": Its composition, major and trace element characteristics. *Geochimica Cosmochimica Acta*, **48**, 2469-2482.

Gross G.A. and Zajac I.S. (1983). Iron-formation in fold belts marginal to the Ungava Craton. In *Banded iron-formations - facts and problems* (eds A.F. Trendall and R.C. Morris), pp. 253-288, Elsevier, Amsterdam.

Harland W.B., Cox A.V., Llewellyn C.A.G., Picton A.G., Smith A.G., and Walters R. (1982). A geological time scale, 128p., Cambridge University Press, New York.

Heath G.R. and Dymond J. (1977). Genesis and transformation of metalliferous sediments from the East Pacific Rise, Bauer Deep and Central basin, northwest Nazca plate. *Geological Society America Bulletin*, **88**, 723-733.

Heath G.R., Kovar R.B., and Lopez C. (1985). Elemental composition of Cenozoic pelagic clays from DSDP sites 576 and 578, western N-Pacific. *Initial Reports of the Deep Sea Drilling Project*, **86**, 657-670.

Heggie D., Klinkhammer G.P., and Cullen D. (1987). Manganese and Copper fluxes from continental margin sediments. *Geochimica Cosmochimica Acta*, **51**, 1059-1070.

Hein J.R. and Karl S.M. (1983). Comparison between open ocean and continental margin chert sequences. In *Siliceous deposits in the Pacific region* (eds. A. Iijima, J.R. Hein, and R. Siever), pp. 25-44, Elsevier, Amsterdam.

Helwig, J. (1967). *Stratigraphy and structural history of the New Bay area, North Central Newfoundland*, 212 p., Ph.D. thesis, Columbia University.

Hem J.D. (1972). Chemical factors that affect the availability of iron and manganese in aqueous systems. *Geological Society of America Bulletin*, **83**, 443-450.

Henderson P. (1982). *Inorganic geochemistry*. 353 p., Pergamon Press, Oxford.

Hoffman P.F. (1987). Early Proterozoic foredeeps, foredeep magmatism and the Superior-type iron formation of the Canadian Shield. *American Geophysical Union*, 85-97.

Holland H.D. (1984). *The chemical evolution of the atmosphere and oceans*. Princeton University Press.

Hower J., Eslinger E.V., Hower M.A., and Perry E.A. (1976). Mechanism of burial metamorphism of argillaceous sediment: 1. Mineralogical and chemical evidence. *Geological Society of America Bulletin*, **87**, 725-737.

Hudson A., Bender M.L. and Graham D.W. (1986). Iron enrichments in hydrothermal plumes over the East Pacific Rise. *Earth and Planetary Science Letters*, **79**, 250-254.

Jacobi R.D. and Wasowski J.J. (1985). Geochemistry and plate-tectonic significance of the volcanic rocks of the Summerford Group, north-central Newfoundland. *Geology*, **13**, 126-130.

Jacobs L., Emerson S., and Huested S.S. (1987). Trace metal geochemistry of the Cariaco trench. *Deep Sea Research*, **34**, 965-981.

James H.L. (1983). Distribution of banded iron formation in space and time. In *Iron formations: Facts and Problems* (eds. A.F. Trendall and R.C. morris), pp. 471-490, Elsevier, Amsterdam.

Jarvis I. and Higgs N. (1987). Trace element mobility during early diagenesis in distal turbidites: late Quaternary of Madeira Abyssal Plain, N-Atlantic. In *Geology and Geochemistry of Abyssal Plains* (eds. P.P.E. Weaver and J. Thomson), pp. 179-214. Geological Society Special Publications No 31.

Jenkyns H. C., Geczy, B., and Marshall, J.D. (1991). Jurassic Manganese carbonates of central Europe and the early Toarcian anoxic event. *J. of Geology*, **99**, 137-149.

Jenner G.A. and Fryer B.J. (1980). Geochemistry of the upper Snooks Arm Group basalts, Burlington Peninsula, Newfoundland: evidence against formation in an island-arc. *Canadian Journal of Earth Sciences*, **17**, 888-900.

Kawachi Y., Grapes R.H. Coombs D.S., and Dowse M. (1983). Mineralogy and petrology of a piemontite-bearing schist, western Otago, New Zealand. *Journal of Metamorphic Geology*, **1**, 353-372.

Klein C. (1978). Regional metamorphism of Proterozoic iron formation, Labrador trough, Canada. *American Mineralogist*, **63**, 898-912.

Klein C. and Gole M. (1981). Mineralogy and parts of the Marra Mamba Iron-formation, Hamersley Basin, Western Australia. *American Mineralogist*, **66**, 507-525.

Klein C. and Beukes N.J. (1989). Geochemistry and sedimentology of a facies transition from limestone to iron- formation deposition in the early Proterozoic Transvaal Supergroup, South Africa. *Econ Geology*, **84**, 1733-1774.

Kuijpers A., De Lange G.J., and Duin E.J.Th. (1987). Areal sedimentation rate patterns of the southern Nares Abyssal Plain, western N Atlantic. In *Geology and Geochemistry of Abyssal Plains* (eds. P.P.E. Weaver and J. Thomson), pp. 13-22. Geological Society Special Publications No 31.

Kusky T.M. (1985). *Geology of the Frozen Ocean Lake - New Bay Pond area, north-central Newfoundland*, 214 p., M.Sc. thesis, SUNY Albany.

LaBerge G.L., Robbins E.I. and Han T.M. (1987). A model for the precipitation of Precambrian banded iron formations A: Geological evidence. In *Precambrian Banded Iron Formations* (eds. P.W.U. Appel and G.L. LaBerge), pp. 69-96, Theophrastus Publications, S.A., Athens, Greece.

Landing E., Benus A.P., and Whitney P.R. (1992). Early and Middle Ordovician continental slope deposition: Shale cycles and sandstones in the New York Promontory and Quebec Reentrant region. *Bulletin Number 474, New York State Museum/Geological Survey*, 39 p., Albany, New York.

Landing W.M. and Bruland K.W. (1987). The contrasting biogeochemistry of iron and manganese in the Pacific ocean. *Geochimica Cosmochimica Acta*, **51**, 29-43.

Leggett J.K. (1982). Geochemistry of Cocos plate pelagic hemipelagic sediments in hole 487, Deep Sea Drilling Project 66. In *Initial Reports of the Deep Sea drilling Project*, **66**, 683-686.

Leggett J.K. (1980). British lower Paleozoic shales and their palaeo-oceanographic significance. *Journal of the Geological Society London*, **137**, 139-156.

Leggett J.K., McKerrow W.S., Cocks L.R.M., and Rickards R.B. (1981). Periodicity in the Paleozoic realm. *Journal of the Geological Society London*, **138**, 167-176.

Leinen M. (1987). The origin of paleochemical signatures in North Pacific pelagic clays: Partitioning experiments. *Geochimica Cosmochimica Acta*, **51**, 305-319.

Leinen, M. (1989). The pelagic clay province of the North-Pacific ocean. In *The Geology of North-America. Vol.N, The Eastern Pacific Ocean and Hawaii.* The Geological Society of America, pp. 323-335, Boulder, Co..

Leinen M. and Stakes D. (1979). Metal accumulation rates in the central equatorial Pacific during Cenozoic time. *Geological Society America,* **90**, 357-375.

Lepp H. (1966). Chemical composition of the Biwabik iron-formation. *Economic Geology*, **61**, 243-250.

Lorenz, B.E. (1985). A study of the igneous intrusive rocks of the Dunnage Mélange, Newfoundland, 219p., Ph.D. thesis, Memorial University, St. John's.

Lupton J.E. and Craig, H. (1981). A major ^{3}He source at $15^{o}S$ on the East Pacific Rise. *Science*, **214**, 13-18.

Lyle M. Owen R.M. and Leinen M. (1986). History of hydrothermal sedimentation at the East Pacific Rise, $19^{o}S$. In *Initial Reports of the Deep Sea Drilling Project*, 92, 585-596.

Marchig V. and Erzinger J. (1986). Chemical composition of Pacific sediments near $20^{o}S$, changes with increasing distances from the East Pacific Rise. In *Initial Reports of the Deep Sea Drilling Project,* **92**, 371-382.

Marchig V. and Gundlach H. (1982). Iron-rich metalliferous sediments on the East Pacific Rise: Prototype of undifferentiated metalliferous sediment on divergent plate boundaries. *Earth and Planetary Science Letters*, **58**, 361-382.

Martin J.H. and Knauer G.A. (1984). VERTEX: Manganese transport through oxygen minima. *Earth and Planetary Science Letters*, **67**, 35-47.

Martin J.H. and Knauer G.A. (1973). The elemental composition of plankton. *Geochimica Cosmochimica Acta*, **37**, 1639-1654.

Maynard J.B. (1983). *Geochemistry of sedimentary ore deposits*, 305 p., Springer Verlag, New York.

McKerrow W.S. (1979). Ordovician and Silurian changes in sea level. *Journal of the Geological Society London*, **136**, 137-145.

Mel'nik Yu.P. (1982). *Precambrian banded iron-formations. Physicochemical conditions of formation.* 310 p., Elsevier, Amsterdam.

Minoura K., Nakaya S., Takemura A. (1991). Origin of manganese carbonates in Jurassic red shale. *Sedimentology*, **38**, 137-152.

Morey G.B. (1983). Animikie basin, Lake Superior region U.S.A.. In *Iron formations: Facts and Problems* (eds. A.F. Trendall and R.C. Morris), pp. 13-67, Elsevier, Amsterdam

Morton A.C., Todd. S.P., and Haughton P.D.W. (eds.) (1991). *Developments in sedimentary provenance studies*, 370 p., Geological Society Special Publications No 57.

Murray J.W, Balistieri L.S., Paul B. (1984). The oxidation state of manganese in marine sediments and ferromanganese nodules. *Geochimica Cosmochimica Acta*, **48**, 1237-1247.

Nelson K.D. (1979). *Geology of the Badger Bay - Seal Bay area, north-central Newfoundland*, 184 p. Ph.D. thesis SUNY Albany.

Neuman, R.B. (1984). Geology and paleobiology of islands in the Ordovician Iapetus Ocean: Review and implications. *Geological Society America Bulletin*, **95**, 1188-1201.

Nisbet E.G. and Price J. (1974). Siliceous turbidites as redeposited ocean ridge derived sediments. In *Pelagic sediments: on land and under the sea* (eds. K.J. Hsü and H.C. Jenkyns), pp. 351-366, Special Publications International Association of Sedimentologists, 1.

Ojakangas R.W. (1983). Tidal deposits in the early Proterozoic basin of the Lake Superior region - the Palms and the Pokegama formations: Evidence for subtidal-shelf deposition of Superior-type banded iron-formation. *Geological Society of America Memoir 160*, 49-66.

Pedersen T.F. and Price N.B. (1982). The geochemistry of manganese carbonate in Panama basin sediments. *Geochimica Cosmochimica Acta*, **46**, 59-68.

Pettijohn F.J., Potter P.E., and Siever R. (1984). *Sand and sandstone*. 553 p. Springer Verlag, New York, 2nd edition.

Pickering K.T., Bassett G., and Siveter D.J. (1988). Late Ordovician - early Silurian destruction of the Iapetus Ocean: Newfoundland, British Isles, and Scandinavia - a discussion. *Transactions of the Royal Society of Edinburgh*, **79**, 361-382.

Piper D.Z., Rude P.D., and Monteith S. (1987). The chemistry and mineralogy of haloed burrows in pelagic sediment at DOMES site A: The equatorial North Pacific. *Marine Geology*, **74**, 41-55.

Piper D.Z., Basler J.R., and Bischoff P.D. (1984). Oxidation state of marine manganese nodules. *Geochimica Cosmochimica Acta*, **48**, 2347-2355.

Roser B.P., and Korsch R.J. (1986). Determination of tectonic setting of sandstone-mudstone suites using SiO_2 content and K_2O/Na_2O ratio. *Journal of Geology*, **94**, 635-650.

Rowley D.B. and Kidd W.S.F. (1981). Stratigraphic relationships and detrital composition of the medial Ordovician flysch of western New England: Implications for the tectonic evolution of the Taconic orogeny. *Journal of Geology*, **89**, 199-218.

Rowley, D.B., Kidd W.S.F., and Delano L.L. (1979). Detailed stratigraphic and structural features of the Giddings Brooks slice of the Taconic Allochthon in the Granville area. In *New York State Geological Association and N.E.I.G.C. Guidebook* (ed. G.M. Friedman), pp. 186-242.

Saager P.M., De Baar H.J.W., and Burkhill P.H. (1989). Manganese and iron in Indian Ocean waters. *Geochimica Cosmochimica Acta*, **53**, 2259-2267.

Sawlan J.J. and Murray J.W. (1983). Trace metal mobilization in the interstitial waters of red clay and hemipelagic marine sediments. *Earth and Planetary Science Letters*, **64**, 213-230.

Schlanger S.O. and Jenkyns H.C. (1976). Cretaceous anoxic events: Causes and consequences. *Geologie en Mijnbouw*, **55**, 179-184.

Simonson B.M. (1985). Sedimentological constraints on the origin of Precambrian iron-formations. *Geological Society America Bulletin*, **96**, 244-252.

Spencer D.W. and Brewers P.G. (1971). Vertical advection diffusion and redox potentials as controls on the distribution of manganese and other trace metals dissolved in waters of the Black Sea. *Journal of Geophysical Research*, **76**, 5877-5892.

Stow D.A.V. (1986). Deep clastic seas. In *Sedimentary environments and facies* (ed. H.G. Reading), pp. 399-444, Blackwells, Oxford.

Suess, E. (1979). Mineral phases formed in anoxic sediments by microbial decomposition of organic matter. *Geochimica Cosmochimica Acta*, **43**, 339-352.

Sugisaki R., Sugitani K., Adachi M. (1991). Manganese carbonate bands as an indicator of hemipelagic sedimentary environments. *Journal of Geology*, **99**, 23-40.

Swinden H.S., Jenner G.A., Fryer B.J., Hertogen J., Roddick J.C. (1990). Petrogenesis and paleotectonic history of the Wild Bight Group, an Ordovician island arc in central Newfoundland. *Contributions Mineralogy Petrology*, **105**, 219-241.

Taylor S.R. and McLennan S.M. (1985). *The continental crust: Its composition and evolution*, 312p., Blackwell Scientific Publications, Oxford.

Thomson J., Higgs N.C., Jarvis I., Hydes D.J., Colley S., Wilson T.R.S. (1986). The behavior of manganese in Atlantic carbonate sediments. *Geochimica Cosmochimica Acta*, **50**, 1807-1818.

Thomson J., Carpenter M.S.N., Colley S., Wilson T.R.S., Elderfield H., and Kennedy H. (1984). Metal accumulation rats in northwest Atlantic pelagic sediments. *Geochimica Cosmochimica Acta*, **48**, 1935-1948.

Toyoda K. and Masuda A. (1990). Sedimentary environments and chemical composition of Pacific pelagic sediments. *Chemical Geology*, **88**, 127-141.

Turekian K.K. and Wedepohl K.H. (1961). Distribution of the elements in some major units of the earth's crust. *Geological Society of America Bulletin*, **72**, 175-192.

Van der Pluijm B.A. and van Staal C.R. (1988). Characteristics and evolution of the central mobile belt, Canadian Appalachians. *Journal of Geology*, **96**, 535-547.

Van der Voo R., Johnson R.E., Van der Pluijm B.A., and Knudson L. (1991). Paleogeography of some vestiges of Iapetus: Paleomagnetism of the Ordovician Robert's Arm Group, and Chanceport Groups, central Newfoundland. *Geological Society of America Bulletin*, **103**, 1564-1575.

Van Weering T.C.E. and Klaver G.Th. (1985). Trace element fractionation and distribution in turbidites, homogeneous and pelagic deposits; the Zaire fan, southeast Atlantic Ocean. *Geomarine Letters*, **5**, 165-170.

Viereck L.G., Griffin B.J., Schmincke H.U., and Pritchard R.G. (1982). Volcaniclastic rocks of the Reydarfjordur Drill Hole, eastern Iceland. 2. Alteration. *Journal of Geophysical Research*, **87**, 6459-6476.

Vine J.D. and Tourtelot E.B. (1970). Geochemistry of black shale deposits - a summary report. *Economic Geology*, **65**, 253-272.

Wasowski J.J. (1987). *Geology and plate-tectonic significance of rock units in the New Bay - Bay of Exploits area, North-central Newfoundland*, 219p., Ph.D. thesis, SUNY Buffalo.

Weber J.N. and Middleton G.V. (1961). Geochemistry of the turbidites of the Normannskill and Charny formations - I. *Geochimica Cosmochimica Acta*, **22**, 200-243.

Wedepohl K.H. (1964). Untersuchungen am Kupferschiefer in Nordwestdeutschland; ein Beitrag zur Deutung der Genese bituminöser Sedimente. *Geochimica Cosmochimica Acta*, **28**, 305-364.

Williams H. (1979). Appalachian orogen in Canada. *Canadian Journal of Earth Sciences*, **16**, 792-807.

Wonder J.D., Spry P.G., and Windom K.E. (1988). Geochemistry and origin of Manganese-rich rocks related to iron formation and Sulfide deposits, Western Georgia. *Econ Geology*, **83**, 1070-1081.

Appendix I

Composition of samples from upper Wild Bight Group, Shoal Arm Formation, and Gull Island Formation

SAMPLE #	Level (m)	SiO2	TiO2	Al2O3	Fe2O3	MnO	MgO	CaO	Na2O	K2O	P2O5	V	Cr2O3	Ni	BaO
	GREYWACKES														
90-005		66.25	0.63	14.54	6.50	0.09	3.34	0.84	1.90	2.59	0.10	104.00	138.00	46.00	522.00
90-006		70.97	0.57	13.14	4.49	0.08	1.87	1.67	3.20	1.71	0.12	78.00	126.00	10.00	279.00
SA-39		59.86	0.62	17.67	6.48	0.07	3.47	1.43	2.98	3.73	0.11	111.00	116.00	44.00	923.00
SA-38		63.26	0.65	15.28	6.85	0.09	3.74	1.41	3.09	2.50	0.12	128.00	177.00	51.00	588.00
SA-26		70.72	0.49	13.07	4.97	0.06	2.34	0.98	2.15	2.58	0.09	84.00	156.00	37.00	388.00
SA-23		58.40	0.75	17.84	8.42	0.12	3.92	1.27	2.08	3.44	0.10	157.00	161.00	72.00	542.00
GI-32	355.00	59.42	0.81	17.33	8.03	0.07	3.29	0.46	2.58	2.86	0.12	155.00	260.00	108.00	1278.00
	BLACK SLATES														
GI-40	348.00	83.47	0.25	6.05	2.87	0.01	0.81	0.04	0.66	1.30	0.05	226.00	121.00	34.00	957.00
GI-33	347.00	77.27	0.53	10.99	0.64	0.01	0.51	0.01	1.65	2.57	0.02	201.00	188.00	10.00	1369.00
GI-39	345.00	82.09	0.30	7.12	2.35	0.01	0.93	0.04	0.77	1.68	0.05	268.00	123.00	82.00	1128.00
GI-41	337.00	88.77	0.21	4.93	0.56	0.01	0.31	0.01	0.29	1.23	0.01	117.00	141.00	10.00	906.00
GI-42	335.00	83.86	0.34	7.57	0.54	0.01	0.46	0.01	0.80	1.80	0.02	188.00	125.00	13.00	1343.00
90-008		87.78	0.27	5.55	1.01	0.02	0.32	0.02	0.07	1.24	0.04	152.00	43.00	10.00	802.00
#332A		84.35	0.31	6.98	2.36	0.02	1.00	0.26	0.24	1.49	0.06	126.00	53.00	85.00	150.00
	GREY CHERTS														
GI-38	325.00	92.52	0.16	2.44	1.13	0.15	0.39	0.57	0.37	0.67	0.03	16.00	17.00	10.00	1137.00
GI-35	320.00	86.56	0.26	4.97	2.01	0.06	0.72	0.45	0.53	1.36	0.04	50.00	37.00	56.00	1979.00
GI-36	310.00	89.02	0.23	3.98	1.81	0.07	0.74	0.61	0.48	1.05	0.03	41.00	39.00	34.00	1532.00
GI-34	300.00	85.69	0.42	6.53	2.82	0.01	0.76	0.14	0.26	1.68	0.12	67.00	15.00	46.00	2754.00
GI-37	280.00	92.15	0.21	2.98	1.43	0.08	0.25	0.21	0.27	0.71	0.03	39.00	27.00	24.00	1093.00
SA-20	255.00	77.35	0.36	7.63	8.42	0.54	1.24	0.59	1.18	0.65	0.07	38.00	78.00	35.00	804.00
90-009		91.65	0.19	3.34	1.15	0.27	0.34	0.52	0.22	0.91	0.03	21.00	15.00	21.00	1325.00
LH-2		83.02	0.29	4.19	7.29	0.32	1.73	0.16	0.35	0.83	0.08	20.00	78.00	158.00	303.00

SAMPLE #	Level (m)	SiO2	TiO2	Al2O3	Fe2O3	MnO	MgO	CaO	Na2O	K2O	P2O5	V	Cr2O3	Ni	BaO
	GREEN ARGILLITES														
SA-18	251.00	71.55	0.57	11.12	7.17	1.10	2.00	0.48	2.24	1.14	0.13	42.00	18.00	15.00	1582.00
SA-17	245.00	72.13	0.44	10.07	5.62	1.50	1.55	1.72	2.65	0.86	0.09	18.00	26.00	10.00	1324.00
SA-16	226.00	80.31	0.16	9.50	3.25	0.59	1.24	0.02	4.01	0.19	0.03	22.00	67.00	10.00	476.00
SA-15	201.00	68.78	0.64	11.51	11.57	0.67	1.86	0.13	1.85	1.11	0.10	69.00	63.00	80.00	810.00
SA-14	195.00	75.85	0.54	8.16	5.54	1.68	0.69	1.58	2.32	0.87	0.08	53.00	99.00	44.00	538.00
SA-13	191.00	84.77	0.28	5.30	5.44	0.38	0.82	0.14	0.70	0.82	0.03	55.00	44.00	25.00	673.00
SA-12	182.50	69.81	0.53	9.52	14.26	0.70	1.44	0.16	0.91	0.87	0.07	67.00	100.00	61.00	466.00
SA-11 top	168.20	78.73	0.56	9.81	3.63	0.40	0.71	0.42	4.29	0.24	0.05	65.00	48.00	48.00	118.00
SA-11 botto	168.00	77.31	0.61	9.79	0.73	0.76	0.08	2.23	5.28	0.11	0.06	47.00	72.00	11.00	44.00
GI-21	167.00	80.86	0.46	8.64	1.89	1.26	1.40	0.24	3.50	0.15	0.08	28.00	31.00	42.00	165.00
SA-10	154.00	78.36	0.36	5.85	8.16	0.99	1.04	1.73	1.07	0.16	0.12	35.00	73.00	39.00	180.00
90-004		76.86	0.37	8.29	9.03	0.48	1.35	0.38	0.94	0.66	0.07	37.00	15.00	33.00	657.00
90-011		75.13	0.41	11.53	3.75	1.12	2.01	0.20	2.49	1.22	0.08	36.00	15.00	71.00	461.00
	Mn-RICH ARGILLITES														
GI-14	138.00	71.04	0.33	5.81	1.79	7.62	0.74	2.93	0.87	1.52	0.07	52.00	92.00	38.00	2103.00
GI-5	114.00	56.38	0.36	6.19	5.18	13.71	1.55	4.03	0.79	0.99	0.08	39.00	57.00	74.00	306.00
GI-4	112.00	58.88	0.60	10.29	7.60	8.57	1.83	2.09	1.80	1.43	0.08	66.00	127.00	55.00	438.00
	RED ARGILLITES														
GI-28	221.00	74.88	0.31	11.32	5.11	1.10	1.81	0.07	1.48	2.22	0.06	26.00	46.00	69.00	1018.00
GI-26	211.00	82.49	0.36	7.36	4.76	0.24	0.40	0.14	2.61	0.87	0.08	30.00	50.00	39.00	500.00
GI-23	182.00	83.20	0.22	4.46	6.85	0.68	0.61	0.88	1.48	0.45	0.35	29.00	90.00	23.00	462.00
GI-22	180.00	82.12	0.23	5.24	6.59	0.96	1.98	0.13	1.12	0.33	0.07	10.00	51.00	31.00	139.00

continued next page

SAMPLE #	Level (m)	SiO2	TiO2	Al2O3	Fe2O3	MnO	MgO	CaO	Na2O	K2O	P2O5	V	Cr2O3	Ni	BaO
	RED ARGILLITES continued from last page														
GI-19	152.00	81.33	0.43	7.01	5.63	0.33	0.46	0.37	1.76	1.28	0.08	28.00	38.00	26.00	390.00
GI-17	145.00	72.29	0.47	8.48	7.41	5.96	0.60	0.56	2.19	1.02	0.09	94.00	81.00	49.00	407.00
GI-16	135.00	72.48	0.44	7.60	13.46	0.59	1.07	0.24	1.36	1.74	0.16	60.00	96.00	92.00	567.00
GI-13	133.00	80.35	0.40	6.94	5.28	2.06	1.26	0.57	1.14	0.98	0.10	68.00	43.00	47.00	214.00
SA-9	132.00	69.22	0.79	12.15	8.26	0.82	2.04	0.57	3.03	1.71	0.16	97.00	106.00	42.00	604.00
SA-8	130.00	62.26	0.98	14.80	11.65	0.68	1.25	0.67	3.79	2.49	0.14	99.00	95.00	41.00	874.00
SA-7	125.00	66.74	0.77	13.19	9.94	0.54	1.27	0.72	2.89	2.51	0.17	61.00	99.00	37.00	912.00
SA-6	123.00	71.47	0.61	10.98	7.15	2.36	0.86	0.49	2.75	1.89	0.10	75.00	114.00	57.00	677.00
BB-16	122.50	77.14	0.38	7.27	9.52	0.86	0.88	0.23	1.26	1.61	0.11	116.00	111.00	62.00	764.00
GI-8	120.00	75.00	0.57	9.66	6.17	1.41	1.00	0.30	3.38	1.05	0.10	43.00	56.00	57.00	384.00
GI-10	117.00	76.70	0.48	9.38	6.46	0.59	0.85	0.29	3.56	0.90	0.09	29.00	65.00	72.00	507.00
SA-5	116.00	76.75	0.44	7.76	7.53	2.62	0.68	0.52	2.16	1.02	0.10	59.00	102.00	64.00	452.00
GI-2	111.00	64.87	0.49	8.64	18.78	0.96	1.52	0.29	1.05	1.63	0.21	72.00	122.00	70.00	538.00
GI-1	110.00	61.72	0.51	8.73	21.65	1.89	2.49	0.27	0.65	0.74	0.19	68.00	86.00	91.00	265.00
BB-15	109.00	68.38	0.77	8.99	14.35	0.82	0.81	0.38	1.83	2.11	0.16	50.00	87.00	88.00	753.00
SA-4	106.00	70.71	0.46	8.40	13.75	0.87	1.10	0.14	1.84	1.58	0.11	68.00	81.00	65.00	858.00
SA-3	105.00	69.57	0.45	8.33	14.64	1.06	1.20	0.36	1.85	1.38	0.26	57.00	84.00	73.00	703.00
BB-14	104.50	71.92	0.41	6.81	13.31	1.72	1.46	0.90	0.29	0.95	0.07	46.00	112.00	37.00	454.00
BB-12	93.00	76.22	0.37	6.51	6.91	1.18	0.89	1.45	1.16	1.61	0.11	56.00	74.00	27.00	376.00
BB-11	73.00	83.16	0.27	5.07	3.54	1.02	0.36	1.70	1.64	0.95	0.05	42.00	60.00	19.00	294.00
BB-7	58.00	83.53	0.33	6.12	5.59	0.45	0.68	0.25	1.08	1.33	0.06	42.00	15.00	30.00	256.00
BB-9	50.00	79.66	0.66	7.74	5.66	0.48	0.83	0.63	1.01	1.87	0.08	51.00	20.00	32.00	537.00
90-010		76.88	0.40	10.23	5.08	0.54	1.44	0.20	1.01	2.01	0.14	52.00	15.00	35.00	886.00
90-003		66.14	1.02	12.76	10.52	1.47	0.94	0.28	3.94	1.85	0.14	75.00	51.00	65.00	785.00
90-001		84.86	0.31	5.70	4.33	0.53	0.37	0.30	1.00	1.46	0.09	21.00	22.00	48.00	280.00
90-007		71.40	0.64	11.51	7.43	2.45	0.83	0.28	2.50	1.94	0.12	46.00	65.00	63.00	558.00

SAMPLE #	Level (m)	SiO2	TiO2	Al2O3	Fe2O3	MnO	MgO	CaO	Na2O	K2O	P2O5	V	Cr2O3	Ni	BaO
	UPPER WILD BIGHT GROUP														
SA-1	102.00	78.87	0.28	7.81	6.26	0.82	1.82	0.40	1.36	0.86	0.04	42.00	34.00	22.00	365.00
SA-2	101.50	75.92	0.35	11.00	4.50	0.63	1.64	0.30	2.06	2.07	0.06	44.00	71.00	14.00	811.00
BB-13	101.00	79.31	0.20	10.23	2.39	0.44	0.64	0.38	5.04	0.25	0.04	29.00	44.00	10.00	170.00
BB-8	61.00	77.63	0.33	6.90	3.46	1.40	0.69	3.31	1.78	0.92	0.06	61.00	77.00	27.00	191.00
BB-10	40.00	80.56	0.36	7.65	2.37	0.93	0.86	1.80	2.74	0.70	0.08	48.00	33.00	78.00	192.00
BB-3	24.00	79.80	0.46	7.40	5.18	0.50	0.76	1.04	2.08	1.26	0.11	51.00	15.00	46.00	277.00
BB-2	18.00	79.59	0.45	6.57	5.96	0.63	0.88	1.55	1.71	0.83	0.11	45.00	46.00	17.00	320.00
BB-1	0.00	75.87	0.34	9.87	3.80	0.42	0.76	1.82	3.50	0.88	0.08	34.00	15.00	10.00	255.00
SB-2		73.90	0.27	13.09	2.41	0.07	0.64	0.27	4.86	3.63	0.07	36.00	49.00	10.00	562.00
SB-9		76.23	0.22	10.63	5.78	0.17	1.03	0.28	4.24	0.87	0.08	33.00	67.00	10.00	155.00
90-002		77.23	0.53	9.66	5.44	0.17	0.73	1.36	1.09	2.42	0.10	40.00	15.00	30.00	542.00
90-012		66.50	0.72	14.48	6.09	0.22	1.38	4.21	1.58	2.63	0.27	32.00	15.00	10.00	446.00
90-013		55.53	1.14	14.29	8.56	0.14	6.67	5.18	3.94	1.74	0.15	128.00	608.00	184.00	289.00

Fe2O3* Total Fe expressed as Fe2O3
Detection limit for major elements: 0.01%, for Cr2O3: 15ppm, rest 10 ppm.
Analyses labelled BB-..:Beaver Bight; SA-..: Shoal Arm; GI-..: Gull Island.
Analyses labelled 90-... are samples from K.D. Nelson
Analysis LH-2 from Lawrence Harbour Peninsula; #332A is an analysis of a black slate collected by T. Kusky.

SAMPLE #	Level (m)	LOI	Total	Nb	Zr	Y	Sr	Rb	Pb	Th	U	Co	Cu	Zn
GREYWACKES														
90-005		3.55	100.40	16.00	132.00	23.00	63.00	79.00	13.00	9.00	5.00			
90-006		2.06	99.94	14.00	151.00	20.00	206.00	50.00	6.00	6.00	5.00			
SA-39		3.92	100.40	8.00	109.00	18.00	169.00	106.00	12.00	8.00	5.00			
SA-38		3.65	100.26	8.00	127.00	18.00	169.00	106.00	12.00	8.00	5.00			
SA-26		2.55	100.13	9.00	108.00	18.00	101.00	78.00	5.00	7.00	5.00			
SA-23		4.31	100.49	11.00	107.00	26.00	82.00	102.00	19.00	9.00	5.00			
GI-32	355.00	4.82	99.84	11.00	113.00	25.00	51.00	92.00	21.00	11.00	5.00	38.00	82.00	101.00
BLACK SLATES														
GI-40	348.00	4.62	100.15	5.00	42.00	16.00	16.00	49.00	7.00	6.00	6.00	10.00	93.00	51.00
GI-33	347.00	5.84	100.01	8.00	91.00	14.00	26.00	87.00	7.00	8.00	8.00	10.00	104.00	10.00
GI-39	345.00	4.56	100.32	10.00	58.00	20.00	19.00	63.00	5.00	5.00	5.00	10.00	102.00	114.00
GI-41	337.00	3.56	99.85	4.00	35.00	5.00	9.00	45.00	5.00	7.00	5.00	10.00	86.00	10.00
GI-42	335.00	4.35	100.13	11.00	61.00	16.00	36.00	67.00	5.00	5.00	5.00	21.00	110.00	10.00
90-008		3.68	100.09	14.00	88.00	18.00	22.00	46.00	5.00	5.00	13.00			
#332A		3.27		11.00	70.32	14.00	45.00	48.00	12.00	5.00	10.00			
GREY CHERTS														
GI-38	325.00	1.34	100.02	9.00	27.00	7.00	56.00	25.00	5.00	5.00	5.00	10.00	62.00	10.00
GI-35	320.00	2.43	99.63	5.00	41.00	11.00	47.00	46.00	14.00	8.00	2.00			
GI-36	310.00	2.36	100.28	9.00	38.00	9.00	59.00	39.00	12.00	5.00	5.00	10.00	102.00	24.00
GI-34	300.00	1.54	100.28	7.00	63.00	16.00	34.00	56.00	10.00	6.00	2.00			
GI-37	280.00	0.98	99.41	4.00	24.00	5.00	22.00	23.00	10.00	5.00	2.00			
SA-20	255.00	2.33	100.37	9.00	52.00	11.00	80.00	21.00	4.00	3.00	2.00	52.00	48.00	71.00
90-009		1.39	100.13	15.00	73.00	10.00	65.00	31.00	8.00	5.00	7.00			
LH-2		2.42	100.58	10.00	49.00	26.00	16.00	34.00	8.00	5.00	5.00	45.00	59.00	38.00

SAMPLE #	Level (m)	LOI	Total	Nb	Zr	Y	Sr	Rb	Pb	Th	U	Co	Cu	Zn
GREEN ARGILLITES														
SA-18	251.00	2.67	100.15	46.00	351.00	72.00	82.00	32.00	6.00	5.00	5.00	16.00	42.00	120.00
SA-17	245.00	3.58	100.21	40.00	355.00	68.00	178.00	25.00	4.00	7.00	2.00	10.00	82.00	115.00
SA-16	226.00	1.27	100.58	38.00	221.00	75.00	75.00	6.00	7.00	11.00	3.00	10.00	71.00	67.00
SA-15	201.00	2.56	100.66	11.00	103.00	20.00	48.00	37.00	6.00	8.00	5.00	99.00	28.00	93.00
SA-14	195.00	3.24	100.59	9.00	79.00	14.00	187.00	29.00	24.00	5.00	2.00	44.00	132.00	33.00
SA-13	191.00	1.54	100.25	6.00	44.00	8.00	20.00	28.00	16.00	7.00	2.00	39.00	60.00	31.00
SA-12	182.50	2.55	100.87	11.00	93.00	25.00	36.00	30.00	10.00	7.00	2.00	134.00	61.00	66.00
SA-11 top	168.20	1.18	99.60	14.00	104.00	15.00	84.00	8.00	33.00	5.00	5.00	32.00	107.00	34.00
SA-11 botto	168.00	2.20	98.80	14.00	113.00	16.00	221.00	5.00	27.00	5.00	5.00	10.00	94.00	10.00
GI-21	167.00	1.47	99.93	15.00	120.00	19.00	52.00	5.00	5.00	5.00	5.00	10.00	385.00	29.00
SA-10	154.00	3.02	100.85	10.00	57.00	17.00	93.00	6.00	4.00	7.00	2.00	51.00	72.00	36.00
90-004		2.23	100.73	16.00	92.00	11.00	71.00	22.00	10.00	7.00	6.00			
90-011		2.28	100.28	25.00	178.00	36.00	53.00	34.00	5.00	5.00	7.00			
Mn-RICH ARGILLITES														
GI-14	138.00	7.18	99.94	10.00	56.00	19.00	136.00	55.00	4.00	6.00	2.00	10.00	117.00	29.00
GI-5	114.00	11.68	95.30	10.00	62.00	23.00	51.00	37.00	10.00	7.00	5.00	44.00	139.00	49.00
GI-4	112.00	7.81	101.01	14.00	109.00	28.00	34.00	51.00	4.00	7.00	3.00	98.00	38.00	67.00
RED ARGILLITES														
GI-28	221.00	2.31	100.62	60.00	189.00	63.00	44.00	62.00	10.00	11.00	5.00	39.00	64.00	80.00
GI-26	211.00	0.76	99.94	12.00	73.00	16.00	34.00	29.00	5.00	5.00	5.00	39.00	51.00	22.00
GI-23	182.00	1.27	100.48	6.00	48.00	33.00	35.00	14.00	10.00	3.00	2.00	40.00	77.00	33.00
GI-22	180.00	1.51	100.16	9.00	54.00	22.00	21.00	13.00	11.00	6.00	5.00	78.00	52.00	78.00

continued next page

SAMPLE #	Level (m)	LOI	Total	Nb	Zr	Y	Sr	Rb	Pb	Th	U	Co	Cu	Zn
RED ARGILLITES (continued from last page)														
GI-19	152.00	1.17	99.72	13.00	73.00	13.00	36.00	42.00	9.00	6.00	5.00	10.00	48.00	21.00
GI-17	145.00	1.82	100.92	10.00	78.00	36.00	80.00	33.00	22.00	8.00	3.00	24.00	202.00	41.00
GI-16	135.00	1.47	100.65	10.00	73.00	29.00	19.00	62.00	19.00	6.00	3.00	170.00	38.00	81.00
GI-13	133.00	1.34	100.37	9.00	73.00	28.00	117.00	32.00	13.00	5.00	5.00	28.00	148.00	75.00
SA-9	132.00	1.85	100.63	15.00	182.00	34.00	82.00	54.00	12.00	10.00	2.00	51.00	102.00	125.00
SA-8	130.00	1.80	100.52	16.00	189.00	45.00	94.00	72.00	23.00	7.00	3.00	71.00	31.00	65.00
SA-7	125.00	1.82	101.57	13.00	170.00	41.00	73.00	73.00	20.00	7.00	2.00	75.00	53.00	74.00
SA-6	123.00	1.50	101.04	12.00	102.00	28.00	88.00	68.00	24.00	8.00	2.00	50.00	44.00	47.00
BB-16	122.50	1.18	100.46	9.00	65.00	35.00	48.00	50.00	24.00	7.00	2.00	103.00	58.00	53.00
GI-8	120.00	1.44	99.76	14.00	107.00	23.00	52.00	37.00	17.00	6.00	5.00	50.00	76.00	62.00
GI-10	117.00	1.12	100.76	12.00	85.00	16.00	52.00	34.00	15.00	5.00	5.00	53.00	82.00	51.00
SA-5	116.00	1.29	100.91	13.00	87.00	28.00	86.00	37.00	26.00	7.00	2.00	56.00	94.00	39.00
GI-2	111.00	1.88	100.33	11.00	78.00	36.00	20.00	60.00	35.00	6.00	3.00	160.00	79.00	48.00
GI-1	110.00	2.60	101.37	13.00	83.00	38.00	16.00	29.00	51.00	11.00	6.00	210.00	10.00	67.00
BB-15	109.00	1.86	100.89	17.00	134.00	37.00	25.00	71.00	27.00	8.00	3.00	143.00	45.00	76.00
SA-4	106.00	1.58	100.57	10.00	76.00	26.00	41.00	59.00	16.00	9.00	2.00	140.00	47.00	57.00
SA-3	105.00	1.77	100.82	10.00	71.00	29.00	53.00	52.00	16.00	5.00	3.00	155.00	55.00	67.00
BB-14	104.50	3.12	101.00	10.00	67.00	22.00	23.00	34.00	4.00	7.00	2.00	95.00	84.00	44.00
BB-12	93.00	3.83	100.24	9.00	80.00	23.00	30.00	48.00	6.00	7.00	3.00	31.00	39.00	50.00
BB-11	73.00	2.37	100.15	9.00	62.00	17.00	35.00	30.00	5.00	7.00	2.00	10.00	85.00	23.00
BB-7	58.00	1.24	100.78	14.00	72.00	12.00	16.00	44.00	5.00	6.00	5.00	34.00	54.00	40.00
BB-9	50.00	1.76	100.49	21.00	119.00	22.00	22.00	63.00	5.00	5.00	6.00	16.00	57.00	51.00
90-010		1.90	99.94	21.00	126.00	26.00	44.00	56.00	7.00	7.00	6.00			
90-003		1.65	100.82	20.00	156.00	42.00	106.00	69.00	24.00	7.00	5.00			
90-001		1.41	100.53	19.00	104.00	19.00	38.00	44.00	5.00	5.00	6.00			
90-007		1.71	100.89	19.00	135.00	30.00	72.00	60.00	28.00	8.00	5.00			

SAMPLE #	Level (m)	LOI	Total	Nb	Zr	Y	Sr	Rb	Pb	Th	U	Co	Cu	Zn
UPPER WILD BIGHT GROUP														
SA-1	102.00	2.17	100.73	12.00	94.00	27.00	27.00	25.00	4.00	7.00	2.00	40.00	108.00	94.00
SA-2	101.50	2.10	100.68	18.00	142.00	43.00	35.00	57.00	4.00	11.00	2.00	10.00	68.00	89.00
BB-13	101.00	1.22	100.15	18.00	137.00	43.00	37.00	6.00	4.00	13.00	3.00	10.00	73.00	55.00
BB-8	61.00	4.06	100.29	12.00	85.00	18.00	66.00	30.00	4.00	6.00	2.00	10.00	109.00	37.00
BB-10	40.00	2.53	100.37	22.00	95.00	18.00	51.00	23.00	5.00	5.00	5.00	10.00	120.00	45.00
BB-3	24.00	1.82	100.42	20.00	119.00	29.00	36.00	35.00	9.00	10.00	2.00			
BB-2	18.00	2.25	100.52	15.00	96.00	19.00	43.00	24.00	4.00	7.00	2.00	18.00	41.00	61.00
BB-1	0.00	2.39	100.40	28.00	232.00	41.00	66.00	27.00	5.00	5.00	5.00	10.00	70.00	90.00
SB-2		0.77	100.89	8.00	180.00	19.00	34.00	38.00	4.00	12.00	3.00	10.00	48.00	5.00
SB-9		0.99	100.54	3.00	30.00	21.00	35.00	29.00	12.00	7.00	2.00	10.00	82.00	64.00
90-002		1.65	100.47	51.00	240.00	165.00	168.00	65.00	6.00	6.00	5.00			
90-012		2.72	100.86	12.00	133.00	36.00	440.00	68.00	9.00	6.00	8.00			
90-013		2.43	99.89	15.00	126.00	19.00	27.00	30.00	5.00	5.00	7.00			

All above trace element analyses done on pressed powder pellets.
Detection limits: for Pb: 4 ppm, rest 2 ppm

Co, Cu, and Zn analyses done on fused beads prepared from ignited samples. Detection limit: 10 ppm

Appendix II

Duplicate analyses of Austin Glen shale (middle Ordovician flysch) to assess the precision of McGill XRF-analyses

	MC 86-017	MC 87-018	MC 87-093	MC 87-129	MC 88-015	UM	UM	MC 88-126	MC 90-014	MC 90-023	MC 90-067	MC 90-087	MC 91-036	MC 92-001	Mean	std. dev.
SiO2	50.54	50.76	50.61	50.47	50.54	50.34	50.82	50.76	50.21	49.97	50.12	50.25	50.19	49.86	50.39	0.29
TiO2	0.93	0.94	0.93	0.95	0.97	0.96	0.95	0.94	0.94	0.94	0.96	0.96	0.93	0.97	0.95	0.01
Al2O3	20.86	20.80	20.22	20.73	20.94	20.00	20.20	21.20	20.90	20.72	20.84	21.09	20.69	20.72	20.71	0.33
Fe2O3	8.11	8.18	8.03	8.26	8.03	7.76	7.83	8.08	7.83	7.95	7.99	7.95	7.97	8.01	8.00	0.13
MnO	0.06	0.06	0.05	0.06	0.06	0.07	0.06	0.07	0.06	0.05	0.05	0.06	0.07	0.05	0.06	0.01
MgO	2.71	2.70	2.70	2.71	2.62	3.10	2.63	2.71	2.57	2.75	2.73	2.74	2.62	2.65	2.71	0.12
CaO	4.00	4.02	3.86	4.12	4.04	3.79	3.96	4.03	3.98	3.97	4.00	4.06	3.94	4.01	3.99	0.08
Na2O	0.42	0.66	0.7	0.71	0.62	n.a	0.69	0.52	0.61	0.98	1.04	0.93	0.82	0.92	0.69	0.26
K2O	4.44	4.59	4.56	4.53	4.71	4.67	4.72	4.48	4.63	4.56	4.55	4.63	4.51	4.66	4.59	0.08
P2O5	0.16	0.16	0.16	0.16	0.16	n.a	0.12	0.16	0.15	0.15	0.16	0.15	0.15	0.15	0.14	0.04
LOI	7.99	8.02	8.18	8.21	8.14	8.04	n.a	7.98	8.19	8.13	8.39	8.39	8.39	8.12	7.56	2.11
ppm V	142	146	149	133	138	137	144	142	117	137	124	125	121	139	135	9.54
ppm Cr2O3	146	*	127	124	121	137	130	142	122	165	153	128	176	*	129	40.56
ppm Ni	44	*	44	46	56	46	27	49	39	69	57	53	41	*	44	15.96
ppm BaO	746	737	675	726	738	726	769	882	670	845	795	857	780	775	766	60.75
ppm Nb	20	21	21	n.a.	19	17	18	18	23	19	19	n.a.	16	18	18	6.89
ppm Zr	148	150	146	n.a.	143	164	163	161	160	145	145	n.a.	147	142	140	53.41
ppm Y	40	40	41	n.a.	41	38	36	37	36	35	36	n.a.	37	36	35	13.35
ppm Sr	141	143	141	n.a.	153	135	134	135	139	126	127	n.a.	127	126	125	46.05
ppm Rb	172	176	173	n.a.	170	174	177	168	172	166	166	n.a.	163	160	157	59.66
ppm Pb	14	24	13	n.a.	16	16	19	21	20	15	18	n.a.	17	17	16	6.72
ppm Th	13	17	7	n.a.	12	17	7	16	17	16	17	n.a.	18	19	14	6.28
ppm U	< 5	< 5	< 5	n.a.	< 5	n.d.	7	< 5	< 5	12	12	n.a.	6	2	--	--
ppm Co	n.a.	n.a.	n.a.	n.a.	n.a.	n.a.	n.a.	n.a.	n.a.	n.a.	n.a.	20	26	n.a.	24	--
ppm Cu	n.a.	n.a.	n.a.	n.a.	n.a.	n.a.	n.a.	n.a.	n.a.	n.a.	n.a.	66	70	n.a.	68	--
ppm Zn	n.a.	n.a.	n.a.	n.a.	n.a.	n.a.	n.a.	n.a.	n.a.	n.a.	n.a.	77	75	n.a.	76	--
Total	100.22	100.89	100.02	100.91	100.83	--	--	100.93	100.07	100.17	100.83	101.21	100.26	100.14	100.54	0.41

n.a. = not analyzed

* contamination indicated

MC = McGill University (Ahmedali); UM = University of Michigan (Arculus)